

# **X-ray Spectroscopic Study of Heterostructure Contacting Schemes for Optoelectronic Devices**

Von der Fakultät MINT - Mathematik, Informatik, Physik, Elektro- und Informationstechnik

der Brandenburgischen Technischen Universität Cottbus-Senftenberg

genehmigte Dissertation zur Erlangung des akademischen Grades eines

Doktor der Naturwissenschaften

(Dr. rer. nat.)

vorgelegt von

Diplom-Physikerin

**Ting Xiao**

geboren am 18.08.1986 in Hubei China

Gutachter: Prof. Dr. Ingo Flege

Gutachter: Prof. Dr. Inga Fischer

Gutachter: Prof. Dr. Marcus Bär

Tag der mündlichen Prüfung: 04. Juli 2019



## Abstract

Films of intrinsic and n-type doped (by Sn or H)  $\text{In}_2\text{O}_3$  variants have been prepared and their properties are studied using photoelectron spectroscopy (HAXPES and XES & XAS), Hall measurements and spectroscopic ellipsometry before and after annealing treatments. Optoelectronic properties that benefit the device applications of  $\text{In}_2\text{O}_3$ -based TCOs are investigated, the understanding of which is necessary to obtain a better combination of improved conductivity and transparency.

Film structures of  $\text{In}_2\text{O}_3$  variants before and after annealing are examined by X-ray diffraction, which indicates an amorphous-to-crystalline transition in  $\text{In}_2\text{O}_3\text{:H}$  during annealing. Annealing-induced solid phase crystallization of  $\text{In}_2\text{O}_3\text{:H}$  leads to a significantly improved electron mobility, which is confirmed by Hall measurements. A combination of hard X-ray (HAXPES) and soft X-ray (XES & XAS) photoelectron spectroscopy is employed to investigate the electronic and chemical structures of  $\text{In}_2\text{O}_3$  variants upon annealing, where the remarkable effects of annealing on the core-level and valence electronic structures are found in  $\text{In}_2\text{O}_3\text{:H}$ . Indium hydroxide dehydroxylation occurs in  $\text{In}_2\text{O}_3\text{:H}$  during annealing, which is well responsible for the structural transformation and a high electron mobility with a decreased carrier concentration in crystallized  $\text{In}_2\text{O}_3\text{:H}$ . A significant decrease in the intensity of occupied gap states is observed in crystallized  $\text{In}_2\text{O}_3\text{:H}$ , possibly due to a decrease in carrier concentration. Combining ellipsometry and photoelectron spectroscopy, the energy-level positions in relation to the gap disparity between the optical- and fundamental-band gaps upon doping is investigated before and after annealing. Doped  $\text{In}_2\text{O}_3$  variants have been found to have a quite deeper allowed transition level below the valence-band edge than undoped  $\text{In}_2\text{O}_3$ , which arises likely from a higher carrier concentration via doping. This in particular applies to crystallized  $\text{In}_2\text{O}_3\text{:H}$ , but most likely attributed to a change of the crystal structure upon annealing and/or a different O 2p-In 4d coupling near the VBM compared to amorphous  $\text{In}_2\text{O}_3\text{:H}$ .

Owing to the very high mobility of crystallized  $\text{In}_2\text{O}_3\text{:H}$ , the Ag/ $\text{In}_2\text{O}_3\text{:H}$  interface as a Schottky contact upon in-situ annealing is investigated using photoelectron spectroscopy. To well understand the interface properties of Ag/ $\text{In}_2\text{O}_3\text{:H}$  (i.e., interfacial chemistry, Schottky-barrier formation, and its variation) upon annealing, a thin Ag film was grown on the  $\text{In}_2\text{O}_3\text{:H}$  substrate and annealed in vacuum up to 300 °C. The annealing-induced changes have been in-situ

monitored by HAXPES, suggesting that the potential Ag diffusion into the bulk  $\text{In}_2\text{O}_3\text{:H}$  and/or a change of an annealing-induced Ag topography (i.e., cluster formation) occurs during annealing, with a small Ag oxidation (i.e.,  $\text{Ag}_2\text{O}$  and  $\text{AgO}$ ). With Ag deposition, an initial downward band bending of  $(0.11\pm 0.05)$  eV was present in  $\text{In}_2\text{O}_3\text{:H}$ , attributed to a Schottky contact formed at the  $\text{Ag}/\text{In}_2\text{O}_3\text{:H}$  interface. Upon annealing, the downward band bending reduces gradually, and the Schottky-barrier height at the  $\text{Ag}/\text{In}_2\text{O}_3\text{:H}$  interface also decreases during annealing.

Another purpose of this thesis has been devoted to obtaining high-quality GaN-based heterostructure used for LED devices. Mechanisms that limit the performance and quality of the GaN-based LEDs devices, i.e., carrier transport and recombination mechanisms, need to be well understood. For this reason, a thickness series of the individual materials on the respective “substrate” (i.e.,  $\text{MnS}/\text{Si}$ ,  $\text{GaN}/\text{MnS}$ , and  $\text{ZnO}/\text{GaN}$ ) was epitaxially grown on Si (100) wafer, and the interfacial chemistry and energy-level alignment at the respective interfaces are examined using photoelectron spectroscopy. At the  $\text{MnS}/\text{Si}$  interface, an interface-induced band bending (IIBB) appears in Si, which of values are found to be  $(0.15\pm 0.07)$  and  $(0.23\pm 0.07)$  eV for 4 and 15 nm  $\text{MnS}/\text{Si}$  stacks, respectively. The  $\text{MnS}/\text{Si}$  heterointerface shows a type-II (staggered) band lineup with a VBO of  $(-0.37\pm 0.10)$  eV and the corresponding CBO of  $(2.27\pm 0.10)$  eV. As for the  $\text{GaN}/\text{MnS}$  interface, a significant diffusion of Mn into the GaN layer takes place during GaN deposition. In addition, an interface-induced band bending (IIBB) by  $\sim 0.30$  eV is observed in MnS. The  $\text{GaN}/\text{MnS}$  interface shows a type-II (staggered) band lineup with a VBO of  $(1.46\pm 0.10)$  eV and the corresponding CBO of  $(-1.09\pm 0.10)$  eV. At the  $\text{ZnO}/\text{GaN}$  interface, a significant N diffusion from GaN into ZnO takes place, i.e., Zn-N bonds, when ZnO is grown on the GaN layer. Also, an interfacial oxide ( $\text{GaO}_x$ ) layer was formed during ZnO deposited on GaN films. In addition, the energy-level alignment at the  $\text{ZnO}/\text{GaN}$  heterointerface has also been determined by photoelectron spectroscopy technique, showing a type-II (staggered) band lineup with a VBO of  $(2.48\pm 0.10)$  eV and the corresponding CBO of  $(-2.50\pm 0.10)$  eV, respectively.

## Zusammenfassung

Filme aus intrinsischen und n-Typ-dotierten (durch Sn oder H)  $\text{In}_2\text{O}_3$ -Varianten wurden hergestellt und ihre Eigenschaften werden unter Verwendung von Photoelektronenspektroskopie (HAXPES und XES & XAS), Hall-Messungen und spektroskopischer Ellipsometrie vor und nach dem Tempern untersucht. Es werden optoelektronische Eigenschaften untersucht, die für die Bauelementanwendungen von  $\text{In}_2\text{O}_3$ -basierten TCOs von Nutzen sind, deren Verständnis für den Erhalt einer besseren Kombination aus verbesserter Leitfähigkeit und Transparenz, notwendig ist.

Filmstrukturen von  $\text{In}_2\text{O}_3$ -Varianten werden vor und nach dem Tempern mit Röntgenbeugung untersucht, welche auf einen Übergang von amorph zu kristallin in  $\text{In}_2\text{O}_3\text{:H}$  während des Temperns hinweisen. Durch Tempern induzierte Festphasenkristallisation von  $\text{In}_2\text{O}_3\text{:H}$  führt zu einer signifikant verbesserten Elektronenbeweglichkeit, was durch Hall-Messungen bestätigt wird. Eine Kombination aus harter (HAXPES) und weicher Röntgenphotoelektronenspektroskopie (XES & XAS) wird verwendet, um die elektronischen und chemischen Strukturen von  $\text{In}_2\text{O}_3$ -Varianten beim Tempern zu untersuchen, wobei bemerkenswerte Auswirkungen des Temperns auf Rumpfniveaus und Valenzelektronischen Strukturen in  $\text{In}_2\text{O}_3\text{:H}$  gefunden werden. Indiumhydroxid-Dehydroxylierung tritt in  $\text{In}_2\text{O}_3\text{:H}$  während des Temperns auf, welches für den Strukturwandel und einer hohen Elektronenbeweglichkeit mit einer verringerten Ladungsträgerkonzentration in kristallisiertem  $\text{In}_2\text{O}_3\text{:H}$  verantwortlich ist. In kristallisiertem  $\text{In}_2\text{O}_3\text{:H}$  wird eine signifikante Abnahme in der Intensität der besetzten Zustände in der Bandlücke beobachtet, möglicherweise aufgrund einer Abnahme in der Ladungsträgerkonzentration. Durch die Kombination von Ellipsometrie und Photoelektronenspektroskopie werden die Positionen der Energieniveaus in Bezug auf die Bandlückenunterschiede zwischen den optischen und den elektronischen Bandlücken beim Dotieren vor und nach dem Tempern untersucht. Für dotierte  $\text{In}_2\text{O}_3$ -Varianten wurde ein tieferer, unterhalb der Valenzbandkante liegender erlaubter Übergang gefunden als für undotiertes  $\text{In}_2\text{O}_3$ . Dies gilt insbesondere für kristallisiertes  $\text{In}_2\text{O}_3\text{:H}$ , das höchstwahrscheinlich auf eine Änderung der Kristallstruktur beim Tempern und/oder eine unterschiedliche O 2p-In 4d-Kopplung in der Nähe der VBM, im Vergleich zu amorphem  $\text{In}_2\text{O}_3\text{:H}$ , zurückzuführen ist.

Aufgrund der sehr hohen Mobilität von kristallisiertem  $\text{In}_2\text{O}_3\text{:H}$  wird die Ag/ $\text{In}_2\text{O}_3\text{:H}$ -

Grenzfläche als Schottky-Kontakt beim in-situ Tempern mit Photoelektronenspektroskopie untersucht. Um die Grenzflächeneigenschaften von Ag/In<sub>2</sub>O<sub>3</sub>:H (i.e., Grenzflächenchemie, Bildung der Schottky-Barriere und deren Variation) beim Tempern gut zu verstehen, wurde ein dünner Ag-Film auf dem In<sub>2</sub>O<sub>3</sub>:H-Substrat gezüchtet und im Vakuum auf bis zu 300 °C geheizt. Die durch Tempern induzierten Änderungen wurden in-situ mit HAXPES beobachtet, welche auf potenzielle Ag-Diffusion in den Bulk-In<sub>2</sub>O<sub>3</sub>:H und/oder auf eine Änderung einer Temper-induzierten Ag-Topographie (i.e., Clusterbildung) während des Tempern, mit geringer Ag-Oxidation (i.e., Ag<sub>2</sub>O und AgO), hindeutet. Bei Ag-Abscheidung war in In<sub>2</sub>O<sub>3</sub>:H eine anfängliche Abwärtsbandkrümmung von  $(0.11 \pm 0.05)$  eV vorhanden, die einem an der Ag/In<sub>2</sub>O<sub>3</sub>:H-Grenzfläche gebildeten Schottky-Kontakt zugeschrieben wird. Beim Tempern nimmt die Abwärtsbandkrümmung allmählich ab, und die Höhe der Schottky-Barriere an der Ag/In<sub>2</sub>O<sub>3</sub>:H-Grenzfläche nimmt während des Temperns ebenfalls ab.

Ein weiterer Zweck dieser Arbeit war der Erhalt einer qualitativ hochwertigen GaN-basierten Heterostruktur, die für LED-Bauelemente verwendet wird. Mechanismen, die Leistung und Qualität der GaN-basierten LED-Vorrichtungen einschränken, i.e., die Ladungsträgertransport- und Rekombinationsmechanismen, müssen gut verstanden werden. Aus diesem Grund wurde eine Schichtdickenserie der einzelnen Materialien auf dem jeweiligen „Substrat“ (i.e., MnS/Si, GaN/MnS und ZnO/GaN) epitaktisch auf Si (100)-Wafer aufgewachsen, und die Grenzflächenchemie und Energieniveauanpassung an den jeweiligen Grenzflächen wird mit Photoelektronenspektroskopie untersucht. An der MnS/Si-Grenzfläche tritt in Si eine grenzflächeninduzierte Bandkrümmung (IIBB) mit Werten von  $(0.15 \pm 0.07)$  und  $(0.23 \pm 0.07)$  eV für 4 und 15 nm MnS/Si-Stapel auf. Die MnS/Si-Hetero-Grenzfläche zeigt eine Typ-II (versetzte) Bandausrichtung mit einem VBO von  $(-0.37 \pm 0.10)$  eV und dem entsprechenden CBO von  $(2.27 \pm 0.10)$  eV. Bei der GaN/MnS-Grenzfläche tritt während der GaN-Abscheidung eine signifikante Diffusion von Mn in die GaN-Schicht auf. Dies führt zur potentiellen Bildung von Mn-N-Bindungen hauptsächlich in 2+ Ladungszuständen, i.e., Mn<sub>3</sub>N<sub>2</sub>, an den GaN/MnS-Stapeln. Zusätzlich wird in MnS eine grenzflächeninduzierte Bandkrümmung (IIBB) von  $\sim 0.30$  eV beobachtet. Die GaN/MnS-Grenzfläche zeigt eine Typ-II (versetzte) Bandausrichtung mit einem VBO von  $(1.46 \pm 0.10)$  eV und dem entsprechenden CBO von  $(-1.09 \pm 0.10)$  eV. An der ZnO/GaN-Grenzfläche wurde herausgefunden, dass eine signifikante N-Diffusion von GaN in ZnO stattfindet, i.e., Zn-N-Bindungen, wenn ZnO auf der GaN-Schicht aufgewachsen wird. Auch eine Grenzflächenoxidschicht (GaO<sub>x</sub>) wurde während des Abscheidens von ZnO auf dem GaN-Film gebildet. Darüber hinaus wurde die Energieniveauanpassung an der ZnO/GaN-

Hetero-Grenzfläche ebenfalls mit Photoelektronenspektroskopie bestimmt, wobei eine Typ-II (versetzte) Bandenausrichtung mit einem VBO von  $(2.48 \pm 0.10)$  eV und dem entsprechenden CBO von  $(-2.50 \pm 0.10)$  eV gefunden wurde.





# Contents

1. Introduction .....	1
1.1 Motivation .....	1
1.2 Outline .....	3
2. In <sub>2</sub> O <sub>3</sub> -based Transparent Conducting Oxides (TCOs) .....	5
2.1 Basic Electronic Structure .....	6
2.2 N-type Donor Defects.....	7
2.3 Bulk Band Gap .....	10
2.4 The Metal/In <sub>2</sub> O <sub>3</sub> Contact .....	14
3. GaN-based Light Emitting Diodes (LEDs).....	17
3.1 Principles of Operation (p-n junction).....	17
3.2 Band Offsets .....	19
3.3 GaN-based LED Structures .....	20
3.3.1 Substrate Considerations.....	20
3.3.2 Buffer Layers .....	22
4. Experimental Techniques .....	25
4.1 Sample Preparation.....	25
4.1.1 Multi-pocket Electron Beam Evaporator (EBE-4) .....	25
4.1.2 Molecular Beam Epitaxy (MBE).....	25
4.1.3 Energy Materials In-situ Laboratory Berlin (EMIL) .....	26
4.2 Characterization Methods.....	28
4.2.1 Photoelectron Spectroscopy .....	28
4.2.2 X-ray Photon-in-photon-out Spectroscopy .....	31
4.2.3 Synchrotron X-ray Sources.....	32
4.2.4 Variable Angle Spectroscopic Ellipsometry (VASE).....	36
5. Characterization and Analysis of Annealing-induced Modifications of In <sub>2</sub> O <sub>3</sub> Variants .....	37
5.1 Introduction .....	37
5.2 Experimental Details .....	38
5.2.1 Sample Preparation .....	38
5.2.2 Sample Characterization .....	38
5.3 Results and Discussion .....	41
5.3.1 Structural Properties.....	41
5.3.2 Electrical Properties .....	42
5.3.3 HAXPES Survey Spectra.....	43

5.3.4 Chemical Environment .....	45
5.3.5 Valence Photoelectron Spectra .....	51
5.3.6 Valence- and Conduction-band Structures .....	56
5.3.7 Band-gap Determination by Spectroscopic Ellipsometry .....	60
5.3.8 Energy-level Positions .....	68
5.4 Conclusion .....	72
6. Monitoring the Structure of the In-situ Annealed Ag/In <sub>2</sub> O <sub>3</sub> :H Interface .....	73
6.1 Introduction .....	73
6.2 Experimental Details .....	74
6.2.1 Sample Preparation .....	74
6.2.2 Sample Characterization .....	74
6.3 Results and Discussion .....	75
6.3.1 Surface Investigation .....	75
6.3.2 In-situ Monitoring of the Interface Chemistry upon Annealing .....	75
6.3.3 Fermi-edge Disappearance.....	84
6.3.5 Work-function Reduction .....	87
6.3.6 Schottky-barrier Height .....	89
6.4 Conclusion .....	90
7. Characterization and Analysis of the ZnO/GaN/MnS/Si Heterostructure .....	93
7.1 Introduction .....	93
7.2 Experimental Details .....	94
7.2.1 Sample Preparation .....	94
7.2.2 Sample Characterization .....	94
7.3 The MnS/Si Interface.....	95
7.3.1 HAXPES Survey Spectra.....	95
7.3.2 Interface Chemistry.....	96
7.3.3 Valence-band Structure.....	103
7.3.4 Interface Band Offset.....	104
7.4 The GaN/MnS Interface .....	106
7.4.1 Survey Spectra .....	106
7.4.2 Interface Chemistry.....	108
7.4.3 Near-surface Chemical Structure .....	115
7.4.4 Valence-band Structure.....	118
7.4.5 Interface Band Offset.....	119

7.5 The ZnO/GaN Interface.....	120
7.5.1 HAXPES Survey Spectra.....	120
7.5.2 Interface Chemistry.....	121
7.5.3 Valence-band Structure.....	126
7.5.4 Interface Band Offsets .....	128
7.6 Interface Energy-level Alignment .....	129
7.7 Conclusion.....	130
8. Conclusion and Outlook.....	131
Appendix A: Descriptions of ellipsometric analysis on In <sub>2</sub> O <sub>3</sub> variants. ....	135
Bibliography.....	137
Acknowledgements .....	153
Conferences .....	155



# 1. Introduction

## 1.1 Motivation

The world's economies are facing a series of challenges in exploiting clean energy, especially renewable energy, to maintain and improve environmental quality. One of the most promising sources of renewable energy is photovoltaic (PV) solar energy, which converts sunlight directly into electricity using semiconductor materials. To gain substantial power generation, the global optoelectronics market continues to seek new technologies based on lower energy consumption and better performance/cost ratios. High-power light-emitting diode (LED) devices have drawn considerable attention, converting electrical energy into light power, which are considered as excellent candidates for the ultimate light sources. Hence, PV and LED are the key technologies for paving the way into a new future.

Transparent conducting oxides (TCOs) are an essential component in many designs of PV and LEDs devices, where they act as a window layer to the cell [1, 2] and the electron-collecting electrode [3]. The potential applications of TCOs as transparent contacts largely benefit from the ideal combination of high transparency in the visible region and high electrical conductivity. Most of the TCOs are n-type semiconductors, of which the electrical conductivity depends on the electron mobility and the electron density in the conduction band. These two factors cannot be independently increased, but the intrinsic defects [i.e., oxygen vacancies ( $V_o^{2+}$ ) and metal interstitials ( $M_i$ )] (as discussed in Sec. 2.2) and extrinsic doping are used to improve the conductivity of TCO materials. Besides high conductivity, effective TCO materials should have a very low optical absorption coefficient in the ultraviolet-visible-near infrared (UV-VIS-NIR) region. The optical property of TCOs absorption is determined by the band gap. High transparency over a wide region requires a wide band gap. Basically, a large carrier density (usually via doping) can lead to an increase in the band gap due to the Burstein-Moss (BM) shift [4, 5]. As a result, doping of TCOs contributes to an improved conductivity and transparency (in most cases except the NIR wavelength range transparency as a result of enhanced free-carrier absorption [6]). In addition, the metal/TCOs interfaces can behave as Schottky contacts, which may have a considerable impact on the macroscopic behavior of electronic devices. Hence, a better understanding of the electrical and optical properties of TCO materials via doping and the Schottky contact interfaces based on them is of great importance.

Indium oxide ( $\text{In}_2\text{O}_3$ ) n-type doped with Sn results in a typical TCO, usually referred to as  $\text{In}_2\text{O}_3:\text{Sn}$  or ITO. At present, ITO dominates the TCO market rather than alternatives such as doped ZnO or  $\text{SnO}_2$  due to its better combination of a nearly metal-like conductivity and good transparency. However, doping  $\text{In}_2\text{O}_3$  with hydrogen, namely hydrogen-doped  $\text{In}_2\text{O}_3$  or  $\text{In}_2\text{O}_3:\text{H}$ , has recently emerged as a potential alternative for ITO.  $\text{In}_2\text{O}_3:\text{H}$  has a relatively higher carrier mobility of  $>100 \text{ cm}^2 \text{ V}^{-1} \cdot \text{s}^{-1}$  with better transparency in NIR (i.e., lower free-carrier absorption in NIR [6]) compared to the traditional low-mobility TCO materials [6]. This high mobility can be achieved by annealing-induced solid phase crystallization of  $\text{In}_2\text{O}_3:\text{H}$ . Despite that, there is no good understanding of the doped  $\text{In}_2\text{O}_3$  materials' optical and electrical properties, and especially the impacts of annealing.

Used as high-brightness LEDs, gallium nitride (GaN)-based heterostructure has attracted increasing research interest due to its efficient optical emission in the spectral region of blue, violet, and ultraviolet (UV) [7]. However, GaN-based heterostructure suffers from many defects, such as threading dislocations and native defects, which can limit the device's efficiency. For this reason, an epitaxial growth technique is required to obtain high-quality GaN epilayers. Generally, limitations for the epitaxial growth of GaN-based heterostructures are caused by the lattice mismatch at the epilayers' interface. The thickness and arrangement of the individual layers also strongly affect the growth quality of GaN epitaxial layers. Hence, a sophisticated structure design is imperative. Another critical issue is the gradual degradation of GaN-based LEDs performance due to the increase in potential barriers that control the carrier transport and recombination mechanisms within the devices. Unfortunately, the possible formation of intermediate layers at the involved heterointerfaces may create different barriers for the electrons and holes. As a result, an interfacial investigation (i.e., interfacial chemistry and electrical properties) on GaN-based heterostructures is of vital importance for the optimization of device performance.

## 1.2 Outline

In this work, an analysis of the chemical and electronic structures that may limit the optical and electrical properties of  $\text{In}_2\text{O}_3$ -based TCOs and GaN-based LEDs is present. To best present the findings of this thesis, it has been structured as follows,

- *Chapter 2:  $\text{In}_2\text{O}_3$ -based Transparent Conducting Oxides (TCOs)*

This chapter gives a brief overview of the basic properties of  $\text{In}_2\text{O}_3$ , including the crystal structure, basic electronic structure, n-type doping, and bulk band gap. Details on Schottky metal contacts to  $\text{In}_2\text{O}_3$  are also provided.

- *Chapter 3: GaN-based Light Emitting Diodes (LEDs)*

This chapter provides background information about the application and basic device operation based on the p-n junction of LEDs, the purpose of which is to introduce GaN-based LEDs. Details on improvements in the quality of epitaxial GaN layers and optimization of the structure design are also briefly discussed.

- *Chapter 4: Experimental Techniques*

This chapter addresses the sample preparation techniques regarding electron-beam evaporation (EBE) for Ag/ $\text{In}_2\text{O}_3$ :H growth and molecular beam epitaxy (MBE) for GaN epilayers growth, and the working principles of the characterization methods including X-ray photoelectron spectroscopy (XPS & HAXPES), soft X-ray spectroscopy (XES & XAS), and variable-angle spectroscopic ellipsometry (VASE) employed in this thesis.

- *Chapter 5: Characterization and Analysis of Annealing-induced Modifications of  $\text{In}_2\text{O}_3$  Variants*

This chapter discusses the impact of annealing on the properties of intrinsic and n-type doped (by Sn or H)  $\text{In}_2\text{O}_3$  variants, emphasizing the beneficial role of H donor on electronic structures of  $\text{In}_2\text{O}_3$ :H during annealing. Annealing-induced changes of the energy-level positions in the band gaps of  $\text{In}_2\text{O}_3$  variants, in particular for  $\text{In}_2\text{O}_3$ :H, are investigated experimentally.

- *Chapter 6: Monitoring the Structure of the In-situ Annealed Ag/In<sub>2</sub>O<sub>3</sub>:H Interface*

This chapter discusses the geometric and electronic structures, interface formation, and physical properties of Ag/In<sub>2</sub>O<sub>3</sub>:H upon in-situ annealing, emphasizing on the Schottky character of Ag/In<sub>2</sub>O<sub>3</sub>:H contact, i.e., Schottky-barrier formation with Ag deposition and barrier height reduction upon annealing.

- *Chapter 7: Characterization and Analysis of the ZnO/GaN/MnS/Si Heterostructure*

This chapter discusses the interface chemistry and the physical mechanisms including carrier transport and recombination of the respective ZnO/GaN/MnS/Si heterointerfaces using photoelectron spectroscopy. The energy-level alignments including the valence-(VBO) and conduction-band offsets (CBO) at the respective ZnO/GaN/MnS/Si interfaces are discussed in detail.

- *Chapter 8: Conclusion and Outlook*

This chapter summarizes the experimental results in this thesis. It also gives an outlook regarding future related work.



## 2. In<sub>2</sub>O<sub>3</sub>-based Transparent Conducting Oxides (TCOs)

Transparent conducting oxides (TCOs) are electrically conductive materials with the remarkable property of having a high transparency (>85%) in the visible region and a high electrical conductivity ( $\sim 1 \times 10^4 \Omega^{-1} \cdot \text{cm}^{-1}$ ) [8]. They are usually prepared with common thin film technologies and already find widespread application in optoelectronics devices such as PV and LEDs, including liquid crystal displays [9, 10], optoelectronic interfaces [3], gas sensors [11, 12] and circuitries [3, 13].

As one of the most commonly used TCOs, indium oxides (In<sub>2</sub>O<sub>3</sub>) has received much attention due to its key properties of good electrical conductivity and transparency. These properties can be unintentionally realized by intrinsic defects, mainly including native oxygen vacancies ( $V_o^{2+}$ ) and indium interstitials ( $In_i$ ), as will be described in Sect. 2.2. Several studies on nominally undoped In<sub>2</sub>O<sub>3</sub> have revealed the evidence for a bulk carrier concentration of around  $1 \times 10^{19} \text{ cm}^{-3}$  or more [14]. In addition, the incorporation of extrinsic dopants into In<sub>2</sub>O<sub>3</sub>, such as Sn and/or H impurities, is also an effective way to achieve an improved electron conductivity. As a prototype n-type In<sub>2</sub>O<sub>3</sub>, tin-doped indium oxide, referred to as indium tin oxide or ITO, is widely used due to its good conductivity and very high electron density of up to  $10^{21} \text{ cm}^{-3}$  [6]. Most importantly, doping with hydrogen in In<sub>2</sub>O<sub>3</sub>, namely H-doped In<sub>2</sub>O<sub>3</sub> or In<sub>2</sub>O<sub>3</sub>:H, has recently emerged as a potential alternative for ITO. Since In<sub>2</sub>O<sub>3</sub>:H has shown to obtain a high carrier mobility ( $>100 \text{ cm}^2/\text{V} \cdot \text{s}$ ) with a good NIR transparency [6, 15]. Owing to that, In<sub>2</sub>O<sub>3</sub> already has received increasing attention over recent years in various optoelectronics applications, such as the most common use as transparent contacts in liquid crystal displays [16], solar cells [17], and the active layers in electronic and short wavelength optoelectronic devices [18].

In<sub>2</sub>O<sub>3</sub> can exist in two main polymorphs [19]: body-centered cubic (*bcc*) and rhombohedral (*rh*) structures. Under standard conditions, In<sub>2</sub>O<sub>3</sub> crystallizes in the *bcc*-bixbyite structure with the space group  $Ia\bar{3}$ . The *bcc*-In<sub>2</sub>O<sub>3</sub> polymorph contains 80 atoms per unit cell, i.e., 48 oxygen atoms and 32 indium atoms. The conventional *bcc* structure is derived from a fluorite geometry (AO<sub>2</sub>), but with every fourth oxygen site left empty. The empty oxygen sites are well-known as “structural vacancies”. A unit cell consists of one type of oxygen atoms and two types of In atoms. The 48 O atoms occupy 48e Wyckoff positions in distorted tetrahedral sites, which contains four different In-O bond lengths of 2.133, 2.161, 2.187, and 2.247 Å, respectively. One quarter of the 32 In atoms locate at Wyckoff positions 8a in a trigonally compressed

octahedral coordination, with an In-O bond length of 2.161 Å. The remaining 24 In atoms occupying Wyckoff 24d sites are surrounded by oxygen in a highly distorted octahedral coordination, with three different In-O bond lengths of 2.133, 2.187, and 2.247 Å, respectively. Whereas, the *rh*-In<sub>2</sub>O<sub>3</sub> polymorph adopts the same structure as corundum (Al<sub>2</sub>O<sub>3</sub>) with the space group  $R\bar{3}c$ . It can also be described in terms of a hexagonal cell with  $a = b = 5.478$  Å and  $c = 14.51$  Å.

## 2.1 Basic Electronic Structure

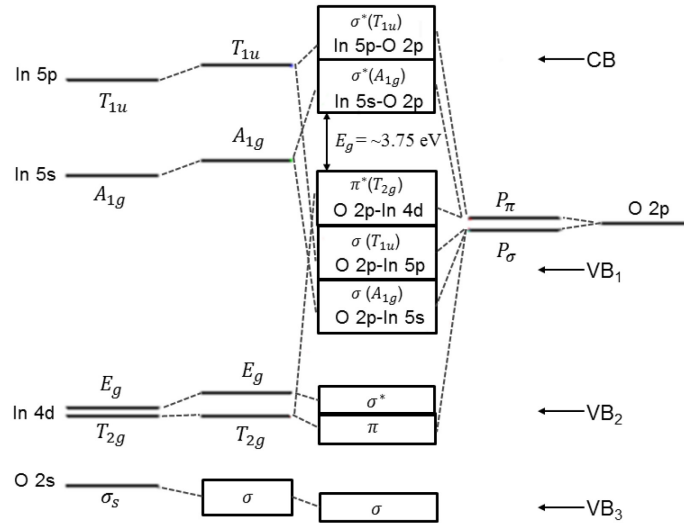


Figure 2.1: The molecular-orbital bonding diagram for pure In<sub>2</sub>O<sub>3</sub> (as taken from Ref. [20]). The whole valence band is comprised of three energy regions VB<sub>1</sub>, VB<sub>2</sub>, and VB<sub>3</sub>.

In terms of the ionic model, In<sub>2</sub>O<sub>3</sub> has a filled valence band of O 2p derived states associated with O<sup>2-</sup> and an empty conduction band of In 5s derived states associated with In<sup>3+</sup>. The shallow In 4d core level lies below the main valence band, but with some small hybridization at the topmost valence band. There is some pronounced hybridization between O 2p and In 5s, 5p derived states in the valence band, together with some hybridized O 2p/In 5s, 5p derived states in the conduction band.

According to the molecular-orbital model [21], the whole valence band (VB) is formed by the coupling between In and O states, consisting of three energy regions VB<sub>1</sub>, VB<sub>2</sub>, and VB<sub>3</sub>. It can be clearly seen in Fig. 2.1 that the bands at the lowest energy region VB<sub>3</sub> are mainly comprised of O 2s with some In 4d derived states. The main contribution to the intermediate energy region VB<sub>2</sub> originates from In 4d with some small O 2s, 2p derived states due to the hybridization interactions. The In 4d orbitals with the  $E_g$  symmetry overlap with six O 2s-p hybrid orbitals to give  $\sigma$  bonding and  $\sigma^*$  antibonding molecular bands. Similarly, the In 4d orbitals with the lower

$T_{2g}$  symmetry can overlap with three of the surrounding O 2p ( $P_{\sigma}$ ) orbitals to form  $\pi$  bonding bands at the bottom of the valence band, and  $\pi^*$  antibonding bands at the top of the valence band. In this case, the constitution of the valence-band edge in  $\text{In}_2\text{O}_3$  is primarily from the O 2p-In 4d hybridization derived states. The strength of the hybridization between O 2p and In 4d derived states is of critical importance in determining the optical-band gap of  $\text{In}_2\text{O}_3$  [22, 23]. The topmost  $\text{VB}_1$  region is mainly composed of O 2p derived states, which has some noticeable hybridizations with In (5s, 5p, 4d) derived states. Within the  $\text{VB}_1$  region, In 5p mixed with O 2p derived states forms  $\sigma$  bonding bands in the middle of  $\text{VB}_1$ , and  $\sigma^*$  antibonding bands on the upper part of the conduction band. Equivalently, the mixing of In 5s and O 2p derived states forms  $\sigma$  bonding bands at the bottom of  $\text{VB}_1$ . The bottommost conduction band is mainly originating from  $\sigma^*$  antibonding bands contributed by In 5s with some small O 2p derived states. In principle, the conduction band mainly consists of the  $\sigma^*$  antibonding bands, which is separated by a large band gap (typically  $\sim 3.75$  eV [24]).

## 2.2 N-type Donor Defects

If Sn replaces In on a bulk site without any compensating defects, it will introduce an extra electron (donor) to the  $\text{In}_2\text{O}_3$  lattice. This is referred to as n-type dopant. Alternately, one can incorporate hydrogen into  $\text{In}_2\text{O}_3$  to donate one valence electron. Some intrinsic point defects, i.e., oxygen vacancies ( $V_o^{2+}$ ) and indium interstitials ( $\text{In}_i$ ), can also explain the n-type conductivity in nominally undoped  $\text{In}_2\text{O}_3$  under a reducing condition. All intrinsic defects would have extra shallow energy states inside the band gap, donating free electrons into the conduction band. This applies in particular to the extrinsic defects as they have very low ionization energy. A release of the free electrons is mainly dependent on the donor transition energy (ionization energy); if the ionization energy of a dopant is sufficiently low to be fully ionized to generate electrons at room temperature which is known as a shallow donor, and vice versa. In the following, an overview of various potential intrinsic/extrinsic donor defects in  $\text{In}_2\text{O}_3$  is present.

### *Oxygen Vacancies ( $V_o^{2+}$ )*

An oxygen vacancy is created by removing an oxygen atom from the lattice sites. It can exist either in the bulk or at the surface of oxides in the charge states of 0 and 2+, where the 1+ charge state is thermodynamically unstable. The neutral oxygen vacancy ( $V_o$ ) is occupied by two electrons and forms a very deep donor level, thus it is not possible to excite these two electrons from the donor level into the conduction band. An oxygen vacancy with 2+ charge state ( $V_o^{2+}$ )

leaves two free valence electrons toward the cation lattices, thereby forming a shallow donor level.

Based on first-principles calculations [25], it was found that  $V_o^{2+}$  in  $\text{In}_2\text{O}_3$  has a large transition energy, i.e.,  $(2+/0) = E_{CBM} - 0.99$  eV, as shown in Table 2.1. It indicates that  $V_o^{2+}$  defect states in the band gap would not be easily ionized to provide large densities of free electrons into the conduction band at room temperature. According to hybrid-functional calculations, however, a  $V_o^{2+}$  in  $\text{In}_2\text{O}_3$  can act as a shallow donor under reducing conditions [26]. This is because  $V_o^{2+}$  can also be produced under oxygen-poor or vacuum conditions, thereby leading to a significant increase in carrier density. Although  $V_o^{2+}$  is an intrinsic defect and can provide electrons under oxygen-poor conditions, it is still not the predominant defect for the intrinsic n-type behavior in nominally undoped  $\text{In}_2\text{O}_3$ .

#### *Indium Interstitial ( $\text{In}_i$ )*

Indium interstitial ( $\text{In}_i$ ) is an intrinsic shallow donor in  $\text{In}_2\text{O}_3$ . There are two distinct types of In interstitial sites: one at an *a*-site ( $\text{In}_{i\_a}$ ) and the other at a *c*-site ( $\text{In}_{i\_c}$ ). Both types of In interstitials donate one electron to the In lattice in the charge state of  $3+$ . The interstitial  $\text{In}_{i\_a}$  is less stable with increased formation energy of around 0.60 eV compared to the interstitial  $\text{In}_{i\_c}$ . [27]. The ionization energies of the  $\text{In}_{i\_a}$  and  $\text{In}_{i\_c}$  are 0.572 eV and 0.187 eV, respectively, as shown in Table 2.1.  $\text{In}_i$  has a higher possibility for carrier generation than  $V_o^{2+}$ . Further,  $\text{In}_i$  can create a shallow donor level close to the bottom of the conduction band, while an even shallower donor level is formed when associating with a  $V_o^{2+}$  in the form of the cluster ( $\text{In}_i\text{-}V_o$ ). In fact, the considerable high conductivity in nominally undoped  $\text{In}_2\text{O}_3$  has been reported to mainly originate from the native  $\text{In}_i$ , but also coexisting with  $V_o^{2+}$  [28].

#### *Hydrogen Interstitial ( $\text{H}_i^+$ ) & Hydrogen Substitutional ( $\text{H}_o^+$ )*

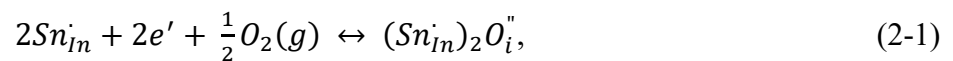
Interstitial hydrogen  $\text{H}_i$  is amphoteric, acting as an electron donor ( $\text{H}_i^+$ ) in n-type samples and as an acceptor ( $\text{H}_i^-$ ) in p-type samples. In this situation, the  $\text{H}(+/-)$  transition level would be located midway between the acceptor  $\text{H}(0/-)$  and donor  $\text{H}(+/0)$  levels, when hydrogen mainly forms donor (acceptor) states. Due to its self-compensation nature, hydrogen cannot be the cause of conductivity in conventional semiconductors, such as GaAs [29]. However, some research based on density-functional theory (DFT) has confirmed that a hydrogen center can act as a shallow donor in some oxide semiconductors, i.e., ZnO [30],  $\text{SnO}_2$  [31] and  $\text{In}_2\text{O}_3$  [32]. In  $\text{In}_2\text{O}_3$ , hydrogen interstitial  $\text{H}_i$  is proposed to form a shallow donor in the form of  $1+$  charge state ( $\text{H}_i^+$ ) as the formation energy of hydrogen interstitial ( $\text{H}_i^+$ ) is much lower than that of  $\text{H}_i^-$

and  $H_i^0$ . Furthermore, hydrogen interstitial ( $H_i^+$ ) is preferably stable since the neutral charge state ( $H_i^0$ ) is never stable, while the negative charge state ( $H_i^-$ ) typically acts as an acceptor. Based on first-principles calculations [32, 33], the estimated  $H(+/-)$  transition level is  $\sim 0.60$  eV above the conduction-band minimum (CBM). In addition to interstitial defects, hydrogen also can replace oxygen sites in the lattice and form substitutional hydrogen ( $H_o^+$ ) that can act exclusively as a donor in  $\text{In}_2\text{O}_3$ .

Either of the interstitial ( $H_i^+$ ) and substitutional ( $H_o^+$ ) hydrogen defect is more favorable than  $V_o^{2+}$  in  $\text{In}_2\text{O}_3:\text{H}$ . Thus, an improved n-type conductivity in  $\text{In}_2\text{O}_3:\text{H}$  is more likely from the interstitial hydrogen ( $H_i^+$ ) and/or coexistence of both ( $H_i^+$  &  $H_o^+$ ).

### *Sn<sup>4+</sup> Dopant*

When doped with  $\text{SnO}_2$ , Sn atoms can be partially incorporated into  $\text{In}_2\text{O}_3$ . Each Sn atom can substitute In at interstitial sites in the form of  $[\text{Sn}'_{\text{In}}]$ . The replacement of  $\text{Sn}^{4+}$  for  $\text{In}^{3+}$  sponsors one free electron to the matrix. Consequently, the substitutional  $[\text{Sn}'_{\text{In}}]$  can form fairly shallow donor states, thereby providing free electrons into the conduction band. It in turn causes a high free carrier concentration in ITO. When Sn doping levels are increased, however, the carrier concentration only attains a maximum value and then slowly decreases. The decrease is governed by inactive Sn dopants, which are attributed to compensation of Sn donors from  $[\text{Sn}'_{\text{In}}]$  by incorporation of oxygen anions into interstitial sites ( $O_i''$ ) [34]. The  $O_i''$  forms so-called “non-reducible” clusters, in which the excess  $O_i''$  reacts with two  $[\text{Sn}'_{\text{In}}]$  to give an electrically neutral  $(\text{Sn}'_{\text{In}})_2O_i''$  cluster,



In general, the amount of inactive  $\text{Sn}^{4+}$  dopants increases steadily with Sn doping concentration higher than 5 at.%. When Sn doping levels surpass  $\sim 10$  at.%, both the carrier concentration and conductivity decrease slowly. The highest carrier concentration attained a value of typically around  $1.5 \times 10^{21} \text{ cm}^{-3}$  can be achieved in about 10 at.% Sn incorporated ITO.

From above, the inactive Sn dopants result in a lower doping efficiency in heavily doped ITO with Sn doping level beyond 5 at.%. Thus, it would be an important challenge to maximize the electrically active concentration of  $\text{Sn}^{4+}$  dopants in  $\text{In}_2\text{O}_3$ .

## Defect Associates

Defects interact with each other and form defect associates, thereby producing new defect states inside the band gap. In  $\text{In}_2\text{O}_3$ , defect associates have been shown to play a dominant role in the determination of the doping/defect behavior and transport properties of the parent material. It has been confirmed that the defect associates can lead to much higher doping levels of up to 10 at.% in ITO. This is a result of coupling between donor defects, which forms an even shallower donor with a significant reduction in their formation energies [35]. Energetically, the ionization energies are also shown for the possible stable configurations of defect clusters in preferential  $\text{In}_2\text{O}_3$  lattice sites in Table 2.1. Evidently, the defect associates indeed have a quite shallow donor ionization energy. These defect associates have also been reported to be more stable with respect to their isolated defects due to their negative binding energies.

TABLE 2.1: List is the stable configurations for each defect cluster in preferential  $\text{In}_2\text{O}_3$  lattice sites with the respective ionization energy  $\Delta E_D$ .

Defect clusters	$\Delta E_D$ (eV)
$V_o^{2+}$	$\sim 0.99$ [25]
$In_{i_a}$	$\sim 0.57$ [27]
$In_{i_c}$	$\sim 0.19$ [27]
$H_i^+$	$\sim (-0.60)$ [32, 33]
$In_{i_a}-V_o$	0.099 [28]
$In_{i_c}-V_o$	0.101 [28]
$Sn_{In_b}-V_o$	$-(0.89)^*$ [35]
$Sn_{In_d}-V_o$	$-(1.29)^*$ [35]

\*The given ionization energies are in general equal to the calculated formation energies without consideration of the entropy effect.

## 2.3 Bulk Band Gap

One of the earliest optical absorption experiments on  $\text{In}_2\text{O}_3$  film was performed by Rupprecht in 1954 [36], in which he identified a significant absorption onset at around 350 nm ( $\sim 3.55$  eV), along with a weak tail of absorption extending to lower energy region. Later work by Weiher [24] suggested a value of 3.75 eV as a direct optical gap based on transmission measurements of  $\text{In}_2\text{O}_3$ . A weak absorption onset at around 2.69 eV was also found, attributed to an indirect transition. Subsequently, it became widely accepted that the band gap of  $\text{In}_2\text{O}_3$  was 3.75 eV, but ignoring the possible existence of the low-energy gap. Later, it was found that the position

of the valence-band maximum (VBM) relative to the Fermi level ( $E_{VBM}$ ) in photoelectron spectra of degenerately doped  $\text{In}_2\text{O}_3$  is less than 3 eV [37]. Apparently, this disagrees with a typical band gap of 3.75 eV unless there is pronounced upward band bending at the surface. Afterwards, it was suggested that an indirect gap could arise from coupling between O 2p and shallow core In 4d derived states, thereby resulting in the topmost valence band moving away from the  $\Gamma$  point [38]. However, it was further argued from band-structure calculations on  $\text{In}_2\text{O}_3$  that the upward dispersion of this sort in  $\text{In}_2\text{O}_3$  was shown to be only around 50 meV [39], disputing the presence of an upward dispersion of the topmost valence band by  $\sim 1$  eV in terms of an indirect gap.

Recently, Walsh *et al.* [40] proposed a new insight to this impasse by proposing that the onset of strong optical transitions from the valence band into conduction band is not at the VBM, but located at 0.81 eV below the VBM, as shown in Fig. 2.2. It was confirmed that the transition from the topmost valence band of ( $T_g$ )  $\Gamma_4$  symmetry to the lowest conduction band of ( $A_g$ )  $\Gamma_1$  symmetry is formally forbidden due to the dipole selection rule. As mentioned in Sect. 2.1, the states at the topmost valence band are a mixture of O 2p and shallow In 4d orbitals with ( $T_g$ )  $\Gamma_4$  symmetry, and the states at the lowest conduction band are derived from In 5s and O 2p hybridized orbitals with ( $A_g$ )  $\Gamma_1$  symmetry. The octahedral point group ( $O_h$ ) for the  $\text{In}_2\text{O}_3$  *bcc*-bixbyite structure has inversion symmetry, in which symmetry representation of  $O_h$  is of odd parity. This symmetry requirement suggests that the strong optical transitions are only allowed between two states with opposite parity. Consequently, the direct transitions from the VBM ( $\Gamma_4$ ) to the CBM ( $\Gamma_1$ ) are apparently forbidden (indicated by the grey arrow in Fig. 2.2). Conversely, strong optical transitions from a band ( $\Gamma_8$ ) 0.81 eV below the VBM into the conduction band is allowed (indicated by the blue arrow in Fig. 2.2). All transitions from valence-band states located in the range between 0-0.80 eV are very weak. Due to the symmetry-forbidden transitions, thus the optical-band gap (i.e., the energy distance from the CBM to the strong allowed transition level in the valence band) in  $\text{In}_2\text{O}_3$  is wider than the fundamental-band gap (i.e., the energy difference between the CBM and the VBM). Most recently, the physical origin of the gap disparity between the optical- and fundamental-band gaps has been investigated using first-principles calculations [22, 23]. It was concluded that stronger coupling between p and d orbitals in  $\text{In}_2\text{O}_3$  would lead to a larger difference between the optical- and fundamental-band gaps.

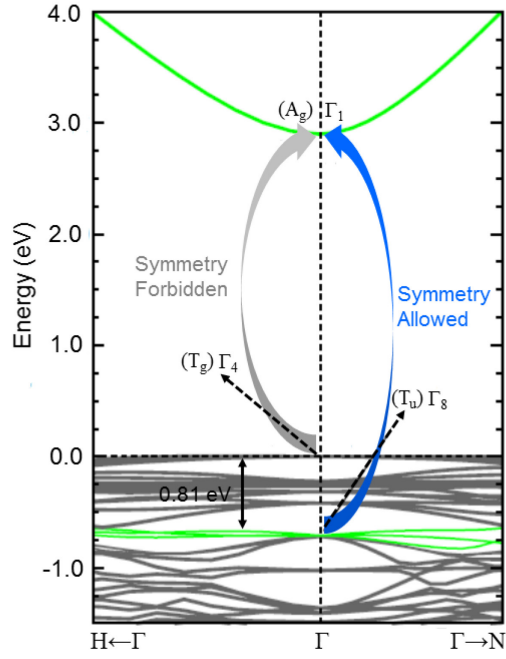


Figure 2.2: Band structure of In<sub>2</sub>O<sub>3</sub> (as adapted from Ref. [40]). The first strong optical transitions from a band located 0.81 eV below the valence-band maximum (VBM) into the conduction band are symmetry allowed (*blue arrow*), while the transitions from the VBM into the conduction band are symmetry forbidden (*grey arrow*). All transitions from valence band states in the energy range of 0-0.80 eV are very weak.

The bulk band gap in In<sub>2</sub>O<sub>3</sub> can be modified strongly by doping. The main effect is the Burstein-Moss (BM) shift [4, 5], which results in a widening of the optical-band gap through occupation of initially unoccupied states in the conduction band [i.e.,  $\Delta E_{g(CB)}^{BM}$  in Fig. 2.3 (b)]. At the same time, the valence band is shifted downwards [i.e.,  $E(k_F, \Delta E_{g(VB)}^{BM})$  in Fig. 2.3 (b)]. Upon degenerate doping above Mott's critical density, this widening effect can be partially compensated by the band-gap renormalization (BGR) effect [41, 42]. The BGR effect originates from many-body interactions between free electrons and the ionized impurities, which leads to a band-gap narrowing. It can shift the conduction band downwards [i.e.,  $E(k_F, \Delta E_{g(CB)}^{BGR})$  in Fig. 2.3 (c)] and the valence band upwards [i.e.,  $E(k_F, \Delta E_{g(VB)}^{BGR})$  in Fig. 2.3 (c)] as a result of electron-impurity and electron-electron scattering. Hence these two competing effects (i.e., the BM shift vs. the BGR effect) are dominant in governing the optical-band gap of degenerately doped In<sub>2</sub>O<sub>3</sub>.



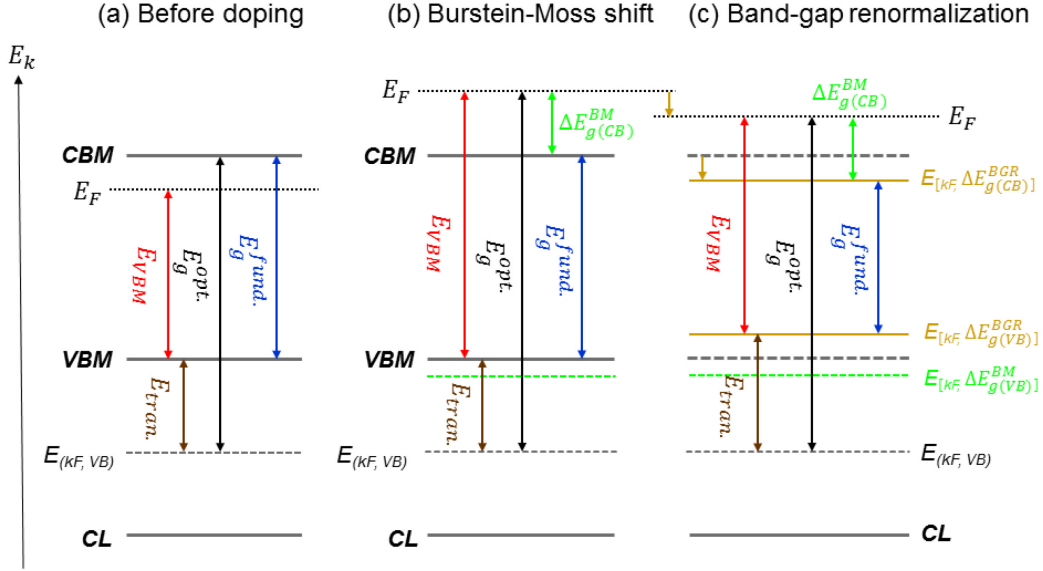


Figure 2.3: Schematic illustration of the effects of degenerate doping on the band gaps of  $\text{In}_2\text{O}_3$  [i.e., the fundamental- ( $E_g^{fund.}$ ) and optical-band gaps ( $E_g^{opt.}$ )]: (a) before doping (i.e., nondegeneracy), (b) after degenerate doping a band-gap widening occurs caused by the Burstein-Moss (BM) shift, (c) after a band-gap narrowing due to the band-gap renormalization (BGR) effect. The filling of conduction band [ $\Delta E_{g(CB)}^{BM}$ ] arises from the Burstein-Moss (BM) shift, which also results in a downward dispersion of the valence band [ $E(k_F, \Delta E_{g(VB)}^{BM})$ ] (green dash lines). An upward dispersion of the topmost valence band [ $E(k_F, \Delta E_{g(VB)}^{BGR})$ ] and a downward dispersion of the lowest conduction band [ $E(k_F, \Delta E_{g(CB)}^{BGR})$ ] are shown after band-gap renormalization (yellow dash lines). Note that the first strong optical transition from the valence into conduction band has been indicated as  $E_{tran.}$  (previously calculated 0.81 eV [40]) below the valence-band edge [ $E_{(k_F, VB)}$ ] (grey dash lines).

In undoped  $\text{In}_2\text{O}_3$  [Fig. 2.3 (a)], the CBM is located well above the Fermi level. The position of the VBM, denoted by  $E_{VBM}$ , is relative to the Fermi level. The fundamental-band gap ( $E_g^{fund.}$ ) is the energy distance from the CBM to the VBM. Due to symmetry-forbidden transitions, the optical-band gap ( $E_g^{opt.}$ ) in  $\text{In}_2\text{O}_3$  is the energy difference between the CBM and the first allowed transition level in the valence band (previously calculated 0.81 eV below the valence-band edge [40]). Upon degenerate doping of  $\text{In}_2\text{O}_3$  [Fig. 2.3 (b)], there is an increased filling of the conduction band caused by the Burstein-Moss (BM) shift. The Fermi level moves into the conduction band indicating the highest occupied states. The optical-band gap ( $E_g^{opt.}$ ) is the energy separation from the Fermi level to the first allowed transition level in the valence band (previously calculated 0.81 eV below the valence-band edge [40]). Upon doping above Mott's critical concentration [Fig. 2.3 (c)], the modification of electronic states occurs, which is known

as the band-gap renormalization (BGR) effect. The  $E_{VBM}$  is derived from the onset of the topmost valence dispersion [ $E(k_F, \Delta E_{g(VB)}^{BGR})$ ] relative to the Fermi level, and the fundamental-band gap ( $E_g^{fund.}$ ) is the energy separation between the topmost valence band [ $E(k_F, \Delta E_{g(VB)}^{BGR})$ ] and the lowest conduction band [ $E(k_F, \Delta E_{g(CB)}^{BGR})$ ] due to the band-gap renormalization (BGR) effect. In general, upon doping the optical-band gap ( $E_g^{opt.}$ ) increases whereas the fundamental-band gap ( $E_g^{fund.}$ ) decreases. Therefore, the gap disparity between the optical- ( $E_g^{opt.}$ ) and the fundamental-band gap ( $E_g^{fund.}$ ) in degenerately doped  $\text{In}_2\text{O}_3$  is strongly related to the Burstein-Moss (BM) shift and the band-gap renormalization (BGR) effect via doping.

## 2.4 The Metal/ $\text{In}_2\text{O}_3$ Contact

As stated previously, the high transparency and electrical conductivity properties of TCOs make them ideal contact materials to metals for thin film optoelectronics device applications, i.e., window layers of solar cells [43], electrodes for displays [44], and thin film transistors [45]. In general,  $\text{In}_2\text{O}_3$  has become an interesting candidate for probing metal/TCO contact due to its relatively high carrier mobility of more than  $100 \text{ cm}^2 \text{ V}^{-1} \cdot \text{s}^{-1}$  [6, 15], in comparison with the traditional low-mobility TCOs materials (e.g.  $\text{ZnO}$  and  $\text{SnO}_2$ ). Furthermore, it possesses a wide band gap and shows a prominent n-type behavior. Basically, the electrical contact between  $\text{In}_2\text{O}_3$  and metal may crucially affect the macroscopic behavior of electronic devices. For this reason, it is essential to understand the electrical properties of the metal/ $\text{In}_2\text{O}_3$  contact to improve the performance of electronic devices.

A rectifying metal/semiconductor interface was identified by Braun in 1874 [46], which was based on a metal/metal sulfide semiconductor device. He found a thin layer with extremely high resistance at the metal/metal sulfides interface. A few decades later, Schottky [47] demonstrated that the rectifying behavior arises from the potential barrier at the semiconductor surface. The presence of the potential barrier is attributed to a depletion layer on the semiconductor side of the interface. Subsequently, a model, named the Schottky-Mott rule, was proposed to predict the barrier height at the metal/semiconductor interface. In this regard, the Schottky-Mott model based on three types of metal contacts on (n-type) semiconductors is discussed below.

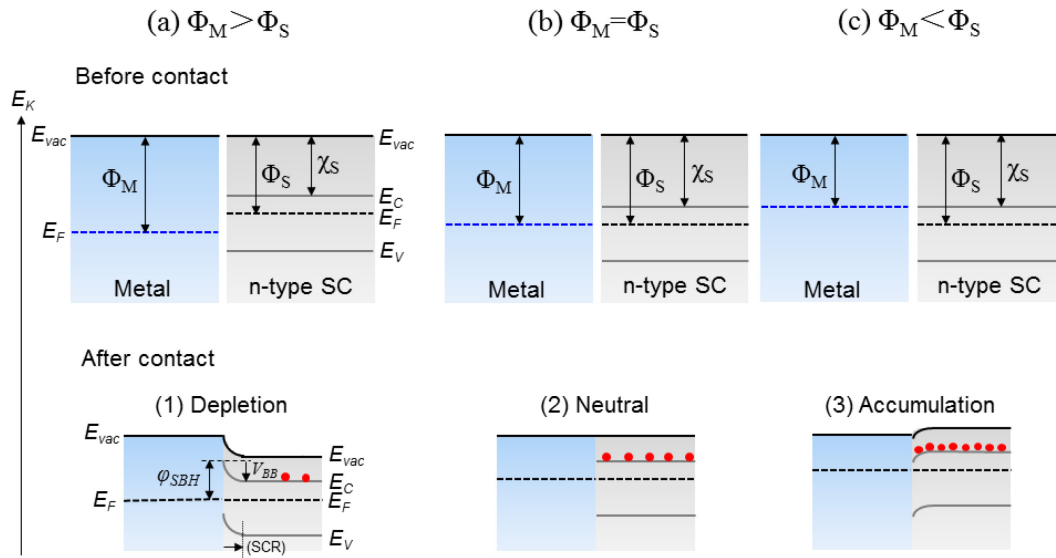


Figure 2.4: Schematic energy-level diagrams for three types of metal/(n-type) semiconductor (SC) junctions based on the simple Schottky model (as taken from Ref. [48]), with the following configurations: (a)  $\Phi_M > \Phi_S$ , (b)  $\Phi_M = \Phi_S$ , and (c)  $\Phi_M < \Phi_S$ . Contact (a) acts as a rectifier where a Schottky barrier height ( $\phi_{SBH} = \Phi_M - \chi_S$ ) exists at the interface, and a band bending ( $V_{BB} = \Phi_M - \Phi_S$ ) occurs at the near-surface region of the semiconductor. Contact (b) is unchanged (neutral), and contact (c) is an accumulation that is the preferred Ohmic contact. The upper and lower parts of the figure show the metal and (n-type) semiconductor before and after contact, respectively.  $E_V$ ,  $E_C$ ,  $E_F$ , and  $E_{vac}$  are the valence-band maximum (VBM), the conduction-band minimum (CBM), the Fermi level, and the local vacuum level, respectively.  $\Phi_M$  and  $\Phi_S$  are the work functions of the metal and the semiconductor;  $\chi_S$  is the electron affinity of the semiconductor;  $\phi_{SBH}$  is the Schottky barrier height of the interface;  $V_{BB}$  is the band bending. The width of the space charge region (SCR) is scaled in the depletion-type contact.

Fig. 2.4 shows the energy-level diagrams expected by the Schottky-Mott rule for different metal/(n-type) semiconductor junction configurations without surface states. When a metal is put into contact with a semiconductor, the free electrons will flow between the metal and the semiconductor due to their work function difference. The work function ( $\Phi$ ) of a material is the difference in energy between the Fermi level ( $E_F$ ) and the vacuum level ( $E_{vac}$ ). In Fig. 2.4 (a), the metal work function ( $\Phi_M$ ) is greater than that of the (n-type) semiconductor ( $\Phi_S$ ), i.e.,  $\Phi_M > \Phi_S$ , so the movement of electrons from the (n-type) semiconductor (high  $E_F$ ) into the metal (low  $E_F$ ) occurs until their Fermi levels are aligned. Under equilibrium, the flow of electrons from the (n-type) semiconductor into the metal results in the semiconductor positively charged with respect to the metal due to the electrostatic induction. In this situation, an internal electric field

is formed across the metal/semiconductor interface. The electric field can extend beyond the semiconductor surface due to the insufficient screening of the low carrier concentration in the semiconductor, whereas the electric-field can be neglected in the metal. This will lead to an electron depletion near the semiconductor surface compared to the bulk [Fig. 2.4 (a)]. The electron-depleted region is also called a space charge region (SCR). On the contrary, if  $\Phi_M$  is smaller than  $\Phi_S$ , i.e.,  $\Phi_M < \Phi_S$ , the electrons are accumulated in the space charge region (SCR) [Fig. 2.4 (c)]. This will produce an accumulation layer in the near-surface region of the semiconductor. If  $\Phi_M$  is equal to  $\Phi_S$ , i.e.,  $\Phi_M = \Phi_S$ , a neutral contact is obtained [Fig. 2.4 (b)].

In the space charge region (SCR), the internal electric field between the semiconductor and the metal allows the band edges of the semiconductor to shift continuously, an effect called band bending. When  $\Phi_M > \Phi_S$  [Fig. 2.4 (a)], the semiconductor bands bend upward near the surface; if the relative magnitudes are reversed, i.e.,  $\Phi_M < \Phi_S$  [Fig. 2.4 (c)], then the bands bend in the opposite direction. The magnitude of the band bending ( $V_{BB}$ ) in the near-surface region of the semiconductor can be expressed by the work function difference between the metal and the semiconductor,

$$V_{BB} = |\Phi_M - \Phi_S|, \quad (2-2)$$

For an (n-type) semiconductor without surface states, when  $\Phi_M > \Phi_S$ , there is a barrier height formed at the metal/semiconductor interface, which is called the Schottky barrier height ( $\varphi_{SBH}$ ) expressed as,

$$\varphi_{SBH} = \Phi_M - \chi_S, \quad (2-3)$$

Where  $\chi_S$  is the electron affinity of a semiconductor, defined as the energy difference between the CBM and the vacuum level. In Fig. 2.4 (a), the Schottky barrier height ( $\varphi_{SBH}$ ) is determined from the metal Fermi level to the conduction-band edge of the semiconductor. While in terms of  $\Phi_M < \Phi_S$ , the accumulation contact is achieved, behaving like a non-rectifying electric junction, i.e., Ohmic, [Fig. 2.4 (c)].

### 3. GaN-based Light Emitting Diodes (LEDs)

Light emitting diodes (LEDs) can be considered as the ultimate light sources due to their high luminescence efficiency, high reliability, low energy consumption and long lifetime [49]. These properties make LEDs ideal for use as displays and light sources, as in the case for roads, rail stations, and airports. In fact, these widespread applications have been significantly limited by the lack of high-brightness blue or green LEDs. Basically, full-color displays are required to reproduce the visible color spectrum, while white light is produced by mixing the three primary colors (i.e., red, green and blue). At present, conventional light sources, such as incandescent bulbs and fluorescent lamps, still face several problems of poor reliability, durability, and low luminescence efficiency. Due to this fact, much research has been conducted on the group-III-nitride semiconductors in efforts toward developing high-brightness blue LEDs. To date, the development of the group-III-nitride semiconductors has paved the way toward a revolution in high-brightness blue LEDs technology [50, 51], which makes them be very likely to replace the conventional light sources in some potential applications.

As an III-V-nitride semiconductor, GaN is one of the most promising materials for blue LEDs. GaN has a wide and direct band gap of 3.39 eV [52], which allows for efficient light emission in the spectral region of blue, violet, and ultraviolet (UV) [7]. GaN is also characterized by good thermal stability and high thermal conductivity, allowing for good heat dissipation within the devices. Furthermore, GaN can form alloys, which makes it possible to produce LEDs with a specific wavelength. All these features have made possible the materialization of high-brightness GaN-based LEDs. In recent years, GaN-based LEDs have already been developed at a breathtaking speed in some applicative fields, such as street lighting, solid-state lighting, projection fields, and automobiles.

#### 3.1 Principles of Operation (p-n junction)

An LED is essentially a p-n junction diode that converts electrical energy into visible optical power when a voltage is applied. The p-n junction in LEDs is of major importance in a wide range of optoelectronics applications. A good understanding of the LEDs requires a fundamental understanding of the p-n junction in semiconductors, including the electrical contacts.

When the n-type and p-type semiconductor materials are brought into contact, the transition region behaves in a very different way, which is generally known as the “p-n junction”. A

scheme of a simple LED p-n junction is shown in Fig. 3.1. Under forward biased conditions, electrons injected from the  $n$  region flow into the  $p$  region, and holes injected from the  $p$  region flow into the  $n$  region. The radiative recombination occurs at or near the junction when the electrons and holes flow as majority carriers across the junction. Throughout this process, the energy of the recombination reaction is released in the form of a photon. Thus, if the current keeps flowing, the electron-hole recombination continues. The radiative recombination occurring in direct band gap semiconductors enables the operation of most practical LEDs.

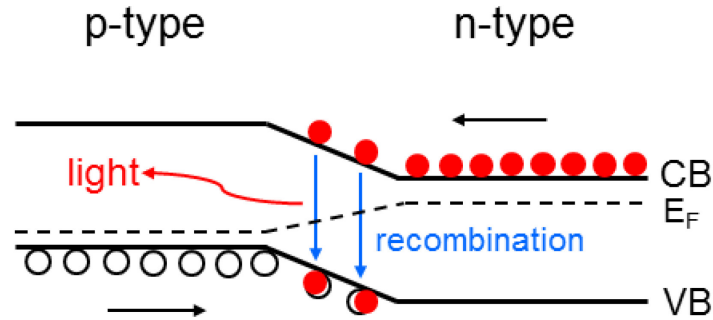


Figure 3.1: A simple LED p-n junction (as taken from Ref. [53]). Light is emitted when electrons and holes recombine radiatively at or near the junction.

Radiative recombination is required for high-efficiency LED devices, which means that the generated photons are not reabsorbed or trapped inside the semiconductors. In Fig. 3.1, an electron-hole pair recombines and makes a transition from the conduction band to the valence band. This recombination process emits a photon with energy almost equal to the energy gap ( $E_g$ ) of the semiconductor,

$$h\nu \approx E_g, \quad (3-1)$$

From the Eq. (3-1), the wavelength  $\lambda$  of photons emitted by a radiative recombination event is governed by the following expression [54],

$$\lambda \approx \frac{hc}{E_g} \approx \frac{1.24}{E_g(\text{eV})} [\mu\text{m}], \quad (3-2)$$

Where  $h$  is Planck's constant, and  $c$  is the speed of light in the vacuum, respectively. In this case, the wavelength of emitted photons is dependent on the energy gap ( $E_g$ ) of the semiconducting material. In fact, this relationship is just an approximation, as the thermal distribution of holes and electrons is slightly broadened to levels below the valence-band edge

and above the conduction-band edge, respectively. This results in a finite linewidth in the energy or wavelength of the emitted light.

### 3.2 Band Offsets

When a heterojunction is formed, the interface region behaves very differently from the bulk properties of the semiconductors, i.e., crystal potential and electronic structure. The individual offsets in the valence ( $\Delta E_V$ ) and conduction band ( $\Delta E_C$ ) determine the barriers for carrier transport and recombination, which are very important for the optimization of LED structures. Over the past few years, many attempts have been made to predict the values of these offsets ( $\Delta E_V$  and  $\Delta E_C$ ) for high-quality heterojunction LEDs. However, accurate determination of the band discontinuities at the heterointerface is extremely difficult in practical measurement.

One of the most popular direct methods of measuring the band offsets ( $\Delta E_V$  and  $\Delta E_C$ ) is by photoelectron spectroscopy. Using photoelectron spectroscopy, the determination of the band offsets mainly focuses on the heterostructures with relatively thin semiconductor overlayers grown on a suitable substrate due to its relatively small photoelectron sampling depth. In the early 1980s, Kraut *et al.* [55] proposed a powerful method to gauge the band offsets using photoelectron spectroscopy. To present the application of this method, the ZnO/GaN heterojunction system is reviewed as an example here.

Upon growing a ZnO overlayer on the top of a GaN film to form the ZnO/GaN heterojunction, the valence-band offset ( $\Delta E_V$ ) is calculated by the following relationship,

$$\Delta E_V = \Delta E_{CL} + [E_{Ga\ 2p} - E_{VBM}]^{GaN} - [E_{Zn\ 2p} - E_{VBM}]^{ZnO}, \quad (3-3)$$

Where  $\Delta E_{CL} = (E_{Zn\ 2p}^{ZnO/GaN} - E_{Ga\ 2p}^{ZnO/GaN})$  is the energy difference of the Zn 2p and Ga 2p core levels at the actual ZnO/GaN heterointerface.  $[E_{Ga\ 2p} - E_{VBM}]^{GaN}$  and  $[E_{Zn\ 2p} - E_{VBM}]^{ZnO}$  are the photoelectron-determined positions of the Ga 2p and Zn 2p core levels relative to the VBM in bulk films, respectively. Usually, the determination of the VBM energy ( $E_{VBM}$ ) relative to the Fermi level is accurately evaluated by a linear extrapolation of the leading band edge to the background. Therefore, the value of the  $\Delta E_V$  can be calculated from the locations of the valence-band edge ( $E_{VBM}$ ) and core-level photoelectron spectra of the overlayer and substrate. In general, the experimental uncertainty in the determination of  $\Delta E_V$  through such methods is typically  $\pm 0.10$  eV [36]. This uncertainty includes two factors: one is derived from the fitting procedure for the smallest variation in parameter space of  $\pm 0.05$  eV; the other one is from the determination of the positions of the valence-band edge ( $E_{VBM}$ ) and core-level photoelectron

spectra ( $\pm 0.05$  eV). In this case, the conduction-band offset ( $\Delta E_C$ ) for the ZnO/GaN heterojunction can be estimated by the following expression,

$$\Delta E_C = (E_g^{ZnO} - E_g^{GaN}) - \Delta E_V, \quad (3-4)$$

Where  $E_g^{ZnO}$  and  $E_g^{GaN}$  represent the band gap energies of bulk ZnO and GaN substrates, respectively. In this regard, the corresponding  $\Delta E_C$  at the ZnO/GaN heterointerface can be obtained from the determined value of  $\Delta E_V$  and the band gap energies of the bulk substrates at room temperature. However, the determination of  $\Delta E_C$  by this method has been valid only if the bulk properties of the sample are similar to the surface. Ideally, the conduction-band offset ( $\Delta E_C$ ) can be measured directly by inverse photoelectron spectroscopy (IPES), a technique not available for the present study.

### 3.3 GaN-based LED Structures

In order to develop GaN-based LEDs, a high crystal quality of the epitaxial layers and a sophisticated structure design are required. The simplest design of a GaN p-n junction LED is shown in Fig. 3.2.

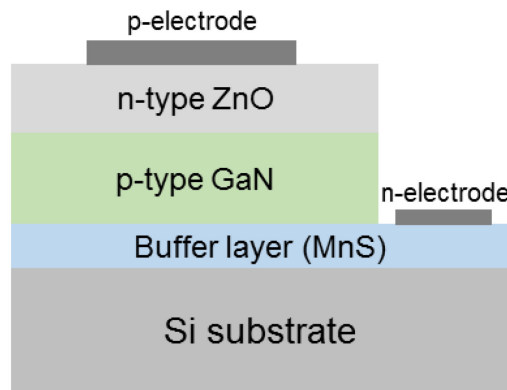


Figure 3.2: The structure of a GaN heterojunction light-emitting diode (LED) consisting of n-type ZnO/p-type GaN epilayers on the MnS buffered-Si substrate.

#### 3.3.1 Substrate Considerations

Over recent years, remarkable progress has been made in high-performance GaN-based LEDs grown on a variety of non-GaN substrates, including sapphire ( $Al_2O_3$ ), silicon carbide (SiC), and silicon (Si). Extensive research and development efforts have focused on these three key materials at present. The choice of substrate materials for the epitaxial growth GaN is a key design consideration to maximize the performance of GaN-based LEDs. In this regard, Table



3.1 summarizes and compares the properties of three key substrate materials including sapphire, SiC, and Si.

TABLE 3.1: Properties of key semiconductor substrates for heteroepitaxial GaN-based LEDs, regarding the lattice mismatch (%), thermal expansion coefficient ( $K^{-1}$ ), thermal stability (relative), relative substrate cost, and band gap (eV) (as taken from Ref. [56]).

Material	Lattice mismatch (%)	Thermal expansion coefficients ( $K^{-1}$ )	Thermal stability (relative)-at Tg	Cost (relative)	Band gap (eV)
6H-SiC	3.3	$4.20 \cdot 10^{-6}$	Very high	Very high	3.03
Si	17	$3.59 \cdot 10^{-6}$	Moderate	Low	1.12
sapphire	14.8	$7.50 \cdot 10^{-6}$	Very high	High	9.90

### *Sapphire*

Currently, the *c*-plane sapphire has been the most common substrate for the heteroepitaxial growth of a GaN epilayer. Because sapphire is transparent to UV and visible light, GaN-based LEDs on sapphire can extract light efficiently. In addition, it is possible to produce large-area and high-quality sapphire, which makes it available to GaN epilayers. However, the large mismatch in lattice constant between GaN and sapphire (approximately 14.8%) leads to a large number of inevitable dislocations ( $10^{10} \text{ cm}^{-2}$ ) in the grown materials. Such a high density of defects reduces the carrier mobility, the thermal conductivity and the non-radiative lifetime, thereby inducing degradation of device performance. For these reasons, several techniques such as lateral epitaxial overgrowth have been developed to minimize the number of growth defects. However, the thermal expansion coefficient of sapphire is significantly higher with respect to that of GaN, thus resulting in a poor crystalline quality of GaN grown epitaxially on sapphire.

### *Silicon Carbide (SiC)*

When compared with sapphire, SiC yields better properties as a substrate for GaN epitaxy. Higher crystal quality of GaN can be grown on SiC substrates because the lattice mismatch between GaN and SiC is only 3.3%, much smaller than that for sapphire and Si. This more suitable match makes it easier to nucleate and grow high-quality GaN on SiC than other non-GaN substrates. Another important advantage is that the thermal expansion coefficient of SiC is relatively close to that of GaN. Additionally, SiC can be doped to give good contact. However, a major drawback to SiC is its high cost. Moreover, the epitaxial growth of GaN on SiC meets

some problems concerning the poor wetting between these materials. Hence certain applications related to SiC have been limited.

### *Silicon (Si)*

When it comes to substrate size and cost, Si is undeniably favored to win because the long-term development and refinement of this semiconductor material make the heteroepitaxial growth of GaN on Si high efficient. At present, the Si industry has also driven the commercial success of substrates across extensive electrical resistivity for both n- and p-type conduction. Therefore, GaN-based LEDs have been largely manufactured on the Si substrates with a wide range of resistivities, such as intrinsic Si for RF power amplifiers and p-type Si for power switching. Moreover, it is widely available to achieve the high-quality, low-cost, and large-size of Si substrates. These properties make Si a very attractive option for the realization of GaN-based LEDs devices.

However, Si has a large lattice mismatch (17%) with GaN, which is inferior to the competing SiC and sapphire substrates. This creates a challenge to grow high-quality epitaxial GaN on Si substrates. Furthermore, the coefficient of thermal expansion between Si and GaN is inferior to SiC. More importantly, Si tends to form an amorphous  $\text{Si}_x\text{N}_y$  layer at the GaN/Si interface when exposed to nitrogen sources.

### 3.3.2 Buffer Layers

To obtain a high-quality GaN epilayer on sapphire or SiC substrates, an epitaxial growth technique is typically required. Considering the lattice mismatch and thermal expansion coefficient between the substrates and GaN, a sequence of layers generally referred to as the buffer layer, must be deposited to obtain GaN in high quality. Normally, the application of this buffer layer in GaN-based LED structures can reduce the threading dislocation density, strain energy, and electrical isolation. In recent years, various buffer layers for use in GaN-based LEDs have been reported in the literature [57]. AlN was first used as a buffer layer for the growth of GaN layers on sapphire substrates [57]. In addition, GaN buffer layers are widely used today. The main advantage of GaN over AlN as a buffer layer is in the absence of lattice mismatch between the film and the buffer layer. However, it has been claimed that the nitridation of the Si substrate may take place during the GaN initial growth on Si substrate [58]. Once a thin amorphous SiN layer is formed at the Si substrate surfaces, the crystallographic information from Si would be blocked.

To improve the surface morphology and crystalline quality of GaN, MnS has been used as a buffer layer for the GaN grown on sapphire substrates [59]. The main advantage of the MnS buffer layer is its wide direct-band gap (in typical around 3.02 eV [60]), high thermal conductivity, thermal and chemical stability, and a very small lattice mismatch ( $\approx -3.8\%$ ) with respect to Si. In addition, GaN films tend to crack on the Si substrates, which makes the production of thick crack-free films an important issue. With the introduction of an MnS buffer layer, however, these problems could be prevented.



## 4. Experimental Techniques

This chapter gives a short overview of the sample preparation techniques relevant to this thesis, including electron beam evaporation (EBE) for Ag deposition on the  $\text{In}_2\text{O}_3\text{:H}$  substrate and molecular beam epitaxy (MBE) for an epitaxial growth of GaN-based heterostructure (i.e., ZnO/GaN/MnS multilayers) on the Si (100) wafer. The working principles of employed characterization methods including X-ray photoelectron spectroscopy (XPS & HAXPES), X-ray emission and absorption spectroscopy (XES & XAS), and variable-angle spectroscopic ellipsometry (VASE) will also be covered.

### 4.1 Sample Preparation

#### 4.1.1 Multi-pocket Electron Beam Evaporator (EBE-4)

Electron beam (E-beam) evaporation is a deposition technique that evaporates a material to form a thin film of it on a substrate in vacuum. E-beam evaporation-4 (EBE-4) is a combined multi-pocket e-beam evaporator which can be used for multilayer films evaporation without breaking vacuum. The multi-pocket EBE-4 used in this thesis is manufactured by SPECS Surface Nano Analysis GmbH. An electron beam is generated from an electron source and used to heat the target material to temperatures of more than 3000 °C. High voltage is applied between the filament and the hearth to accelerate the electron beam towards the crucibles (or rods). The material from rods or crucibles is heated by electron bombardment from the surrounding filament. The energy of the electron beam is transferred to the deposition material, causing it to evaporate and deposit onto the substrate. Up to four species can be evaporated individually or in any combination for actual co-evaporation. Adding reactive gas, such as  $\text{O}_2$  or  $\text{N}_2$ , to the chamber can allow for the deposition of non-metallic films during evaporation.

#### 4.1.2 Molecular Beam Epitaxy (MBE)

Molecular beam epitaxy (MBE) is one of the most widely used techniques for the growth of high-quality III-V nitride semiconductors. In the MBE process, the source materials in shuttered cells are heated to form molecular beams. It consists of a manipulator for heating and rotating the substrate, shuttered effusion cells for sources of molecular beams, reflection high-energy electron diffraction (RHEED) gun, and a phosphor screen to monitor film surface structure [61]. The MBE crystal growth is a two-step process: the incident atoms are adsorbed to the crystal surface; the atoms at the surface are incorporated into the crystal. These two steps are dependent

on sublimates, temperature and crystal surface. Using MBE techniques could grow layers with controlled composition, doping, with crystal perfection, and with precisely controlled thickness.

MBE growth of GaN is a non-equilibrium process. A Ga vapor beam from an effusion cell and an activated N<sub>2</sub> beam from a plasma source are directed toward a heated substrate. Under suitable conditions, it is possible to produce high mobility GaN using layer-by-layer deposition of Ga and N atomic planes. However, it is difficult to incorporate molecular nitrogen (N<sub>2</sub>) source on Ga due to the very high binding energy of N<sub>2</sub> molecule in its ground state (9.9 eV) [62]. In order to obtain high-quality GaN film grown by MBE, a nitrogen plasma source is used and generated by inductively coupled radio frequency (RF). The RF nitrogen plasma source can emit a large number of atomic nitrogen and 1<sup>st</sup>-positive molecular nitrogen as the “active” nitrogen [62].

#### 4.1.3 Energy Materials In-situ Laboratory Berlin (EMIL)

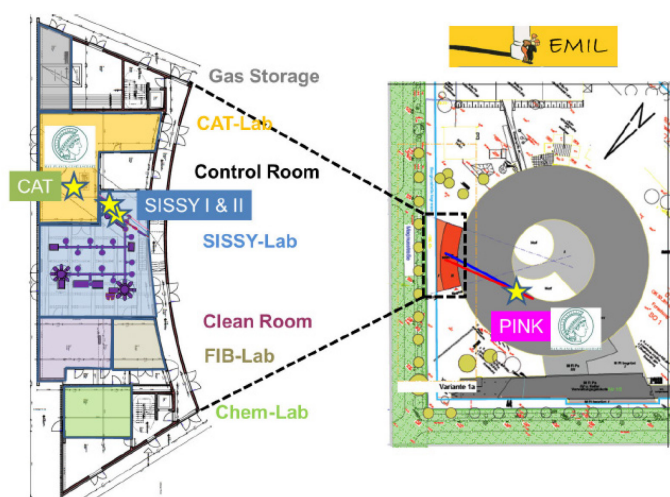


Figure 4.1: Sketch of the laboratory layout of EMIL and its location at the BESSY II synchrotron light source (as taken from Ref. [63]).

The Energy Materials In-situ Laboratory Berlin (EMIL) is a unique facility at the BESSY II synchrotron light source in Berlin, combining the Helmholtz-Zentrum Berlin für Materialien und Energie GmbH (HZB) and the Max-Planck-Gesellschaft (MPG) directed to research for sustainable renewable energy. Access to a dedicated beamline delivering high-brilliance light in the energy range of 80 eV-10 keV allows for a unique synchrotron-based X-ray analysis setup. Two canted undulators provide the energy ranges of 80-2200 eV (UE48) and 700 eV-10 keV (U17) for the radiation of soft- and hard X-rays, respectively. They are both installed inside the BESSY II storage ring in one straight section. At EMIL, an in-system and in-situ X-ray

spectroscopy technique can be employed to investigate the growth of materials and their interface properties (i.e., the formation and evolution).

The infrastructure layout of EMIL is illustrated in Fig. 4.1. The EMIL building attached to the BESSY II light source hosts three end-stations connected to several deposition clusters and a large integrated UHV-transfer system. The three main end-stations at EMIL are Solar Energy Material In-situ Spectroscopy at the Synchrotron (SISSY I), in-situ deposition/analysis chamber (SISSY II) and Catalysis Research for sustainable Energy Supply (CAT). SISSY has a combination of the state-of-the-art X-ray analytical techniques, and CAT focuses on fundamental research on catalytic processes under ambient conditions using near-ambient-pressure hard X-ray photoelectron spectroscopy. Two additional end-stations will be added to EMIL and located on the experimental floor of BESSY II: a scanning transmission X-ray microscope (STXM) and a hard X-ray emission spectroscopy end-station PINK. In addition, EMIL has a chemistry lab, a clean room, and a gas handling system with up to 30 different gases.

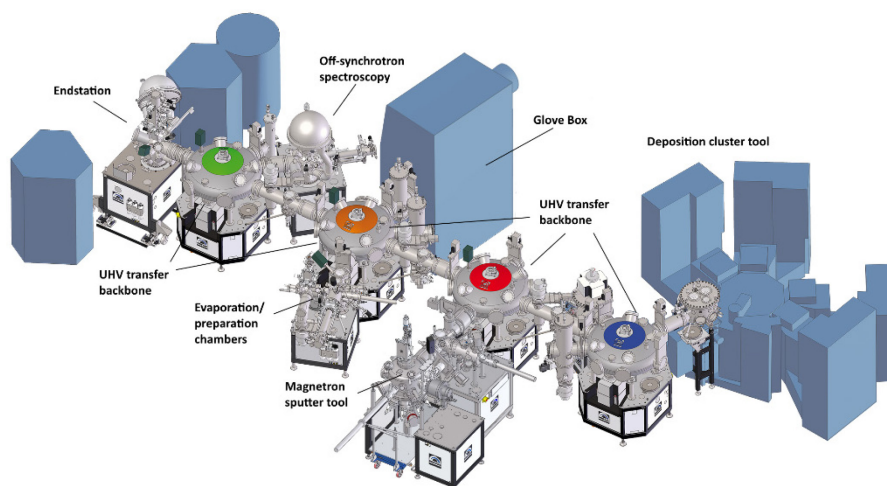


Figure 4.2: Integrated UHV system for automatic sample transfer across all the deposition and preparation chambers (as taken from Ref. [63]).

The SISSY lab provides the deposition and preparation facilities that are connected by an integrated UHV system, as shown in Fig. 4.2. A silicon deposition cluster tool with six deposition chambers are directly connected to the automated UHV transfer line. X-ray photoelectron spectroscopy ( $\text{Mg } K_{\alpha}$  and  $\text{Al } K_{\alpha}$ ) and ultraviolet photoelectron spectroscopy (UPS) can be carried out in the off-synchrotron analyzer chamber, which is connected to the preparation chamber in the UHV transfer system. The preparation chamber is equipped with an Argon ion gun for sample surface cleaning and a multi-pocket e-beam evaporator (EBE-4) (as

mentioned in Sect. 4.1.1). The samples in the UHV system can be automatically transferred across all the deposition/preparation chambers. This minimizes the time needed for sample transfer and reduces the probability of contamination, allowing for step-by-step deposition/analysis sequences.

## 4.2 Characterization Methods

### 4.2.1 Photoelectron Spectroscopy

Photoelectron spectroscopy (PES), specifically X-ray photoelectron spectroscopy (XPS), has been established as a widely-used technique for studying the elemental composition and electronic structure of solid surfaces and thin films nondestructively (in most cases). This technique utilizes X-ray photons to excite electrons from core and valence levels of the atoms in a solid surface into a vacuum, also known as the photoelectric effect.

#### *Basic Principles*

As mentioned above, XPS is based on the photoelectric effect, in which a solid surface is irradiated with X-ray photons of sufficient energy to excite electrons from their energy level in the solid into the vacuum. The emission of electrons is a simple process that can be divided into three stages: X-ray photons interact with the electrons of an atom within a matter and photoelectrons are generated; part of these ejected electrons travel through the solid and are scattered by various processes; electrons reach the solid surface and are emitted into the vacuum. The energy-level diagram for a direct photoelectron process is schematically shown in Fig. 4.3. An X-ray with the energy  $h\nu$  produces a core hole after interaction with a solid surface and transfers its energy to a core electron with the binding energy of  $E_{Bin}$  (with respect to the Fermi level  $E_F$ ). The emitted electron needs to overcome the work function of the sample ( $\Phi_S$ ) to escape into vacuum. Thus, the kinetic energy of that electron in a vacuum is given by  $(h\nu - E_{Bin} - \Phi_S)$ . Owing to the fact that the electric contact between the sample and the analyzer aligns their Fermi levels, the measured kinetic energy of photoelectrons is relative to the work function of the analyzer ( $\Phi_A$ ). Therefore, the kinetic energy ( $E_{Kin}$ ) measured by the analyzer is given by [64],

$$E_{Bin} = h\nu - E_{Kin} - \Phi_A, \quad (4-1)$$

In Eq. (4-1), the X-ray energy  $h\nu$  is given and the analyzer work function ( $\Phi_A$ ) is constant, the kinetic energy  $E_{Kin}$  is dependent solely on the binding energy  $E_{Bin}$ . The analyzer work function



is usually found to be about 4-5 eV, which is obtained empirically by setting the Fermi edge emission of a metallic sample (such as Au or Ni) to zero binding energy. After calibrating the energy scale ( $\Phi_A = 0$ ), thus the energy balance in Eq. (4-1) is described as follows,

$$E_{Kin} = h\nu - E_{Bin}, \quad (4-2)$$

It is obvious that Eq. (4-2) is valid only for conductive samples where their Fermi levels are aligned for the sample and the analyzer. While for insulators or sample charging, the Fermi level is not well defined, thereby causing energy shifts or preventing sample characterization.

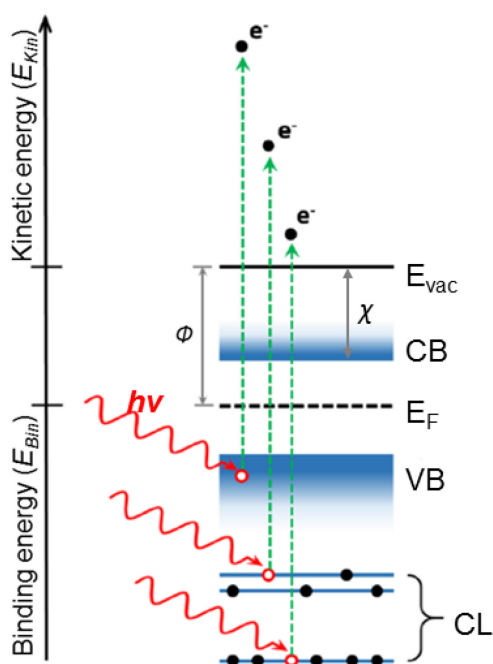


Figure 4.3: Schematic diagram of relevant energy levels in a direct photoelectron process of a semiconductor: the incident photon with the energy  $h\nu$  excites electrons from the core levels and valence band above the vacuum level ( $E_{vac}$ ).  $\Phi$ ,  $\chi$ , and  $E_F$  are the work function, electron affinity, and Fermi level, respectively.

Ultraviolet photoelectron spectroscopy (UPS) operates on the same principles as XPS, but it uses ionizing radiation in the energy range between 10 and 100 eV. In the laboratory, ultraviolet photons are typically produced using a helium discharge lamp with the energies of 21.2 eV for He I and 40.8 eV for He II. Furthermore, UPS is a very useful technique to determine the work function of a material.

#### *Inelastic Mean Free Path (IMFP)*

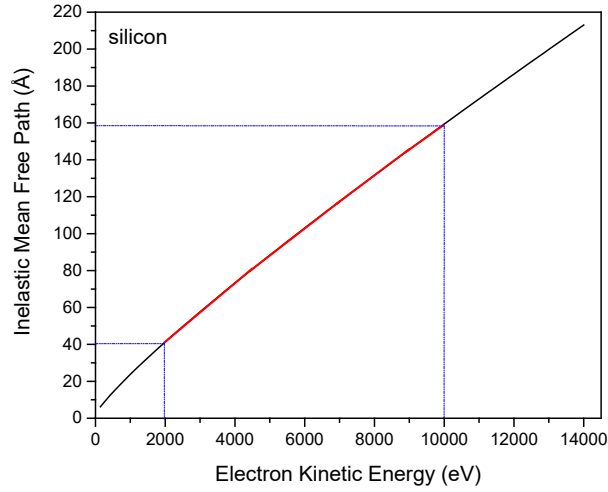


Figure 4.4: Inelastic mean free paths (IMFPs) of electrons in silicon as a function of electron kinetic energy according to Eq. (4-3).

For photoelectron spectroscopy analysis of solids, a key material parameter is the electron inelastic mean free path (IMFP), which is a measure of the average distance traveled by an electron through a solid without sustaining scattering-related energy losses. It is a function of the photoelectron energy and the nature of the material. Typically, the IMFP dependence on energy is defined for each material by the following equation [65],

$$\lambda = \frac{E}{E_p^2[\beta \ln(\gamma E) - (C/E) + (D/E^2)]} \quad (4-3)$$

Here  $\lambda$  is the IMFP for the electrons at a given electron energy  $E$ , and  $\gamma$ ,  $\beta$ ,  $C$ , and  $D$  are parameters dependent on the materials. In addition,  $E_p = 28.8(N_v\rho/M)^{1/2}$  is the bulk plasmon energy where  $N_v$  is the number of valence electrons per atom or molecule,  $\rho$  is the bulk density (in  $\text{g}/\text{cm}^3$ ), and  $M$  is the atomic or molecular weight. With Eq. (4-3), the fits for the calculated IMFPs yield a similar tendency for a large number of solids for photon energies between 0.1 eV and 30 keV. Fig. 4.4 shows IMFPs of electrons in silicon as a function of electron energy according to Eq. (4-3). It indicates that the electron energies within the range of 10 eV-2 keV yield inelastic mean free path (IMFP) values ranging from 1-4 nm for silicon. In conventional XPS setups employing Mg  $K_\alpha$  (1253.56 eV) and Al  $K_\alpha$  (1486.58 eV) radiation, the maximum IMFP values of the detected photoelectrons from thin film samples are  $\sim 2$  nm. It is possible to reach photoelectron signals from tens of nanometers below the surface by increasing the photon energies. For example, the IMFP of photoelectrons excited by a photon energy of 10 keV can be about 16 nm, almost four times larger than that at 2 keV photon energy ( $\sim 4$  nm).

## 4.2.2 X-ray Photon-in-photon-out Spectroscopy

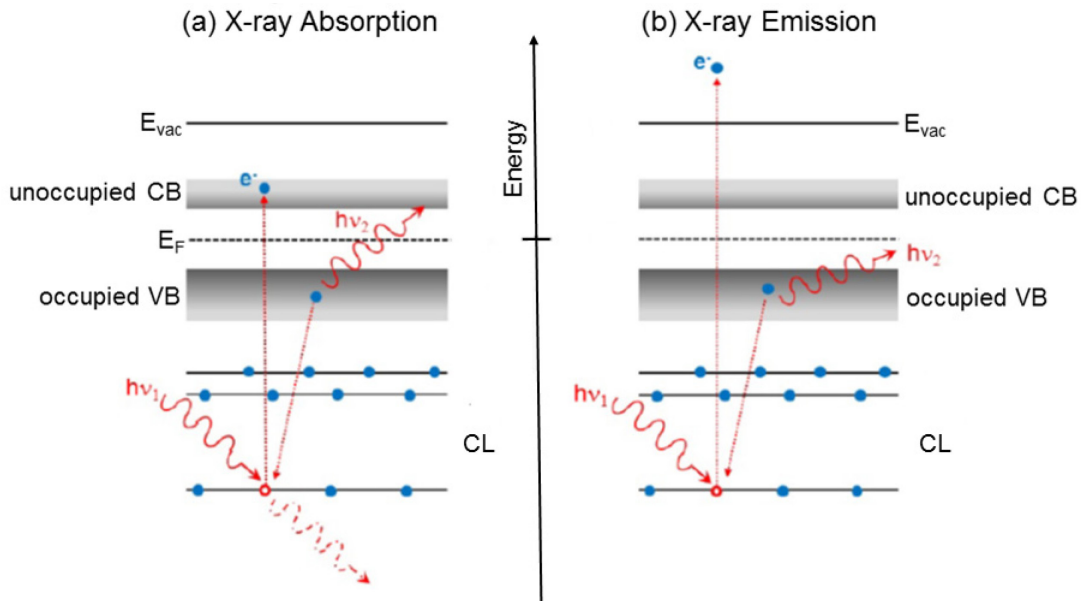


Figure 4.5: (a) X-ray absorption process, photon ( $h\nu_1$ ) excites an electron into the conduction band, as it probes the density of unoccupied electronic states. (b) X-ray emission process, photon ( $h\nu_1$ ) excites an electron above the vacuum level ( $E_{vac}$ ), and a valence electron decays by emitting a photon ( $h\nu_2$ ) to fill the excited hole, as it probes the density of occupied electronic states.

X-ray photon-in-photon-out spectroscopy with energies in the range of approximately 100 eV to 2 keV is used to provide valuable information for characterizing surfaces and near-surface interfacial layers. Photon-in-photon-out spectroscopy experiments use a tunable synchrotron radiation source and focus it onto a sample to be studied. Two techniques provide complementary information: X-ray absorption (XAS) and emission spectroscopy (XES).

### *X-ray Absorption Spectroscopy (XAS)*

X-ray absorption spectroscopy (XAS) is used to effectively probe the partial density of unoccupied electronic states of a material. Fig. 4.5 (a) shows an available absorption process. In this technique, when the synchrotron radiation interacts with the material, photons are absorbed by exciting core electrons into the conduction band. Absorption spectroscopy measures the absorption rate of photons as a function of their energy. According to the selection rule for dipole radiation, electron transitions with a change in orbital angular momentum quantum number  $\Delta l = \pm 1$  are only allowed, since momentum must be conserved, and photons have angular momentum (spin) of one unit. Each element has characteristic binding energy for

a certain core level and thus XAS is an element-specific technique. The absorption will increase for energies where the transition probability is higher; therefore, the absorption spectrum is actually a measure of the density of unoccupied states for electrons in materials.

#### *X-ray Emission Spectroscopy (XES)*

X-ray emission spectroscopy (XES) probes the partial density of occupied electronic states of a material, as shown in Fig. 4.5 (b). When a core electron is excited to the continuum or to some unoccupied states, a core hole is left in its excited state. There are many ways for the system to collapse back to the ground state, there is a small probability that some valence electrons will decay to fill the core holes by the emission of photons. Since the energy of the emitted photon will match the energy difference between that valence electron and the core level, the intensity distribution of all emitted photons will correspond to the probability of finding electrons in the valence band at those energies. Therefore, emission spectroscopy is a measure of the density of occupied states for electrons in materials. Similar to XAS, XES is also an element specific and site-specific technique that makes it a useful tool to study and distinguish different elements.

#### 4.2.3 Synchrotron X-ray Sources

To obtain a larger probing depth on a sample, hard X-ray photoelectron spectroscopy (HAXPES) with high-energy X-rays has been employed from a multi-GeV storage ring. The use of synchrotron radiation enables us to investigate the intrinsic bulk electronic structures and buried interface properties of the materials. In this thesis, HAXPES measurements were performed using synchrotron X-ray sources at BESSY II (KMC-1) in Germany and SPring-8 (BL47XU) in Japan. In addition, soft X-ray photon-in-photon-out methods (XAS & XES) were performed at the high flux synchrotron source ALS (8.0.1) (Lawrence Berkeley National Laboratory, USA). This section presents a brief overview of the synchrotron radiation infrastructure used in our experiments. Also, the physical principles behind the synchrotron-based spectroscopic techniques are discussed.

## BESSY II (Beamline KMC-1)

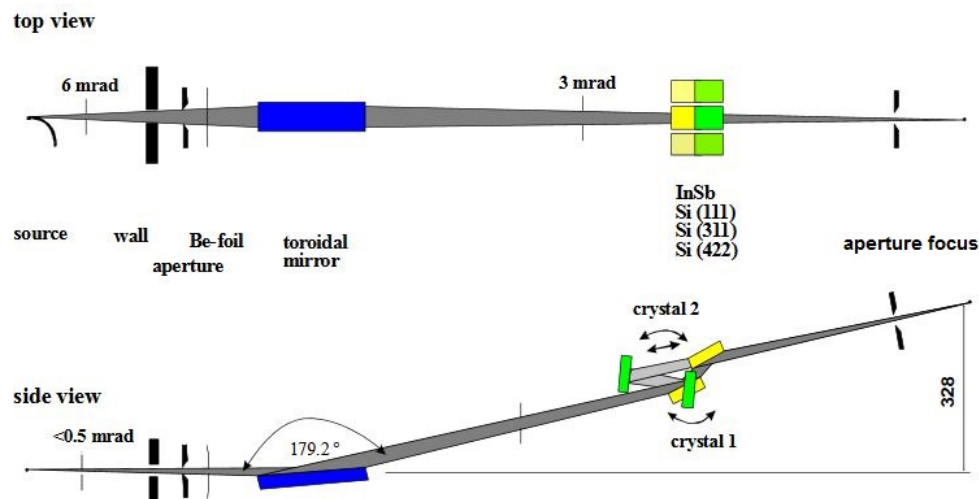


Figure 4.6: Schematic setup of the beamline KMC-1 at BESSY II (as taken from Ref. [66]).

As a third-generation synchrotron source, BESSY II with a ring energy of 1.7 GeV has been optimized to produce vacuum ultraviolet (VUV) and soft X-ray radiation. At BESSY II, ring currents of up to 300 mA are used, and the photon flux in the range of  $10^{11}$ - $10^{12}$  photons/s can be typically achieved throughout the whole energy range.

The KMC-1 beamline at BESSY II is a tender X-ray double crystal monochromator beamline and covers the energy range from “tender” (2.0 keV) to hard X-rays (12 keV). Fig. 4.6 shows the schematic setup of the beamline KMC-1 at BESSY II [66]. The purpose of this design is to focus monochromatic photons with a high energy resolution as much as possible onto the sample. A collimating mirror with an available surface size of  $800 \times 130$  mm is required to be very close to the electron beam source. The minimum distance between the focusing mirror and the source point is about 13 m. This toroidal mirror focuses the beam into a well-focused spot with the size of approx.  $0.3 \times 0.5$  mm<sup>2</sup>. In front of the mirror, a water-cooled Be foil is used to remove the heat load. About 15 m away from the mirror, an ( $n$ ,  $-n$ ) double crystal monochromator (DCM) is placed for reflecting the beam light from the mirror upwards to the aperture focus. The DCM is equipped with three sets of exchangeable single crystals: Si (111), Si (311) and Si (422). The first crystal is water cooled and can be changed in situ within a few minutes. The crystal Si (422) is higher energy resolution, but with less flux. A Bragg angle of as much as  $82^\circ$  is required for the minimum photon energy.

KMC-1 beamline is now extensively employed for the developing fields of hard X-ray photoelectron spectroscopy (HAXPES), X-ray absorption spectroscopy (XAS) and near-edge X-ray absorption fine structure (NEXAFS).

### *SPring-8 (Beamline BL47XU)*

SPring-8 (Super Photon ring-8 GeV) is a third-generation synchrotron radiation facility in Japan. With a ring energy of 8 GeV, the SPring-8 storage ring circulates a stored current of 100 mA. In SPring-8, a 25-m-long undulator is found, making it the most brilliant hard X-ray source in the world. In-vacuum undulators have been adopted as standard X-ray sources to provide synchrotron radiation in the X-ray region from 500 eV to 300 keV.

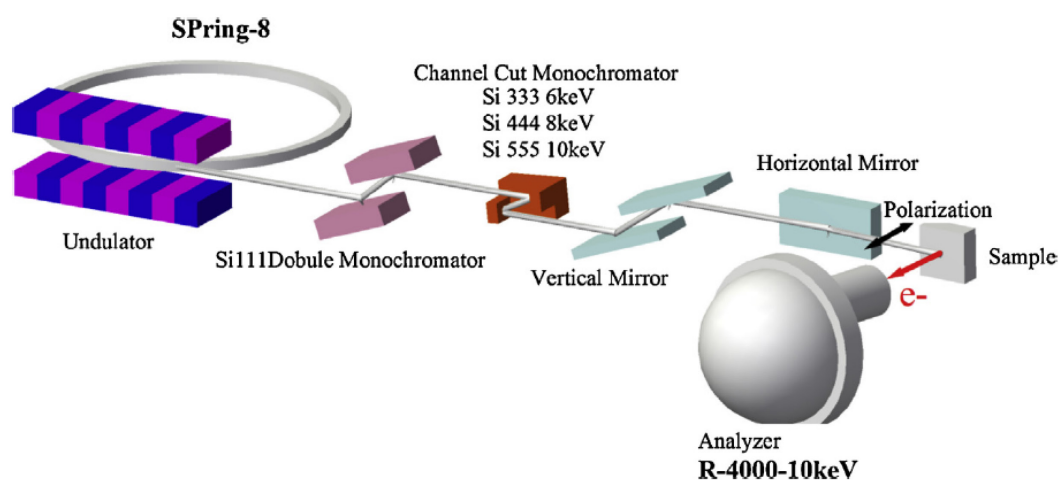


Figure 4.7: Schematic of the standard optical and experimental set up at BL47XU (as taken from Ref. [67]).

Fig. 4.7 shows a schematic of the optical and experimental set up at BL47XU [67]. A Si (111) DCM is used to produce monochromatic X-ray beams, followed by the Si (111) channel cut post-monochromator to reduce the band widths of X-rays. Using the 333, 444 and 555 Bragg reflections, X-ray beams with photon energies of 6, 8 and 10 keV can be introduced, respectively. Two mirrors in vertical and horizontal directions are employed to focus the beams onto the experiments. Using this two focusing mirrors, for example, an available photon flux of  $2.8 \times 10^{11}$  photon/s is obtained with a beam size of 30 (horizontal)  $\times$  40  $\mu\text{m}$  (vertical) at 8 keV photon energy. A hemispherical electron energy analyzer (R-4000-VG-SCIENIA) is placed perpendicular to the incident X-ray beams. This analyzer can measure the photoelectrons with kinetic energies up to 10 keV. The total energy resolution for commonly used parameters, e.g.,

pass energy of 200 eV and curved analyzer slit of 0.5 mm width, is about 228 meV by calibrating the Fermi edge of clean Au reference.

The beamline BL47XU is mainly used for experiments of X-ray photoelectron spectroscopy and micro-tomography in the hard X-ray region. In addition, it can be used for any kind of experiments which require high flux and/or clean X-ray beam.

#### *ALS (Beamline 8.0.1)*

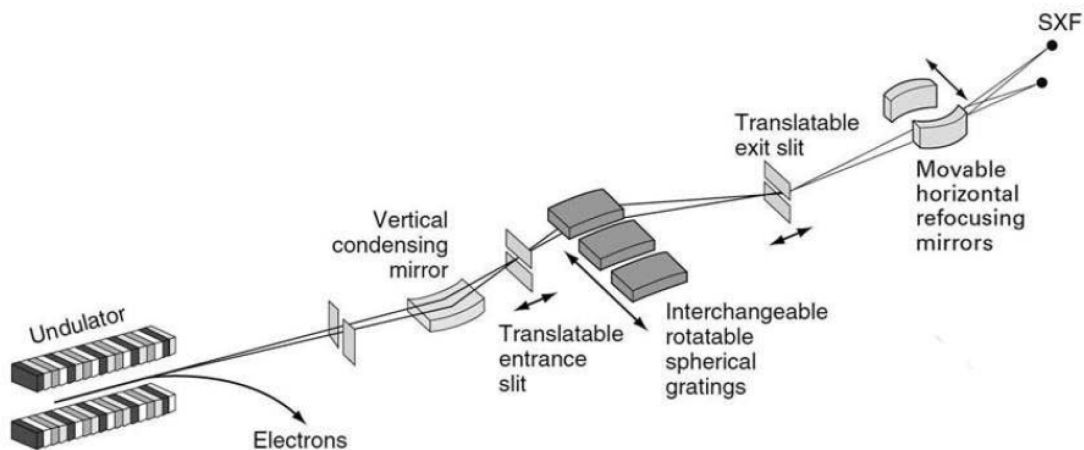


Figure 4.8: Schematic layout of the beamline 8.0.1 at the ALS (as taken from Ref. [68]).

In this work, X-ray emission (XES) and absorption spectroscopy (XAS) measurements were performed on beamline 8.0.1 at Advanced Light Source (ALS), Lawrence Berkeley National Laboratory. Fig. 4.8 shows a schematic layout of the beamline 8.0.1 at ALS [68]. Beamline 8.0.1 at the ALS is a U5.0 undulator based beamline, which can produce X-ray photons with the energy range of 65-1409 eV. The undulator consists of 89 magnetic pole pairs with a period  $\lambda_u$  of 5.0 cm allowing the first, third and fifth harmonics. A condensing mirror is perpendicular to the monochromator to focus the beam light. The monochromator of beamline consists of a translatable entrance slit, a spherical grating monochromator (SGM) and a translatable exit slit. The beamline's high-resolution SGM operates with a resolving power of 2000 with three interchangeable gratings. The desired resolution of the monochromator can be selected by choosing the width of the entrance slit and the exit slit. A soft X-ray fluorescence (SXF) spectrometer has a fixed entrance slit, four selectable spherical gratings, and a multi-channel plate (MCP) detector. The spectrometer operates in Rowland geometry.

The beamline 8.0.1 at ALS can provide experiments of X-ray absorption spectroscopy (XAS) and X-ray emission spectroscopy (XES) spectroscopy.

#### 4.2.4 Variable Angle Spectroscopic Ellipsometry (VASE)

Spectroscopic ellipsometry (SE) is a non-destructive optical technique, which operates by reflecting linearly polarized light from the surface of a sample [69]. A light beam with known polarization illuminates the sample. After interacting with the sample surface, the reflected light beam is directed back into the detector. The ellipsometer measures the polarization changes of the reflected light beam involving the mutually perpendicular components (named, the  $p$ - and  $s$ -direction waves). The measured ellipsometric parameters are expressed by the ratio of the amplitudes  $\Psi$  and the relative phase shift  $\Delta$  of the mutually perpendicular  $p$ - and  $s$ -waves. Afterwards, the experimental data  $\Psi$  and  $\Delta$  is converted into the quantities of interest, such as the film thickness and optical functions of the films.

In this thesis, variable-angle spectroscopic ellipsometry (VASE) was used to investigate the optical properties of  $\text{In}_2\text{O}_3$  films. A Sentech SE 850 DUV was employed to measure the ellipsometric parameters  $\Psi$  and  $\Delta$  for five different angles of incidence ranging from  $50^\circ$  to  $70^\circ$  and a light wavelength range from 190 to 850 nm. The  $\text{In}_2\text{O}_3$  samples used in this thesis had been deposited on various substrates, including bare silicon, silicon with a coating of amorphous silicon and different glass types. Therefore, the spectra were analyzed using different models. For  $\text{In}_2\text{O}_3\text{:H}$  and ITO samples, it was sufficient to model a single layer on the respective substrate with a small contribution by surface roughness. The dielectric function of the film was modeled by using three Tauc-Lorentz oscillators with different critical points  $E_0$  and a simple Drude term, while the surface roughness was described by an effective Bruggeman medium consisting of a 50%/50% mixture of film and air. In all cases, spectra were modeled within a wavelength range of 250 to 750 nm, corresponding to photon energies from 1.65 to 4.9 eV.



## 5. Characterization and Analysis of Annealing-induced Modifications of In<sub>2</sub>O<sub>3</sub> Variants

This chapter discusses the impacts of annealing on the properties of intrinsic and n-type doped (by Sn or H) In<sub>2</sub>O<sub>3</sub> variants, in particular emphasizing the beneficial role of H donor during annealing-induced crystallization of In<sub>2</sub>O<sub>3</sub>:H. Topics covered here include the change of the structural and electrical properties of In<sub>2</sub>O<sub>3</sub> variants during annealing, as well as the profound effects of doping on core-level and valence photoelectron structures. In addition, the energy-level positions including the gap disparity between the optical- and fundamental-band gaps are also discussed in detail.

### 5.1 Introduction

As described in Ch. 2, indium oxide (In<sub>2</sub>O<sub>3</sub>), when doped with SnO<sub>2</sub> (i.e., typically referred to In<sub>2</sub>O<sub>3</sub>:Sn or ITO) or incorporated with hydrogen (i.e., namely In<sub>2</sub>O<sub>3</sub>:H or IOH), it dominates the TCO market with a higher electrical conductivity and transparency than alternatives such as doped ZnO or SnO<sub>2</sub> [6]. In<sub>2</sub>O<sub>3</sub>:H has proved to yield a high electron mobility (>100 cm<sup>2</sup>/V/s) with improved near-infrared (NIR) transparency compared to ITO [6, 15]. Furthermore, annealing of In<sub>2</sub>O<sub>3</sub>:H can induce a solid phase crystallization of the films with a remarkable increase in the electron mobility. As a result, In<sub>2</sub>O<sub>3</sub>:H has been considered a promising candidate replacing ITO. However, very little is known about the influence of hydrogen incorporation on the optoelectronic properties of In<sub>2</sub>O<sub>3</sub>:H, especially annealing-induced changes in electronic structure are not well understood.

In addition, the nature and magnitude of the bulk and surface band gap in In<sub>2</sub>O<sub>3</sub> are still under discussion. An indirect transition in the range of 2.3-2.9 eV has been reported for In<sub>2</sub>O<sub>3</sub>, with a typical band gap of around 3.75 eV [70-72]. Regarding that, Walsh *et al.* [40] demonstrated that the strong allowed optical transition into the conduction band arises from a band located 0.81 eV below the valence-band edge, with transitions from states closer to the edge being symmetry forbidden. This results in measurements of the optical-band gap that are larger than the fundamental-band gap of In<sub>2</sub>O<sub>3</sub>. Further, a physical model of the gap disparity between the fundamental- and optical-band gaps was proposed from first-principles calculations [22, 23]; it was concluded that a strong coupling between O 2p and In 4d orbitals is well responsible for the difference between optical- and fundamental-band gaps of In<sub>2</sub>O<sub>3</sub>.

For these reasons, a better understanding of the electronic and chemical structures of intrinsic and n-type doped (by Sn or H)  $\text{In}_2\text{O}_3$  variants is necessary, which is investigated by a combination of photoelectron spectroscopy (HAXPES and XES & XAS), Hall measurements and spectroscopic ellipsometry in this work. The energy-level positions will be discussed in relation to the gap disparity between the optical- and fundamental-band gaps upon doping before and after annealing.

## 5.2 Experimental Details

### 5.2.1 Sample Preparation

All  $\text{In}_2\text{O}_3$  films used in this work were fabricated at HZB's Photovoltaic Competence Center Berlin (PVcomB) by a radio frequency (RF) magnetron sputtering of a 2-inch ceramic  $\text{In}_2\text{O}_3$  target (99.99%) at room temperature. The deposition chamber had a base pressure of  $3.8 \times 10^{-7}$  mbar, and the RF supply power was 70 W. A 75 nm thick ITO film was deposited on a 20 nm intrinsic amorphous silicon ( $\alpha$ -Si) layer grown on an n-type crystalline silicon (c-Si) wafer, using an ITO sintered target with a weight proportion of 90%  $\text{In}_2\text{O}_3$  and 10%  $\text{SnO}_2$  for reference. The other ITO sample with the thickness of 75 nm was prepared on a 0.7 mm Corning glass substrate. The  $\text{In}_2\text{O}_3$ :H films were 80 nm-thick and deposited on the thin ( $\sim 10$  nm) intrinsic amorphous silicon ( $\alpha$ -Si) layers grown on p-type crystalline silicon (c-Si) wafers by introducing  $\text{H}_2\text{O}$  vapor into the chamber as hydrogen donor during the RF deposition. The sputtering gasses are Ar,  $\text{O}_2$  and  $\text{H}_2\text{O}$  vapor with an  $[\text{O}_2/(\text{Ar}+\text{O}_2)]$  ratio of 0.0032, and the  $\text{H}_2\text{O}$  partial pressure was  $1.6 \times 10^{-6}$  mbar. For comparison, the nominally undoped  $\text{In}_2\text{O}_3$  films of approximately 230 nm thickness were prepared on 3.1 mm Saint-Gobain glass substrates. After deposition, the undoped  $\text{In}_2\text{O}_3$  and  $\text{In}_2\text{O}_3$ :H thin films were annealed at about 180 °C for 1 h in vacuum. In the case of ITO films, the annealing process was carried out in air at about 200 °C for 5 min. Details of the thin films preparation can be found in Ref. [73].

### 5.2.2 Sample Characterization

X-ray diffraction (XRD) was carried out by Dr. M. Meixner [HZB, Department Microstructure and Residual Stress Analysis (EM-AME)] to evaluate the films' structure and crystallinity. This was done by using a Bruker ETA diffractometer in the angle dispersive (AD) mode with monochromatic  $\text{Cu } K_\alpha$  radiation ( $\lambda = 1.5405 \text{ \AA}$ ). The optoelectronic properties of the films were investigated by Hall measurements and Spectroscopic Ellipsometry (SE) at room temperature. Hall measurements with an Ecopia HMS-3000 system were performed by Dr. H. Scherg-

Kurmes (HZB, PVcomB), through measuring the four-point-resistance in van-der-Pauw geometry. Varying Angle Spectroscopic Ellipsometry (VASE) was carried out by Dr. F. Ruske [HZB, Institute Silicon Photovoltaics (EE-IS)], with incident angles ranging from 50° to 70° in the spectral range from 190 to 850 nm.

In addition, hard X-ray photoelectron spectroscopy (HAXPES) was employed to characterize the core-level and valence electronic structures of the In<sub>2</sub>O<sub>3</sub> different thin films before and after annealing. HAXPES measurements with excitation energies of 2 and 8 keV were conducted at the HiKE end-station (Beamline KMC-1) at BESSY II in Berlin and SPring-8 (Beamline BL47XU) synchrotron radiation facility in Japan, respectively. Combining X-ray emission (XES) and absorption spectroscopy (XAS) of the O *K*-edge measurements were used to investigate the occupied and unoccupied partial density of states (PDOS) in each In<sub>2</sub>O<sub>3</sub> sample, respectively. The XES & XAS experiments were performed at the Advanced Light Source (ALS) (beamline 8.0.1) at Lawrence Berkeley National Laboratory (LBNL). The working principle of the spectroscopic analysis (HAXPES and XES & XAS) used in this work has been described in Sect. 4.2.

Owing to the In<sub>2</sub>O<sub>3</sub> variants deposited on different underlying substrates, the experiments performed with different light sources would have different sample depths of thin films. Fig. 5.1 schematically shows the relevant probing depths collected from HAXPES, O-*K* edge XES & XAS, and spectroscopic ellipsometry (SE) measurements for the In<sub>2</sub>O<sub>3</sub> variants. As depicted in Fig. 5.1, mean probe depths of HAXPES at the excitation energies of 2 and 8 keV are approximately 12 and 39 nm, respectively, given by three times the inelastic mean free paths (IMFP)  $\lambda$  ( $\sim 4$  and  $\sim 13$  nm [74]) of the generated O 1s photoelectrons. Here when the intensity of the photoelectrons has decayed to  $1/e^3$  of its original value, then 95% of the signal comes from a distance  $3\lambda$  or attenuation length within the solid [65]. Unlike HAXPES, there are two yield modes for the XAS experiments in the soft X-ray region, the electron yield (EY) mode, and the fluorescence yield (FY) mode. The total electron yield (TEY) detection mode is surface-sensitive, with the probing depth of  $\sim 10$  nm at most limited by the electron escape depth. While the FY mode is bulk-sensitive and can probe depth up to  $\sim 200$  nm depending on the X-ray attenuation length in materials. In our experiments, the energy-sensitive partial fluorescence yield (PFY) mode has been utilized for O-*K* edge XAS measurements. The effective attenuation length  $L_{eff}$  for O fluorescence X-rays above the *K*-edge ( $h\nu = 550$  eV) in In<sub>2</sub>O<sub>3</sub> is  $\sim 43.74$  nm according to the expression  $L_{eff} = \left( \frac{1}{L_{absorption}} + \frac{1}{L_{emission}} \right)^{-1}$  [The attenuation lengths near O *K*-absorption edge at 550 eV ( $L_{absorption}$ ) and *K*-emission edge at 528 eV ( $L_{emission}$ ) used in our

work are about 80 and 96.50 nm [75], respectively.]. Hence the effective probing depth of O *K*-edge XAS & XES in In<sub>2</sub>O<sub>3</sub> is ~131 nm, given by three times the effective attenuation length. As mentioned in Sect. 4.2.4, spectroscopic ellipsometry (SE) analysis is based on the change of polarization of an incident light beam upon reflection by a single or multilayered thin film on a suitable substrate (i.e., glass, silicon, and plastic). For In<sub>2</sub>O<sub>3</sub> on Saint Gobain glass [Fig. 5.1 (a)] and ITO on Corning glass substrates [Fig. 5.1 (d)], the refractive index of the glass is known and it is fully transparent to the incident light, thus the samples can be treated as a single layer film. In the cases of the multilayered In<sub>2</sub>O<sub>3</sub>:H/a-Si(i)/c-Si(p) wafer [Fig. 5.1 (b)] and ITO/a-Si(i)/c-Si(n) wafer [Fig. 5.1 (c)] samples, the film thickness *d* is determined by the extinction coefficient *k* as a function of photon wavelength  $\lambda$  according to  $d = 1/\alpha = \lambda/(4\pi k)$  (here  $\alpha$  is the absorption coefficient of the film) [76]. Thus SE can measure for low and high *k* to probe the air-film and film-substrate interfaces interfere; for high *k* the information depth is low where you can only probe the air-film interface at the very top, and the low *k* means that the incident photon can reach the film-substrate interface. In our work, the range of the extinction coefficient *k* for In<sub>2</sub>O<sub>3</sub> within the used wavelength range (190-850 nm) is around 0.578-0.007, thereby giving a high information depth of ~10  $\mu$ m.

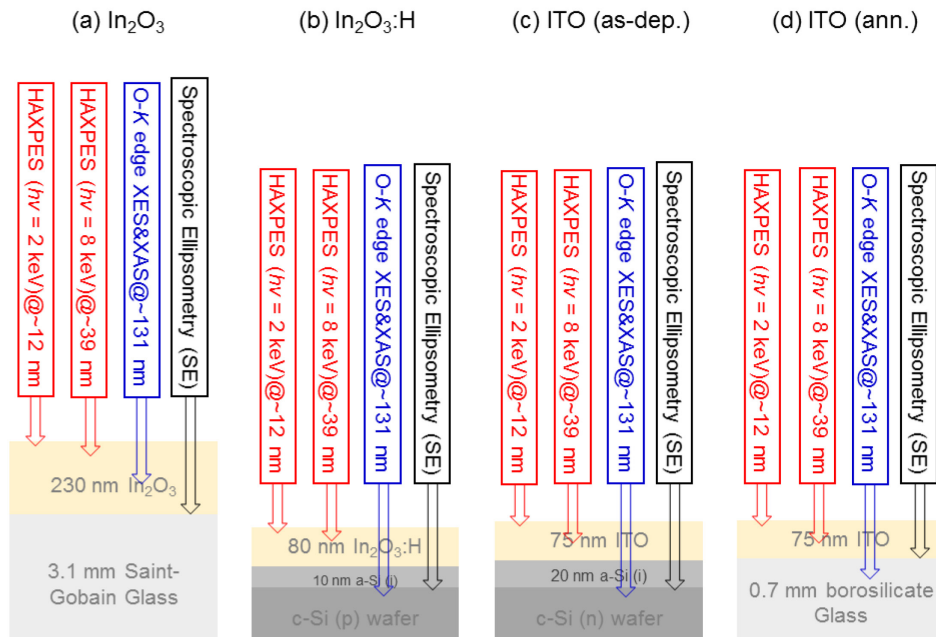


Figure 5.1: Schematics of the probing depth distributions measured by HAXPES (*red lines*), O-*K* edge XES & XAS (*blue lines*), and SE (*black lines*) experiments for (a) nominally undoped In<sub>2</sub>O<sub>3</sub>, (b) In<sub>2</sub>O<sub>3</sub>:H, (c) as-deposited ITO, and (d) annealed ITO films grown on different underlying substrates.

## 5.3 Results and Discussion

### 5.3.1 Structural Properties

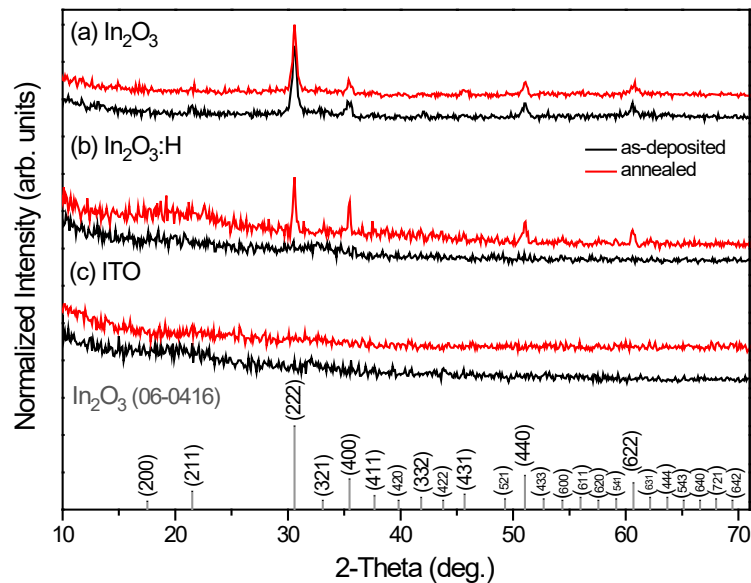


Figure 5.2: X-ray diffraction patterns of (a) nominally undoped  $\text{In}_2\text{O}_3$ , (b)  $\text{In}_2\text{O}_3:\text{H}$  and (c) ITO films before and after annealing measured at room temperature. For comparison, the powder reference patterns of  $\text{In}_2\text{O}_3$  are shown.

Fig. 5.2 shows the typical XRD patterns of the as-deposited nominally undoped  $\text{In}_2\text{O}_3$ ,  $\text{In}_2\text{O}_3:\text{H}$ , ITO films and the annealed ones, respectively. All intense diffraction peaks in the spectra, i.e., (222), (400), (440) and (622), can correspond well to  $\text{In}_2\text{O}_3$  powder reference patterns (JCPDS Card No. 06-0416), except for some small diffraction peaks. In Fig. 5.2 (a), the undoped  $\text{In}_2\text{O}_3$  has a polycrystalline structure independent on annealing. The film grows amorphously when deposited under water vapor atmosphere, but shows polycrystalline phase after vacuum annealing [Fig. 5.2 (b)]. Annealed  $\text{In}_2\text{O}_3:\text{H}$  exhibits similar diffraction peaks to undoped  $\text{In}_2\text{O}_3$ . As reported previously [6, 77], the incorporation of  $\text{H}_2\text{O}$  vapor during deposition could prevent the growth of  $\text{In}_2\text{O}_3$  crystallites. It is most likely that the presence of hydrogen in as-deposited  $\text{In}_2\text{O}_3:\text{H}$  is in the form of hydrogen (-H) and/or hydroxide bonding (-OH), which can suppress the construction of In-O-In bond networks within the growing films [6, 77]. During subsequent vacuum annealing, the  $\text{H}_2\text{O}$  (and/or  $\text{H}_2$ ) desorption from the grain surface occurs. It was confirmed from the  $\text{H}_2\text{O}$  thermal desorption spectroscopy (TDS) [6] that OH or H segregating at grain surface reacts with the neighboring H to form  $\text{H}_2\text{O}$  (and/or  $\text{H}_2$ ) molecules during crystallization. Fig. 5.2 (c) shows that the as-deposited ITO film is amorphous, in good agreement with other studies based on ITO films prepared by RF magnetron sputtering

technique [78]. The crystal growth of ITO films depends on the preparation techniques; the as-deposited film is mostly amorphous when prepared by magnetron sputtering, while displaying crystal phase during subsequent annealing [79]. However, the film studied here remains amorphous after annealing in air. It might be because that the annealing time in our experimental work is not sufficient to fully activate the thermal crystallization process in ITO despite the annealing temperature being above the crystallization temperature ( $\sim 150$  °C).

### 5.3.2 Electrical Properties

TABLE 5.1: Results of the Hall-effect measurements (Mobility  $\mu$ , Resistivity  $\rho$ , and Carrier concentration  $N_e$ ) are listed below.

Samples	Mobility $\mu$ ( $\text{cm}^2/\text{V}\cdot\text{s}$ )	Resistivity $\rho$ ( $\Omega$ cm)	Carrier concentration $N_e$ ( $\text{cm}^{-3}$ )
In <sub>2</sub> O <sub>3</sub> (as-dep.)	45.2	$8.69 \times 10^{-4}$	$1.59 \times 10^{20}$
In <sub>2</sub> O <sub>3</sub> (ann.)	32.6	$1.14 \times 10^{-3}$	$1.68 \times 10^{20}$
In <sub>2</sub> O <sub>3</sub> :H (as-dep.)	39.9	$4.05 \times 10^{-4}$	$3.86 \times 10^{20}$
In <sub>2</sub> O <sub>3</sub> :H (ann.)	127.0	$2.99 \times 10^{-4}$	$1.64 \times 10^{20}$
ITO (as-dep.)	47.6	$4.63 \times 10^{-4}$	$2.84 \times 10^{20}$
ITO (ann.)	54.5	$4.72 \times 10^{-4}$	$2.43 \times 10^{20}$

Table 5.1 summarizes the bulk carrier concentration  $N_e$ , resistivity  $\rho$ , and Hall mobility  $\mu$  of the films measured by Hall-effect at room temperature. The electrical properties exhibit a complex variation. A slightly increased  $N_e$  with a small decrease in  $\mu$  is observed in undoped In<sub>2</sub>O<sub>3</sub> after annealing. This is attributed to the formation of oxygen vacancies during vacuum annealing [80]. The crystallized In<sub>2</sub>O<sub>3</sub>:H shows a large increase in  $\mu$  by a factor of approximate 3 to 127  $\text{cm}^2 \text{V}^{-1}\cdot\text{s}^{-1}$  and a decrease in  $N_e$  by a factor of approximate 2 to  $1.64 \times 10^{20} \text{ cm}^{-3}$  with a corresponding reduction in  $\rho$ , in comparison with the amorphous one. Such remarkable changes in  $\mu$  and  $N_e$  upon crystallization may be associated with the structural transformation from amorphous to polycrystalline phases. In crystallized In<sub>2</sub>O<sub>3</sub>:H, the greatly increased mobility has been reported to be due to either a change from doubly charged donors (i.e., oxygen vacancy  $V_o^{2+}$ ), which is dominated in amorphous In<sub>2</sub>O<sub>3</sub>:H, to singly charged donors (i.e., hydrogen in either an interstitial  $H_i^+$  or substitutional  $H_o^+$  site) or a reduction in other defect scattering mechanisms (i.e., neutral impurity) or both [81]. Another potential explanation for this high mobility is assigned to hydrogen passivation of grain boundaries after crystallization [82]. During annealing, a release of hydrogen takes place, which provides an internal source for hydrogen to saturate grain boundary states within the crystallized In<sub>2</sub>O<sub>3</sub>:H. This could also be well responsible for a significantly higher mobility in annealed In<sub>2</sub>O<sub>3</sub>:H than that typically

obtained in ITO. No large annealing-induced variations have been observed in ITO films, except that the carrier concentration  $N_e$  is considerably less than the bulk concentration of Sn atoms ( $3.08 \times 10^{21}$  atoms $\cdot$ cm $^{-3}$ ). Apparently, not all Sn atoms effectively act as dopants in the amorphous structure, and the inactive neutral Sn does not contribute to carrier concentration [83].

### 5.3.3 HAXPES Survey Spectra

Fig. 5.3 shows the HAXPES survey spectra of nominally undoped  $\text{In}_2\text{O}_3$ ,  $\text{In}_2\text{O}_3\text{:H}$  and ITO films before and after annealing measured at 2 and 8 keV photon energies, respectively. The films exhibit expected photoelectron signals from the main elements (In, Sn, O) and C. The more bulk sensitive spectra excited at 8 keV photon energy show just a small carbon signal, which we thus ascribe to surface contamination. The change of the relative intensities of the core levels is attributed to the photon energy dependence among the photoionization cross-sections for different atomic subshells [84, 85]. In general, the photoionization cross-sections decrease remarkably with increasing photon energy. The decrease for In 3d state relative to O 1s state is much more pronounced than other In core lines including In 3s, 3p, 4s, and 4p states.

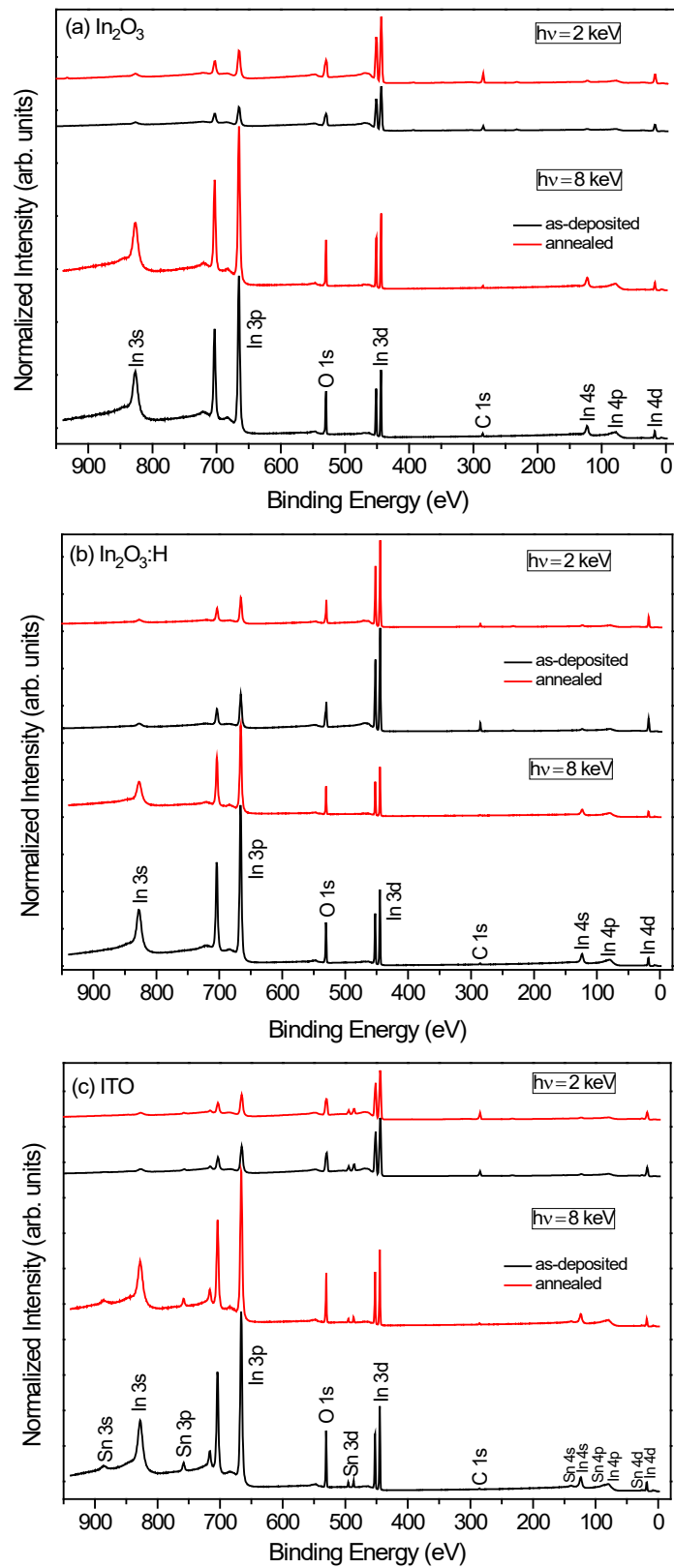


Figure 5.3: HAXPES survey spectra for (a) nominally undoped  $\text{In}_2\text{O}_3$ , (b)  $\text{In}_2\text{O}_3\text{:H}$  and (c) ITO films before and after annealing measured at 2 and 8 keV photon energies, respectively. Vertical offsets are added for clarity.



### 5.3.4 Chemical Environment

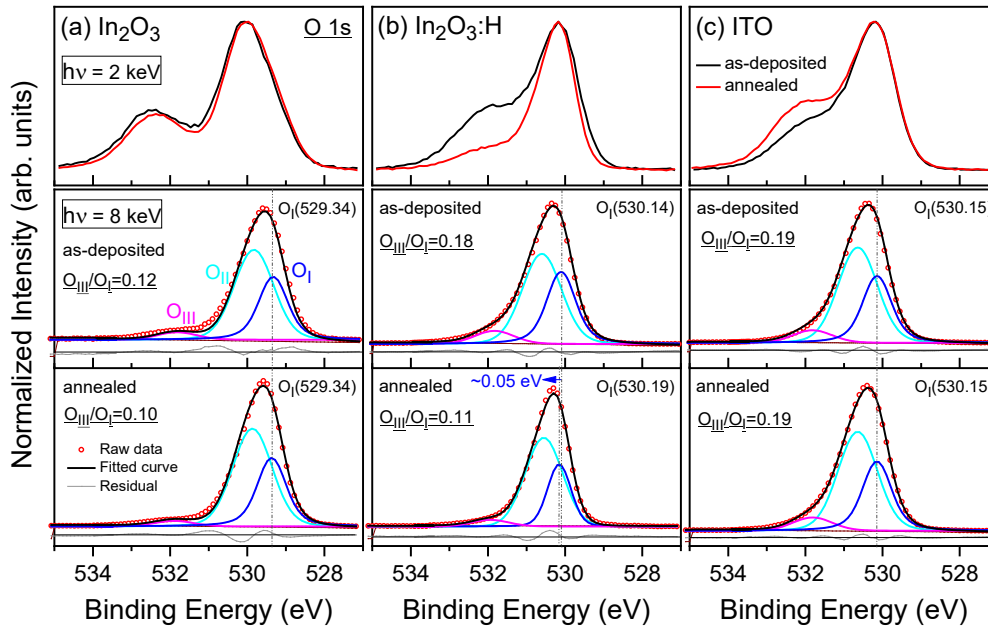


Figure 5.4: O 1s core-level spectra measured at photon energies of 2 (*top panels*) and 8 keV (*bottom panels*) for (a) nominally undoped  $\text{In}_2\text{O}_3$ , (b)  $\text{In}_2\text{O}_3\text{:H}$  and (c) ITO films before and after annealing, respectively. The spectra measured at 8 keV photon energy are fitted by three components (*color solid lines*) using Voigt profiles with a linear background subtraction.

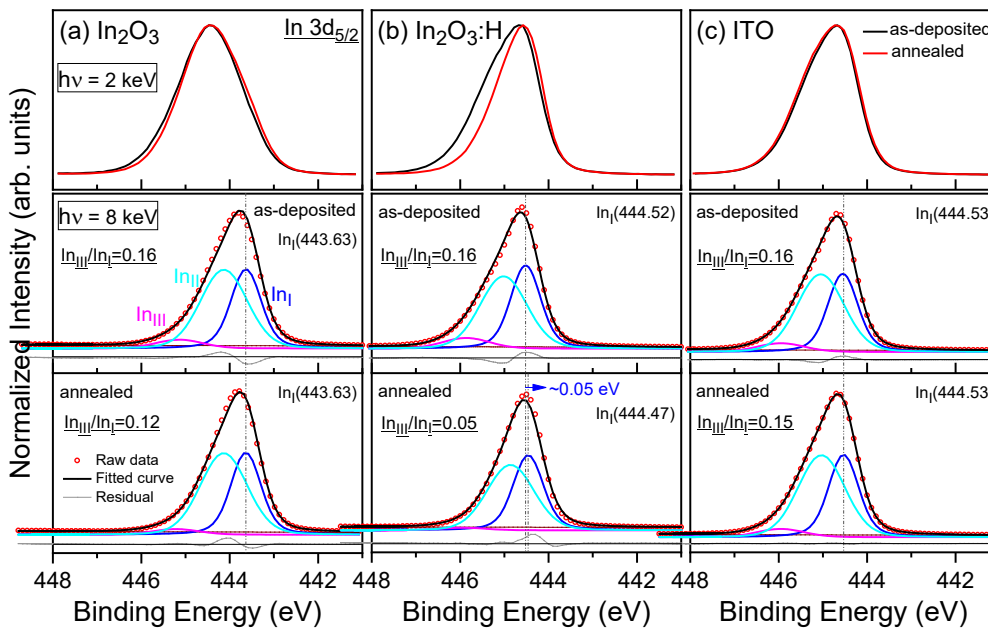


Figure 5.5: In  $3d_{5/2}$  core-level spectra measured at photon energies of 2 (*top panels*) and 8 keV (*bottom panels*) for (a) nominally undoped  $\text{In}_2\text{O}_3$ , (b)  $\text{In}_2\text{O}_3\text{:H}$  and (c) ITO films before and after annealing, respectively. The spectra measured at 8 keV photon energy are fitted by three components (*color solid lines*) using Voigt profiles with a linear background subtraction.

Hard X-ray photoelectron spectroscopy (HAXPES) is used to obtain information about the compositions and chemical states of the species on  $\text{In}_2\text{O}_3$  films. O 1s and In 3d<sub>5/2</sub> HAXPES spectra of nominally undoped  $\text{In}_2\text{O}_3$ ,  $\text{In}_2\text{O}_3\text{:H}$  and ITO films before and after annealing measured at 2 and 8 keV photon energies are shown in Fig. 5.4 and 5.5, respectively. It should first be noted that the O 1s and In 3d<sub>5/2</sub> photoemission lines in the doped  $\text{In}_2\text{O}_3$  variants shift to higher binding energies by  $\sim 1.00$  eV compared to that of undoped films when measured at 8 keV photon energy, as already indicated in Fig. 5.4 and 5.5. As seen in Fig. 5.4, a high binding energy structure is clearly present in the O 1s spectra measured with 2 keV photon energy. The high binding energy structure's intensity decreases largely when measured with a high excitation energy of 8 keV (i.e., more bulk sensitive). It is also much reduced after vacuum annealing, especially for  $\text{In}_2\text{O}_3\text{:H}$  films, but increases when annealed in air for ITO films. Thus, it could be most likely attributed to adventitious surface contamination associated with surface absorbed water and/or peroxide-like species.

TABLE 5.2: Binding energy values (eV) for In 3d<sub>5/2</sub> and O 1s photoemission lines from related indium oxide and hydroxide standards.

Compound	In 3d <sub>5/2</sub> (eV)	O 1s (eV)
In metal	443.2 [86] 443.7 [87]	-
$\text{In}_2\text{O}_3$	444.9 [86] 444.6 [87, 88] 444.7 [89]	529.5 [86] 529.6 [87] 530.3 [90-92]
$\text{In}(\text{OH})_3$	446.0 [93] 445.8 [94]	531.0 [37] 530.9 [94]

To minimize the contribution of the surface contamination to the spectral lineshape, the O 1s and In 3d<sub>5/2</sub> peaks measured at 8 keV photon energy are used to investigate the potential chemical changes within these films. When measured at 8 keV photon energy, the O 1s and In 3d<sub>5/2</sub> spectra both exhibit a noticeable asymmetric broadening on the high binding energy side. Although there is a small possibility that the adventitious contamination can modify the O 1s spectral shape, it would not be considered as the origin of asymmetry at such high excitation energy. Some previous XPS studies on  $\text{In}_2\text{O}_3$  [90, 95, 96] have generally fitted the O 1s peak with three components: stoichiometric  $\text{In}_2\text{O}_3$ -like oxygen, nonstoichiometric  $\text{In}_2\text{O}_{3-x}$ -like oxygen (i.e., oxygen vacancy  $V_o^{2+}$ ), and hydroxide (OH). These components used for fitting are based on the binding energy positions of the related indium oxide standards listed in Table 5.2. The oxygen vacancies ( $V_o^{2+}$ ) have been assigned to oxygen that is adjacent to oxygen-deficient sites, mostly located at  $\sim 531.0$  eV, which donate two electrons toward the In lattice [88, 90].

This is unlikely given that the bulk concentration of oxygen vacancies ( $V_o^{2+}$ ) is estimated at  $\ll 1\%$  based on carrier concentration, and thus would not explain the presence of multiple peaks with similar intensity, unless the oxygen vacancies are highly concentrated within the interaction volume of the measurements, e.g., if they are produced through beam damage during measurements. If such high carrier concentration of oxygen vacancies ( $V_o^{2+}$ ) is assumed to exist within  $\text{In}_2\text{O}_3$ , the related spectral density of states (DOS) around the Fermi level should be observed by photoelectron spectroscopy, which is not the case in our valence photoelectron spectra of undoped  $\text{In}_2\text{O}_3$  [Fig. 5.8 (a)]. Moreover, the O 1s spectra of undoped  $\text{In}_2\text{O}_3$  [Fig. 5.4 (a)] in our work exhibit little or no change in the intensity before and after annealing in vacuum, i.e., a reducing atmosphere. These results are inconsistent with assigning a separate O 1s/In  $3d_{5/2}$  peak to oxygen vacancies in  $\text{In}_2\text{O}_3$  films studied here.

Also for the In  $3d_{5/2}$  spectra, it has been in the literature [86] fitted with two components, indium oxide, and indium hydroxide. In order to obtain a satisfactory peak fitting, however, a third unidentified component is unavoidably required for the possible fitting errors. Several studies [87, 88] have fitted the In  $3d_{5/2}$  spectra with three components at binding energies of  $(444.2 \pm 0.1)$ ,  $(444.5 \pm 0.1)$  and  $(444.6 \pm 0.1)$  eV, corresponding to crystalline indium oxide, amorphous indium oxide, and indium hydroxide species. While undoped  $\text{In}_2\text{O}_3$  studied in this work has been shown by XRD pattern [Fig. 5.2 (a)] to be crystalline. This also is unlikely given that a significant increase in the amount of the crystalline phase is present for  $\text{In}_2\text{O}_3\text{:H}$  after vacuum annealing [Fig. 5.2 (b)], but the annealed  $\text{In}_2\text{O}_3\text{:H}$  film exhibits only a slightly narrower lineshape in the In  $3d_{5/2}$  spectrum than as-deposited one.

Other recent research has attributed the asymmetric spectral shape to a screening mechanism [97, 98], which has already been developed to model the lineshape of core levels in doped oxides including  $\text{In}_2\text{O}_3$  [99], ITO [37], and Sb-doped  $\text{SnO}_2$  [100]. It is assumed that the unrelaxed Koopmans' state from the excitation of core electrons is projected to "screened" and "unscreened" final states by Coulomb interaction between the excited core holes and the conduction electrons. In this model, the In  $3d_{5/2}$  spectra can be fitted with a pair of Voigt functions: a narrow low binding energy component assigned to a screened final state, and a broad high binding energy component corresponding to an unscreened final state. The model indicates that the screened and unscreened final states have different lifetimes and hence different Lorentzian contributions. The relative intensity of the screened component is expected to increase with increasing carrier density. However, there is no indication of this effect in our data; the spectral shapes of the  $\text{In}_2\text{O}_3\text{:H}$  films are largely unchanged despite an approximate 50%

reduction in carrier concentration before and after annealing. The width of the high binding energy unscreened component is determined by a broadening mechanism due to decreased lifetime. Alternatively, the high binding energy shoulder can also be described as a strong plasmon loss satellite. In the plasmon model, the high binding energy satellite intensity  $I$  is inversely proportional to the conduction electron density  $N_e$  according to the expression of  $I \propto N_e^{-1/3}$  [101]. A low density of conduction electrons reflects a high intensity of the high binding energy satellite structure, thereby leading to a large asymmetric broadening in the photoelectron spectra. While a reduced asymmetry is observed in the In 3d<sub>5/2</sub> spectrum of annealed In<sub>2</sub>O<sub>3</sub>:H [Fig. 5.5 (b)], which is in contradiction to the plasmon model. Furthermore, it remains a challenge to get a reasonable fit with a pair of Voigt profiles in these two models. Although Körber [99] and Christou [37] have used a pair of pseudo-Voigt functions to fit the In 3d<sub>5/2</sub> spectra, the apparently distinct Lorentzian contributions (i.e., lifetimes) have been applied even at the same doping level of In<sub>2</sub>O<sub>3</sub>. In contrast to that, a fitting model using three Voigt components, a main screened line and two satellite lines, with different energy spacings  $\Delta E$  and  $2\Delta E$  is developed by Gassenbauer *et al.* [37].

The above discussion illustrates the difficulty in consistently fitting of the O 1s and In 3d<sub>5/2</sub> spectra. In this work, we use a fitting procedure for an asymmetry with two contributions of different widths (“narrow” and “wide” as in the “screening” and “plasmon” models above) for the O 1s and In 3d<sub>5/2</sub> spectra, although we do not find a satisfying explanation. The expression of the asymmetry is assigned to In<sub>2</sub>O<sub>3</sub>, indicating a different stoichiometric configuration of In<sub>2</sub>O<sub>3</sub>. The arguments on the above models in the fitting of the O1s and In 3d<sub>5/2</sub> spectra are still ongoing, and a combination may be necessary.

In our model, the O 1s peak measured at 8 keV photon energy has been fitted with three components (O<sub>I</sub>, O<sub>II</sub>, and O<sub>III</sub>), using Voigt profiles by a linear background subtraction, as shown in Fig. 5.4. The two main peaks (“narrow” O<sub>I</sub> and “wide” O<sub>II</sub>) are both assigned to O-In bonding, specifically In<sub>2</sub>O<sub>3</sub>, and the high binding energy shoulder (O<sub>III</sub>) is related to hydroxide. In the fit routine, the fitted O<sub>II</sub> and O<sub>III</sub> Voigt components were all constrained to have the same Gaussian-Lorentzian mix, and the fitted O<sub>I</sub> Voigt component was fixed to have a different Gaussian-Lorentzian function. The energy separation and the intensity ratio between the fitted components of O<sub>I</sub> and O<sub>II</sub> were both fixed for all the films, along with the same energy position of O<sub>III</sub> component. The related parameters in the fitting of O 1s photoemission line are given in Table 5.3. In order to achieve a good fit, the fitting parameters (i.e., the energy separation and the intensity ratio between O<sub>I</sub> and O<sub>II</sub> components) for In<sub>2</sub>O<sub>3</sub>:H were intentionally adjusted,

being slightly different from that of undoped  $\text{In}_2\text{O}_3$  and ITO. The fitted  $\text{O}_I$ ,  $\text{O}_{II}$ , and  $\text{O}_{III}$  components are centered at binding energies of  $(530.14 \pm 0.05)$ ,  $(530.64 \pm 0.05)$ , and  $(531.82 \pm 0.05)$  eV, respectively.

TABLE 5.3: Fitting parameters of O 1s and In  $3d_{5/2}$  core lines by two different Voigt functions. Values of the full width at half maximum height (FWHM) (eV), energy separation (eV) and the intensity ratio between the fitted components are listed below.

Samples	O 1s core line				In $3d_{5/2}$ core line			
	FWHM (eV)		$E_{\text{sep. (OII-OI)}}$ (eV)	$\text{O}_I/\text{O}_{II}$ ratio	FWHM (eV)		$E_{\text{sep. (InII-InI)}}$ (eV)	$\text{In}_I/\text{In}_{II}$ ratio
	$\text{O}_I$	$\text{O}_{II}(\text{O}_{III})$			$\text{In}_I$	$\text{In}_{II}(\text{In}_{III})$		
$\text{In}_2\text{O}_3$ (as-dep.)	0.89	1.06	0.50	0.70	0.54	1.09	0.50	0.70
$\text{In}_2\text{O}_3$ (ann.)	0.89	1.06	0.50	0.70	0.54	1.09	0.50	0.70
$\text{In}_2\text{O}_3:\text{H}$ (as-dep.)	0.89	1.06	0.50	0.80	0.54	1.09	0.50	0.80
$\text{In}_2\text{O}_3:\text{H}$ (ann.)	0.89	1.06	0.40	0.80	0.54	1.09	0.40	0.80
ITO (as-dep.)	0.89	1.06	0.50	0.70	0.54	1.09	0.50	0.70
ITO (ann.)	0.89	1.06	0.50	0.70	0.54	1.09	0.50	0.70

The fitted O 1s peak in  $\text{In}_2\text{O}_3:\text{H}$  shows a very small shift of  $\sim 0.05$  eV towards higher binding energy after annealing. Meanwhile, the intensity ratio of hydroxide and  $\text{In}_2\text{O}_3$  components ( $\text{O}_{III}/\text{O}_I$ ) is found to decrease for annealed  $\text{In}_2\text{O}_3:\text{H}$ . This is most likely related to the indium hydroxide dehydroxylation during annealing according to the chemical reaction  $2\text{In}(\text{OH})_3 \rightarrow \text{In}_2\text{O}_3 + 3\text{H}_2\text{O}$ . While in terms of undoped  $\text{In}_2\text{O}_3$  and ITO, very little or no changes, i.e., w.r.t. energy shifts and intensity ratio, are observed before and after annealing.

The similar fitting procedure employed for the O 1s spectra, i.e., two contributions of “narrow” and “wide” widths, was used to fit the In  $3d_{5/2}$  spectra measured at 8 keV photon energy. The corresponding fitting parameters of In  $3d_{5/2}$  photoemission line are shown in Table 5.3. They have similar values of the energy separation and intensity ratio between “narrow”  $\text{In}_I$  and “wide”  $\text{In}_{II}$  components as O 1s photoemission lines, as well for the FWHM of “wide”  $\text{In}_{II}$  component, except that the  $\text{In}_I$  component has a smaller FWHM than  $\text{O}_I$  component. The two main peaks, “narrow”  $\text{In}_I$  located at  $(444.55 \pm 0.05)$  eV and “wide”  $\text{In}_{II}$  located at  $(445.05 \pm 0.05)$  eV, both correspond to In-O bonding, specifically  $\text{In}_2\text{O}_3$ , and the high binding energy shoulder ( $\text{In}_{III}$ ) located at  $(445.95 \pm 0.05)$  eV is attributed to In-OH bonding states from indium hydroxide. Obviously, the intensity ratio of indium hydroxide and  $\text{In}_2\text{O}_3$  components ( $\text{In}_{III}/\text{In}_I$ ) also decreases largely in  $\text{In}_2\text{O}_3:\text{H}$  after annealing, which gives further evidence for the dehydroxylation of indium hydroxide during annealing. The dehydroxylation of indium hydroxide may induce crystallization and grain growth of the films [82]. At the same time, the release of hydrogen from  $\text{In}_2\text{O}_3:\text{H}$  may passivate the grain boundaries, thus leading to high

mobility in annealed  $\text{In}_2\text{O}_3:\text{H}$ . This is in good agreement with the results of our XRD and Hall measurements on  $\text{In}_2\text{O}_3:\text{H}$  after annealing. Abstractly, a more significant decrease in the  $(\text{In}_{\text{III}}/\text{In}_{\text{I}})$  ratio is present in  $\text{In}_2\text{O}_3:\text{H}$  during annealing than the  $(\text{O}_{\text{III}}/\text{O}_{\text{I}})$  ratio according to the chemical reaction  $2\text{In}(\text{OH})_3 \rightarrow \text{In}_2\text{O}_3 + 3\text{H}_2\text{O}$ . That is generally consistent with our results; the  $(\text{In}_{\text{III}}/\text{In}_{\text{I}})$  ratio decreases from 0.16 to 0.05 after annealing (nearly by three), while the  $(\text{O}_{\text{III}}/\text{O}_{\text{I}})$  ratio just slightly changes from 0.18 to 0.11. An opposite shift by  $\sim 0.05$  eV towards lower binding energy is found in the  $\text{In } 3d_{5/2}$  spectra of  $\text{In}_2\text{O}_3:\text{H}$  after annealing. The observed chemical shifts in the  $\text{In } 3d_{5/2}$  and  $\text{O } 1s$  spectra are rather small, and mainly negligible w.r.t. our energy resolution. Both undoped  $\text{In}_2\text{O}_3$  and ITO films exhibit little or no changes in the  $\text{In } 3d_{5/2}$  spectra before and after annealing.

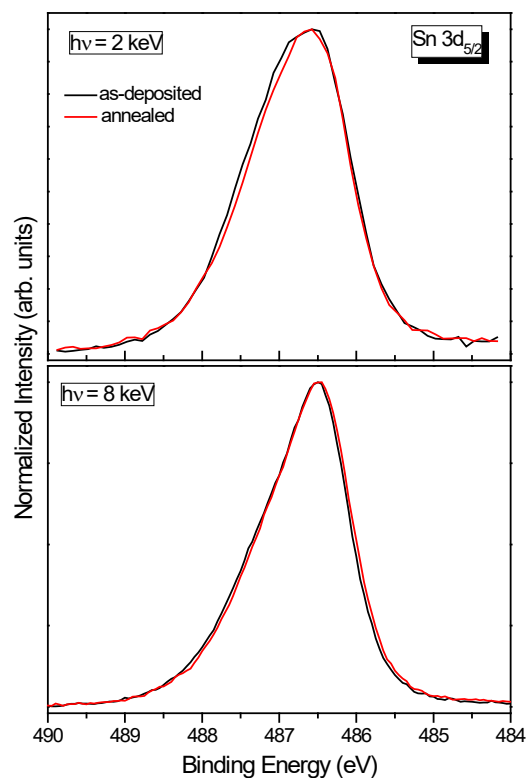


Figure 5.6:  $\text{Sn } 3d_{5/2}$  core-level spectra measured at photon energies of 2 (*top panel*) and 8 keV (*bottom panel*) for ITO films before and after annealing, respectively.

Fig. 5.6 shows  $\text{Sn } 3d_{5/2}$  core-level spectra of ITO films measured at photon energies of 2 and 8 keV before and after annealing. The spectra exhibit an asymmetric peak centered at  $(486.50 \pm 0.05)$  eV, with a high binding energy shoulder. A slight narrowing in lineshape is observed in the  $\text{Sn } 3d_{5/2}$  spectra of ITO after annealing when measured with 2 keV photon energy, probably due to slight thermal dehydroxylation of tin hydroxide at the surface. While when measured at 8 keV photon energy there are little or no changes, i.e., spectral lineshape

and w.r.t. energy shifts, in the Sn  $3d_{5/2}$  spectra of ITO before and after annealing. This is largely due to the same amorphous structure in ITO during annealing.

### 5.3.5 Valence Photoelectron Spectra

Figure 5.7 shows the valence-band (VB) spectra of nominally undoped  $\text{In}_2\text{O}_3$ ,  $\text{In}_2\text{O}_3\text{:H}$  and ITO films measured at photon energies of 2 and 8 keV before and after annealing. The spectra have a significant O 2p character. They exhibit four main features, labeled I-IV, which we assign according to Körber [99]. They are attributed to very pronounced O 2p derived states mixed with some shallow In 4d states (I), strong O 2p hybridized with In 5p derived states (II), hybridized In 5p and O 2p derived states (III), and strongly mixed In 5s and O 2p derived states (IV), respectively. Another feature “V” seen at  $\sim 10$  eV in ITO films [Fig. 5.7 (c)] is associated with strongly hybridized Sn 5s-O 2p derived states. The difference in the spectral shape measured with different excitation energies is mainly due to the changes of photoionization cross-sections for the different involved atomic subshells, as discussed in detail in Sect. 5.3.3. Basically, with increasing excitation energy the decrease for In 5s states (and to a lesser extent for In 5p and In 4d states) is much less pronounced than that for O 2p derived states.

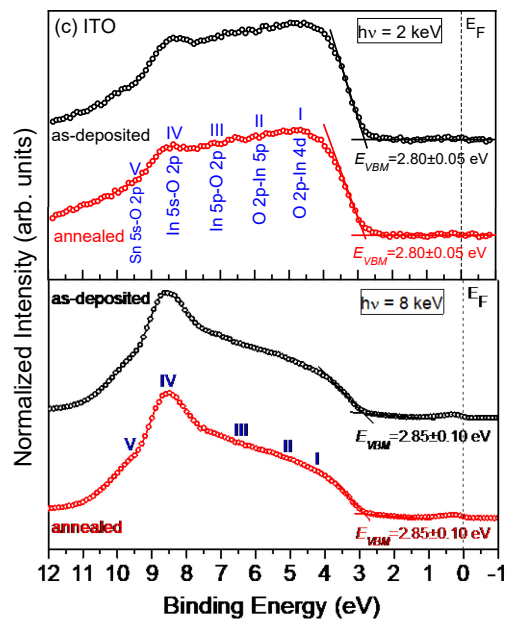
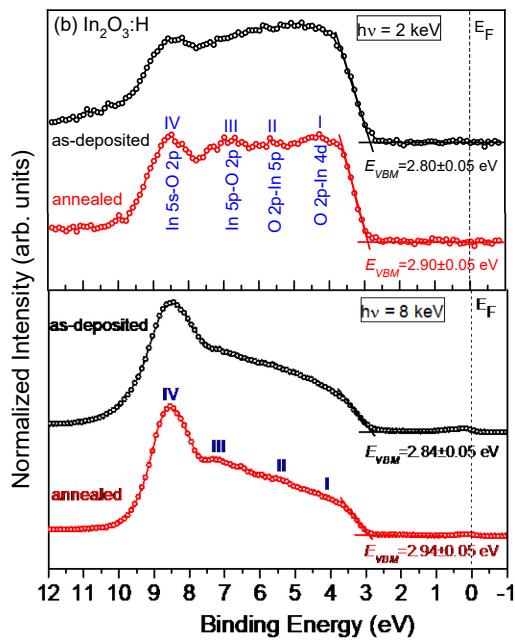
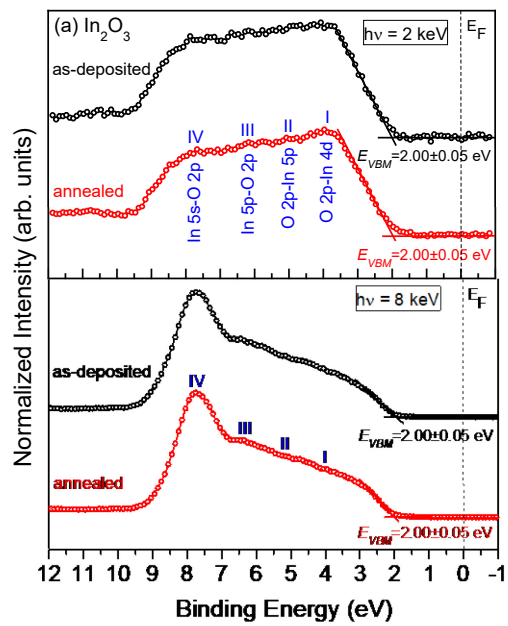




Figure 5.7: Valence-band photoelectron spectra of (a) nominally undoped  $\text{In}_2\text{O}_3$ , (b)  $\text{In}_2\text{O}_3\text{:H}$  and (c) ITO films before and after annealing measured at photon energies of 2 and 8 keV, respectively. The position of the valence-band maximum (VBM) relative to the Fermi level is derived by a linear extrapolation of the leading edge to the background. The spectra are shifted vertically by 1 for better visibility. Open circles represent the experimental data, the lines exhibit the data extrapolation for the experimental data.

The position of the valence-band maximum ( $E_{VBM}$ ) relative to the Fermi level ( $E_F$ ) is derived by a linear extrapolation of the leading edge to the background, as indicated in the figures. Obviously, the  $E_{VBM}$  of indium oxide increases (i.e., moves away from  $E_F$ ) upon doping. We derive  $E_{VBM}$  to be at binding energies of  $(2.00 \pm 0.05)$  eV in undoped  $\text{In}_2\text{O}_3$ , and moves to higher binding energies of  $(2.84 \pm 0.05)$  eV for amorphous  $\text{In}_2\text{O}_3\text{:H}$  and  $(2.85 \pm 0.10)$  eV for ITO, respectively, when measured at 8 keV photon energy. In the spectra of ITO, we observe significant tailing of DOS. We thus determine the extrapolation uncertainty of deriving  $E_{VBM}$  to be  $\pm 0.10$  eV. The evident shift of  $E_{VBM}$  ( $\sim 0.85$  eV) towards higher binding energy upon doping in  $\text{In}_2\text{O}_3$  mirrors the shifts ( $\sim 1.00$  eV) in the O 1s (see Fig. 5.4) and In  $3d_{5/2}$  (see Fig. 5.5) core-level spectra. This is attributed to the shift of  $E_F$  into the conduction band in n-type doped semiconductors caused by the Burstein-Moss (BM) shift and will be described later. For each  $\text{In}_2\text{O}_3$  film, no  $E_{VBM}$  shifts are observed when taken with different photon energies of 2 and 8 keV. Furthermore, it is very important to realize that the crystallized  $\text{In}_2\text{O}_3\text{:H}$  (i.e., annealed sample) shows a shift of  $\sim 0.10$  eV in  $E_{VBM}$  towards higher binding energy compared to amorphous one (i.e., as-deposited sample), which can most likely be explained by the changes in crystal structure.

TABLE 5.4: Binding energies (eV) of In  $3d_{5/2}$  [ $BE(\text{In } 3d_{5/2})$ ] and O 1s [ $BE(\text{O } 1s)$ ] core levels, the VBM energy ( $E_{VBM}$ ) relative to the Fermi level, and the respective values of  $BE_{VB}(\text{In } 3d_{5/2})$  and  $BE_{VB}(\text{O } 1s)$  for each film before and after annealing.

Samples	$BE(\text{In } 3d_{5/2})$ $\pm 0.05$ (eV)	$BE(\text{O } 1s)$ $\pm 0.05$ (eV)	$E_{VBM}$ $\pm 0.05$ (eV)	$BE_{VB}(\text{In } 3d_{5/2})$ $\pm 0.10$ (eV)	$BE_{VB}(\text{O } 1s)$ $\pm 0.10$ (eV)
$\text{In}_2\text{O}_3$ (as-dep.)	443.63	529.34	2.00	441.63	527.34
$\text{In}_2\text{O}_3$ (ann.)	443.63	529.34	2.00	441.63	527.34
$\text{In}_2\text{O}_3\text{:H}$ (as-dep.)	444.52	530.14	2.84	441.68	527.30
$\text{In}_2\text{O}_3\text{:H}$ (ann.)	444.47	530.19	2.94	441.53	527.25
ITO (as-dep.)	444.53	530.15	$2.85(\pm 0.10)$	$441.68(\pm 0.15)$	$527.30(\pm 0.15)$
ITO (ann.)	444.53	530.15	$2.85(\pm 0.10)$	$441.68(\pm 0.15)$	$527.30(\pm 0.15)$

The binding energy difference between the core level ( $CL = \text{In } 3d_{5/2}, \text{O } 1s$ ) and the VBM ( $E_{VBM}$ ), given by  $BE_{VB}(CL) = BE(CL) - E_{VBM}$ , is a material constant. Table 5.4 shows the respective

values of  $BE_{VB}(\text{In } 3d_{5/2})$  and  $BE_{VB}(\text{O } 1s)$ , with the binding energies of In  $3d_{5/2}$  and O  $1s$  core levels and the VBM energy ( $E_{VBM}$ ) relative to the Fermi level for each film. Clearly, the magnitudes of the shifts corresponding to  $BE_{VB}(\text{In } 3d_{5/2})$  and  $BE_{VB}(\text{O } 1s)$  in undoped  $\text{In}_2\text{O}_3$  are very similar to that in doped  $\text{In}_2\text{O}_3$ , except for annealed  $\text{In}_2\text{O}_3\text{:H}$ , determined to be  $(441.63 \pm 0.10)$  and  $(527.34 \pm 0.10)$  eV, respectively. This suggests a strict upward movement of the Fermi level upon doping. However, the annealed  $\text{In}_2\text{O}_3\text{:H}$  exhibits smaller  $BE_{VB}(\text{In } 3d_{5/2})$  and  $BE_{VB}(\text{O } 1s)$  in energy by  $\sim 0.10$  eV than other samples. It may be attributed to some changes in the chemical environment (i.e., the indium hydroxide dehydroxylation) occurring in  $\text{In}_2\text{O}_3\text{:H}$  during annealing.

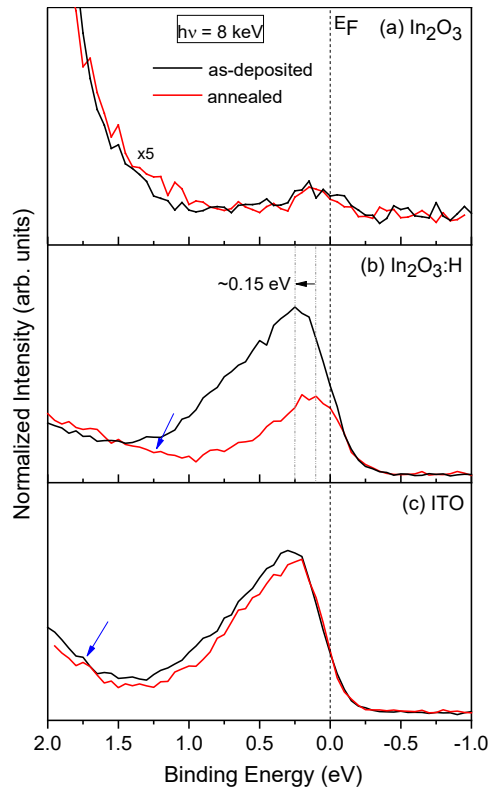


Figure 5.8: HAXPES spectra taken from the low binding energy region around the Fermi level for (a) nominally undoped  $\text{In}_2\text{O}_3$ , (b)  $\text{In}_2\text{O}_3\text{:H}$  and (c) ITO films measured at 8 keV photon energy before and after annealing. Note that the spectra for (a) nominally undoped  $\text{In}_2\text{O}_3$  are magnified by 5 times compared to that of (b)  $\text{In}_2\text{O}_3\text{:H}$  and (c) ITO.

A magnification of the low binding energy region around the Fermi level measured at 8 keV photon energy is shown in Fig. 5.8. A relatively weak feature centered at  $\sim 0.10$  eV below  $E_F$  is observed for undoped  $\text{In}_2\text{O}_3$  [Fig. 5.8 (a)], whereas a well-defined feature around the Fermi level is seen in doped  $\text{In}_2\text{O}_3$  [Fig. 5.8 (b) and (c)]. In ITO, the maximum of this feature located at around 0.25 eV below  $E_F$  exhibits a slight reduction in relative intensity after annealing [Fig.

5.8 (c)]. However, it is strongly decreased in  $\text{In}_2\text{O}_3\text{:H}$  after vacuum annealing [Fig. 5.8 (b)]. We ascribe this reduction to the decrease in carrier density upon annealing. During crystallization, the rearrangement of atomic structures could release oxygen and hydrogen [82]. A release of oxygen and/or hydrogen decreases the donor defect concentration, i.e., the concentration of oxygen vacancies ( $V_o^{2+}$ ) and/or hydrogen donor ( $H_i^+$ ), which is responsible for the decrease in carrier concentration. This would also explain the shift of this feature towards lower binding energy by  $\sim 0.15$  eV.

Such a gap feature is attributed to occupied gap states around the Fermi level, which is largely expected to exist in degenerately doped  $\text{In}_2\text{O}_3$ . To illustrate its nature more clearly, the ionization energies for the corresponding stable configurations of defect clusters in preferential  $\text{In}_2\text{O}_3$  lattice sites are listed in Table 5.5. One first notices that the ionization energies of defect clusters are all negative in ITO. It implies that the defect-related states of Sn dopant are located well above the conduction-band minimum (CBM), thereby allowing hybridization with the conduction band [102]. This behavior leads to the formation of stable gap states inside the band gap [Fig. 5.8 (c)]. In  $\text{In}_2\text{O}_3\text{:H}$ , hydrogen is identified as a shallow donor with an estimated transition level  $H(+/-)$  at about 0.60 eV above the CBM, and it is mostly in the form of interstitial hydrogen ( $H_i^+$ ) [32, 81]. Thus a visible gap state around the Fermi level could also be expected to form in  $\text{In}_2\text{O}_3\text{:H}$  [Fig. 5.8 (b)]. The intrinsic defect cluster ( $In_i-V_o$ ) formed in nominally undoped  $\text{In}_2\text{O}_3$  is reported to be located at approximately 0.10 eV below the bottom of the conduction band [28]. Regarding this, the very weak gap state observed in undoped  $\text{In}_2\text{O}_3$ , to a large extent, might be caused by the intrinsic defect (i.e.,  $In_i-V_o$ ) induced states. As a result, such gap features in the  $\text{In}_2\text{O}_3$  variants could either be attributed to occupied conduction-band states or occupied defect states or both. It needs to be noted that the carrier concentration in undoped  $\text{In}_2\text{O}_3$  shown in Table 5.1 is already over the Mott's critical concentration ( $\sim 5.5 \times 10^{18} \text{ cm}^{-3}$ ) [103], but no well-defined gap features observed in the photoelectron spectra when measured with 2 and 8 keV photon energies [Fig. 5.7 (a) and 5.8 (a)]. It could be most probably attributed to the existence of a surface depletion layer, while the bulk is supposed to be degenerate in undoped  $\text{In}_2\text{O}_3$ . In addition, a band tail near the VB edge is seen in  $\text{In}_2\text{O}_3\text{:H}$  [Fig. 5.8 (b)] and ITO [Fig. 5.8 (c)], as indicated by arrows. It has been previously suggested to arise from the disordered coordination of O atoms in amorphous oxide semiconductors [104, 105]. While the VB tail has been demonstrated to be not intrinsic to the amorphous phase, mostly attributed to varied coordination numbers of O atoms [106, 107]. Thus, a greater band tail observed in crystallized  $\text{In}_2\text{O}_3\text{:H}$  might be due to a much lower coordination of oxygen because of the indium hydroxide dehydroxylation during annealing.

TABLE 5.5: Listed are the most stable configurations for each defect cluster in preferential  $\text{In}_2\text{O}_3$  lattice sites with their ionization energies  $\Delta E_D$ . Note that the calculated band gap for these materials is 3.75 eV.

Samples	Defect Cluster	$\Delta E_D$ (eV)
$\text{In}_2\text{O}_3$	$\text{In}_i^{(a)}-\text{V}_o$	0.099 [28]
	$\text{In}_i^{(c)}-\text{V}_o$	0.101 [28]
$\text{In}_2\text{O}_3:\text{H}$	$\text{H}_i^+$	$\sim(-0.60)$ [32, 81]
ITO	$\text{Sn}_{\text{In}}^{(b)}-\text{V}_o$	$-(0.89)^*$ [102]
	$\text{Sn}_{\text{In}}^{(d)}-\text{V}_o$	$-(1.29)^*$ [102]

\*The given ionization energies are in general equal to their calculated formation energies without consideration of the entropy effect.

### 5.3.6 Valence- and Conduction-band Structures

Fig. 5.9 shows the valence- and conduction-band structure for each film measured using a combination of hard X-ray photoelectron spectroscopy (HAXPES) excited with 8 keV photon energy, O  $K$ -edge emission (XES) and absorption spectroscopy (XAS). All spectra are plotted on a common binding energy scale using the respective HAXPES binding energy of  $\text{O}_I$  peak available in Fig. 5.4. Vertical lines are placed on the spectra to distinguish the energy shifts. O  $K$ -edge XES and XAS techniques can directly probe the occupied and unoccupied O 2p partial density of states (PDOS) in  $\text{In}_2\text{O}_3$ , respectively. Whereas valence-band (VB) HAXPES measurements effectively give the total VB-DOS, which has previously been discussed in detail in Sect. 5.3.5. In VB-HAXPES spectra, an intense peak located at  $\sim 18$  eV below  $E_F$  is assigned to shallow In 4d photoemission line. An additional small peak at a higher binding energy of  $\sim 23$  eV is associated with O 2s photoemission line. An apparent shoulder is observed on the low binding energy side of the In 4d peak in the doped  $\text{In}_2\text{O}_3$  variants, as indicated by black arrows. This is attributed to hybridized In 4d-O 2s derived states, suggesting a different d-s hybridization in the doped  $\text{In}_2\text{O}_3$  variants. In addition, the main In 4d peak in  $\text{In}_2\text{O}_3:\text{H}$  shows a shift of  $\sim 0.20$  eV towards lower binding energy after annealing, but little or no energy shifts are seen for undoped  $\text{In}_2\text{O}_3$  and ITO.

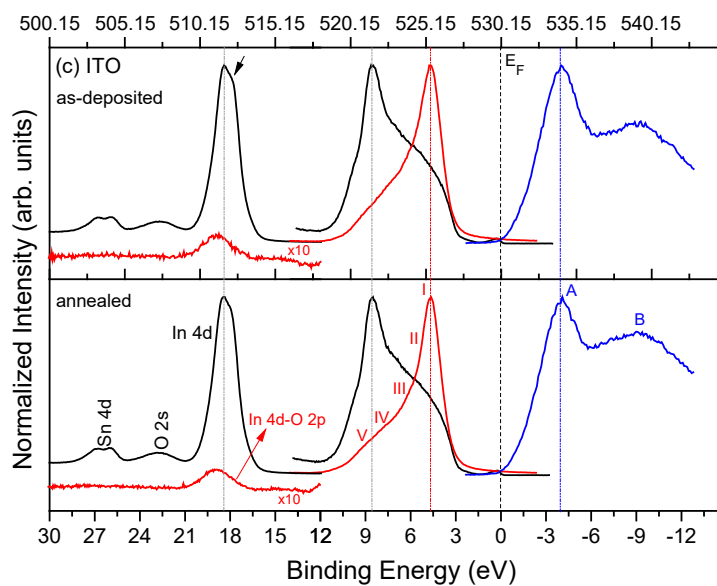
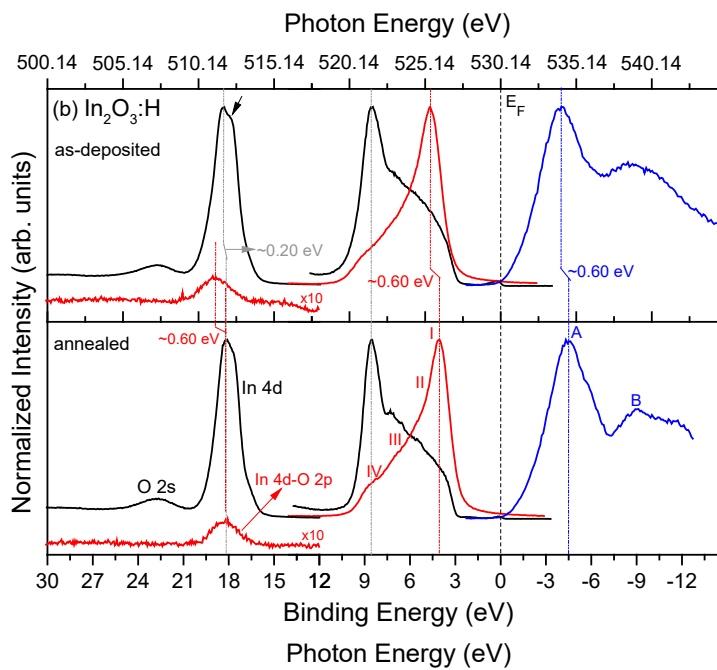
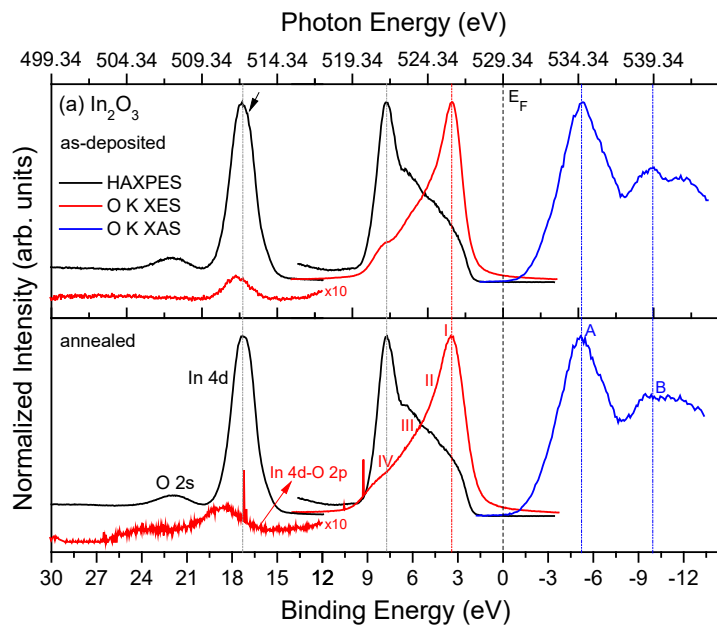


Figure 5.9: The O *K*-edge X-ray emission (XES-*red lines*) and absorption spectra (XAS-*blue lines*) for (a) nominally undoped In<sub>2</sub>O<sub>3</sub>, (b) In<sub>2</sub>O<sub>3</sub>:H and (c) ITO films before and after annealing, together with the shallow Sn 4d and In 4d core levels and valence photoelectron spectra (HAXPES-*black lines*) measured with 8 keV photon energy. All spectra are plotted on a common binding energy scale. Emission from In 4d-O 2p hybridized states at around 18 eV below the Fermi level is magnified by  $\times 10$  for clarity.

The four main features (labeled I-IV) from the HAXPES valence spectra (Fig. 5.7) have been shown in XES spectra for each film. They are assigned to hybridized O 2p-In 4d (I), O 2p-In 5p (II), In 5p-O 2p (III) and In 5s-O 2p (IV) derived states, respectively, along with hybridized Sn 5s-O 2p derived states (V) in ITO. In addition, a peak located at the binding energy of the shallow In 4d core level is observed, corresponding to In 4d-O 2p hybridization (as indicated by red arrows). This indicates that there is not only an O 2p-In 4d hybridization through the O 2p valence band, but also a hybridization of the In 4d with the O 2s and 2p orbitals at the binding energy of shallow In 4d peak. The Sn 4d photoemission peak is located at  $\sim 26$  eV below  $E_F$  in ITO, however, the expected signal of hybridized Sn 4d-O 2p derived states could not be seen in the emission spectra, possibly due to the insufficient signal-to-noise ratio. The XAS spectra yield two main features (A and B), which are assigned to hybridized O 2p-In 5s (A) and O 2p-In 5p (B) derived states, respectively. The XES and XAS data, i.e., spectral shape and w.r.t. energy shifts, changes very little in ITO before and after annealing, whereas for undoped In<sub>2</sub>O<sub>3</sub> there is a slight broadening in the spectral shape of XES and XAS data after annealing. In terms of In<sub>2</sub>O<sub>3</sub>:H, two main features, i.e., feature “I” in XES valence spectrum and feature “A” in XAS conduction spectrum, both show a clear shift of  $\sim 0.60$  eV towards lower binding energies after annealing, respectively, as well emerges for the peak assigned to hybridized In 4d-O 2p derived states. This is broadly consistent with the shift of HAXPES-In 4d peak ( $\sim 0.20$  eV) towards lower binding energy in In<sub>2</sub>O<sub>3</sub>:H after annealing. It might arise from a different coupling of O 2p-In 4d derived states in annealed In<sub>2</sub>O<sub>3</sub>:H, thereby leading to the band states moving away from the VBM and the CBM.

Figure 5.10 shows the O *K*-edge XES and XAS spectra of the low binding energy region around the Fermi level for each film before and after annealing. In good agreement with the occupied gap states (mostly the occupied conduction-band states) observed in HAXPES valence spectra (shown in Fig. 5.8), a weak pre-edge spectral intensity right above the Fermi level governs onset of the absorption spectra in the doped In<sub>2</sub>O<sub>3</sub> variants; in this case the Fermi level lays inside the conduction band [indicated by black arrows in Fig. 5.10 (b) and (c)]. In comparison to emission

spectra, the absorption spectra show a slow (or “tail-like”) onset of the conduction band rather than a sharp valence edge. In general, there are three factors for these different spectral weights in onsets of the XES and XAS spectra. The main reason is that the O 2p partial density of states (PDOS) in  $\text{In}_2\text{O}_3$  have always shown a sharp onset of the XES valence spectrum and a broad tail below the onset of the XAS conduction spectrum [99]. Another possible effect is due to an asymmetric response of the core holes to the valence and conduction electrons. As previously mentioned in Sect. 5.3.4, the O 1s photoemission line exhibits an asymmetric shape, with a “narrow” low binding energy and a “broad” high binding energy contribution. This can produce an asymmetric energy distribution of the core holes, which could be reflected in both the absorption and emission processes. In this situation, the core-hole potential would have an asymmetric modification of the spectral distribution in the XES valence and XAS conduction band; a “narrow” low energy and a “broad” high energy contribution in both the XES and XAS spectra. The VBM is the high energy part of the XES spectrum, while the CBM is the low energy part of the XAS spectrum. Also, it might be caused by the instrumental broadening that is limited by the experimental setup. Those effects can bring up an extrapolation uncertainty ( $\pm 0.30$  eV) in the determination of the onsets of spectral weight in the XES & XAS spectra.

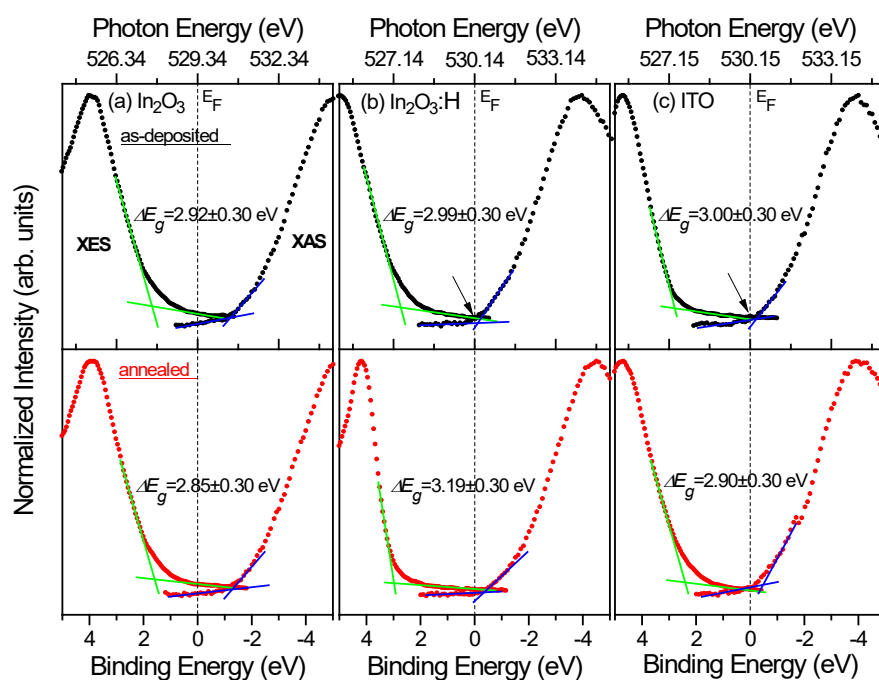


Figure 5.10: O *K*-edge XES and XAS spectra taken from the low binding energy region around the Fermi level for (a) nominally undoped  $\text{In}_2\text{O}_3$ , (b)  $\text{In}_2\text{O}_3\text{:H}$  and (c) ITO films before and after annealing. The energy positions of the onsets of the XES valence (*green lines*) and XAS conduction spectra (*blue lines*) relative to the Fermi level are derived by a linear extrapolation of the leading edges to the background.

Typically, XES and XAS techniques can be combined to reveal the band gaps of the near-surface bulk of the films from the XES-XAS separation. The onset of spectral weight in the XES and XAS spectra is determined by a linear extrapolation of the leading edge to the background, as indicated in Fig. 5.10. As mentioned above, the XAS spectra of each film has a broad tail below the conduction-band onset, we thus determine the onset of spectral weight in the XAS spectra by extrapolating the band tail to the background, instead of the valence-band edge in the XES spectra. The measured band gaps of undoped In<sub>2</sub>O<sub>3</sub> before and after annealing are determined to be (2.92±0.30) and (2.85±0.30) eV, respectively. These experimental band gaps agree with other theoretical literature band gaps of In<sub>2</sub>O<sub>3</sub>, with calculated values of 2.90 and 2.87 eV [70-72], respectively. Compared to undoped In<sub>2</sub>O<sub>3</sub>, the doped In<sub>2</sub>O<sub>3</sub> variants appear to show a larger gap size, which could be attributed to occupancy of the conduction band. The ITO films have the band gaps of (3.00±0.30) and (2.90±0.30) eV before and after annealing, respectively. The energy difference (~0.10 eV) between them might be caused by the substrate difference [shown in Fig. 5.1 (c) and (d)]. For In<sub>2</sub>O<sub>3</sub>:H, the measured band gaps of (2.99±0.30) and (3.19±0.30) eV are shown before and after annealing.

### 5.3.7 Band-gap Determination by Spectroscopic Ellipsometry

As described previously in Sect. 2.3, upon doping of In<sub>2</sub>O<sub>3</sub> above the onset of degeneracy there is an increased electron filling in the conduction band. In this situation, electronic transitions into states will be blocked at the bottom of the conduction band, which shifts the onset of optical absorption towards higher energies. This is typically explained as the Burstein-Moss (BM) shift. Given that the valence and conduction bands are nonparabolic, in a simple free-electron model, the magnitude of the Burstein-Moss (BM) shift ( $\Delta E_g^{BM}$ ) as carrier density increasing in heavily doped semiconductors is expressed through the following relationship [4, 5],

$$\Delta E_g^{BM} = \left(\frac{h}{2\pi}\right)^2 \frac{(3\pi^2 N_e)^{2/3}}{2m_{cv}^*}, \quad (5-1)$$

Here  $h$  is the Plank's constant, and  $N_e$  is the carrier density inside the conduction band.  $m_{cv}^*$  is the reduced effective mass given by  $1/m_{cv}^* = 1/m_c^* + 1/m_v^*$ , in which  $m_c^*$  and  $m_v^*$  are the effective masses of conduction electrons and valence holes, respectively. For In<sub>2</sub>O<sub>3</sub>, it has been reported in previous literature [108-110] that the effective electron masses  $m_c^*$  for amorphous and crystallized In<sub>2</sub>O<sub>3</sub> are 0.31  $m_0$  and 0.23  $m_0$ , respectively, where  $m_0$  is the free-electron mass. They are both in good agreement with the reported experimental range ( $m_c^* \approx 0.20-0.35 m_0$ ) [111]. The valence-band effective mass for In<sub>2</sub>O<sub>3</sub> has been generally reported as  $m_v^* \approx 0.60 m_0$



[65]. Combining that with Eq. (5-1), the magnitudes of the Burstein-Moss (BM) shift in the conduction  $[\Delta E_{g(CB)}^{BM}]$  and valence band  $[\Delta E_{g(VB)}^{BM}]$  for each  $\text{In}_2\text{O}_3$  film are estimated before and after annealing and shown in Table 5.6. In this work, the undoped  $\text{In}_2\text{O}_3$  is likely degenerate in the bulk according to its high hall concentration (see Table 5.1), thus a band-gap widening caused by the Burstein-Moss (BM) shift could be considered. In general, the calculated magnitude of the Burstein-Moss (BM) shift is proportional to the carrier density.

TABLE 5.6: Values of the calculated magnitudes of the experimental shifts caused by the Burstein-Moss (BM) and the band-gap renormalization (BGR) effects in the conduction  $[\Delta E_{g(CB)}^{BM}, \Delta E_{g(CB)}^{BGR}]$  and valence band  $[\Delta E_{g(VB)}^{BM}, \Delta E_{g(VB)}^{BGR}]$ .

Samples	Carrier concentration $N_e$ ( $\text{cm}^{-3}$ )	$\Delta E_{g(CB)}^{BM}$ $\pm 0.10$ (eV)	$\Delta E_{g(VB)}^{BM}$ $\pm 0.10$ (eV)	$\Delta E_{g(CB)}^{BGR}$ $\pm 0.10$ (eV)	$\Delta E_{g(VB)}^{BGR}$ $\pm 0.10$ (eV)	$\Delta E_g^{BM}$ $\pm 0.15$ (eV)	$\Delta E_g^{BGR}$ $\pm 0.15$ (eV)
$\text{In}_2\text{O}_3$ (as-dep.)	$1.59 \times 10^{20}$	0.46	0.18	0.29	0.47	0.64	0.76
$\text{In}_2\text{O}_3$ (ann.)	$1.68 \times 10^{20}$	0.48	0.18	0.30	0.48	0.66	0.78
$\text{In}_2\text{O}_3:\text{H}$ (as-dep.)	$3.86 \times 10^{20}$	0.62	0.32	0.40	0.49	0.94	0.89
$\text{In}_2\text{O}_3:\text{H}$ (ann.)	$1.64 \times 10^{20}$	0.48	0.18	0.30	0.47	0.66	0.77
ITO (as-dep.)	$2.84 \times 10^{20}$	0.51	0.26	0.35	0.43	0.77	0.78
ITO (ann.)	$2.43 \times 10^{20}$	0.46	0.24	0.33	0.40	0.70	0.73

Meanwhile, the optical-band gap as a function of carrier concentration in degenerately doped semiconductors cannot only be interpreted by the Burstein-Moss (BM) shift, a band-gap narrowing from many-body interaction effects also needs to be taken into consideration. This is referred to as the band-gap renormalization (BGR) effect. As listed in Table 5.1, all the  $\text{In}_2\text{O}_3$  variants have carrier densities above the Mott's critical concentration ( $\sim 5.5 \times 10^{18} \text{ cm}^{-3}$  [103]) due to intrinsic (i.e.,  $V_o^{2+}$  and  $In_i$ ) and/or extrinsic defects (i.e.,  $Sn^{4+}$  and  $Hi^+$ ) so they are expected to be degenerate in the bulk. Above Mott's critical density when the material is degenerate, the mutual exchange and Coulomb interactions in the conduction and valence band would exist, which leads to a considerable shrinkage of the optical-band gap. Based on Jain's analysis [112], a developed model for the band-gap renormalization (BGR) effect ( $\Delta E_g^{BGR}$ ) in a degenerate n-type semiconductor is given by the following simple expression,

$$\Delta E_g^{BGR} = K_1 N_e^{1/3} + K_2 \left( \frac{m_c^*}{m_0} \right)^{1/4} \times N_e^{1/4} + K_3 \left( \frac{m_0}{m_c^*} \right)^{1/2} \left( 1 + \frac{m_v^*}{m_c^*} \right) N_e^{1/2}, \quad (5-2)$$

In this expression, the four terms account for conduction electrons exchange interaction, valence electrons correlation energy, conduction electron-impurity interaction, and valence electron-impurity interaction, respectively. The first and third terms represent contributions of

the lowering of the conduction band on the band-gap narrowing, while the second and fourth terms contribute to upward shift of the valence band. Here  $K_1$ ,  $K_2$ ,  $K_3$  are the coefficients, which have been theoretically determined to be  $K_1 = 2.58 \times 10^{-8}$  eV cm,  $K_2 = 8.25 \times 10^{-7}$  eV cm<sup>3/4</sup>, and  $K_3 = 5.91 \times 10^{-12}$  eV cm<sup>3/2</sup> for degenerately doped In<sub>2</sub>O<sub>3</sub>. In this way, the magnitudes of the band-gap renormalization (BGR) effect in the conduction [ $\Delta E_{g(CB)}^{BGR}$ ] and valence band [ $\Delta E_{g(VB)}^{BGR}$ ] for each In<sub>2</sub>O<sub>3</sub> film are estimated before and after annealing and also shown in Table 5.6. Note that the values for  $\Delta E_{g(CB)}^{BGR}$  and  $\Delta E_{g(VB)}^{BGR}$  in this work are both positive quantities, consistent with the convention used in device modeling. It can be seen that the conduction-band term [ $\Delta E_{g(CB)}^{BGR}$ ] is smaller than that of the valence band [ $\Delta E_{g(VB)}^{BGR}$ ], which is in agreement with Sans *et al*'s calculations [113]. By comparing the calculated values of the  $\Delta E_g^{BM}$  and  $\Delta E_g^{BGR}$ , it appears that the Burstein-Moss (BM) shift is largely compensated by the band-gap renormalization (BGR) effect.

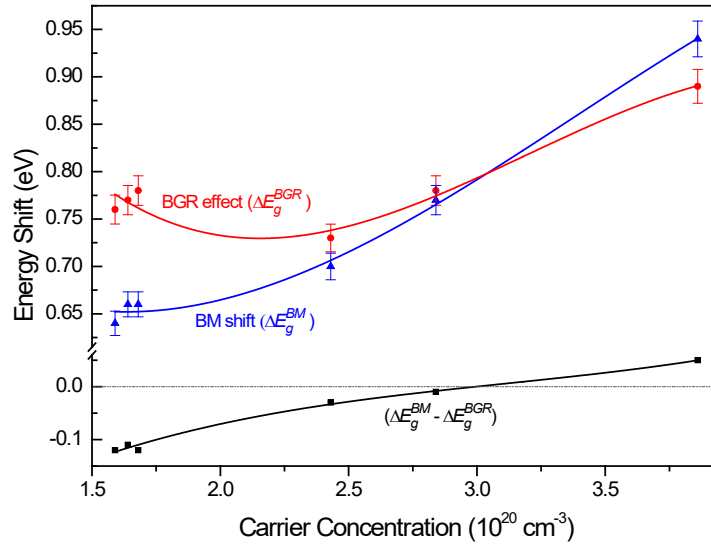


Figure 5.11: Calculated energy shifts caused by the Burstein-Moss (BM,  $\Delta E_g^{BM}$ ) and the band-gap renormalization (BGR,  $\Delta E_g^{BGR}$ ) effects as a function of carrier concentrations determined by Hall-effect measurements. The blue-dotted curve corresponds to the BM shift, and the red-dotted curve corresponds to the BGR effect. The black-dotted curve is the sum of these two competing contributions (i.e.,  $\Delta E_g^{BM} - \Delta E_g^{BGR}$ ).

To gain more insights into the theoretical models, the calculated energy shifts caused by the Burstein-Moss (BM,  $\Delta E_g^{BM}$ ) and the band-gap renormalization (BGR,  $\Delta E_g^{BGR}$ ) effects as a function of carrier concentrations determined by Hall-effect measurements are shown in Fig 5.11. In general, the energy shifts (i.e.,  $\Delta E_g^{BM}$  and  $\Delta E_g^{BGR}$ ) are proportional to the carrier densities. At the doping concentration below around  $3.0 \times 10^{20}$  cm<sup>-3</sup>, the BGR is the dominating

effect. With further increase in doping concentration, the effect of the BM shift overcomes that of the BGR effect. That agrees well with Jia *et al.*'s theoretical calculations of the BM shift and the BGR effect [114].

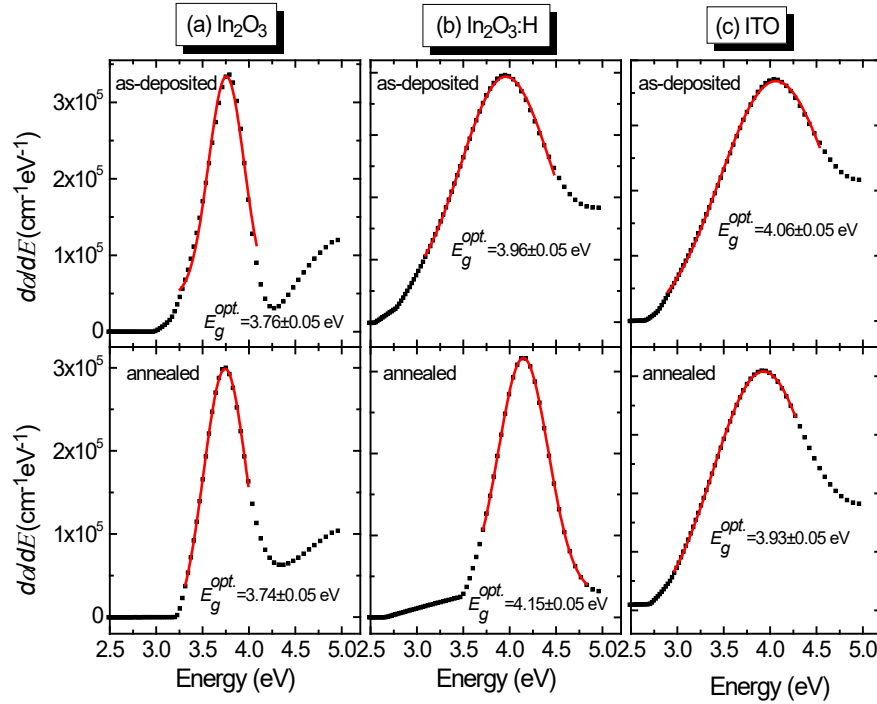


Figure 5.12: Derivation ( $da/dE$ ) of absorption coefficient  $\alpha$  and photon energy  $E$  in the near gap spectral range for (a) nominally undoped  $\text{In}_2\text{O}_3$ , (b)  $\text{In}_2\text{O}_3\text{:H}$  and (c) ITO films before and after annealing. Solid dots represent the experimental data, and the curved red line exhibits the data fitting for each experimental data.

In this work, an estimation of the optical-band gap ( $E_g^{opt.}$ ) is simply done by locating the maximum of  $da/dE$  [115]. Here the absorption coefficient  $\alpha$  and photon energy  $E$  are obtained through spectroscopic ellipsometry measurements, as described in Sect. 4.2.2. This method enables an accurately determined optical-band gap by taking into consideration the Burstein-Moss (BM) shift and the band-gap renormalization (BGR) effect in degenerately doped semiconductors [65]. Owing to that the samples used in this work have been deposited on various substrates, the spectra are analyzed using different models. For  $\text{In}_2\text{O}_3\text{:H}$  and ITO films, it is sufficient to model a single layer on the respective substrate with a small contribution by surface roughness. While a two-layer approach with additional surface roughness has to be implemented in undoped  $\text{In}_2\text{O}_3$ . More details on the ellipsometry model analysis have been in detail provided in Appendix A. The resulting plots of  $da/dE$  derivation as a function of photon energy  $E$  based on ellipsometry analysis are shown in Fig. 5.12 for each film before and after annealing. In Fig. 5.12 (a), the  $da/dE$  derived  $E_g^{opt.}$  of undoped  $\text{In}_2\text{O}_3$  are determined to be

( $3.76\pm 0.05$ ) and ( $3.74\pm 0.05$ ) eV before and after annealing, respectively. They are very close in energy to the typically reported band gap of  $\sim 3.75$  eV from the onset of significant optical absorption in  $\text{In}_2\text{O}_3$  [70-72]. Compared to undoped  $\text{In}_2\text{O}_3$ , the doped  $\text{In}_2\text{O}_3$  tends to have a larger  $da/dE$  derived  $E_g^{opt.}$ , mainly attributed to the band-gap widening caused by the Burstein-Moss (BM) shift via doping. Although this widening could be counteracted by the band-gap renormalization (BGR) effect, the net effect is to increase the gap of the degenerately doped  $\text{In}_2\text{O}_3$ . A significantly large  $da/dE$  derived  $E_g^{opt.}$  of ( $4.15\pm 0.05$ ) eV is present in annealed  $\text{In}_2\text{O}_3:\text{H}$  [Fig. 5.12 (b)], most likely due to the changes of the crystal structure during annealing. The ITO films yield the  $da/dE$  derived  $E_g^{opt.}$  of ( $4.06\pm 0.05$ ) and ( $3.93\pm 0.05$ ) eV before and after annealing [Fig. 5.12 (c)], respectively, where the energy difference ( $\sim 0.13$  eV) would be due to the substrate difference [shown in Fig. 5.1 (c) and (d)]. From that, the band gaps of these films do not well increase with increasing carrier density.

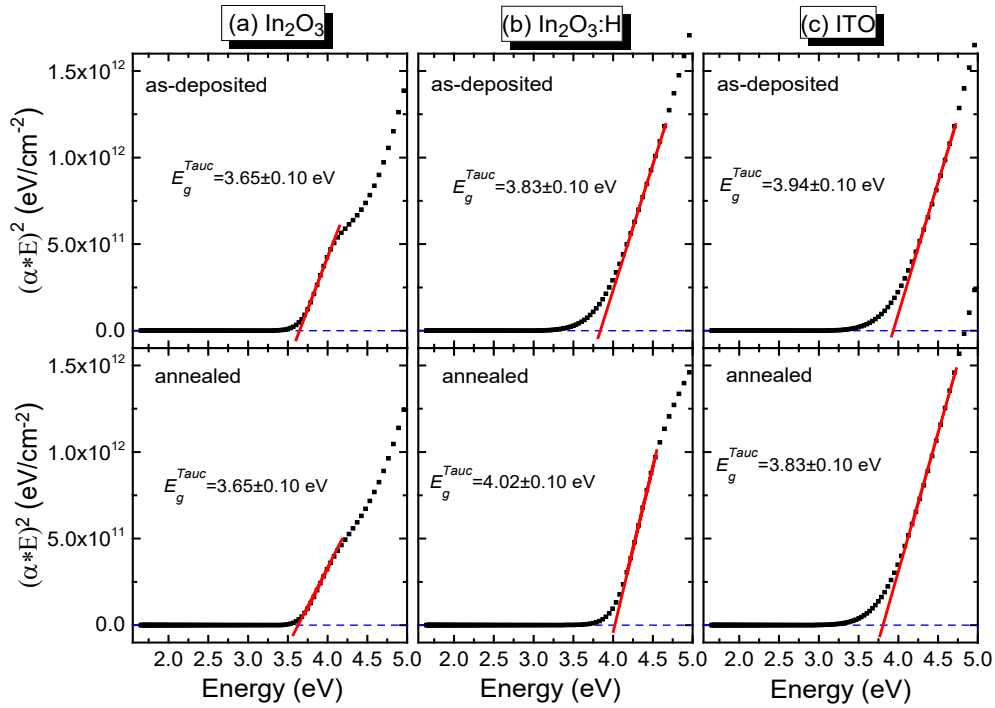


Figure 5.13: Square of absorption coefficient  $\alpha^2$  against photon energy  $E$  in the near gap spectral range for (a) nominally undoped  $\text{In}_2\text{O}_3$ , (b)  $\text{In}_2\text{O}_3:\text{H}$  and (c) ITO films before and after annealing. Solid dots represent the experimental data, and the straight-red line exhibits the linear extrapolation for each experimental data.

Tauc extrapolation technique is adapted to determine the band gaps of  $\text{In}_2\text{O}_3$  from ellipsometry measurements [116]. The Tauc gap ( $E_g^{Tauc}$ ) was estimated by extrapolating the linear portion of the square of absorption coefficient against the photon energy ( $\alpha^2$  vs.  $E$ ), as shown in Fig. 5.13, which gives a direct band gap. This is an approximate method as the value of  $E_g^{Tauc}$  is not

as correct as that determined by the maximum of  $d\alpha/dE$  ( $E_g^{opt.}$ ) due to lifetime broadening effect [65]. In Fig. 5.13 (a), undoped  $\text{In}_2\text{O}_3$  has a  $E_g^{Tauc}$  of  $(3.65\pm 0.10)$  eV, which agrees well with the literature values [70-72]. Compared to undoped  $\text{In}_2\text{O}_3$ , the doped  $\text{In}_2\text{O}_3$  shows a larger  $E_g^{Tauc}$  [Fig. 5.13 (b) and (c)]. In  $\text{In}_2\text{O}_3:\text{H}$  [Fig. 5.13 (b)], it changes during vacuum annealing from  $(3.83\pm 0.10)$  to  $(4.02\pm 0.10)$  eV. For ITO, the  $E_g^{Tauc}$  is determined to be  $(3.94\pm 0.10)$  and  $(3.83\pm 0.10)$  eV before and after annealing, respectively.

TABLE 5.7: Values of band gaps (eV) derived by the XES-XAS separation ( $E_g^{XES-XAS}$ ),  $d\alpha/dE$  derived ellipsometry analysis (optical-band gap,  $E_g^{opt.}$ ), and Tauc gap based on ellipsometry analysis ( $E_g^{Tauc}$ ), and the valence-band maximum ( $E_{VBM}$ ) relative to the Fermi level measured with 8 keV photon energy. The fundamental-band gap ( $E_g^{fund.}$ ), extracted from the energy distance between the  $E_{VBM}$  (or  $E_g^{XES-XAS}$  for undoped  $\text{In}_2\text{O}_3$ ) and the width of conduction-band filling [ $\Delta E_{g(CB)}^{BM}$ ] (shown in Table 5.6), and the intrinsic-band gap ( $E_g^0$ ), derived by the energy separation from the  $E_g^{fund.}$  to the band shrinkage by the BGR effect ( $\Delta E_g^{BGR}$ ) (shown in Table 5.6), as well as the energy difference between the optical-band gap ( $E_g^{opt.}$ ) and the  $E_{VBM}$  (also  $E_g^{XES-XAS}$ ) for each film are given below.

Samples	$E_{VBM}$ ( $\pm 0.05$ )	$E_g^{XES-XAS}$ ( $\pm 0.30$ )	$E_g^{opt.}$ ( $\pm 0.05$ )	$E_g^{Tauc}$ ( $\pm 0.10$ )	$E_g^{fund.}$ ( $\pm 0.10$ )	$E_g^0$ ( $\pm 0.15$ )	$(E_g^{opt.} - E_g^{XES-XAS})$ ( $\pm 0.35$ )	$(E_g^{opt.} - E_{VBM})$ ( $\pm 0.10$ )
$\text{In}_2\text{O}_3$ (as-dep.)	2.00	2.92	3.76	3.65	2.46	3.22	0.84	
$\text{In}_2\text{O}_3$ (ann.)	2.00	2.85	3.74	3.65	2.37	3.15	0.89	
$\text{In}_2\text{O}_3:\text{H}$ (as-dep.)	2.84	2.99	3.96	3.83	2.22	3.11	0.97	1.12
$\text{In}_2\text{O}_3:\text{H}$ (ann.)	2.94	3.19	4.15	4.02	2.46	3.23	0.96	1.21
ITO (as-dep.)	2.85( $\pm 0.10$ )	3.00	4.06	3.94	2.34( $\pm 0.15$ )	3.12( $\pm 0.20$ )	1.06	1.21( $\pm 0.15$ )
ITO (ann.)	2.85( $\pm 0.10$ )	2.90	3.93	3.83	2.39( $\pm 0.15$ )	3.12( $\pm 0.20$ )	1.03	1.08( $\pm 0.15$ )

Table 5.7 summarizes the values of band gaps derived from the XES-XAS separation ( $E_g^{XES-XAS}$ ),  $d\alpha/dE$  derived ellipsometry analysis (optical-band gap,  $E_g^{opt.}$ ), Tauc gap based on ellipsometry analysis ( $E_g^{Tauc}$ ), as well as the extracted fundamental- ( $E_g^{fund.}$ ) and intrinsic-band gap ( $E_g^0$ ), together with the valence-band maximum ( $E_{VBM}$ ) relative to the Fermi level when measured at 8 keV photon energy. Obviously, the  $d\alpha/dE$  derived  $E_g^{opt.}$  for each film is similar but somewhat larger in energy by (0.09-0.13) eV than the measured  $E_g^{Tauc}$ . This is in good agreement with the Hamberg *et al*'s theoretical prediction [65], where the gap estimation by locating of the maximum of  $d\alpha/dE$  is greater than that by extrapolation of ( $\alpha^2$  vs.  $E$ ), ranging from 0.07 eV for the lowest carrier density ( $4.0\times 10^{19}$   $\text{cm}^{-3}$ ) to 0.25 eV for the highest carrier density ( $8.0\times 10^{20}$   $\text{cm}^{-3}$ ). This discrepancy can be strongly dependent on the width of the lifetime

broadening ( $\tau$ ). The size of the energy gap ( $E_g^{XES-XAS}$ ) from the emission-absorption spectrum represents the energy distance from the highest occupied valence to the lowest unoccupied conduction states, i.e., the VBM-CBM separation in an undoped semiconductor. The fundamental-band gap ( $E_g^{fund.}$ ) can be extracted from the energy distance between the  $E_{VBM}$  (or  $E_g^{XES-XAS}$  for undoped  $\text{In}_2\text{O}_3$ ) and the width of conduction-band filling [ $\Delta E_{g(CB)}^{BM}$ ], and will be described in Fig. 5.14. All  $\text{In}_2\text{O}_3$  variants yield very similar  $E_g^{fund.}$  with the average value of  $(2.37 \pm 0.10)$  eV. This value is much smaller than that (about 2.9 eV) determined by Walsh *et al.* [40]. As previously mentioned in Sec. 2.3, the  $E_g^{fund.}$  in a semiconductor material will decrease after doping due to the band-gap renormalization (BGR) effect. However, our calculated  $E_g^{fund.}$  is generally independent on doping behavior. In addition, the intrinsic-band gap ( $E_g^0$ ) can be derived from the  $E_g^{fund.}$  under considerations of the band shrinkage by the BGR effect ( $\Delta E_g^{BGR}$ ), giving very similar value [ $(3.15 \pm 0.15)$  eV on average] for each film. In undoped  $\text{In}_2\text{O}_3$ , the  $E_g^{XES-XAS}$  can correspond to the fundamental-band gap ( $E_g^{fund.}$ ). While for degenerately doped  $\text{In}_2\text{O}_3$ , the  $E_g^{XES-XAS}$  can roughly correspond to the VBM ( $E_{VBM}$ ) relative to the Fermi level. In that connections, the gap disparity between the  $da/dE$  derived  $E_g^{opt.}$  and the  $E_{VBM}$  for doped  $\text{In}_2\text{O}_3$  (i.e.,  $E_g^{XES-XAS}$  for each  $\text{In}_2\text{O}_3$ ) is also shown in Table 5.7. The doped  $\text{In}_2\text{O}_3$  variants have a much larger gap disparity than undoped  $\text{In}_2\text{O}_3$ . The values of the gap disparities between the  $da/dE$  derived  $E_g^{opt.}$  and the  $E_{VBM}$  are greater than that between the  $da/dE$  derived  $E_g^{opt.}$  and the  $E_g^{XES-XAS}$  for the doped  $\text{In}_2\text{O}_3$  variants, but still being well within an uncertainty of  $\pm 0.30$  eV. This discrepancy might be caused by the core-hole effects on the onset of the XAS spectra. Note that the crystallized  $\text{In}_2\text{O}_3:\text{H}$  shows a larger gap disparity by  $\sim 0.10$  eV than the amorphous one. An energy difference of about 0.10 eV in the gap disparity is also seen for ITO before and after annealing, probably due to a different sample substrate [shown in Fig. 5.1 (c) and (d)].

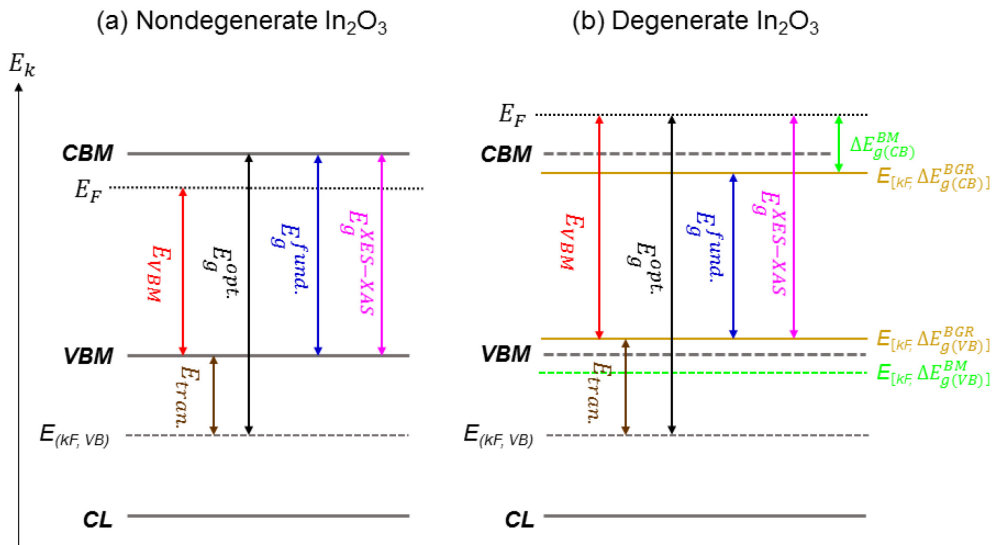


Figure 5.14: Schematic illustration of the respective band gaps derived from Table 5.7, including  $d\alpha/dE$  derived  $E_g^{opt.}$  (black arrows),  $E_g^{fund.}$  (blue arrows), and  $E_g^{XES-XAS}$  (magenta arrows), as well as the HAXPES derived  $E_{VBM}$  (red arrows) relative to the Fermi level upon degenerate doping in  $\text{In}_2\text{O}_3$ : (a) before doping (i.e., nondegeneracy), (b) after degenerate doping with the band-gap widening from the Burstein-Moss (BM) shift and a band-gap narrowing from the band-gap renormalization (BGR) effect towards both valence and conduction bands. An upward dispersion of the topmost valence band [ $E(k_F, \Delta E_{g(VB)}^{BGR})$ ] and a downward dispersion of the lowest conduction band [ $E(k_F, \Delta E_{g(CB)}^{BGR})$ ] are present after band-gap renormalization (yellow dash lines). The conduction-band filling [ $\Delta E_{g(CB)}^{BM}$ ] arises from the Burstein-Moss (BM) shift, which also results in a downward dispersion of the valence band [ $E(k_F, \Delta E_{g(VB)}^{BM})$ ] (green dash lines). In the case of degenerately doped  $\text{In}_2\text{O}_3$ , the top of the valence band and the bottom of the conduction band act as references [i.e., the VBM and the CBM in a nondegenerate  $\text{In}_2\text{O}_3$  shown in 5.14 (a)]. Note that the first allowed optical transition from the valence into conduction band in  $\text{In}_2\text{O}_3$  is below the valence-band edge ( $E_{trans.}$ ), as indicated by [ $E(k_F, VB)$ ].

For a better visualization of the energy-level positions, the respective band gaps including the  $d\alpha/dE$  derived  $E_g^{opt.}$ ,  $E_g^{fund.}$ , and  $E_g^{XES-XAS}$ , together with the HAXPES derived position of the valence-band maximum ( $E_{VBM}$ ) relative to the Fermi level are schematically shown in Fig. 5.14. Meanwhile, the respective dispersions of the valence and conduction band caused by the Burstein-Moss (BM) shift and the band-gap renormalization (BGR) effect in degenerate doping of  $\text{In}_2\text{O}_3$  are considered and already discussed in detail in Sect. 2.3. In a nondegenerate  $\text{In}_2\text{O}_3$  [before doping in Fig. 5.14 (a)], the conduction-band minimum (CBM) is located well above the Fermi level. The HAXPES derived  $E_{VBM}$  represents the energy difference between the VBM and the Fermi level. In most nondegenerate semiconductors, the  $d\alpha/dE$  derived  $E_g^{opt.}$  is actually the fundamental-band gap ( $E_g^{fund.}$ ) (i.e., the energy difference between the VBM and the CBM). While in the case of  $\text{In}_2\text{O}_3$ , the optical transitions from the electronic states close to the VBM into the CBM are symmetry forbidden, which are only allowed from a band below the VBM [40], as discussed in Sect. 2.3. Consequently, the  $d\alpha/dE$  derived  $E_g^{opt.}$  in  $\text{In}_2\text{O}_3$  is larger than the corresponding  $E_g^{fund.}$ , which is calculated as the energy separation from the first allowed transition level in the valence band to the CBM. In a nondegenerate semiconductor, the fundamental-band gap ( $E_g^{fund.}$ ) is defined as the intrinsic-band gap ( $E_g^0$ ), corresponding to the  $E_g^{XES-XAS}$ . In this connection, the position of the first allowed transition level below the VBM ( $E_{tran.}$ ) can be derived by the gap disparity between the  $d\alpha/dE$  derived  $E_g^{opt.}$  and the  $E_g^{fund.}$  (i.e.,  $E_g^{XES-XAS}$ ) in a nondegenerate  $\text{In}_2\text{O}_3$ .

Upon degenerate doping in  $\text{In}_2\text{O}_3$  [Fig. 5.14 (b)], the Burstein-Moss (BM) shift results in filling of the conduction band [ $\Delta E_{g(\text{CB})}^{\text{BM}}$ ] and a downward dispersion of the valence band [ $E(k_F, \Delta E_{g(\text{VB})}^{\text{BM}})$ ]. While the competitive band-gap renormalization (BGR) effect would lead to the respective dispersions of the topmost valence band [ $E(k_F, \Delta E_{g(\text{VB})}^{\text{BGR}})$ ] and the lowest conduction band [ $E(k_F, \Delta E_{g(\text{CB})}^{\text{BGR}})$ ] in the opposite way. The position of the  $E_{\text{VBM}}$  is the highest occupied valence-band edge [ $E(k_F, \Delta E_{g(\text{VB})}^{\text{BGR}})$ ] relative to the Fermi level, similar to the  $E_g^{\text{XES-XAS}}$ . In this situation, the  $d\alpha/dE$  derived  $E_g^{\text{opt.}}$  of degenerately doped  $\text{In}_2\text{O}_3$  will increase and is defined as the energy distance from the first allowed transition level in the valence band to the Fermi level. While the  $E_g^{\text{fund.}}$  will decrease due to the band-gap renormalization (BGR) effect, determined by the energy difference between the  $E_{\text{VBM}}$  and the width of conduction-band filling [ $\Delta E_{g(\text{CB})}^{\text{BM}}$ ]. As a result, the position of the first allowed transition level in the valence band ( $E_{\text{tran.}}$ ) in a degenerately doped  $\text{In}_2\text{O}_3$  would be determined by the energy separation from the  $d\alpha/dE$  derived  $E_g^{\text{opt.}}$  to the  $E_{\text{VBM}}$  (or  $E_g^{\text{XES-XAS}}$ ), rather than just from the  $d\alpha/dE$  derived  $E_g^{\text{opt.}}$  to the  $E_g^{\text{fund.}}$ . Obviously, the position of the first allowed transition level in the valence band ( $E_{\text{tran.}}$ ) for a degenerately doped  $\text{In}_2\text{O}_3$  would be deeper than that in a nondegenerate film due to the BM and BGR effects.

### 5.3.8 Energy-level Positions

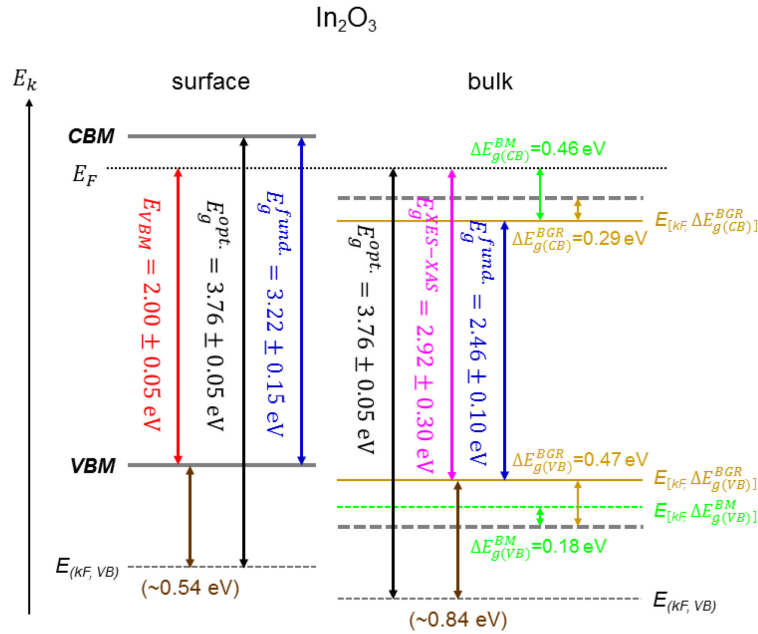


Figure 5.15: Schematic band-gap structure for nominally undoped  $\text{In}_2\text{O}_3$  at the surface and in the bulk, respectively. For the degenerate bulk, the Burstein-Moss (BM) shift and the band-gap renormalization (BGR) effect are considered, and the calculated values of the band dispersions caused by the BM and BGR effects are indicated. For the nondegenerate surface,



the HAXPES derived  $E_{VBM}$  relative to the Fermi level is taken with 8 keV photon energy. Note that the first allowed transition level in the valence into conduction band is identified by  $[E(k_F, VB)]$ .

To well understand the allowed transition level in the valence band, the energy-level positions based on the band structures of nominally undoped  $\text{In}_2\text{O}_3$ ,  $\text{In}_2\text{O}_3\text{:H}$  and ITO films before and after annealing are schematically investigated here. As discussed above, there is a potential surface depletion existing in undoped  $\text{In}_2\text{O}_3$ , i.e., a nondegenerate surface, while it is supposed to be degenerate in the bulk. Fig. 5.15 shows the energy-level structure for nominally undoped  $\text{In}_2\text{O}_3$  at the surface and in the bulk, respectively. In the degenerate bulk, the Burstein-Moss (BM) shift and the band-gap renormalization (BGR) effect on the valence and conduction band are considered. In a simple nonparabolic band model, the respective energy separations between the valence and conduction bands derived from Table 5.7 are indicated in the figure. As shown in Fig. 5.1 (a), the HAXPES measurements even taken with 8 keV photon energy is still very surface sensitive for undoped  $\text{In}_2\text{O}_3$ , unlike the more bulk-sensitive XES & XAS measurements. Hence the HAXPES derived  $E_{VBM}$  ( $h\nu = 8$  keV) represents the surface VBM relative to the Fermi level. On the nondegenerate surface, the  $E_g^{fund.}$ , corresponding to the intrinsic-band gap ( $E_g^0$ ), is determined to be  $(3.22 \pm 0.15)$  eV. Hence the position of the first allowed transition level ( $E_{tran.}$ ), derived by the gap disparity between the  $d\alpha/dE$  derived  $E_g^{opt.}$  and the  $E_g^{fund.}$ , is determined to be  $\sim 0.54$  eV below the VBM at the nondegenerate surface of undoped  $\text{In}_2\text{O}_3$ . While in the degenerate bulk, the  $E_g^{fund.}$  is getting narrow due to the BGR effect. As a result, the position of the first allowed optical transition level in the valence band is determined by the energy separation from the  $d\alpha/dE$  derived  $E_g^{opt.}$  to the  $E_g^{XES-XAS}$  in undoped  $\text{In}_2\text{O}_3$  bulk, being  $\sim 0.84$  eV below the upward dispersion of the topmost valence band  $[E(k_F, \Delta E_{g(VB)}^{BGR})]$ .



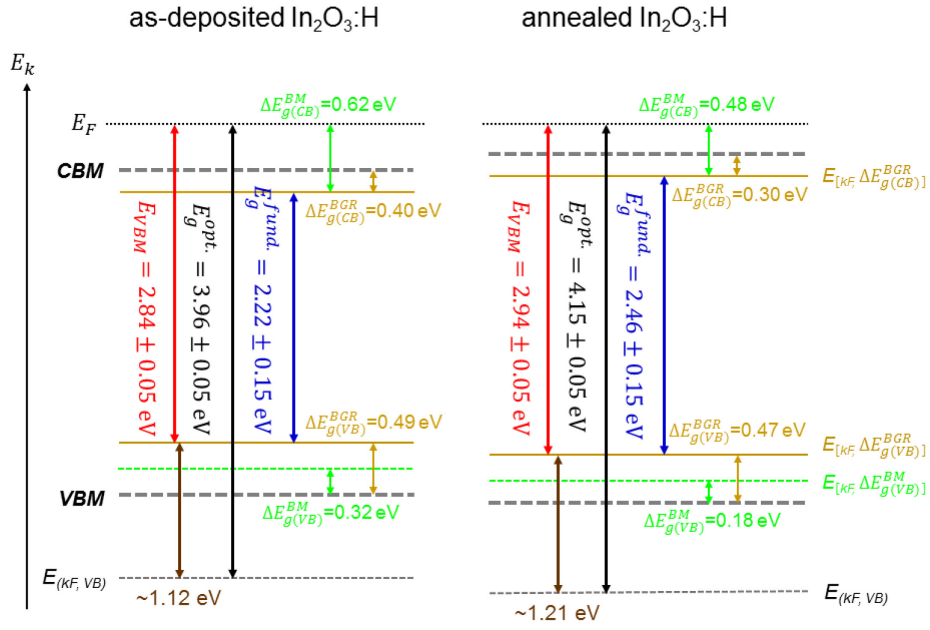


Figure 5.17: Schematic band-gap structure for  $\text{In}_2\text{O}_3:\text{H}$  before and after annealing by considering the Burstein-Moss (BM) shift and the band-gap renormalization (BGR) effect. The calculated values of the band dispersions caused by the BM and BGR effects are indicated. The HAXPES derived  $E_{VBM}$  relative to the Fermi level is taken with 8 keV photon energy. Note that the first allowed transition from the valence to conduction band is identified by  $[E_{(kF, VB)}]$ .

In  $\text{In}_2\text{O}_3:\text{H}$ , the band-gap structure exhibits a complex variation before and after annealing, as shown in Fig. 5.17. According to the above-mentioned descriptions, the first allowed optical transition levels in  $\text{In}_2\text{O}_3:\text{H}$  before and after annealing are determined to be  $\sim 1.12$  and  $\sim 1.21$  eV below the  $[E_{(kF, \Delta E_{g(VB)}^{BGR})}]$ , respectively. A slightly increased energy ( $\sim 0.10$  eV) in the first allowed transition level is present in  $\text{In}_2\text{O}_3:\text{H}$  after annealing. It means that the crystallized  $\text{In}_2\text{O}_3:\text{H}$  has a deeper allowed transition level in the valence band compared to amorphous one.

Above, the degenerate bulk of undoped  $\text{In}_2\text{O}_3$  is found to have a greater energy ( $\sim 0.84$  eV) in the first allowed transition level below the valence-band edge than the nondegenerate surface ( $\sim 0.54$  eV). While this value is very similar to that ( $\sim 0.81$  eV) identified by theoretical calculations of Walsh *et al.* [40]. Furthermore, the doped  $\text{In}_2\text{O}_3$  tends to have a much deeper first allowed transition level below the  $[E_{(kF, \Delta E_{g(VB)}^{BGR})}]$  compared to undoped  $\text{In}_2\text{O}_3$ . That could be strongly correlated with the doping concentration, i.e., the Burstein-Moss (BM) and the band-gap renormalization (BGR) effects. More importantly, the crystallized  $\text{In}_2\text{O}_3:\text{H}$  appears to have a deeper first allowed transition level in the valence band than amorphous  $\text{In}_2\text{O}_3:\text{H}$ . It is most likely due to the structural transformation from amorphous to crystalline

phase in  $\text{In}_2\text{O}_3:\text{H}$  during annealing. Another well possible explanation is that the crystallized  $\text{In}_2\text{O}_3:\text{H}$  has shown a different O 2p-In 4d coupling in the vicinity of the VBM compared to amorphous  $\text{In}_2\text{O}_3:\text{H}$ , as pointed out in our discussion of Fig. 5.9 (b). The p-d coupling at the VBM governs the parity of the bands in  $\text{In}_2\text{O}_3$ , thereby affecting the selection rule of optical transitions [22, 23]. Those would be well responsible for a deeper allowed transition level below the valence-band edge in annealed  $\text{In}_2\text{O}_3:\text{H}$ .

## 5.4 Conclusion

Annealing-induced properties of the  $\text{In}_2\text{O}_3$  variants have been investigated by a combination of photoelectron spectroscopy, Hall measurements, and spectroscopic ellipsometry. Doping in  $\text{In}_2\text{O}_3$  leads to pronounced changes in core-level and valence photoelectron structures before and after annealing. A model has been suggested to fit the O 1s and In  $3d_{5/2}$  spectra with two contributions of different widths, both corresponding to  $\text{In}_2\text{O}_3$ . This offers apparent evidence for the indium hydroxide dehydroxylation in  $\text{In}_2\text{O}_3:\text{H}$  during annealing, which is well responsible for the structural transformation from amorphous to polycrystalline phases, and a high electron mobility with a decreased carrier concentration in crystallized  $\text{In}_2\text{O}_3:\text{H}$ . The doped  $\text{In}_2\text{O}_3$  variants exhibit clear occupied gap states around the Fermi level in the VB spectra excited at 8 keV photon energy. A significant decrease in the intensity of occupied gap states is observed in crystallized  $\text{In}_2\text{O}_3:\text{H}$  after annealing, possibly due to a decrease in carrier concentration. Doping in  $\text{In}_2\text{O}_3$  seems to affect little the fundamental-band gap. For doped  $\text{In}_2\text{O}_3$ , the gap disparity between the optical- and fundamental-band gaps is strongly dependent on the doping concentration. In addition, the doped  $\text{In}_2\text{O}_3$  variants have a quite deeper allowed transition level below the valence-band edge than undoped films, attributed to the Burstein-Moss (BM) shift and the band-gap renormalization (BGR) effect via doping. This in particular applies to crystallized  $\text{In}_2\text{O}_3:\text{H}$ , but most likely due to a change of the crystal structure upon annealing and/or a different O 2p-In 4d coupling near the valence-band edge compared to amorphous  $\text{In}_2\text{O}_3:\text{H}$ .

## 6. Monitoring the Structure of the In-situ Annealed Ag/In<sub>2</sub>O<sub>3</sub>:H Interface

This chapter discusses the geometric and electronic structures, interface formation, and physical properties of the Ag/In<sub>2</sub>O<sub>3</sub>:H interface and how they change upon in-situ annealing. The emphasis is on the Schottky-barrier formation and barrier height reduction, which is investigated in detail using photoelectron spectroscopy.

### 6.1 Introduction

As discussed in Ch. 5, hydrogen doped In<sub>2</sub>O<sub>3</sub> (In<sub>2</sub>O<sub>3</sub>:H) is a very promising candidate for TCO applications due to a relatively high electron mobility of more than 100 cm<sup>2</sup> V<sup>-1</sup>·s<sup>-1</sup> compared to the traditional low-mobility TCO materials [15, 81]. As a predominantly ionic oxide semiconductor, In<sub>2</sub>O<sub>3</sub>:H shows a prominent n-type behavior. Application of In<sub>2</sub>O<sub>3</sub>:H in electronic devices necessitates Ohmic contacts with metal electrodes. The metal/In<sub>2</sub>O<sub>3</sub>:H interface can behave as a Schottky contact, if not designed carefully, which may have a considerable impact on the macroscopic behavior of electronic devices. Thus, understanding of how the interface forms and its electronic properties, i.e., Schottky-barrier heights, is of great importance. Recently, the Schottky character of metal (e.g., Ag, Pd, and Au) on In<sub>2</sub>O<sub>3</sub> has been extensively investigated by different techniques [117, 118], which reveals the formation of a metal/In<sub>2</sub>O<sub>3</sub> Schottky contact in these cases. Barraud *et al.* [119] found that high contact resistance is formed at the Ag/In<sub>2</sub>O<sub>3</sub>:H interface if different annealing treatments are applied, inconsistent with what the Schottky-Mott rule predicts [47]. He previously suggested this poor conductivity is due to an insulating interfacial layer (i.e., Ag<sub>2</sub>O) formed during annealing. At present, however, the experimental evidence regarding the microscopic origin of the poor contact on In<sub>2</sub>O<sub>3</sub>:H with Ag remains uncertain.

In this chapter, we study samples for which Ag was grown on In<sub>2</sub>O<sub>3</sub>:H surfaces by electron-beam evaporation (EBE). Photoelectron spectroscopy was employed to investigate the contact and interface formation on Ag/In<sub>2</sub>O<sub>3</sub>:H. A dependence of the barrier heights on annealing of the Ag/In<sub>2</sub>O<sub>3</sub>:H contact was investigated, which demonstrates the evolution of the barrier heights upon annealing and its origin.

## 6.2 Experimental Details

### 6.2.1 Sample Preparation

A 200 nm-thick  $\text{In}_2\text{O}_3\text{:H}$  film on the silicon wafer was prepared by D. Erfurt at PVcomB using a radio frequency (RF) magnetron sputtering prior to Ag deposition. During sputtering,  $\text{H}_2\text{O}$  vapor was introduced into the chamber at room temperature to act as a hydrogen donor. The deposition chamber had a base pressure of  $3.8 \times 10^{-7}$  mbar and the RF supply power was 70 W. Solid-phase crystallization of the deposited  $\text{In}_2\text{O}_3\text{:H}$  thin film was performed in vacuum by annealing at  $\sim 200$  °C for 1 h.

Afterwards, the annealed  $\text{In}_2\text{O}_3\text{:H}$  was inserted into the SISSY UHV system at EMIL (see Sect. 4.1.3), followed by a gentle surface-clean process with the low-energy (150 eV) argon ion ( $\text{Ar}^+$ ) sputtering for 30 min in the preparation chamber. After surface-cleaning, the bare  $\text{In}_2\text{O}_3\text{:H}$  was changed for Ag deposition. The growth of Ag on  $\text{In}_2\text{O}_3\text{:H}$  was conducted by evaporation of Ag powder with a multi-pocket electron beam evaporator (EBE-4) (see Sect. 4.1.1). During Ag evaporation, the base pressure in the preparation chamber was  $3.8 \times 10^{-7}$  mbar, and the power supply for EBE-4 evaporator was at 300W. A small filament current of about 3.32 Å for dozens of seconds was applied to be able to deposit thin Ag films. Finally, annealing of Ag/ $\text{In}_2\text{O}_3\text{:H}$  layer stacks was performed in vacuum at the HiKE end-station (KMC-1 beamline, BESSY II in Berlin) by increasing the temperature up to 300 °C. For transfer between EMIL and HiKE, the samples were sealed inside the  $\text{N}_2$ -purged glovebox directly alteded to EMIL. Meanwhile, the sample mounting and transferring at HiKE were done inside  $\text{N}_2$ -purged glovebag.

### 6.2.2 Sample Characterization

The surface morphology of the thin Ag films was inspected using scanning electron microscopy (SEM) performed by C. Klimm [HZB, Institute Silicon Photovoltaics (EE-IS)]. The SEM system (HITACHI S-4100) is equipped with a cold field emission gun, and the maximum resolution is 1.5 nm. Hard X-ray photoelectron spectroscopy (HAXPES) measurements with the excitation energy of 2 keV were carried out at the HiKE end-station (Beamline KMC-1) at BESSY II in Berlin. In-system ultraviolet photoelectron spectroscopy (UPS) was employed to examine the work function of thin films. The UPS experiments were done in the analysis chamber of SISSY lab at EMIL (see Sect. 4.1.3), taken with He I (21.2 eV) radiation. The working principle of the spectroscopic analysis (HAXPES & UPS) used in this work has been described in Sect. 4.2.1, respectively.

## 6.3 Results and Discussion

### 6.3.1 Surface Investigation

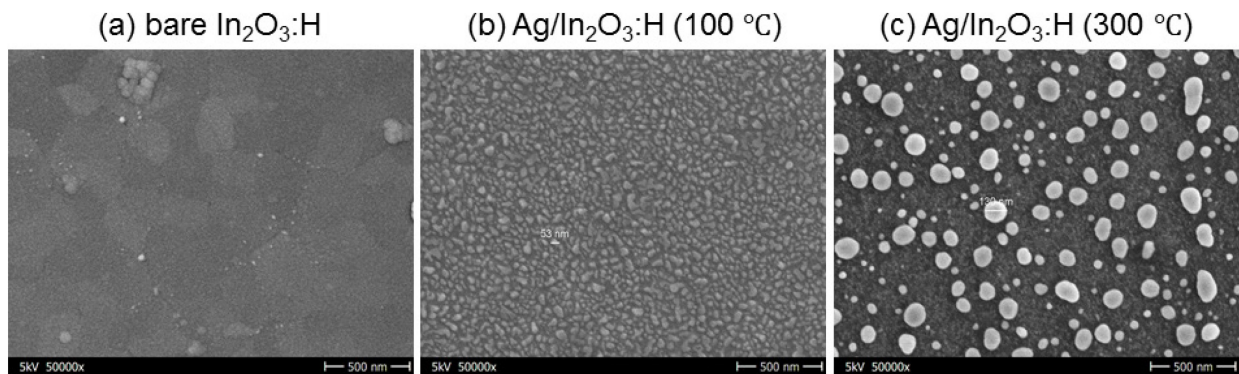


Figure 6.1: SEM micrograph of (a) bare  $\text{In}_2\text{O}_3:\text{H}$ , and  $\text{Ag}/\text{In}_2\text{O}_3:\text{H}$  after a (b) 100 °C and (c) 300 °C annealing.

Fig. 6.1 shows the scanning electron microscopy (SEM) images of bare  $\text{In}_2\text{O}_3:\text{H}$  and  $\text{Ag}/\text{In}_2\text{O}_3:\text{H}$  films after 100 and 300 °C annealing. As clearly seen from Fig. 6.1 (a), the bare  $\text{In}_2\text{O}_3:\text{H}$  has a nearly flat surface except for some particles, probably due to surface contamination. The surface morphology of the 100 °C annealed  $\text{Ag}/\text{In}_2\text{O}_3:\text{H}$  stack [Fig. 6.1 (b)] shows particles with an average size of ~50 nm on the  $\text{In}_2\text{O}_3:\text{H}$  substrate. When annealed at 300 °C [Fig. 6.1 (c)], the Ag nanoparticles on the  $\text{In}_2\text{O}_3:\text{H}$  surface increase in size and/or reach a maximum size of about 130 nm, indicating an annealing-induced modification of the Ag-topography (i.e., cluster formation).

### 6.3.2 In-situ Monitoring of the Interface Chemistry upon Annealing

#### *Ag 3d Spectra*

Fig. 6.2 shows the Ag 3d spectra in-situ monitored upon annealing taken with the excitation energy of 2 keV. In Fig. 6.2 (a), exemplary Ag 3d photoelectron spectra are shown and dominated by a spin-orbit doublet located at  $(368.30 \pm 0.05)$  and  $(374.32 \pm 0.05)$  eV for Ag  $3d_{5/2}$  and Ag  $3d_{3/2}$ , respectively. The position and spectral shape of the Ag 3d line before annealing is consistent with metallic Ag [120], indicating that Ag is present mostly in metallic state after deposition. Another clear observation is that the overall Ag 3d intensity decreases upon annealing [Fig. 6.2 (b)], which is in agreement with the observed change in topography (i.e., cluster formation). An Ag diffusion into the bulk  $\text{In}_2\text{O}_3:\text{H}$  can, however, also be excluded. The quantified information on the reduction of Ag 3d intensity is depicted over temperature in Fig.

6.2 (c). In addition, taking a closer look at the Ag 3d<sub>5/2</sub> spectra [Fig. 6.2 (a)], a noticeable broadening at a high binding energy of around 369.00 eV occurs upon annealing, together with a small broadening on the low binding energy side.

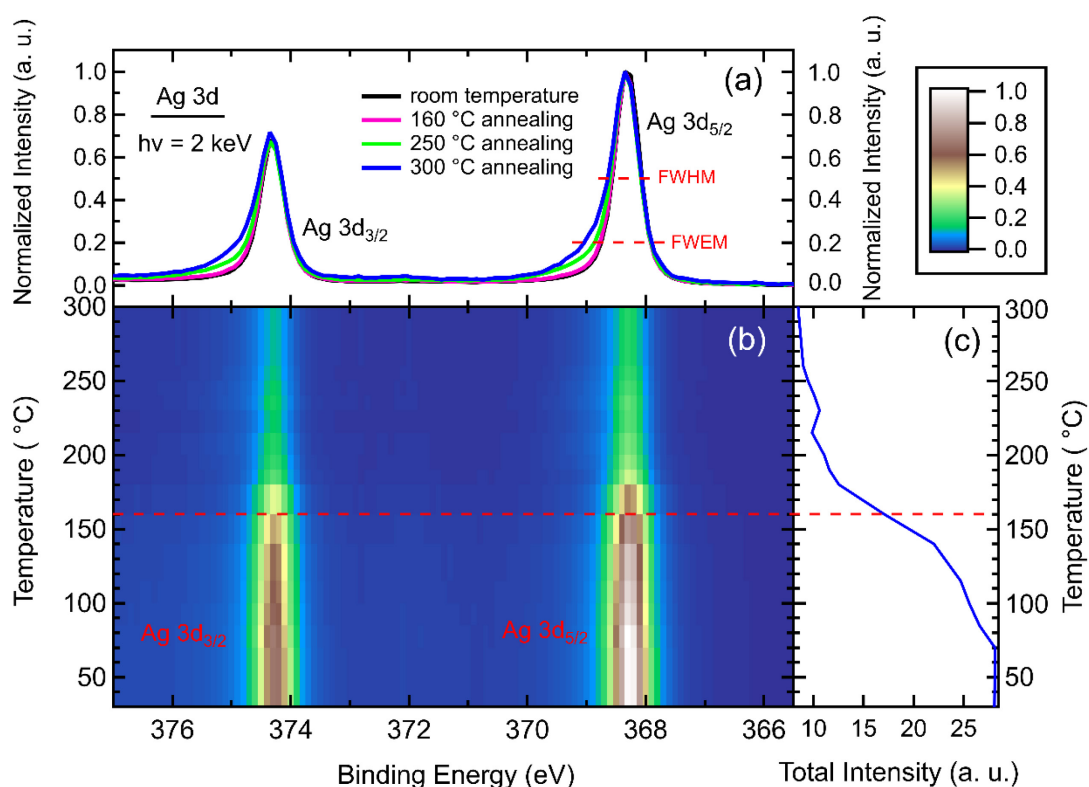


Figure 6.2: (a) HAXPES of the Ag 3d region of the Ag/In<sub>2</sub>O<sub>3</sub>:H sample at different annealing temperatures recorded in-situ with an excitation energy of 2 keV. (b) Corresponding color-coded intensity map of Ag 3d spectra as a function of temperature. (c) Evolution of the normalized Ag 3d line intensity in the shown range during annealing. The spectra in panel (a) are normalized to uniform peak and background heights and the data in panel (b) are normalized to the background at 366.50 eV. The horizontal dashed red line in panels (b) and (c) is a guide to the eye and indicates a temperature of 160 °C.



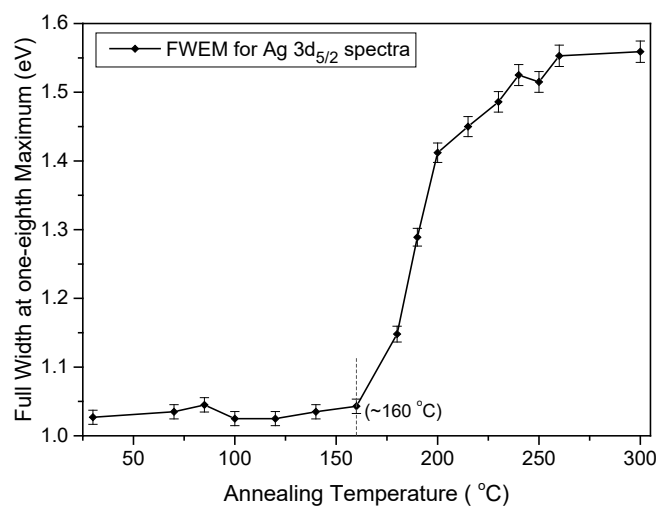


Figure 6.3: Full width at one-eighth maximum (FWEM) of Ag 3d<sub>5/2</sub> spectra as a function of annealing temperature.

For better visualization, the full width at one-eighth maximum (FWEM) of Ag 3d<sub>5/2</sub> spectra dependent on temperature is given in Fig. 6.3. FWEM is chosen to accentuate the emergence of the high and low binding energy shoulders, which have negligible effects on full width at half maximum (FWHM), as indicated in Fig. 6.2 (a). Obviously, the lineshape broadening in Ag 3d<sub>5/2</sub> spectra starts at around 160 °C, and increases during further annealing. This indicates the formation of a 2<sup>nd</sup> Ag species during annealing, on which a detailed discussion will follow below.

For Ag/Ag oxide system, the chemical shifts on a binding energy scale in the photoelectron spectra of Ag oxides have long been suggested as negative relative to metallic Ag [121-124]. Similar results are also obtained in other metal-metal oxide systems such as cobalt (Co) [125] and barium (Ba) [126], where respective photoelectron lines of the oxides are at lower binding energies than the metal. In fact, a large number of binding energy values for Ag oxidation states in the Ag 3d spectra are mostly dispersed within a small interval of 1.20 eV [121, 122, 124]. Considering that some experiments had to correct for charging, it is difficult to identify Ag oxidation based on this information alone. Recently, an advisable way to distinguish metallic Ag and its oxides was provided by Ferraria *et al.* [120], where the complex lineshape and width of Ag 3d spectra in silver salts is characterized rather than just their binding energy positions. It has been suggested that Ag oxides mainly exist in the form of Ag<sub>2</sub>O and AgO, along with different FWHMs (or different asymmetric profiles). Regarding this, a specific description of the assignments of Ag oxides for our samples is present below.

Fig. 6.4 shows reference data for Ag foil, Ag<sub>2</sub>O, and AgO digitized from [120] including fits. Based on [120], the Ag 3d<sub>5/2</sub> peak for Ag (0) located at (368.3±0.1) eV shows asymmetric Gaussian-Lorentzian characteristics of metal on the high binding energy side. The Ag 3d<sub>5/2</sub> peak position for Ag<sub>2</sub>O is reported to be at (368.6±0.1) eV, having a single symmetric Ag (I) state. The Ag 3d<sub>5/2</sub> peak of AgO yields an asymmetric profile with a large full width at half-maximum (FWHM), attributed to the mixed valence Ag (I) and Ag (III) in AgO. It is well established that AgO consists of two different chemical states [122, 127]: Ag (I) centered at (368.4±0.1) eV and Ag (III) centered at (367.8±0.1) eV. Concerning Ag (III) in AgO, two associated broad satellite peaks are present at high binding energies of (369.4±0.1) and (371.5±0.1) eV, having a similar intensity sum as the peak assigned to Ag (III) in AgO. They are responsible for the broad asymmetric tail towards higher binding energy in AgO. Such a broad satellite has been also previously reported in the Ag 3d<sub>5/2</sub> spectra of AgO [123], suggested to originate from oxides and clearly linked to Ag (III) derived core-level photoelectrons. The Ag 3d<sub>5/2</sub> spectrum of Ag foil was fitted with an asymmetric Doniach-Sunjic profile, typically corresponding to metallic Ag [Ag(0)], while symmetrical Voigt profiles were applied for the fits of Ag<sub>2</sub>O and AgO with a linear background subtraction.

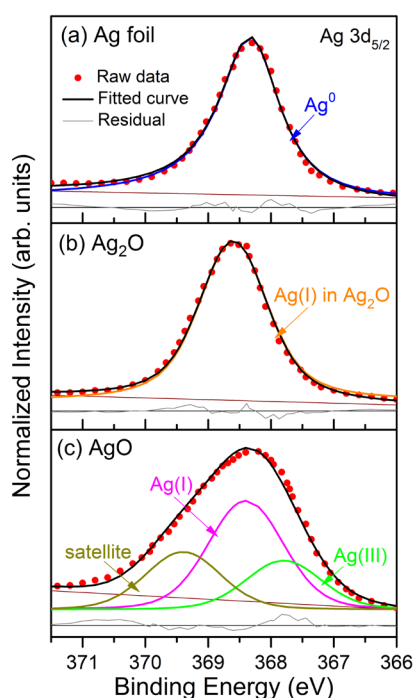


Figure 6.4: Ag 3d<sub>5/2</sub> core-level spectra for (a) Ag foil, (b) Ag<sub>2</sub>O and (c) AgO digitized from [120]. The spectra are fitted according to [120] with symmetric Voigt (mixed Gaussian-Lorentzian) profiles for Ag<sub>2</sub>O and AgO, while an asymmetric Doniach-Sunjic profile and a

linear background subtraction are used for Ag foil. The corresponding assignments of metal Ag and oxides (i.e., Ag<sub>2</sub>O and AgO) are indicated according to [120].

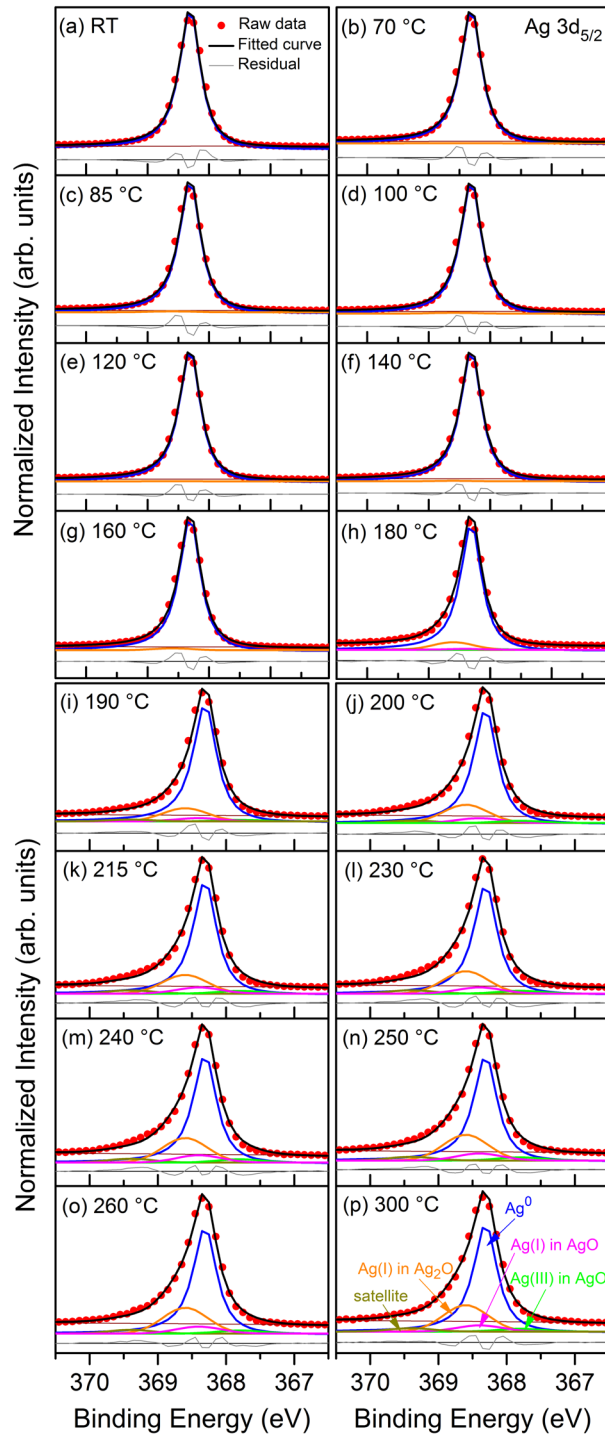


Figure 6.5: Ag 3d<sub>5/2</sub> core-level spectra measured at the excitation energy of 2 keV for Ag/In<sub>2</sub>O<sub>3</sub>:H upon annealing. All spectra are fitted by symmetrical Voigt profiles for Ag oxides (i.e., Ag<sub>2</sub>O and AgO), and a Doniach-Sunjic profile for metallic Ag [Ag(0)] with a linear background subtraction. The fit procedure for the Ag 3d<sub>5/2</sub> spectra is based on the fitting parameters used in Fig. 6.4, and suggested in Ref. [120].

For comparison, the same fit procedure, i.e., peak parameters and assignments as defined based on [120], is used for the quantitative fitting of Ag 3d<sub>5/2</sub> spectra for our samples. In our spectra, the peak parameters including the energy positions and intensity ratio were thus all fixed according to [120]. Smaller widths of the used fit profiles (i.e., the Doniach-Sunjic profile for Ag metal and the Gaussian width for Ag oxides) were applied for our spectra compared to that used in Fig. 6.4 due to the different instrumental resolutions. While the Lorentzian parameter of these spectra was kept the same due to the same lifetime broadening. All spectra in our work were constrained to have the same Doniach-Sunjic profile for Ag metal and Gaussian-Lorentzian contribution for Ag oxides, respectively. According to that, the results of the fitted Ag 3d<sub>5/2</sub> spectra for the Ag/In<sub>2</sub>O<sub>3</sub>:H stack as a function of annealing temperature are present in Fig. 6.5.

In Fig. 6.5, the spectrum of as-deposited Ag/In<sub>2</sub>O<sub>3</sub>:H shows a single peak for Ag metal. The spectra of the annealed Ag/In<sub>2</sub>O<sub>3</sub>:H sample yield a main Ag (0) and a very small Ag<sub>2</sub>O contribution, but with a mixture of (Ag<sub>2</sub>O+AgO) occurring first at around 160 °C. This can well explain the lineshape broadening of the Ag 3d spectra, discussed in conjunction with Fig. 6.3. For clarity, the respective intensity of the metallic Ag, Ag<sub>2</sub>O and AgO components at the Ag/In<sub>2</sub>O<sub>3</sub>:H samples over temperature is shown in Fig. 6.6, which is derived from the fitting results of Ag 3d<sub>5/2</sub> spectra in Fig. 6.5. Clearly, the intensity of the metallic Ag [Ag(0)] contribution to the Ag 3d<sub>5/2</sub> spectra of the Ag/In<sub>2</sub>O<sub>3</sub>:H sample decreases upon annealing, with a more pronounced reduction at ~160 °C. When annealing above ~160 °C, Ag<sub>2</sub>O shows a gentle increase in the intensity, while AgO appears and increases in intensity up to ~200 °C. This is broadly consistent with the lineshape broadening in the Ag 3d spectra occurring at the same temperature (~160 °C) and leveling off at ~200 °C. In addition, the magnitude of the decrease of the metallic Ag intensity is about 2× larger than that of the increase of the Ag<sub>2</sub>O intensity when annealing below ~160 °C, as indicated by grey arrows in Fig. 6.6. This in general agrees with the thermal oxidation of Ag according to the chemical reactions  $2\text{Ag} + 2\text{H}_2\text{O} \rightarrow 2\text{AgOH} + \text{H}_2$  and  $2\text{AgOH} \rightarrow \text{Ag}_2\text{O} + \text{H}_2\text{O}$ . It means that the overall decrease of the metallic Ag [Ag(0)] is mainly attributed to Ag oxidation (i.e., Ag<sub>2</sub>O) when annealing below ~160 °C, and the formation of AgO proceeds when annealing above ~160 °C. Thermal desorption spectroscopy (TDS) measurements from Koida *et al.* [6] have shown that the H<sub>2</sub>O desorption in solid-phase-crystallized In<sub>2</sub>O<sub>3</sub>:H occurs at below around 160 °C and reaches a broad plateau at above around 200 °C. This provides an internal source of H<sub>2</sub>O for the thermal oxidation of Ag during annealing. With H<sub>2</sub>O desorption (above ~160 °C), the generated Ag<sub>2</sub>O is exposed to H<sub>2</sub>O and produces OH<sup>-</sup> to exhibit an “alkaline” environment according to the chemical reaction  $\text{Ag}_2\text{O} +$

$\text{H}_2\text{O} \rightarrow 2\text{Ag}^+ + 2\text{OH}^-$ . In this “alkaline” environment, the electrochemical oxidation of Ag occurs and leads to the formation of  $\text{Ag}_2\text{O}$  and  $\text{AgO}$  according to the chemical reactions  $2\text{Ag} + 2\text{OH}^- \rightarrow \text{Ag}_2\text{O} + \text{H}_2\text{O} + 2\text{e}^-$  and  $\text{Ag}_2\text{O} + 2\text{OH}^- \rightarrow 2\text{AgO} + \text{H}_2\text{O} + 2\text{e}^-$ .

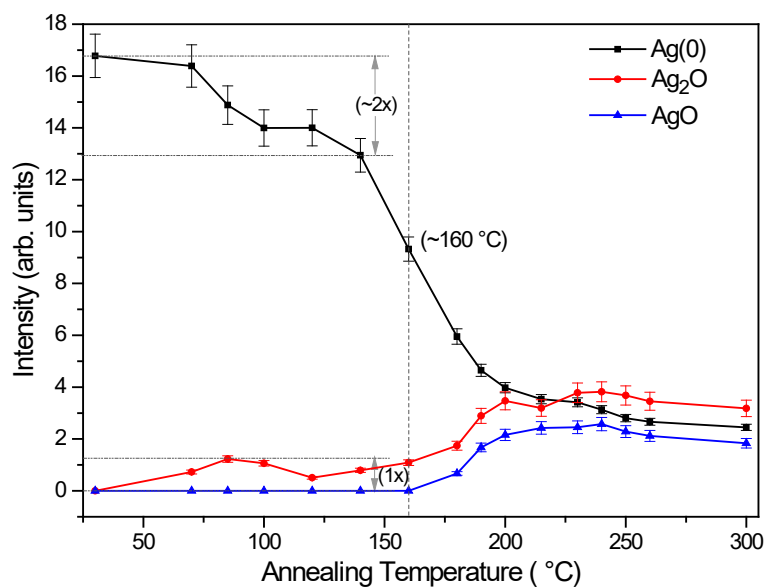


Figure 6.6: Plots of the respective intensity of the metallic Ag [Ag(0)] (*black line*),  $\text{Ag}_2\text{O}$  (*red line*), and  $\text{AgO}$  (*blue line*) contribution to the Ag  $3d_{5/2}$  line over temperature derived from the fitting results in Fig. 6.5.

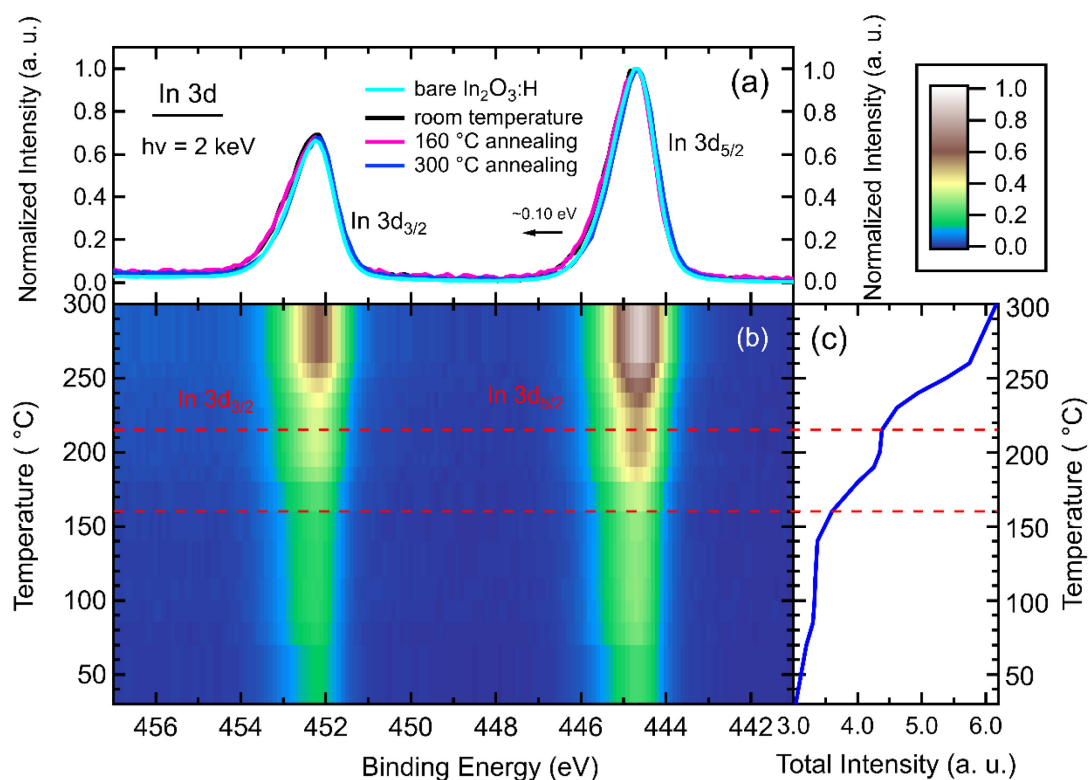


Figure 6.7: (a) Hard x-ray photoelectron spectra of the In 3d region of room temperature bare  $\text{In}_2\text{O}_3\text{:H}$  and of  $\text{Ag}/\text{In}_2\text{O}_3\text{:H}$  at different annealing temperatures measured with an excitation energy of 2 keV. (b) Corresponding color-coded intensity map of In 3d spectra as a function of temperature. (c) Evolution of the normalized In 3d line intensity in the shown range during annealing. The spectra in panel (a) are normalized to uniform peak and background heights and the data in panel (b) is normalized to the background at 442.50 eV. The horizontal dashed red lines in panels (b) and (c) are guides to the eye and indicate temperatures of 160 °C and 215 °C.

The evolution of In 3d core-level spectra during in-situ annealing taken with the excitation energy of 2 keV is present in Fig. 6.7. A shift of the In 3d spectra up to  $\sim 0.10$  eV towards lower binding energy is observed during annealing, as indicated in Fig. 6.7 (a). There is no clear spectral evidence for a changing In chemical composition upon annealing, except a small narrowing in the lineshape. Based on our previous studies on  $\text{In}_2\text{O}_3\text{:H}$  during annealing (see Ch. 5), this may be due to a slight dehydroxylation of potentially present indium hydroxide occurring upon vacuum annealing, which would provide an internal  $\text{H}_2\text{O}$  source for Ag oxidation. In addition, Fig. 6.7 (b) and (c) show that the In 3d intensity increases upon annealing.

Again, this is in agreement with the observed annealing-induced change of Ag topography (i.e., cluster formation). However, a diffusion of Ag into the bulk of In<sub>2</sub>O<sub>3</sub>:H cannot be excluded.

### Shallow Core-level Spectra

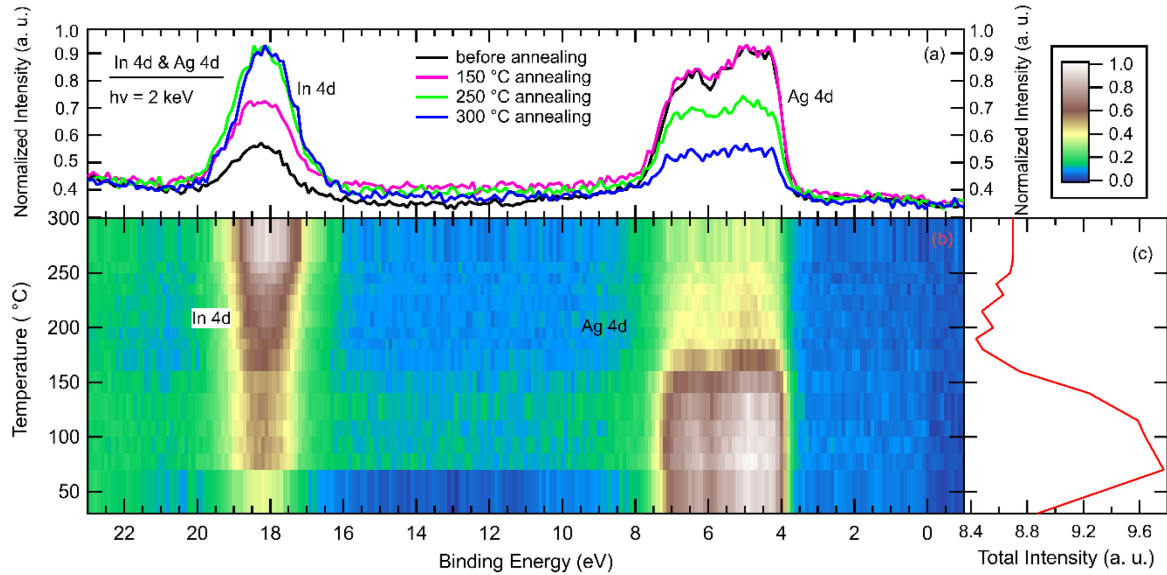


Figure 6.8: (a) Photoelectron spectra of the shallow core-level region as a function of temperature upon annealing employing the excitation energy of 2 keV (*left panel*). (b) Corresponding color-coded intensity map of the shallow core-level spectra over temperature. (c) Evolution of the integrated intensity of the shallow In 4d and Ag 4d lines [23-0 eV] during annealing (*right panel*). All the data is normalized to the background at 1 eV.

Fig. 6.8 displays the shallow core-level spectra during in-situ annealing taken with the excitation energy of 2 keV. As clearly seen in Fig. 6.8 (a) and (b), the intensity of In 4d line increases with the Ag 4d line intensity decreasing upon annealing. This is consistent with the changes in the intensities of In 3d (Fig. 6.7) and Ag 3d lines (Fig. 6.2) during annealing. Regarding this, the intensity ratios of the Ag 3d to In 3d and Ag 4d to In 4d core levels upon annealing are shown in Fig. 6.9, with consideration of the corrections of the atomic photoionization cross sections. The Ag 3d/In 3d and Ag 4d/In 4d intensity ratios exhibit a similar decrease with the temperature increasing. According to the expression  $d = \lambda_i \cos \alpha \ln \left( \frac{I_{Ag\ 3d} \sigma_{In\ 3d}}{I_{In\ 3d} \sigma_{Ag\ 3d}} + 1 \right)$ , the thickness of Ag film is decreasing upon annealing. According to that, it can further indicate the potential diffusion of Ag into the In<sub>2</sub>O<sub>3</sub>:H bulk.

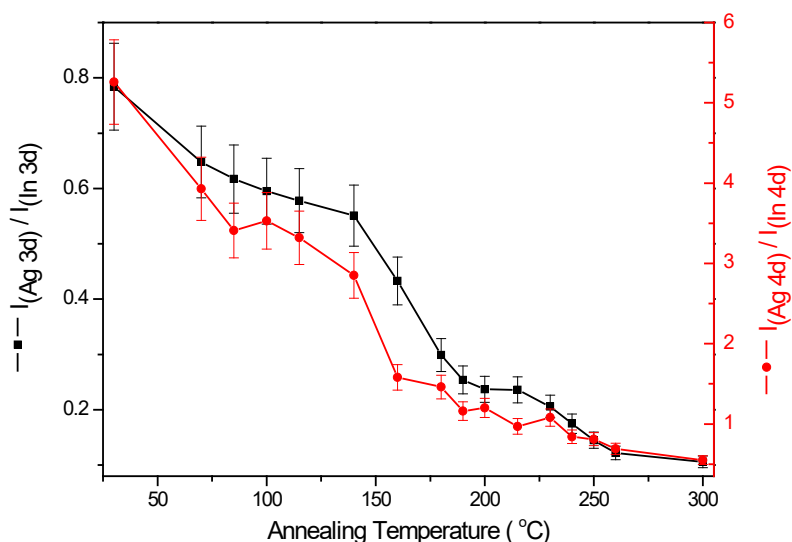


Figure 6.9: Evolution of the Ag 3d/In 3d and Ag 4d/In 4d intensity ratios over temperature. The relative intensity of each core level was corrected for the photoionization cross section.

### 6.3.3 Fermi-edge Disappearance

To clarify whether and how much the Fermi edge changes upon annealing, the temperature dependence of the photoelectron spectra around the Fermi edge is shown in Fig. 6.10. In order to improve statistics, The 240 °C and 280 °C spectra are sum spectra of the 230-250 °C data and the 260-300 °C data, respectively, to improve signal-to-noise ratio. The thermal distribution of electrons around the Fermi level in metals is governed by the Fermi-Dirac (F-D) distribution function [128, 129]. With the temperature increasing, the shape of the F-D function around the Fermi level broadens. For comparison, thus the calculated F-D distribution function at corresponding temperatures has been added here. To adjust the step height of the Fermi edge, the calculated F-D distribution curve is scaled to match with each experimental data. In Fig. 6.10, the experimental Fermi edge tends to broaden upon annealing, as expected by the F-D distribution function. Initially, a clear Fermi edge is seen (30-100 °C), indicating the presence of metallic Ag. Upon annealing, the Fermi edge decreases until it almost vanishes in the noise of the acquired data. When annealing at ~300 °C it turns out to be hardly distinguishable, indicating that there is very little metallic Ag left.



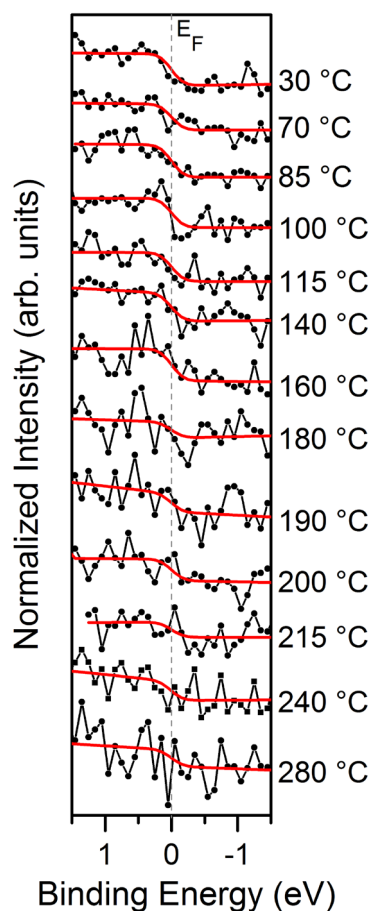


Figure 6.10: HAXPES spectra of the low binding energy region around the Fermi edge measured during the in-situ annealing experiment. The experimental data (black-dotted lines) were fitted by Fermi-Dirac type profiles (red lines). The stated temperatures are mean temperatures during the measurement cycle. The 240 °C and 280 °C spectra are sum spectra of the 230-250 °C data and the 260-300 °C data, respectively, to improve signal-to-noise ratio.

#### 6.3.4 Band Bending

In order to explore the band bending at the Ag/In<sub>2</sub>O<sub>3</sub>:H interface, the photoelectron spectra of In 3d<sub>5/2</sub> and In 4d core levels upon annealing are present in Fig. 6.11. In Fig. 6.11 (a), the In 3d<sub>5/2</sub> spectrum for bare In<sub>2</sub>O<sub>3</sub>:H exhibits an apparent shift towards high binding energy with Ag deposition. Upon annealing, while the binding energy of the In 3d<sub>5/2</sub> spectra for Ag/In<sub>2</sub>O<sub>3</sub>:H shifts continuously back to lower binding energies. The main In 4d spectra, as shown in Fig. 6.11 (b), also exhibits a very similar energy shift as In 3d<sub>5/2</sub> spectra during annealing [Fig. 6.11 (a)].

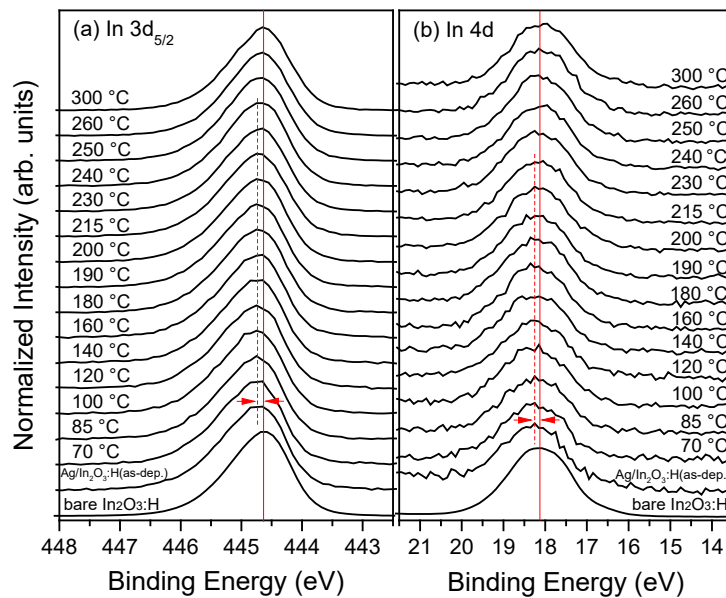


Figure 6.11: Photoelectron spectra of the (a) In  $3d_{5/2}$  and (b) In 4d core levels as a function of annealing temperature collected at the excitation energy of 2 keV. All spectra shown here are normalized to the maximum intensity values.

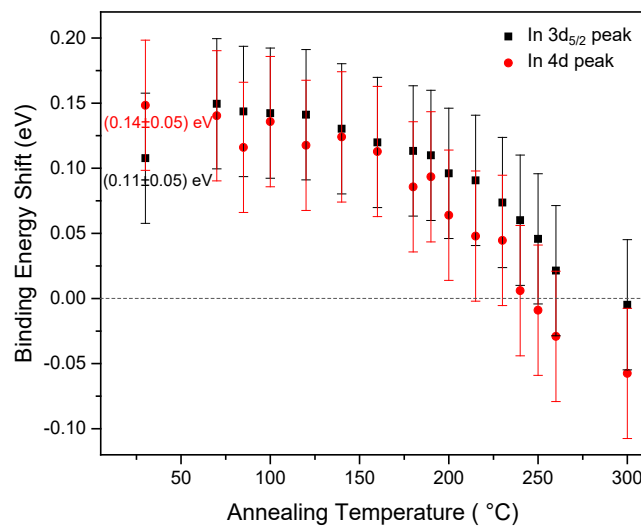


Figure 6.12: Plots of binding energy shifts of the In  $3d_{5/2}$  and In 4d core levels for Ag/In $_2$ O $_3$ :H relative to bare In $_2$ O $_3$ :H as a function of annealing temperature. Binding energy is taken as the highest peak intensity in each spectrum.

Fig. 6.12 shows the evolution on binding energy of the In  $3d_{5/2}$  and In 4d core levels as a function of temperature. All values of the binding energy shifts for Ag/In $_2$ O $_3$ :H during annealing are obtained relative to that of bare In $_2$ O $_3$ :H. In this case, each value of the binding energy is taken from the highest peak intensity of each spectrum shown in Fig. 6.11. As depicted in Fig. 6.12, the behavior of binding energy shifts for both In lines is quite similar during

annealing. When Ag is deposited, clear energy shifts of  $(0.11\pm 0.05)$  and  $(0.14\pm 0.05)$  eV towards higher binding energies are observed for In  $3d_{5/2}$  and In 4d spectra, respectively. Taking into account that a potential overlapping with the O 2s peak and the resulting increased uncertainty of binding energy position determination exists in the In 4d spectra, the binding energy shift of  $(0.11\pm 0.05)$  eV in the In  $3d_{5/2}$  spectra is employed in the following considerations. This means that the initial Ag deposition leads to a downward band bending of  $(0.11\pm 0.05)$  eV in  $\text{In}_2\text{O}_3:\text{H}$ . Upon annealing, the binding energies gradually move backward, indicating a decrease in downward band bending. The most straightforward interpretation of this behavior is that a Schottky contact is initially formed at the Ag/ $\text{In}_2\text{O}_3:\text{H}$  interface, which is modified upon annealing. As predicted by the Schottky-Mott rule [47], a charge transfer across the Ag/ $\text{In}_2\text{O}_3:\text{H}$  interface results in a depletion layer at the near-surface of  $\text{In}_2\text{O}_3:\text{H}$ , which is responsible for the downward band bending observed in  $\text{In}_2\text{O}_3:\text{H}$ .

### 6.3.5 Work-function Reduction

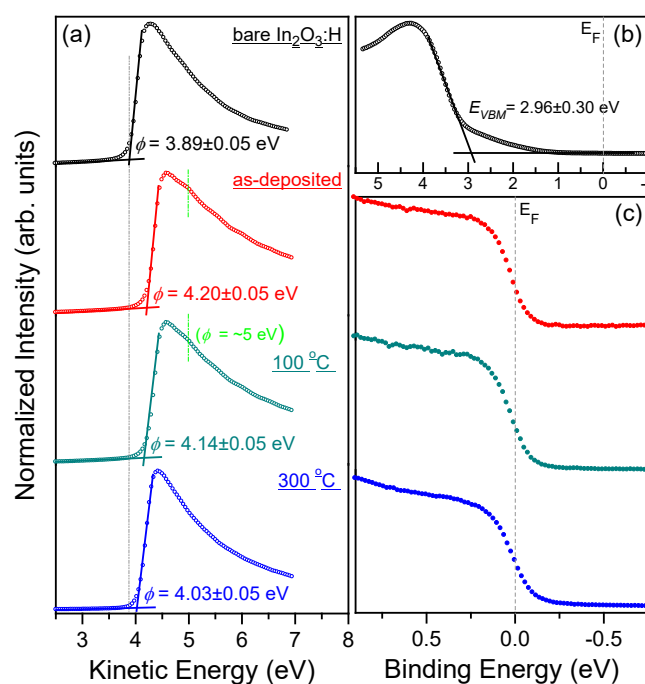


Figure 6.13: UPS spectra excited with He I ( $h\nu = 21.2$  eV) of bare  $\text{In}_2\text{O}_3:\text{H}$  and  $\text{Ag}/\text{In}_2\text{O}_3:\text{H}$  samples before/after annealing at  $100$  °C and  $300$  °C for 1h, showing (a) the low energy side of the secondary electron cut-off indicating the sample's work function ( $\Phi$ ) with a bias voltage of 15 V, (b) the high energy side of the valence-band maximum ( $E_{VBM}$ ) and the Fermi level for bare  $\text{In}_2\text{O}_3:\text{H}$ , (c) the high energy side of the Fermi edge for  $\text{Ag}/\text{In}_2\text{O}_3:\text{H}$  before and after annealing. The energy positions of the secondary electron cut-off indicating the sample's work function ( $\Phi$ ), and the valence-band maximum ( $E_{VBM}$ ) relative to the Fermi level is

derived by a linear extrapolation of the leading edge to the background. It can be seen that a secondary work function ( $\Phi = \sim 5$  eV) is observed in the spectra of Ag/In<sub>2</sub>O<sub>3</sub>:H before and after annealing at 100 °C.

The typical UPS spectra of bare In<sub>2</sub>O<sub>3</sub>:H and Ag/In<sub>2</sub>O<sub>3</sub>:H samples measured using He I ( $h\nu = 21.2$  eV) is shown in Fig. 6.13. The spectra consist of the low kinetic energy edge [Fig. 6.13 (a)], corresponding to the secondary electron cut-off indicating the sample's work function ( $\Phi$ ), and the high kinetic energy side [Fig. 6.13 (b) and (c)] showing the valence band and the Fermi level region. The valence-band maximum (VBM) relative to the Fermi level for bare In<sub>2</sub>O<sub>3</sub>:H is determined by a linear extrapolation of the leading edge of high energy electrons to the background. Note that the tail states above the VBM are seen in the VB spectrum of bare In<sub>2</sub>O<sub>3</sub>:H. It agrees well with the observations in the VB-HAXPES spectrum of annealed In<sub>2</sub>O<sub>3</sub>:H [see Fig. 5.8 (b)], previously attributed to varied coordination numbers of oxygen atoms in annealed In<sub>2</sub>O<sub>3</sub>:H. The existence of such states causes an increased uncertainty of  $\pm 0.30$  eV in the determined  $E_{VBM}$  with the value of  $(2.96 \pm 0.30)$  eV. However, no occupied gap states around the Fermi level can be observed here, most likely due to the photon energy dependence of the photoionization cross-section of involved states between HAXPES and UPS [84, 130]. A similar linear extrapolation of the leading edge of low kinetic energy electrons to the background is used to determine the secondary electron cut-off (i.e., the work function  $\Phi$ ). Initially, the work function of Ag/In<sub>2</sub>O<sub>3</sub>:H shifts towards higher kinetic energy by  $\sim 0.31$  eV with the initial Ag deposition. Upon annealing, it gradually decreases, so does the density of states (DOS) around the Fermi edge. Compared to Fig. 6.10, the DOS around the Fermi edge obtained from UPS seems much larger than that measured by HAXPES. It is probably attributed to excitation energy dependent photoionization cross-section [84, 130] and/or a different information depth. That means annealing modifies the work function of the Ag/In<sub>2</sub>O<sub>3</sub>:H surface. Note that a secondary work function could be observed in the spectra of Ag/In<sub>2</sub>O<sub>3</sub>:H before and after annealing at 100 °C, yielding a value of around 5 eV. This is very close to the work functions of Ag<sub>2</sub>O (5.3 eV [131]) and AgO (5.1 eV [132]), again indicating Ag oxidation occurs during annealing.

### 6.3.6 Schottky-barrier Height

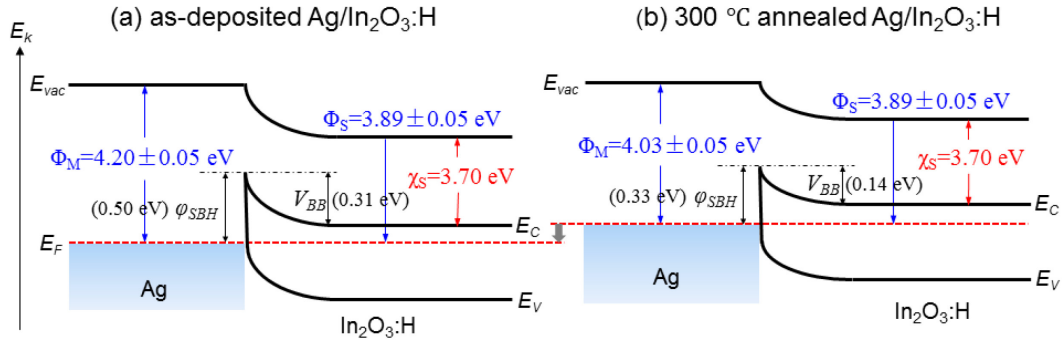


Figure 6.14: Schematic energy-level diagrams for Ag/In<sub>2</sub>O<sub>3</sub>:H contact (a) before annealing and (b) after 300 °C annealing without surface states.  $E_{vac}$ ,  $E_F$ ,  $E_V$ ,  $E_C$ ,  $\Phi_M$ ,  $\Phi_S$ ,  $\chi_S$ ,  $\phi_{SBH}$ , and  $V_{BB}$  are the vacuum level, the Fermi level, the valence-band maximum (VBM), the conduction-band minimum (CBM), the work functions of Ag and In<sub>2</sub>O<sub>3</sub>:H, the electron affinity of In<sub>2</sub>O<sub>3</sub>:H, Schottky barrier height (SBH), and the band bending, respectively. The electron affinity of In<sub>2</sub>O<sub>3</sub>:H ( $\chi_S = 3.70$  eV) is taken from Ref. [133], and the values of the work functions of Ag and In<sub>2</sub>O<sub>3</sub>:H are derived from Fig. 6.13.

According to the Schottky-Mott rule [47], the Schottky-barrier height can be estimated by the work function difference between the metal and the semiconductor without considering the surface states. In our case, the change of the work functions between bare In<sub>2</sub>O<sub>3</sub>:H and Ag/In<sub>2</sub>O<sub>3</sub>:H is generally calculated as the magnitude of Schottky-barrier height ( $\phi_{SBH}$ ). Thus, it reveals a reduction in  $\phi_{SBH}$  at the Ag/In<sub>2</sub>O<sub>3</sub>:H interface upon annealing, consistent with the decrease in downward band bending ( $V_{BB}$ ) of In<sub>2</sub>O<sub>3</sub>:H. When Ag comes in contact with In<sub>2</sub>O<sub>3</sub>:H, it induces bending of the energy level near the surface of In<sub>2</sub>O<sub>3</sub>:H. Since the work function of Ag [(4.30 ± 0.05) eV] [47] is larger than that of In<sub>2</sub>O<sub>3</sub>:H [(3.89 ± 0.05) eV] measured in this work, electrons will transfer across the interface from In<sub>2</sub>O<sub>3</sub>:H to Ag until their Fermi levels are aligned. At the interface, a Schottky barrier is formed, thereby leading to a downward band bending in In<sub>2</sub>O<sub>3</sub>:H. Upon annealing the potential Ag diffusion and/or an annealing-induced Ag topography (i.e., cluster formation) modifies the work function of Ag. This results in a gradual decrease of the Schottky barrier height ( $\phi_{SBH}$ ) at the interface, as well for the surface band bending ( $V_{BB}$ ) in In<sub>2</sub>O<sub>3</sub>:H. Fig. 6.14 shows the schematic energy-level diagram of the Ag/In<sub>2</sub>O<sub>3</sub>:H interface before and after 300 °C annealing. The surface band bending ( $V_{BB}$ ) of In<sub>2</sub>O<sub>3</sub>:H, which is given by the energy difference between the work functions of Ag [ $\Phi_M = (4.20 \pm 0.05)$  eV] and In<sub>2</sub>O<sub>3</sub>:H [ $\Phi_S = (3.89 \pm 0.05)$  eV], then amounts to  $V_{BB} = (0.31 \pm 0.07)$  eV for the as-deposited Ag/In<sub>2</sub>O<sub>3</sub>:H sample. As discussed above, an initial downward band bending of

( $0.11 \pm 0.05$ ) eV was found in the near-surface of  $\text{In}_2\text{O}_3:\text{H}$  with Ag deposition. A possible explanation for this discrepancy is derived from the experimental uncertainty in the extrapolation of the data and/or a preexisting downward band bending at the  $\text{In}_2\text{O}_3:\text{H}$  surface. The Schottky barrier height ( $\phi_{SBH}$ ) is calculated by the energy difference between the  $\Phi_M$  of Ag and the electron affinity of  $\text{In}_2\text{O}_3:\text{H}$  ( $\chi_S = 3.7$  eV [133]), determined to be ( $0.50 \pm 0.05$ ) eV for the as-deposited Ag/ $\text{In}_2\text{O}_3:\text{H}$  sample. When annealing up to 300 °C, the  $\Phi_M$  of Ag decreases to ( $4.03 \pm 0.05$ ) eV and the  $\phi_{SBH}$  amounts to ( $0.33 \pm 0.05$ ) eV, with a small  $V_{BB}$  of ( $0.14 \pm 0.07$ ) eV in  $\text{In}_2\text{O}_3:\text{H}$ . Obviously, the vacuum annealing has led to a strong decrease in the barrier height, a result attributed to the potential Ag diffusion and/or an annealing-induced Ag topography (i.e., cluster formation). However, the annealing-induced reduction of the Schottky barrier height ( $\phi_{SBH}$ ) contributes an increased contact resistance at the Ag/ $\text{In}_2\text{O}_3:\text{H}$  interface, as previously hypothesized by Barraud *et al.* [119]. On the other hand, the formation of Ag oxides (i.e.,  $\text{Ag}_2\text{O}$  and AgO) during annealing, i.e., an insulating interfacial layer, can possibly lead to a further increase of contact resistance at the Ag/ $\text{In}_2\text{O}_3:\text{H}$  interface. It would build a high barrier for electron transport across the Ag/ $\text{In}_2\text{O}_3:\text{H}$  interface. In addition, defects at the Ag/ $\text{In}_2\text{O}_3:\text{H}$  interface may act as intermediate states and/or recombination centers for the trap-assisted tunneling.

To avoid this degradation, it has been suggested to introduce a very thin ITO layer (~10 nm) into the Ag/ $\text{In}_2\text{O}_3:\text{H}$  interface [119], which is expected to suppress the interdiffusion of Ag and  $\text{H}_2\text{O}$  species and/or modify the  $\text{In}_2\text{O}_3:\text{H}$  surface. Although the exact nature of the Ag/ITO/ $\text{In}_2\text{O}_3:\text{H}$  interface, i.e., the microstructure, chemical, and physical properties, is still under investigation, it will be our further work in the future.

## 6.4 Conclusion

Ag thin film on  $\text{In}_2\text{O}_3:\text{H}$  was formed by e-beam evaporation of Ag powder, followed by an annealing up to 300 °C in vacuum. The annealing-induced changes have been in-situ monitored by HAXPES. During annealing, the Ag line intensity significantly decreases with In line intensity increasing. Combining with SEM surface morphology of the annealed Ag/ $\text{In}_2\text{O}_3:\text{H}$  samples, it suggests that the potential Ag diffusion into the bulk  $\text{In}_2\text{O}_3:\text{H}$  and/or a change of an annealing-induced Ag topography (i.e., cluster formation) occurs during annealing. In addition, a clear line broadening in the Ag 3d spectra was observed upon annealing, which is due to Ag oxidation (i.e.,  $\text{Ag}_2\text{O}$  and AgO). With Ag deposition, an initial downward band bending of ( $0.11 \pm 0.05$ ) eV was calculated in  $\text{In}_2\text{O}_3:\text{H}$ , attributed to a Schottky contact formed at the

Ag/In<sub>2</sub>O<sub>3</sub>:H interface. Upon annealing, the downward band bending reduces gradually, along with a decrease in the density of states (DOS) around the Fermi edge and the work function difference between bare In<sub>2</sub>O<sub>3</sub>:H and the Ag/In<sub>2</sub>O<sub>3</sub>:H samples. The Schottky-barrier height at the Ag/In<sub>2</sub>O<sub>3</sub>:H interface also decreases during annealing. These annealing-induced variations are most likely attributed to the potential Ag diffusion into the bulk In<sub>2</sub>O<sub>3</sub>:H and/or an annealing-induced change of Ag topography (i.e., cluster formation) together with a small Ag oxidation (i.e., Ag<sub>2</sub>O and AgO).





## 7. Characterization and Analysis of the ZnO/GaN/MnS/Si Heterostructure

This chapter characterizes the ZnO/GaN/MnS/Si heterostructure using photoelectron spectroscopy. Topics covered here include the core-level and valence electronic structures at the conjoint ZnO/GaN/MnS/Si stacks. The interfacial chemistry and energy-level alignment at the respective ZnO/GaN/MnS/Si heterointerface are derivated and discussed in detail, which will provide the insights needed for a deliberate and rapid optimization of the GaN-based LED structures.

### 7.1 Introduction

As described in Ch. 3, MnS is a promising buffer layer due to its very small lattice mismatch ( $\approx -3.8\%$ ) with respect to Si. In addition, MnS has the stable NaCl structure [134, 135], and so can grow epitaxially on bare Si (100) substrates with small strain and dislocation defects. The introduction of MnS into the GaN system can decrease significantly the strain and threading dislocation density of subsequently grown GaN epilayers on sapphire or Si substrates [59]. The conjoint GaN/MnS/Si stacks are found to be stable even up to the typical growth temperature ( $\sim 700$  °C) of GaN [59]. Up to now, however, the interface properties of the MnS/Si stack have not been sufficiently explored experimentally yet. Furthermore, there is still an important challenge to obtain high-quality GaN epilayers. Possible formation of Mn-N bonds at the GaN/MnS interface would degrade the devices' performance. The presence of the secondary phase, i.e.,  $Mn_xN_y$ , could impact the charge carrier transport and recombination mechanisms in GaN/MnS heterostructure-based LEDs devices [134, 135].

In addition, ZnO is very attractive for the realization of GaN-based LEDs devices due to its wide direct band gap of 3.37 eV at room temperature [136, 137]. It allows efficient light emission in the ultraviolet (UV) spectral region. The availability of a large exciton binding energy of 60 meV [137-139] makes ZnO a promising material to be used with III-nitride materials owing to high-efficient excitonic emission at room temperature [140]. Recently, most work on ZnO heterojunction-based LEDs has focused on ZnO/GaN epilayers as they have the same crystal structure (wurtzite) and a small lattice mismatch ( $\sim 1.8\%$ ) [141]. However, it has been reported that the possible formation of an interfacial  $GaO_x$  layer at the ZnO/GaN stacks would degrade the heterojunction LEDs performance [141, 142].

To well understand and modify the interface properties at the conjoint ZnO/GaN/MnS/Si heterostructure, a thickness series of the individual materials on the respective “substrate” (i.e., MnS/Si, GaN/MnS, and ZnO/GaN) was epitaxially grown and studied in this work. Photoelectron spectroscopy is employed to investigate the interfacial chemistry and energy-level alignment at the respective interfaces with the ultimate aim to achieve a complete chemical and electronic structure prelevel of the whole ZnO/GaN/MnS/Si stack. This is essential to optimize the GaN-based LEDs devices significantly.

## 7.2 Experimental Details

### 7.2.1 Sample Preparation

MnS buffer layers with different thicknesses of 4, 15 and 50 nm were grown on Si (100) wafer. In order to reduce the surface contamination, the Si substrate was subjected to the standard cleaning process, followed by HF solution treatment for 1 min. During deposition, a high purity (99.9%) MnS polycrystalline target was employed for MnS growth on clean Si (100) surface. The deposition chamber had a base pressure of  $7 \times 10^{-7}$  mbar and the substrate temperature was around 700 °C. Afterwards, the GaN thin films with different thicknesses of 2, 4, 15 and 50 nm were deposited by molecular beam epitaxy (MBE) on 50 nm MnS-buffered Si substrates. For GaN epitaxial growth, a single crystalline GaN target was used under the nitrogen partial pressure of  $5 \times 10^{-5}$  mbar. The base pressure was kept at  $1 \times 10^{-9}$  mbar, and the substrate temperature was maintained at around 700 °C. For comparison, a bare p-type GaN (0001) film [p+GaN (10 nm)/p-GaN (1  $\mu$ m)/GaN (3  $\mu$ m)] was grown on an *r*-plane sapphire substrate as a reference. Finally, ZnO films with different thicknesses of 4, 15 and 50 nm were grown using metal-organic chemical vapor deposition (MOCVD) on the 50 nm-thick GaN/ epilayers. During ZnO deposition, the diethyl zinc (DEZn) ZnO and O<sub>2</sub> were employed as the source materials. The chamber pressure was kept at about 1 mbar, and the substrate temperature was maintained at around 500 °C. Thin films of MnS and GaN deposition were done by K. Takahashi and Sung-Gi Ri, and the MOCVD-ZnO growth was carried out by Dr. M. Sumiya at COMET Inc., National Institute for Materials Science (NIMS) (Tsukuba, Ibaraki, Japan) [143].

### 7.2.2 Sample Characterization

X-ray photoelectron spectroscopy (XPS) was carried out in the analysis chamber at EMIL (see Sect. 4.1.3). These XPS measurements were done with a Scienta Omicron Argus CU electron analyzer using Mg  $K_{\alpha}$  ( $h\nu = 1253.56$  eV) and Al  $K_{\alpha}$  ( $h\nu = 1486.58$  eV) excitation energies.

Accompanying hard X-ray photoelectron spectroscopy (HAXPES) measurements with excitation energies of 2 and 6 keV were conducted at the HiKE end-station (Beamline KMC-1) at BESSY II in Berlin and SPring-8 (Beamline BL15XU) synchrotron radiation facility in Japan, respectively. X-ray emission (XES) and absorption spectroscopy (XAS) were used to investigate the occupied and unoccupied partial density of states (PDOS). The XES and XAS experiments were performed at the Advanced Light Source (ALS) (beamline 8.0.1) at Lawrence Berkeley National Laboratory (LBNL). The working principle of the spectroscopic analysis (XPS, HAXPES and XES & XAS) used in this work has been described in Sect. 4.2.

## 7.3 The MnS/Si Interface

### 7.3.1 HAXPES Survey Spectra

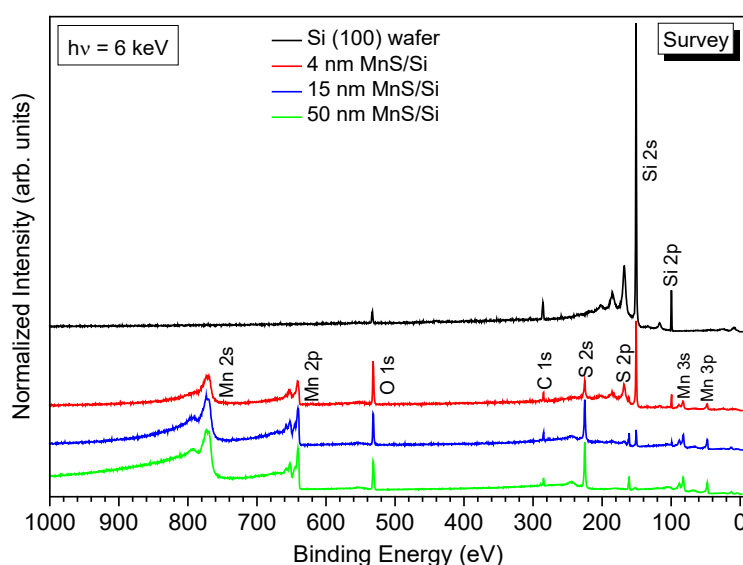


Figure 7.3.1: HAXPES survey spectra for Si (100) wafer, 4, 15 and 50 nm MnS/Si stacks measured with the excitation energy of 6 keV. All spectra shown here are normalized to the background of the Mn 2p photoelectron line at 630 eV.

Fig. 7.3.1 shows the HAXPES survey spectra of Si (100) wafer, 4, 15 and 50 nm MnS/Si stacks measured with a photon energy of 6 keV. All spectra exhibit the expected photoelectron signals attributed to (Mn, S, and Si), and C, O-related signals. The presence of the C 1s (or O 1s) photoelectron line may result from surface contamination occurring during the sample transfer through ambient conditions into the UHV analysis system. Another origin of the observed O 1s signal could be an indication for Mn oxidation. Significant Si signal from the underlying Si (100) wafer is seen in the photoelectron spectra of the 4 and 15 nm MnS/Si stacks. It indicates that either the MnS coverage of the Si (100) wafer is not complete or the inelastic mean free

path (IMFP) of electrons at 6 keV photon energy (i.e., about 10 nm for Si [74]) exceeds the MnS thickness. A very small Si signal is found in the spectrum of 50 nm MnS/Si substrate, probably due to surface contamination from Si (100) wafer.

### 7.3.2 Interface Chemistry

#### *Si 2s Spectra*

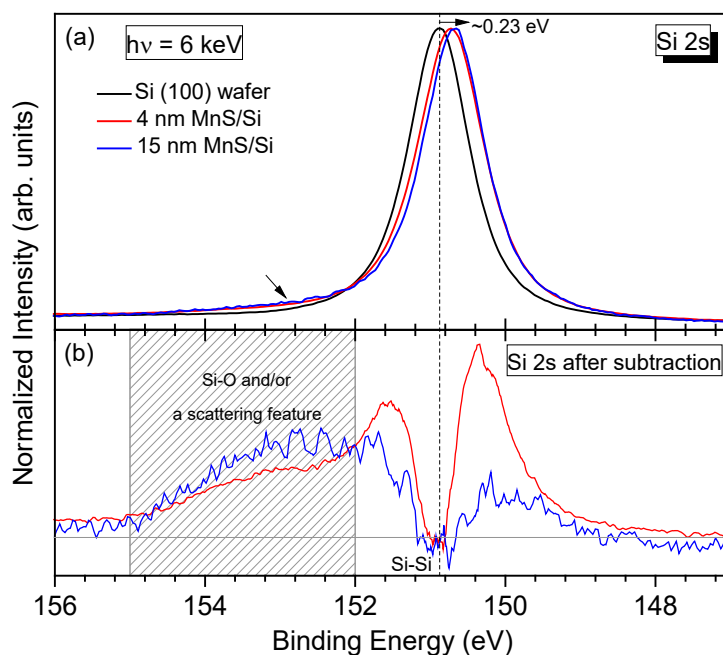


Figure 7.3.2: (a) Si 2s core-level spectra for Si (100) wafer, 4 and 15 nm MnS/Si stacks collected at the excitation energy of 6 keV. All spectra shown here are normalized to the maximum intensity values. (b) Spectral difference around Si 2s region between the MnS/Si stacks and Si (100) wafer by subtracting the background spectrum of Si (100) wafer from that of the MnS/Si stacks. Before subtraction, the energy positions of Si 2s peaks for the MnS/Si stacks are intentionally shifted to overlap with that of Si (100) wafer.

Si 2s core-level spectra of 4, 15 nm MnS/Si stacks and Si (100) wafer are shown in Fig. 7.3.2 (a). Compared to Si (100) wafer, the spectra exhibit lower binding energies by  $\sim 0.15$  and  $\sim 0.23$  eV for 4 and 15 nm MnS/Si stacks, respectively, along with a slight broadening in lineshape. In addition, a high binding energy shoulder indicated by the arrow is observed in the spectra of the MnS/Si stacks. To examine the possible chemical changes behind that, the spectral difference between the MnS/Si stacks and Si (100) wafer is considered [Fig. 7.3.2 (b)]. The difference was derived by subtracting the background spectrum of Si (100) wafer from that of the MnS/Si stacks. Prior to the background subtraction, the energy positions of Si 2s peaks for

the MnS/Si stacks and Si (100) wafer are intentionally aligned to achieve maximum overlap. As clearly seen from Fig. 7.3.2 (b), the zero-intensity region centered at  $(150.88 \pm 0.05)$  eV is typically related to Si-Si bonds [144]. Two sharp emission features appear on both sides of the Si-Si bonding region, in particular for 4 nm MnS/Si stack, indicating that some other Si-related species form when MnS has grown on Si (100) wafer. This could be well possibly explained by the presence of Si-S bonds (i.e.,  $\text{SiS}_x$  species), as will be further discussed later. In addition, a broad high binding energy structure located at around 152-155 eV is seen, possibly due to silicon oxides ( $\text{SiO}_x$  or  $\text{SiO}_2$ ) [144] and/or a scattering feature caused by loss of energy of a photon when it passes through the MnS overlayer.

### Si 2p Spectra

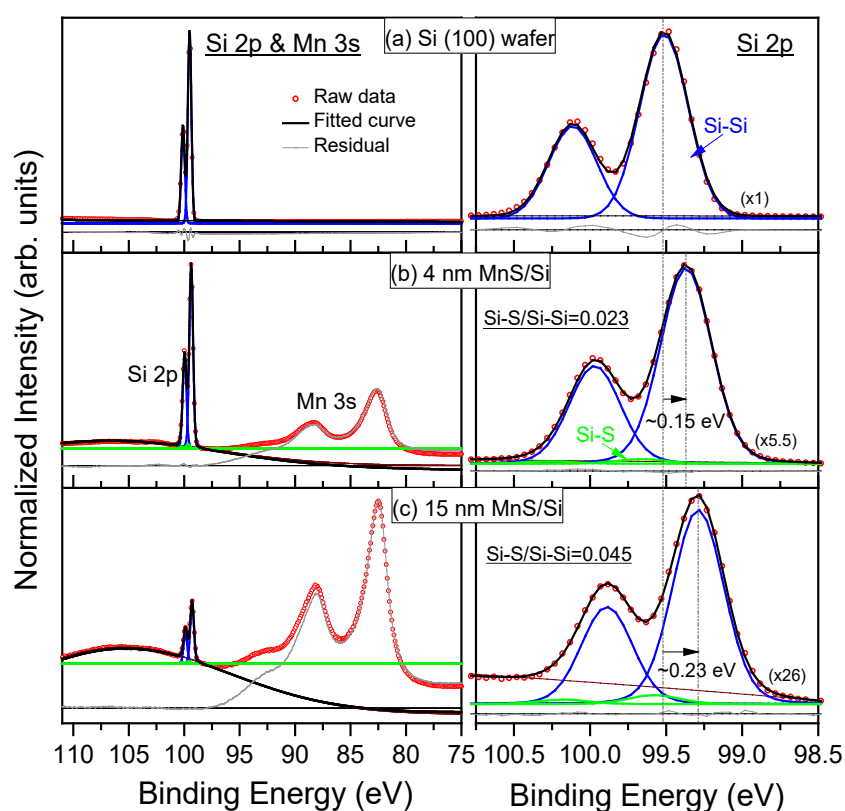


Figure 7.3.3: Si 2p and Mn 3s core-level spectra for (a) Si (100) wafer, (b) 4 nm and (c) 15 nm MnS/Si stacks collected with the excitation energy of 6 keV (*left panel*). Si 2p spectra are fitted by Voigt profiles using a linear background subtraction. Before fitting the data, an additional background subtraction based on Gaussian mixture model (GMM) [145] (*thin wine lines*) is applied for the whole Si 2p and Mn 3s spectra of 4 and 15 nm MnS/Si stacks to minimize the spectral weight of Mn 3s satellite. The detailed Si 2p spectra fitted with Voigt functions are shown (*right panel*), where the intensity scale for the fitted spectra of 4 and 15

nm MnS/Si stacks was magnified by  $\times 5.5$  and  $\times 26$  relative to that of Si (100) wafer, respectively.

In order to clarify the presence of Si-S bonds at the MnS/Si stacks, the Si 2p and S 2p photoelectron spectra are chosen to study in this work. Fig. 7.3.3 shows the Si 2p and Mn 3s core-level spectra for Si (100) wafer, 4 and 15 nm MnS/Si stacks measured at 6 keV photon energy. The Mn 3s spectra of the MnS/Si stacks are split into two peaks at  $(82.46 \pm 0.05)$  and  $(88.09 \pm 0.05)$  eV, respectively, corresponding to  $^7\text{S}$  and  $^5\text{S}$  components in MnS. The energy separation between the  $^7\text{S}$  and  $^5\text{S}$  multiplet components is around 5.6 eV, consistent with published literature on MnS [146]. A broad feature is observed on the high binding energy side of the main lines. The broad high binding energy structure, associated with Mn 3s satellite, would contribute some spectral weight to the Si 2p spectra of the MnS/Si stacks. In order to minimize the contribution from Mn 3s satellite structure, a background subtraction based on Gaussian mixture model (GMM) [145] was applied for the whole Si 2p and Mn 3s spectra of the MnS/Si stacks. After GMM background subtraction, the Si 2p spectra within the whole region (i.e., Si 2p and Mn 3s binding energies region) were fitted with Voigt (mixed Gaussian-Lorentzian) profiles using a linear background subtraction. The detailed fits of the Si 2p spectra are shown on the right side of Fig. 7.3.3. The Si 2p spectra yield a well-resolved spin-orbit splitting. The energy separation and the intensity ratio between the spin-orbit doublets of Si 2p spectra are both fixed according to literature values [147, 148]. For Si (100) wafer [Fig. 7.3.3 (a)], the Si 2p spectrum is composed of a spin-orbit doublet: Si 2p<sub>3/2</sub> ( $99.52 \pm 0.05$  eV) and Si 2p<sub>1/2</sub> ( $100.12 \pm 0.05$  eV), typically related to Si-Si bonds [149]. The Si 2p doublet assigned to Si-Si bonds slightly shifts  $\sim 0.15$  and  $\sim 0.23$  eV towards lower binding energies in the spectra of 4 and 15 nm MnS/Si stacks [Fig. 7.3.3 (b) and (c)], respectively. It agrees well with the energy shifts observed in the Si 2s spectra, suggesting an upwards interface-induced band bending (IIBB) in Si when MnS is grown on Si (100) wafer. In addition, a pair of the small spin-orbit doublet is seen in the spectra of 4 and 15 nm MnS/Si stacks [Fig. 7.3.3 (b) and (c)]. This weak doublet is due to S-induced Si 2p component, i.e., the bonding configuration Si-S or SiS<sub>x</sub>. The Si-S component exhibits a small chemical shift of  $\sim 0.30$  eV towards higher binding energy with respect to bulk Si, in agreement with literature values [150]. The existence of a SiS<sub>2-x</sub>-rich phase was also revealed at the MnS/Si and ZnS/Si interfaces during the initial growth stage of sulfides on Si substrates [151]. The signal intensity ratios of Si-S and Si-Si bonds are determined to be 0.023 and 0.045 for 4 and 15 nm MnS/Si stacks, respectively.

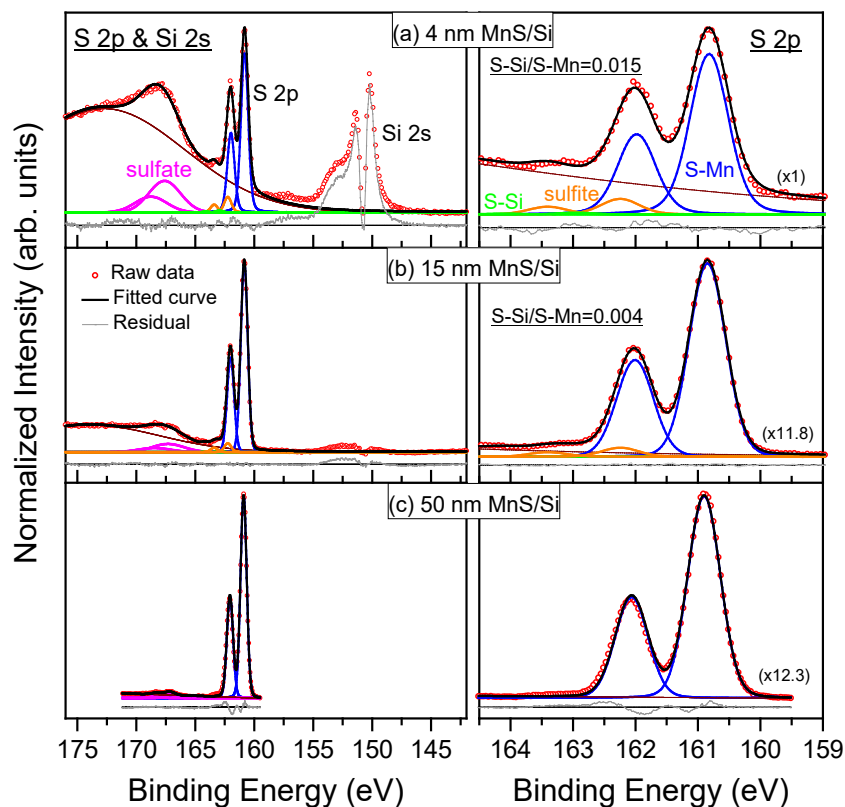


Figure 7.3.4: S 2p and Si 2s core-level difference spectra for (a) 4 nm and (b) 15 nm, and (c) 50 nm MnS/Si stacks collected with the excitation energy of 6 keV (*left panel*). S 2p spectra are fitted with Voigt profiles using a linear background subtraction. Prior to fitting the data, the Si 2s spectral weight of Si (100) wafer as a reference was subtracted from that of 4 and 15 nm MnS/Si stacks, as referring to Fig. 7.3.2. Before spectral weight subtraction, the energy positions of the Si 2s spectra for 4 and 15 nm MnS/Si stacks are intentionally shifted to overlap with that of Si (100) wafer. Afterwards, a background subtraction based on Gaussian mixture model (GMM) [145] was applied for the whole S 2p and Si 2s spectra of 4 and 15 nm MnS/Si stacks to minimize the contribution from Si 2s spectra. The detailed fits of the S 2p spectra are shown (*right panel*), where the intensity scale for the fitted spectra of 15 and 50 nm MnS/Si stacks was magnified by  $\times 11.8$  and  $\times 12.3$  relative to that of 4 nm MnS/Si stack, respectively.

Fig. 7.3.4 shows the S 2p and Si 2s photoelectron spectra of the 4, 15 and 50 nm MnS/Si stacks measured at 6 keV photon energy. As mentioned above, the Si 2s spectra of 4 and 15 nm MnS/Si stacks show a broad high binding energy structure that would contribute a high energy background to the S 2p spectra. In addition, a very broad peak in the binding energy region between 165-175 eV is shown in the S 2p spectrum of 50 nm MnS/Si substrate, generally related

to S bonded as a sulfate [152], which makes the S 2p spectra complex. To minimize that background contribution, a spectral weight removal of Si 2s peak was done by subtracting the background spectrum of Si (100) wafer from that of 4 and 15 nm MnS/Si stacks, as referring to Fig. 7.3.2. Before spectra subtraction, the energy positions of the Si 2s spectra for 4 and 15 nm MnS/Si stacks are intentionally shifted to overlap with that of Si (100) wafer. Subsequently, an additional background subtraction based on Gaussian mixture model (GMM) [145] is applied for the whole S 2p and Si 2s spectra (i.e., S 2p and Si 2s binding energies region) of 4 and 15 nm MnS/Si stacks to minimize the contribution from Si 2s spectra. After that, the S 2p spectra of 4, 15 and 50 nm MnS/Si stacks were fitted with Voigt profiles using a linear background subtraction. For clarity, the detailed S 2p spectra of these stacks are shown on the right side of Fig. 7.3.4. One can observe a single well-resolved spin-orbit doublet in the spectrum of 50 nm MnS/Si substrate [Fig. 7.3.4 (c)], located at  $(160.90\pm 0.05)$  and  $(162.06\pm 0.05)$  eV, corresponding to S-Mn bonds [153]. For 4 and 15 nm MnS/Si stacks [Fig. 7.3.4 (a) and (b)], the spectra are fitted with three doublets. The prominent doublet occurring at  $(160.82\pm 0.05)$  and  $(161.98\pm 0.05)$  eV is consistent with the main  $S^{2-}$  species of MnS (S-Mn bonds) [153]. The second one located at  $(162.25\pm 0.05)$  and  $(163.41\pm 0.05)$  eV can be associated with Mn sulfite at the surface. The additional much weaker doublet is located at  $(162.95\pm 0.05)$  and  $(164.11\pm 0.05)$  eV, which we contribute to S-Si bonds in this work. In addition, the signal intensity ratios (S-Si/S-Mn) are determined to be 0.015 to 0.004 for 4 and 15 nm MnS/Si stacks, respectively.

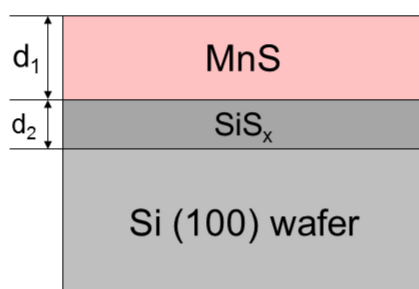


Figure 7.3.5: A simple two-layer model for the homogeneous MnS/SiS<sub>x</sub>/Si structure.  $d_1$  and  $d_2$  are the thicknesses of the MnS and SiS<sub>x</sub> layers, respectively.

To further confirm the fit results (i.e., Si-S bonds) of the Si 2p and S 2p spectra, a simple two-layer model for the homogeneous MnS/SiS<sub>x</sub>/Si structure is provided in Fig. 7.3.5 to calculate the photoelectron intensities as expressed by the following relations [154],



$$I^{MnS} = I_{\infty}^{MnS} \left[ 1 - \exp\left(-\frac{d_1}{\lambda_{MnS} \sin \theta}\right) \right], \quad (7-1)$$

$$I^{SiSx} = I_{\infty}^{SiSx} \left[ 1 - \exp\left(-\frac{d_2}{\lambda_{SiSx} \sin \theta}\right) \right] \exp\left(-\frac{d_1}{\lambda_{MnS} \sin \theta}\right), \quad (7-2)$$

$$I^{Si} = I_{\infty}^{Si} \exp\left(-\frac{d_2}{\lambda_{SiSx} \sin \theta}\right) \exp\left(-\frac{d_1}{\lambda_{MnS} \sin \theta}\right), \quad (7-3)$$

Where  $I^{MnS}$ ,  $I^{SiSx}$ , and  $I^{Si}$  are the integrated intensities of the photoelectrons from MnS, SiS<sub>x</sub>, and Si layers, respectively;  $I_{\infty}^{MnS}$ ,  $I_{\infty}^{SiSx}$  and  $I_{\infty}^{Si}$  are the intensities of the homogeneous bulk MnS, SiS<sub>x</sub>, and Si substrates, respectively;  $\lambda_{SiSx}$  and  $\lambda_{MnS}$  are the inelastic mean free paths (IMFPs) of the Si 2p (or S 2p) photoelectrons in SiS<sub>x</sub> and MnS layers, respectively;  $\theta$  is the photoelectron collecting angle of 90° in this work;  $d_1$  and  $d_2$  are the thicknesses of the MnS and SiS<sub>x</sub> layers. According to Eqs. (7-1), (7-2) and (7-3), the relative intensities of ( $I^{SiSx}/I^{Si}$ ) and ( $I^{SiSx}/I^{MnS}$ ) in the homogeneous MnS/SiS<sub>x</sub>/Si structure can be evaluated as,

$$\frac{I^{SiSx}}{I^{Si}} = \frac{I_{\infty}^{SiSx}}{I_{\infty}^{Si}} \left[ \exp\left(\frac{d_2}{\lambda_{SiSx} \sin \theta}\right) - 1 \right], \quad (7-4)$$

$$\frac{I^{SiSx}}{I^{MnS}} = \frac{I_{\infty}^{SiSx}}{I_{\infty}^{MnS}} \frac{\left[ 1 - \exp\left(-\frac{d_2}{\lambda_{SiSx} \sin \theta}\right) \right] \exp\left(-\frac{d_1}{\lambda_{MnS} \sin \theta}\right)}{\left[ 1 - \exp\left(-\frac{d_1}{\lambda_{MnS} \sin \theta}\right) \right]}, \quad (7-5)$$

In this work, the Si 2p photoelectrons are employed to evaluate the thickness ( $d_2$ ) of the interfacial SiS<sub>x</sub> layer. Note that the photoionization cross sections for Si 2p core level in different bonding states are similar, thus the ( $I_{\infty}^{SiSx}/I_{\infty}^{Si}$ ) ratio can be related to the ratio of the atomic densities of SiS<sub>x</sub> and Si (2.329 g/cm<sup>3</sup>). Owing to that the atomic density of SiS<sub>x</sub> is difficult to estimate, a value of 1.853 g/cm<sup>3</sup> for SiS<sub>2</sub> is chosen for a stoichiometric SiS<sub>x</sub>. In this connection, the ratio of ( $I_{\infty}^{SiSx}/I_{\infty}^{Si}$ ) is determined to be 0.80. Similar to S 2p photoelectrons used for the MnS/SiS<sub>x</sub> system, the ( $I_{\infty}^{SiSx}/I_{\infty}^{MnS}$ ) ratio is determined to be 0.46 with the atomic density of MnS (3.99 g/cm<sup>3</sup>). In Eq. (7-4), the ratio of ( $I^{SiSx}/I^{Si}$ ) extracted by the values of the (Si-S/Si-Si) signal intensity ratios obtained from the Si 2p fits [as shown in Fig. 7.3.3 (b) and (c)] are 0.023 and 0.045, as taking  $\lambda^{Si\ 2p}_{SiSx} \approx \lambda^{Si\ 2p}_{SiS2} = 10.9$  nm, the effective thicknesses ( $d_2$ ) of the interfacial SiS<sub>x</sub> layers for 4 and 15 nm MnS/Si stacks are determined to be 0.31 and 0.60 nm, as listed in Table 7.1. Compared with an average thickness of SiS<sub>2</sub> monolayer (~0.70 nm), it indicates that an ultrathin SiS<sub>x</sub> layer forms at the MnS/Si interface (i.e., about a half monolayer and one monolayer for 4 and 15 nm MnS/Si stacks, respectively). Based on that, the ratio of ( $I^{SiSx}/I^{MnS}$ ) extracted by the values of the (S-Si/S-Mn) signal intensity ratios obtained from the S 2p fits [as shown in Fig. 7.3.4 (a) and (b)] are 0.015 and 0.004, as taking  $\lambda^{S\ 2p}_{SiSx} \approx \lambda^{S\ 2p}_{SiS2} =$

10.8 nm and  $\lambda^{S\ 2p}_{MnS} = 8.8$  nm, the effective thicknesses ( $d_1$ ) of the MnS layers for 4 and 15 nm MnS/Si stacks are determined to be 5.54 and 17.46 nm, as listed in Table 7.1. The calculated effective thickness of the MnS layer is very close to that grown experimentally in this work. Consequently, it can be concluded that an ultrathin SiS<sub>x</sub> layer (i.e., Si-S bonds) forms between the MnS and Si layers when MnS is grown on Si (100) wafer.

TABLE 7.1: Calculated effective thicknesses (nm) of the SiS<sub>x</sub> ( $d_2$ ) and MnS layers ( $d_1$ ).  $\lambda$  values (nm) are obtained from Ref. [74], the values of the (Si-S/Si-Si) signal intensity ratios ( $I^{SiS_x}/I^{Si}$ ) and the (S-Si/S-Mn) signal intensity ratios ( $I^{SiS_x}/I^{MnS}$ ) are obtained from the Si 2p and S 2p fits (Fig. 7.3.3 and 7.3.4), respectively.

Samples	Si 2p		$d_2$ SiS <sub>x</sub> thickness	S 2p			$d_1$ MnS thickness
	$I^{SiS_x}/I^{Si}$	$\lambda_{SiS_x}$		$I^{SiS_x}/I^{MnS}$	$\lambda_{SiS_x}$	$\lambda_{MnS}$	
4 nm MnS/Si	0.023	10.9	0.31	0.015	10.8	8.8	5.54
15 nm MnS/Si	0.045	10.9	0.60	0.004	10.8	8.8	17.46

### Mn 2p Spectra

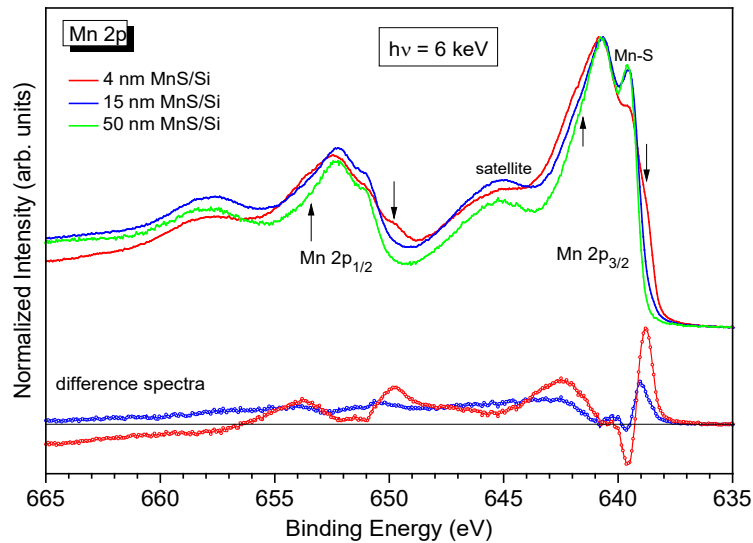


Figure 7.3.6: Mn 2p core-level spectra of 4, 15 and 50 nm MnS/Si stacks collected at the excitation energy of 6 keV. The spectral difference between (4, 15) nm MnS/Si and 50 nm MnS/Si stacks is derived by subtracting the reference spectrum of 50 nm MnS/Si stacks from that of (4, 15) nm MnS/Si stacks.

Fig. 7.3.6 shows the Mn 2p core-level spectra for 4, 15 and 50 nm MnS/Si stacks. The difference in the Mn 2p spectra between (4, 15) nm and 50 nm MnS/Si stacks is given by subtracting the reference spectrum of 50 nm MnS/Si substrate from that of (4, 15) nm MnS/Si stacks. All

spectra exhibit Mn  $2p_{3/2}$  and Mn  $2p_{1/2}$  spin-orbit doublet peaks located at  $(640.70 \pm 0.05)$  and  $(652.30 \pm 0.05)$  eV, respectively, in agreement with literature values for MnS [155, 156]. In Fig. 7.3.6, the Mn 2p spectra of 4 and 15 nm MnS/Si stacks exhibit a broader lineshape compared to that of 50 nm MnS/Si substrate. A low binding energy shoulder centered at  $(638.80 \pm 0.05)$  eV is clearly seen in the spectra of 4 and 15 nm MnS/Si stacks. Such a low binding energy shoulder in the Mn 2p spectra has been previously attributed to metallic Mn and/or metallicity in Mn<sup>3+</sup> compounds [157-160]. From HAXPES valence spectra shown in Fig. 7.3.7 (b), no related occupied density of states (DOS) around the Fermi level are present, which is contradictory to a simple metallic behavior. Note that a clear broadening also occurs near the binding energy of  $(641.30 \pm 0.05)$  eV in the Mn  $2p_{3/2}$  spectra of 4 and 15 nm MnS/Si stacks, usually related to Mn<sup>3+</sup> states [157, 158]. Combining with that, the low binding energy shoulder could be attributed to a well-screened final state at Mn<sup>3+</sup> sites. The relative intensity of this shoulder (also the Mn<sup>3+</sup> related feature) and the main line significantly decreases for 15 nm compared to 4 nm MnS/Si stacks, obviously seen in the difference spectra.

### 7.3.3 Valence-band Structure

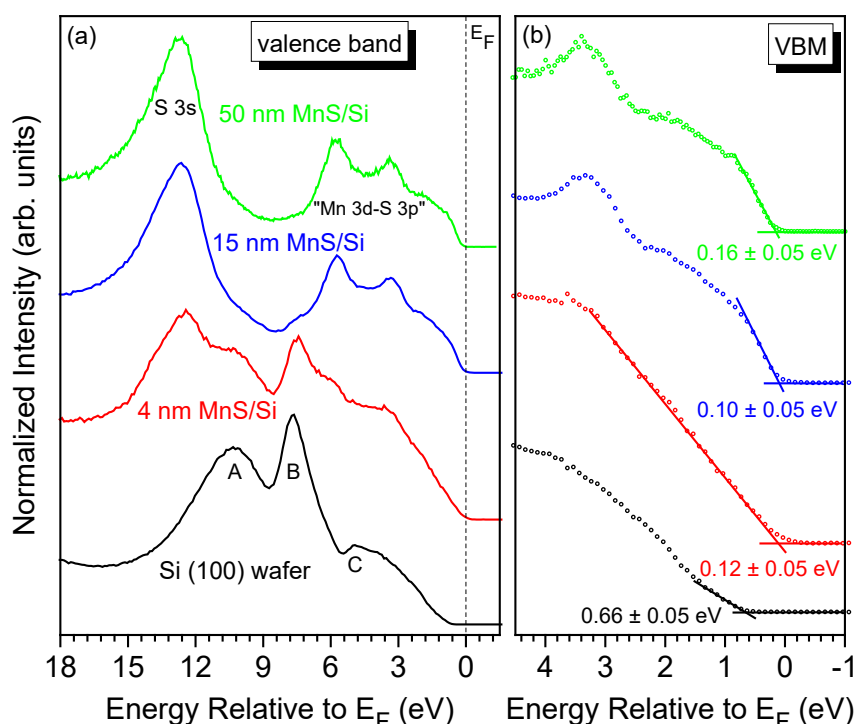


Figure 7.3.7: (a) Valence-band spectra of Si (100) wafer, 4, 15 and 50 nm MnS/Si stacks measured with the excitation energy of 6 keV. (b) Detailed spectra around the valence-band edge and the Fermi level region for each sample. The position of the valence-band maximum

(VBM) relative to the Fermi level is derived by a linear extrapolation of the leading edge to the background.

To better understand the electronic structure at the MnS/Si interface, the photoelectron spectra around the valence-band (VB) region for Si (100) wafer, 4, 15 and 50 nm MnS/Si stacks are shown in Fig. 7.3.7. In Fig. 7.3.7 (a), the VB spectrum of Si (100) wafer shows three well-known features that can be ascribed to Si 3s (A), hybridized s-p (B), and 3p-derived (C) density of states (DOS) [161]. For 50 nm MnS/Si substrate, the VB region is dominated by two main parts: the feature between  $\sim 8.5$  and  $\sim 17.0$  eV mainly corresponds to S 3s derived states. The other broad feature between 0 and  $\sim 7.5$  eV is related to Mn 3d-S 3p hybridization derived states [161]. The spectrum of 15 nm MnS/Si stack agrees very well with that of 50 nm MnS/Si substrate, having a strong p-d hybridization. The intermediate 4 nm MnS/Si stack shows VB features of both: the Si (100) wafer and 50 nm MnS/Si substrate.

The position of the valence-band maximum (VBM) relative to the Fermi level is determined by a linear extrapolation of the leading edge to the background with the precision of  $\pm 0.05$  eV, as indicated in Fig. 7.3.7 (b). The VB spectrum of the Si (100) wafer gives a VBM of  $(0.66 \pm 0.05)$  eV, and a VBM value of  $(0.16 \pm 0.05)$  eV is obtained for 50 nm MnS/Si substrate. Taking the optical-band gaps for MnS ( $E_g^{MnS} = 3.02$  eV) [60] and Si ( $E_g^{Si} = 1.12$  eV) [162] at room temperature, it suggests that the (50 nm) MnS has a significant p-type character, while a slight n-type character is suggested for the Si (100) wafer.

#### 7.3.4 Interface Band Offset

According to Kraut's method [55] (see Sect. 3.3), the valence-band offset VBO ( $\Delta E_V$ ) at the MnS/Si interface can be ascertained using the following relationship,

$$\Delta E_V = \Delta E_{CL} + [E_{Si\ 2p} - E_{VBM}]^{Si} - [E_{S\ 2p} - E_{VBM}]^{MnS}, \quad (7-6)$$

Where  $\Delta E_{CL} = (E_{S\ 2p}^{MnS/Si} - E_{Si\ 2p}^{MnS/Si})$  is the energy difference between S 2p and Si 2p core levels at the MnS/Si heterostructure.  $[E_{Si\ 2p} - E_{VBM}]^{Si}$  and  $[E_{S\ 2p} - E_{VBM}]^{MnS}$  are the energy separations between the core levels and the corresponding VBMs for Si (100) wafer and bare MnS substrate, respectively. In this work, 50 nm MnS/Si substrate can be treated as a bare MnS substrate for the band offset calculations. For clarity, Table 7.2 summarizes the corresponding energy positions of the Si  $2p_{3/2}$  and S  $2p_{3/2}$  peaks obtained from the fits (see Figs. 7.3.3 and 7.3.4) for each sample, together with the VBM values for Si (100) wafer and 50 nm MnS/Si substrate.

TABLE 7.2: Binding energies (eV) of the Si 2p<sub>3/2</sub> and S 2p<sub>3/2</sub> photoelectron peaks and VBM energies (eV) for each sample. All energies are referenced to the Fermi level with the experimental errors of ±0.05 eV.

States	Si (100) wafer	50 nm MnS/Si	15 nm MnS/Si	4 nm MnS/Si
Si 2p <sub>3/2</sub>	99.52	-	99.29	99.37
S 2p <sub>3/2</sub>	-	160.90	160.85	160.83
VBM	0.66	0.16	0.10	0.12
$E_{CL}-E_{VBM}$	98.86	160.74	-	-
$\Delta E_{CL}$	-	-	61.56	61.46

By substituting the results given in Table 7.2 into Eq. (7-6), the VBOs are determined to be (-0.32±0.10) and (-0.42±0.10) eV for 4 and 15 nm MnS/Si stacks, respectively. To improve the accuracy of the VBO value for the MnS/Si heterostructure, thus an average value of (-0.37±0.10) eV is employed in this work. Meanwhile, the conduction-band offset CBO ( $\Delta E_C$ ) can also be estimated by,

$$\Delta E_C = (E_g^{MnS} - E_g^{Si}) - \Delta E_V, \quad (7-7)$$

Where  $E_g^{MnS}$  and  $E_g^{Si}$  represent the optical-band gap energies of bare MnS and Si substrates, respectively. Taking  $\Delta E_V$  to be (-0.37±0.10) eV, then the corresponding  $\Delta E_C$  is calculated to be (2.27±0.10) eV at the MnS/Si heterointerface. These results indicate there has a type-II (staggered) band line-up forming at the MnS/Si heterointerface.

## 7.4 The GaN/MnS Interface

### 7.4.1 Survey Spectra

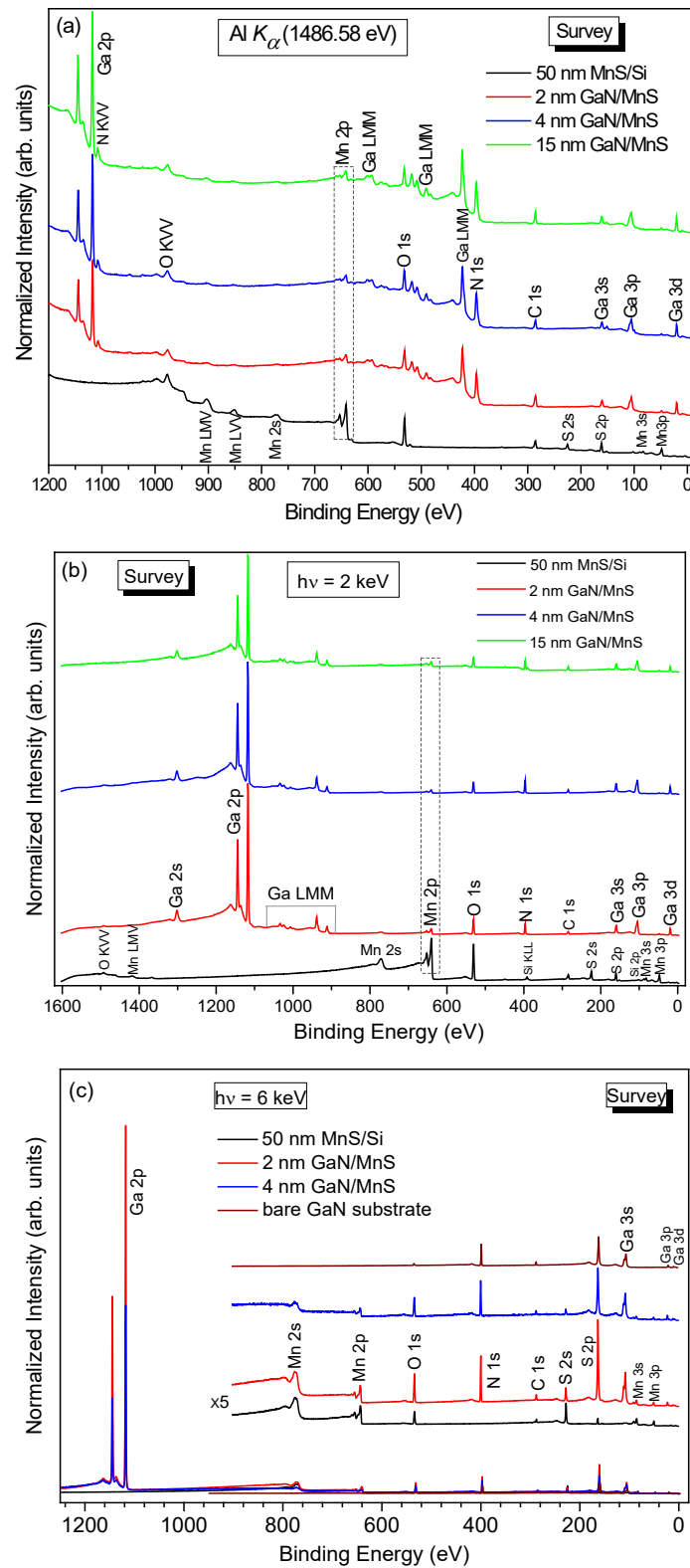


Figure 7.4.1: Survey spectra for 2, 4 and 15 nm GaN/MnS/Si stacks measured with different excitation energies of (a)  $h\nu = 1486.58 \text{ eV}$  (Al  $K\alpha$ ), (b)  $h\nu = 2 \text{ keV}$ , and (c)  $h\nu = 6 \text{ keV}$ ,

respectively, together with 50 nm MnS/Si and bare GaN substrate. The insert shows the magnification (by  $\times 5$ ) of the photoelectron spectra excited with 6 keV photon energy. The spectra excited with Al  $K_{\alpha}$  radiation ( $h\nu = 1486.58$  eV) are normalized to the background of N 1s core line at 376 eV; the spectra excited with 2 keV photon energy are normalized to the background of Mn 2p core line at 621 eV; the spectra excited with 6 keV photon energy are normalized to the background of Ga 3s core line at 144 eV.

Fig. 7.4.1 shows the photoelectron survey spectra for 2, 4 and 15 nm GaN/MnS/Si stacks measured with different photon energies of  $h\nu = 1486.58$  eV (Al  $K_{\alpha}$ ),  $h\nu = 2$  keV, and  $h\nu = 6$  keV, together with 50 nm MnS/Si and bare GaN substrate. All survey spectra exhibit the expected photoelectron signals attributed to (Mn, Ga, N, S). O and C ascribed signals can also be seen in the spectra of these samples, possibly attributed to surface contamination occurring during the samples transfer through ambient conditions into the UHV analysis system. Some silicon photoelectron signals appear in the spectrum of 50 nm MnS/Si substrate when measured with 2 keV excitation energy. This is due to the surface contamination from the Si (100) wafer during sample cutting. Note that a significant Mn emission from the underlying MnS on Si (100) wafer is seen in the spectra of the GaN/MnS stacks, even measured with a surface-sensitive photon energy of 1486.58 eV. It indicates that either the GaN coverage is not complete or Mn diffuses significantly into the GaN overlayer during the GaN growth on MnS-buffered Si substrate. Furthermore, the relative intensity of Mn (i.e., Mn 2p core line) and Ga emission (i.e., Ga 2p core line) is independent on the GaN thickness. It could be that prior to GaN deposition the evaporation of MnS from the substrate surface occurs, then followed by the redeposition of MnS after GaN is finished.

## 7.4.2 Interface Chemistry

### *Ga 2p<sub>3/2</sub> Spectra*

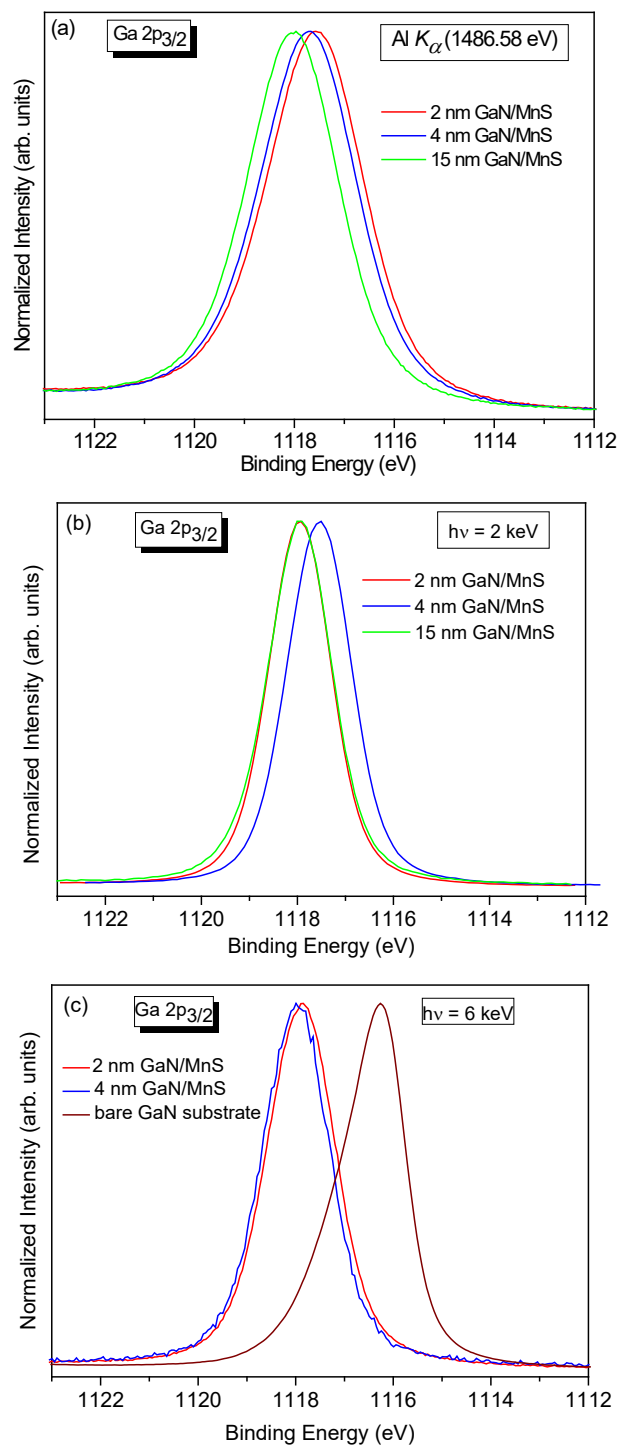


Figure 7.4.2: Ga 2p<sub>3/2</sub> core-level spectra for 2, 4 and 15 nm GaN/MnS/Si stacks measured with different excitation energies of (a)  $h\nu = 1486.58$  eV (Al  $K_{\alpha}$ ), (b)  $h\nu = 2$  keV, and (c)  $h\nu = 6$  keV, respectively. All spectra shown here are normalized to the maximum intensity values.



Fig. 7.4.2 shows the Ga  $2p_{3/2}$  core-level spectra for 2, 4 and 15 nm GaN/MnS/Si stacks measured with different excitation energies of 1486.58 eV ( $Al K_{\alpha}$ ), 2 and 6 keV, respectively. In Fig. 7.4.2 (a), the Ga  $2p_{3/2}$  spectrum of 2 nm GaN/MnS/Si stack exhibits the main peak at the binding energy of  $(1117.55 \pm 0.05)$  eV, corresponding to Ga-N bonds [163-165]. A slight shift by  $\sim 0.15$  eV and a large shift by  $\sim 0.50$  eV towards higher binding energies are observed in the spectra of 4 and 15 nm GaN/MnS/Si stacks, respectively, compared to that of 2 nm GaN/MnS/Si stack. When measured with a higher photon energy of 2 keV, the spectrum of 4 nm GaN/MnS/Si stack shows a lower binding energy by  $\sim 0.40$  eV than that of 2 and 15 nm GaN/MnS/Si stacks [Fig. 7.4.2 (b)]. While the spectrum of 4 nm GaN/MnS/Si stack exhibits a small shift of  $\sim 0.10$  eV towards higher binding energy compared to that of 2 nm GaN/MnS/Si stack under high photon energy of 6 keV [Fig. 7.4.2 (c)]. There are little or no changes on the spectral shape of these GaN/MnS/Si stacks, except some small energy shifts. In this situation, these small energy shifts might be attributed to the native oxide ( $GaO_x$ ) formed at the GaN/MnS/Si surfaces when exposed to air. There is another possibility of the nitridation of MnS surface during the pre-deposition process of GaN, which has been experimentally confirmed by Dr. T. Nagata [143] recently. However, the bare GaN substrate exhibits a broad spectral shape located at  $(1116.25 \pm 0.05)$  eV [Fig. 7.4.2 (c)], which is against the generally reported energy position ( $\sim 1117.80$  eV) [163-165] for GaN. This could be attributed to the different carrier concentrations between p<sup>+</sup>GaN (10 nm) and p-GaN (1  $\mu$ m) layers on the p-type GaN (0001) substrate.

## Mn 2p<sub>3/2</sub> Spectra

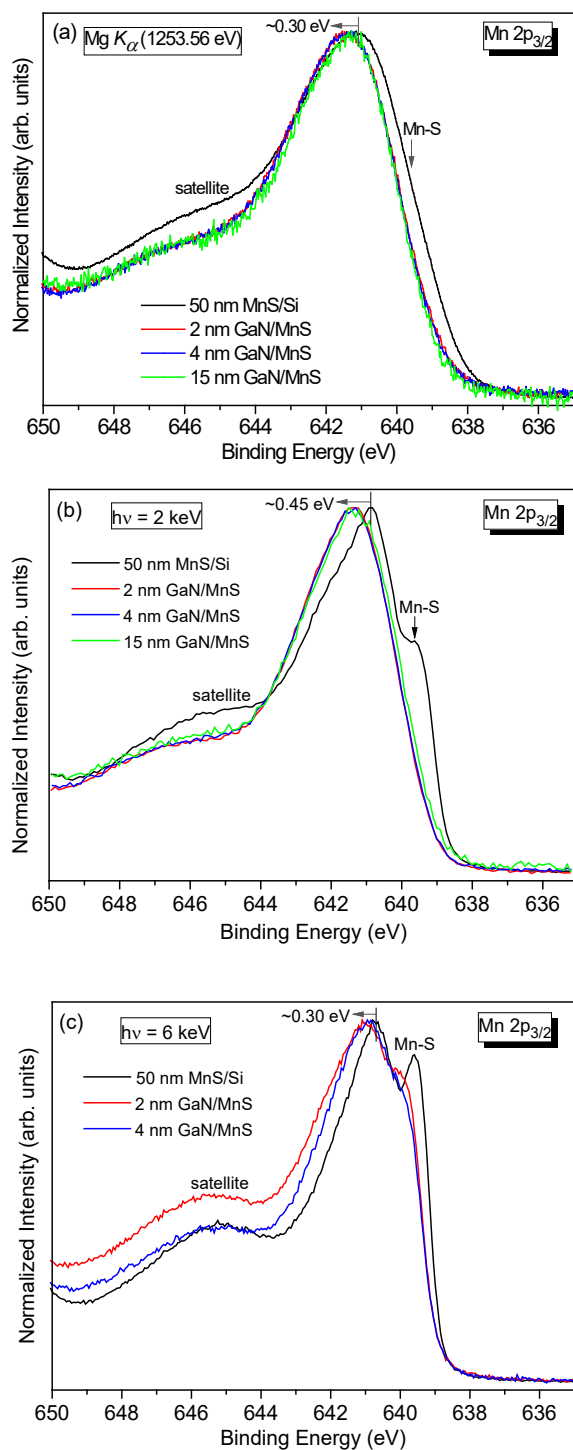


Figure 7.4.3: Mn 2p<sub>3/2</sub> core-level spectra for 2, 4 and 15 nm GaN/MnS/Si stacks measured with different excitation energies of (a)  $h\nu = 1253.56$  eV (Mg  $K_{\alpha}$ ), (b)  $h\nu = 2$  keV, and (c)  $h\nu = 6$  keV, respectively, compared to 50 nm MnS/Si substrate. All spectra shown here are normalized to the maximum intensity values.

Fig. 7.4.3 shows the Mn  $2p_{3/2}$  core-level spectra for 2, 4 and 15 nm GaN/MnS/Si stacks, in comparison with that of 50 nm MnS/Si substrate. In Fig. 7.4.3 (a), the Mn  $2p_{3/2}$  spectrum for 50 nm MnS/Si substrate exhibits a low binding energy feature centered at  $(639.58 \pm 0.05)$  eV, related to Mn-S bonds, as described in Sect. 7.3.2. The spectra of the GaN/MnS/Si stacks show a shift by  $\sim 0.30$  eV towards higher binding energy, along with an apparent narrowing at the low binding energy side compared to that of 50 nm MnS/Si substrate. When measured with high excitation energies of 2 and 6 keV, the low binding energy shoulder, assigned to Mn-S bonds, becomes very significant in the spectra of 50 nm MnS/Si substrate [Fig. 7.4.3 (b) and (c)]. This shoulder also appears in the spectra of the GaN/MnS/Si stacks when measured with the photon energy of 6 keV [Fig. 7.4.3 (c)]. A higher excitation energy provides a larger photoelectron depth profiling for the sample analysis, thereby yielding more Mn photoelectron signals from the underlying MnS layer. In addition, the spectra of the GaN/MnS/Si stacks shift towards higher binding energies by  $\sim 0.45$  eV at 2 keV excitation energy [Fig. 7.4.3 (b)], and by  $\sim 0.30$  eV at high excitation energy of 6 keV [Fig. 7.4.3 (c)] compared to that of 50 nm MnS/Si substrate, respectively. Note that a significant line broadening around the main line is observed in the spectra of the GaN/MnS/Si stacks [Fig. 7.4.3 (b) and (c)]. These results indicate that the atomic bonding state of Mn at the GaN/MnS/Si stacks is different from 50 nm MnS/Si substrate, suggesting some related chemical changes in Mn take place when GaN is grown on MnS. In this case, it is most likely due to the presence of Mn-N bonds at the GaN/MnS/Si stacks. As discussed above, a significant Mn diffusion into GaN layer might occur during GaN deposition, and the potential nitridation of MnS surface takes place prior GaN deposition. That opens a high possibility for Mn combining with N in a chemical bonding form of  $Mn_xN_y$  at the GaN/MnS/Si stacks.

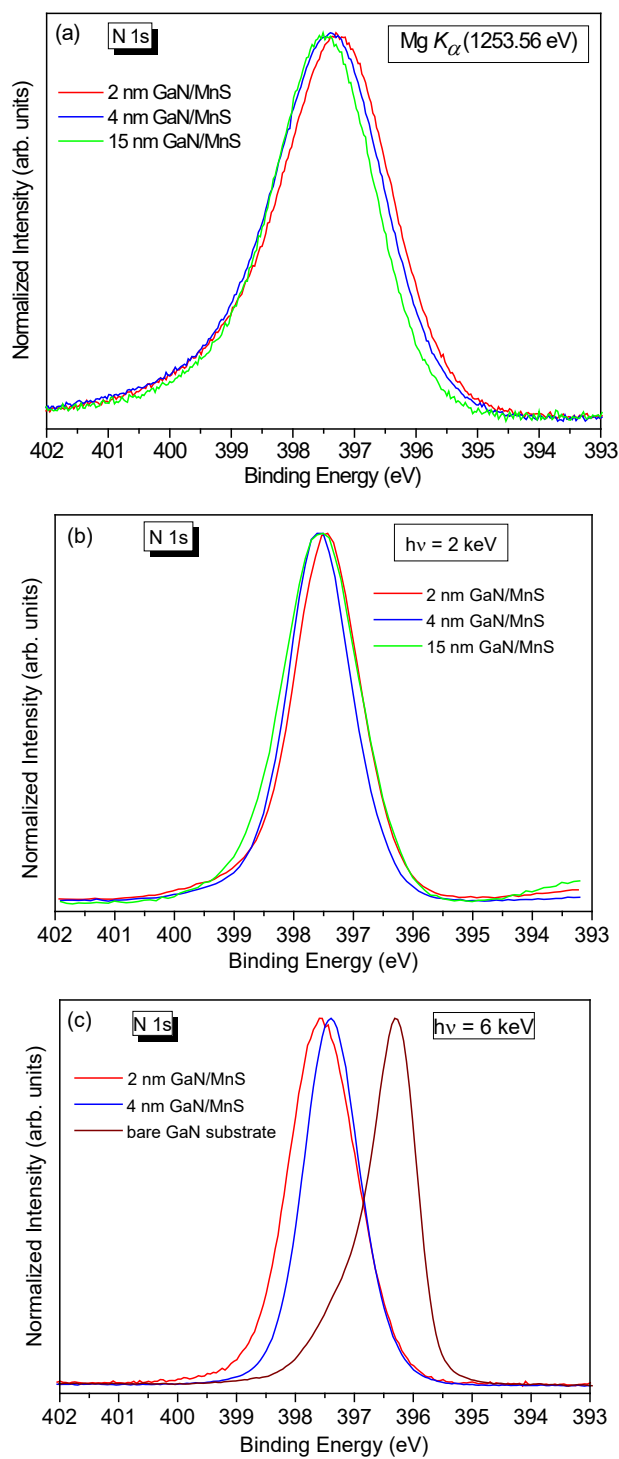


Figure 7.4.4: N 1s core-level spectra for 2, 4 and 15 nm GaN/MnS/Si stacks measured with different excitation energies of (a)  $h\nu = 1253.56$  eV (Mg  $K_{\alpha}$ ), (b)  $h\nu = 2$  keV, and (c)  $h\nu = 6$  keV, respectively. All spectra shown here are normalized to the maximum intensity values.

Fig. 7.4.4 shows the N 1s core-level spectra for 2, 4 and 15 nm GaN/MnS/Si stacks measured with different excitation energies of 1253.56 (Mg  $K_{\alpha}$ ), 2 and 6 keV, respectively. In Fig. 7.4.4

(a), the spectrum of 2 nm GaN/MnS/Si stack exhibits a broad peak centered at  $(397.30 \pm 0.05)$  eV, attributed to N-Ga bonds [165, 166], with a slight asymmetry to high binding energy. This high binding energy shoulder is possibly derived from the presence of chemisorbed nitrogen [167, 168], but also might be due to the gallium Auger peaks. The spectrum shows a clear shift of  $\sim 0.10$  eV towards higher binding energy for 4 nm GaN/MnS/Si stack, and a similar shift by  $\sim 0.20$  eV for 15 nm GaN/MnS/Si stack, respectively, compared to 2 nm GaN/MnS/Si stack. When measured with the excitation energy of 2 keV, a small shift of  $\sim 0.10$  eV towards higher binding energy is also observed in the spectra of 4 and 15 nm GaN/MnS/Si stacks compared to 2 nm GaN/MnS/Si stack [Fig. 7.4.4 (b)]. While the spectrum of 4 nm GaN/MnS/Si stack shows a lower binding energy by  $\sim 0.15$  eV than that of 2 nm GaN/MnS/Si stack at 6 keV excitation energy [Fig. 7.4.4 (c)]. These changes (i.e., mainly w.r.t. energy shifts) might be caused by the potential nitridation of MnS surface [143], similar to that in the Ga  $2p_{3/2}$  spectra (Fig. 7.4.2). In addition, the spectrum for bare GaN substrate has a large shift of  $\sim 1.20$  eV towards lower binding energy, along with an apparent high binding energy shoulder [Fig. 7.4.4 (c)]. This is also consistent with the observations in the Ga  $2p_{3/2}$  spectrum [Fig. 7.4.2 (c)], attributed to the different carrier concentrations between p<sup>+</sup>GaN (10 nm) and p-GaN (1  $\mu$ m) layers on the p-type GaN (0001) substrate.

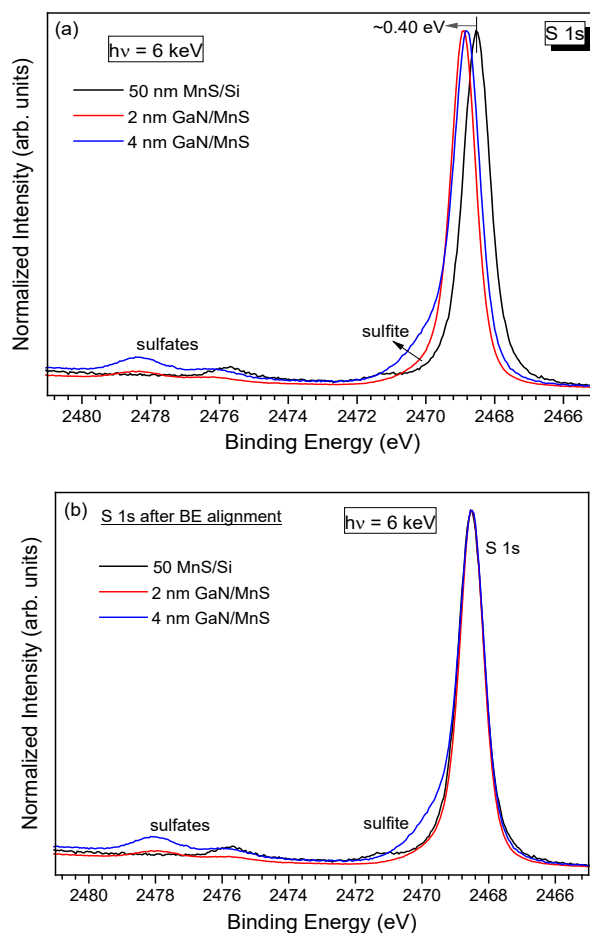


Figure 7.4.5: (a) S 1s core-level spectra for 2 and 4 nm GaN/MnS/Si stacks measured with the excitation energy of 6 keV, together with 50 nm MnS/Si substrate. (b) S 1s spectra after binding energy alignment for the GaN/MnS/Si stacks relative to 50 nm MnS/Si substrate. All spectra shown here are normalized to the maximum intensity values.

Fig. 7.4.5 shows the S 1s core-level spectra for 2 and 4 nm GaN/MnS/Si stacks measured with the excitation energy of 6 keV, in comparison with that of 50 nm MnS/Si substrate. In Fig. 7.4.5(a), the spectrum of 50 nm MnS/Si substrate exhibits a prominent peak located at  $(2468.53 \pm 0.05)$  eV, typically associated with S-Mn bonds, together with a broad feature in the region of 2474.5-2480.5 eV corresponding to S bonded as sulfates. An apparent (also broad) high binding energy shoulder is observed in the spectra within the region of 2469.5-2472.5 eV, related to S bonded as sulfites. Compared to 50 nm MnS/Si substrate, the spectra of 2 and 4 nm GaN/MnS/Si stacks show apparent shifts of  $\sim 0.40$  eV and  $\sim 0.30$  eV towards higher binding energies, respectively. After binding energy alignment, all the spectra show a quite similar lineshape [Fig. 7.4.5(b)]. Combining with the energy shifts observed in the Mn 2p spectra (Fig.

7.4.3), it can be inferred that an interface-induced band bending (IIBB) appears in MnS during GaN grown on MnS-buffered Si substrate.

### 7.4.3 Near-surface Chemical Structure

#### *Mn L<sub>2,3</sub>-edge XAS*

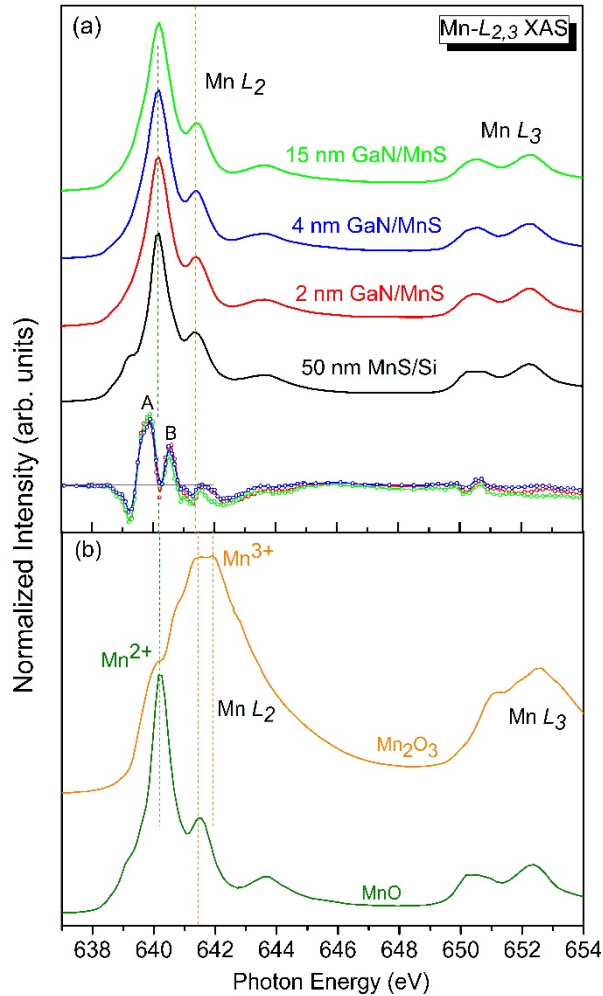


Figure 7.4.6: (a) Mn  $L_{2,3}$ -edge absorption spectra for 2, 4 and 15 nm GaN/MnS/Si stacks compared to 50 nm MnS/Si substrate (*top panel*). Difference spectra at Mn  $L$ -edge absorption between the GaN/MnS/Si stacks and 50 nm MnS/Si substrate are shown (*bottom panel*). (b) Mn  $L_{2,3}$ -edge absorption spectra collected on references including MnO (Mn<sup>2+</sup>) and Mn<sub>2</sub>O<sub>3</sub> (Mn<sup>3+</sup>).

Mn  $L_{2,3}$ -edge absorption spectra (XAS) for 2, 4 and 15 nm GaN/MnS/Si stacks are shown in Fig. 7.4.6 (a), together with 50 nm MnS/Si substrate for comparison. The spectra consist of well-separated absorption features in two regions:  $L_3$ -edge in the region of 638-646 eV assigned to the Mn  $2p_{3/2}$ -3d transitions, and  $L_2$ -edge at around 650-655 eV ascribed to the Mn  $2p_{1/2}$ -3d

transitions. The complex structure of Mn  $L_{2,3}$ -edge originates from Coulomb and exchange interactions between the intra-atomic Mn 3d-3d and core-hole 2p-3d states. It has been demonstrated that the lineshape and the energy position of the Mn- $L$  absorption spectra fingerprint the valence state of Mn ions, especially on  $L_3$  edge [169-171]. Compared to the referenced Mn  $L_{2,3}$ -edge for MnO and Mn<sub>2</sub>O<sub>3</sub> [Fig. 7.4.6 (b)] obtained experimentally in our work and the results of the calculations [171-173], the spectrum of 50 nm MnS/Si substrate shows clear features corresponding to Mn<sup>2+</sup> (3d<sup>5</sup>) states. The high-intensity peak at around ~640.15 eV can support the existence of Mn<sup>2+</sup> in each spectrum, while the high-energy feature between 641 and 642 eV possibly corresponds to the contribution from Mn<sup>3+</sup>. Note that the overall Mn- $L$  spectral lineshape for the GaN/MnS/Si stacks resembles that of 50 nm MnS/Si substrate, suggesting that most of Mn atoms at the GaN/MnS/Si stacks are in the 2+ charge state. In addition, a weak pre-edge feature at the low-energy side is clearly seen in the spectrum of 50 nm MnS/Si substrate, associated with Mn<sup>2+</sup> states in Mn-S bonds. It is noted that the Mn  $L_3$ -edge for the GaN/MnS/Si stacks shows a slight broadening of the high-intensity feature, in comparison with that of 50 nm MnS/Si substrate. To confirm the spectral changes clearly, the difference spectra between the GaN/MnS/Si stacks and 50 nm MnS/Si substrate is given on the bottom of Fig. 7.4.6 (a). Obviously, a zero-intensity region is seen, mainly assign to Mn<sup>2+</sup> in Mn-S bonds. While two sharp features (labeled “A” at ~639.86 eV and “B” at ~640.53 eV) are found on both sides of the zero-intensity region. The two features merge in almost the energy position of Mn<sup>2+</sup> states, probably due to the existence of Mn-N bonds primarily in the 2+ valence state, i.e., Mn<sub>3</sub>N<sub>2</sub>.



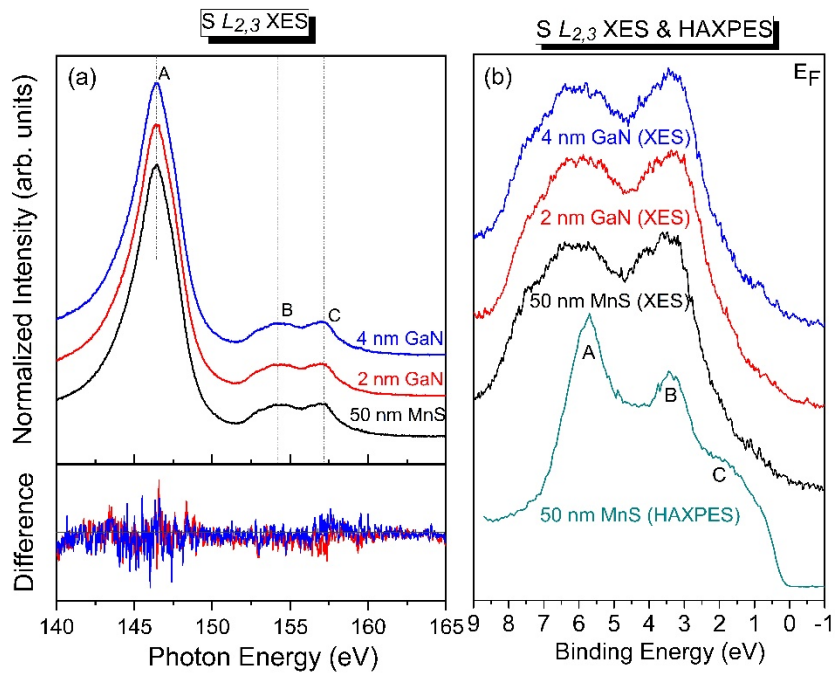


Figure 7.4.7: (a) S  $L_{2,3}$ -edge emission spectra for 2 and 4 nm GaN/MnS/Si stacks compared to 50 nm MnS/Si substrate (*top panel*). Difference spectra at S  $L$ -edge emission between the GaN/MnS/Si stacks and 50 nm MnS/Si substrate are shown (*bottom panel*). (b) A combination of S  $L_{2,3}$ -edge emission spectra and the valence-band (VB) HAXPES spectra measured at 6 keV photon energy for each sample. All spectra are plotted on a common binding energy scale.

The obtained emission spectra (XES) at the S  $L_{2,3}$ -edge region for the GaN/MnS/Si stacks are shown in Fig. 7.4.7 (a), together with the difference spectra between the GaN/MnS/Si stacks and 50 nm MnS/Si substrate. The S  $L$ -edge emission spectra correspond to the electronic transitions from the unoccupied 3s3d states to an atomic-like 2p state, probing S 3s3d partial density of states (PDOS) in the valence band. In this view, three different structures identified as “A” (~146.44 eV), “B” (~154.18 eV), and “C” (~157.17 eV) are observed, corresponding to S 3s, hybridized s-d, and 3d-derived PDOS [161], respectively. It indicates that the local symmetry and chemical states related to S are very similar for all the samples, mainly involved in the form of S-Mn bonds.

In addition, a combination of the obtained S  $L_{2,3}$ -edge XES spectra and the valence-band (VB) HAXPES spectra measured at 6 keV photon energy is present for each sample in Fig. 7.4.7 (b). All spectra are plotted on the binding energy scale by taking the corresponding HAXPES

binding energy of S  $2p_{3/2}$  peak. The S  $L$ -edge XES spectra directly probe the occupied S  $2p$  PDOS in the valence band, whereas the VB-HAXPES spectra effectively exhibit the total VB-DOS. The VB-HAXPES spectrum of 50 nm MnS/Si substrate shows three different features identified as “A” ( $\sim 5.69$  eV), “B” ( $\sim 3.43$  eV), and “C” ( $\sim 1.82$  eV), associated with Mn  $3d$ -S  $3p$  hybridization derived states [161]. The difference in the spectral shape between S  $L$ -edge XES and VB-HAXPES is observed, which is due to the different excitation energy dependence among the photoionization cross-sections for different involved atomic subshells [84, 85] (see Sect. 5.3.3).

#### 7.4.4 Valence-band Structure

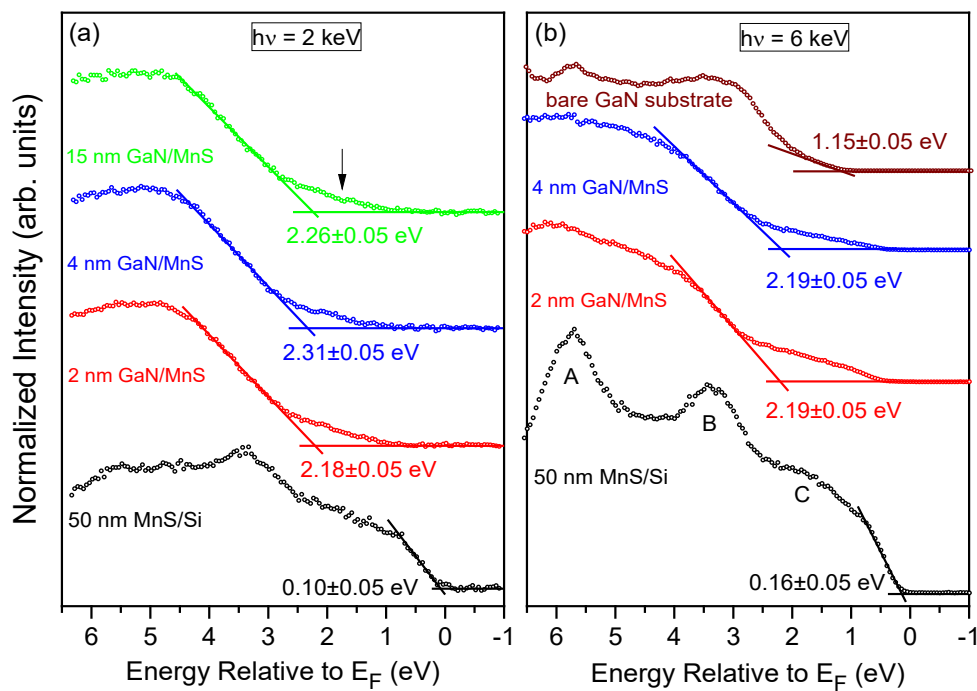


Figure 7.4.8: Valence-band spectra for 2, 4 and 15 nm GaN/MnS/Si stacks measured at different excitation energies of (a) 2 keV and (b) 6 keV, respectively, together with bare GaN and 50 nm MnS/Si substrates. The position of the valence-band maximum (VBM) relative to the Fermi level is derived by a linear extrapolation of the leading edge to the background.

The HAXPES valence-band (VB) spectra for 2, 4 and 15 nm GaN/MnS/Si stacks at different excitation energies of 2 and 6 keV are shown in Fig. 7.4.8, in comparison with that of bare GaN and 50 nm MnS/Si substrates. The position of the valence-band maximum (VBM) relative to the Fermi level has been determined by linearly extrapolating the VB edge to the background, as indicated in the figure. In Fig. 7.4.8 (a), the VB spectrum of 50 nm MnS/Si substrate gives a VBM of  $(0.10\pm 0.05)$  eV. The VBM value for 15 nm GaN/MnS/Si stack is determined to be

( $2.26 \pm 0.05$  eV). In Fig. 7.4.8 (b), linear extrapolation indicates that the VBM lies at ( $0.16 \pm 0.05$ ) eV below the Fermi level for 50 nm MnS/Si substrate, and a VBM value of ( $1.15 \pm 0.05$ ) eV is obtained for bare GaN substrate. Taking the band gaps for MnS ( $E_g^{MnS} = 3.02$  eV) [60] and GaN ( $E_g^{GaN} = 3.39$  eV) [52] at room temperature, it suggests that the (50 nm) MnS yields a significant p-type character, while an n-type doping of (15 nm) GaN. Note that a significant feature above the VBM is observed in the VB spectra of the GaN/MnS/Si stacks. The onsets of these features are generally  $\sim 1.00$  and  $\sim 0.40$  eV binding energy higher than the corresponding VBM positions when measured with 2 and 6 keV photon energies, respectively. The energy difference ( $\sim 0.40$  eV) appeared in the VB spectra at 6 keV excitation energy (i.e., more bulk-sensitive) seems similar as the energy shifts observed in the core-level (i.e., Mn 2p and S 1s) spectra of the GaN/MnS/Si stacks. In this case, the spectral weight above the VBM appears to decrease gradually with the GaN thickness increasing. That is most likely due to the interface-induced band bending (IIBB) in MnS with a reduction of MnS emission. While the large energy difference ( $\sim 1.00$  eV) occurs in the VB spectra at 2 keV photon energy (i.e., more surface-sensitive), along with the very similar spectral weight above the VBM independent on the GaN thickness. Furthermore, the onset of this feature is determined to be around 1.25 eV (energy on average) at the excitation energy of 2 keV, broadly consistent with the reported value (1.32 eV) for the band-gap energy of  $Mn_3N_2$  [171-173]. That could be mainly from some Mn-induced states (i.e., Mn 3d-N 2p derived states) due to a small sample depth profiling. Apart from this, the VB spectrum of 50 nm MnS/Si substrate shows three densities of states detected at  $\sim 5.69$ ,  $\sim 3.43$  and  $\sim 1.82$  eV, associated with Mn 3d-S 3p derived states [161]. The observed different lineshapes at different excitation energies of 2 and 6 keV, i.e., the intensity of feature “A” at around 5.69 eV is enhanced under high excitation energy of 6 keV, is attributed to a larger photoionization cross section of the p-orbital in HAXPES than that in conventional XPS [130, 174].

#### 7.4.5 Interface Band Offset

As mentioned in Sect. 7.3.4, the valence-band offset VBO ( $\Delta E_V$ ) and the corresponding conduction-band offset CBO ( $\Delta E_C$ ) at the GaN/MnS interface can be estimated according to Kraut’s method [55],

$$\Delta E_V = \Delta E_{CL} + [E_{Mn\ 2p} - E_{VBM}]^{MnS} - [E_{Ga\ 2p} - E_{VBM}]^{GaN}, \quad (7-8)$$

$$\Delta E_C = (E_g^{GaN} - E_g^{MnS}) - \Delta E_V, \quad (7-9)$$

For clarity, Table 7.3 summarizes the corresponding binding energies of the Mn 2p<sub>3/2</sub> and Ga 2p<sub>3/2</sub> peaks under the excitation energy of 2 keV, together with the VBM values for each sample.

TABLE 7.3: Energy positions (eV) of the Mn 2p<sub>3/2</sub> and Ga 2p<sub>3/2</sub> photoelectron peaks and VBM energies (eV) for each sample. The data is collected with the excitation energy of 2 keV. All energies are referenced to the Fermi level with the experimental errors of ±0.05 eV.

State	50 nm MnS/Si	15 nm GaN/MnS	4 nm GaN/MnS	2 nm GaN/MnS
Mn 2p <sub>3/2</sub>	640.88	641.30	641.30	641.38
Ga 2p <sub>3/2</sub>	-	1117.95	1117.51	1117.91
VBM	0.10	2.26	2.31	2.18
$E_{CL}-E_{VBM}$	640.78	1115.69	-	-
$\Delta E_{CL}$	-	-	476.21	476.53

By substituting the results given in Table 7.3 into Eqs. (7-8) and (7-9), an average value of the VBO ( $\Delta E_V$ ) and the corresponding CBO ( $\Delta E_C$ ) are determined to be (1.46±0.10) and (-1.09±0.10) eV for the GaN/MnS heterostructure, with taking the optical-band gaps for MnS ( $E_g^{MnS} = 3.02$  eV) [60] and GaN ( $E_g^{GaN} = 3.39$  eV) [52] at room temperature. This indicates there has a type-II (staggered) band alignment for GaN/MnS heterointerface.

## 7.5 The ZnO/GaN Interface

### 7.5.1 HAXPES Survey Spectra

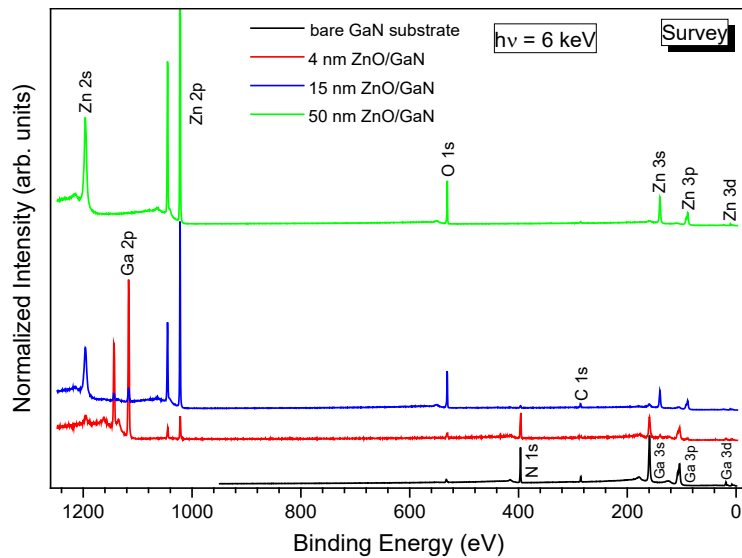


Figure 7.5.1: HAXPES survey spectra of bare GaN substrate, 4, 15 and 50 nm ZnO/GaN stacks on sapphire substrates measured with the photon energy of 6 keV.

Fig. 7.5.1 shows HAXPES survey spectra for bare GaN substrate, 4, 15 and 50 nm ZnO/GaN stacks on sapphire substrates measured at 6 keV photon energy. The expected photoelectron peaks for (Zn, Ga, N, and O) are present in the spectra, with a small C signal. The observed carbon signal might be due to the hydrocarbon contamination in the transfer process of the samples into the UHV analysis system. Some photoelectron signals of Ga and N from the underlying GaN layer are clearly seen in the spectrum of 15 nm ZnO/GaN stack, indicating that either the ZnO coverage of the GaN layer is not complete or Ga (or N) atoms diffuse into the ZnO layer during ZnO growth.

## 7.5.2 Interface Chemistry

### *Ga 2p<sub>3/2</sub> Spectra*

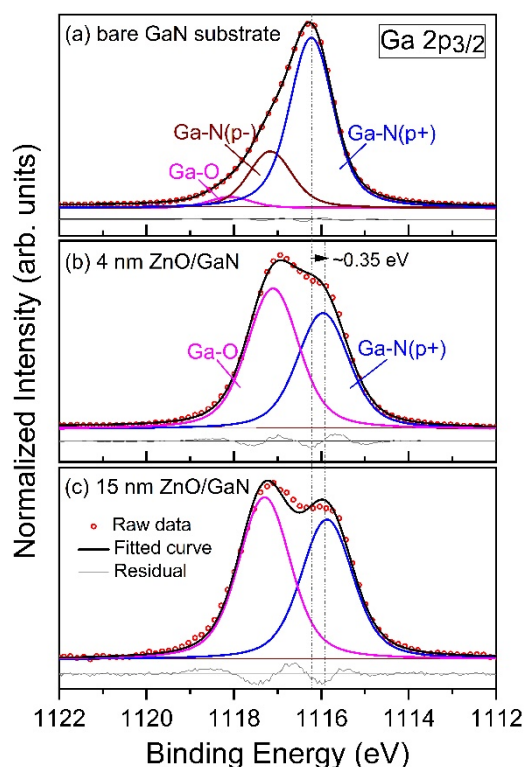


Figure 7.5.2: Ga 2p<sub>3/2</sub> core-level spectra for (a) bare GaN substrate, (b) 4 nm and (c) 15 nm ZnO/GaN stacks on sapphire substrates. All spectra are collected at the excitation energy of 6 keV. The spectra have been fitted by Voigt (mixed Lorentzian-Gaussian) profiles with a linear background subtraction.

Ga  $2p_{3/2}$ , N 1s, Zn  $2p_{3/2}$ , and O 1s core levels have been selected to investigate the interface chemical properties of the ZnO/GaN stacks on sapphire substrates. All core-level spectra have been fitted with Voigt (mixed Lorentzian-Gaussian) profiles using a linear background subtraction. As seen in Fig. 7.5.2 (a), the Ga  $2p_{3/2}$  spectrum of bare GaN substrate exhibits three peaks: two situated on  $(1116.32 \pm 0.05)$  and  $(1117.17 \pm 0.05)$  eV, assigned to Ga-N (p+)[163, 165] and Ga-N (p-) bonds[163], respectively; the other weak one located at  $(1118.09 \pm 0.05)$  eV, assigned to Ga-O bonds [163]. The Ga-O bonds at the bare GaN surface are usually related to the native oxide ( $\text{GaO}_x$ ) that forms when the sample is exposed to air. For the ZnO/GaN stacks, a prominent peak  $(1117.11 \pm 0.05)$  eV assignable to Ga-O bonds appears in the spectra, suggesting a significant interfacial oxidation ( $\text{GaO}_x$ ) occurs when ZnO deposited on GaN [Fig. 7.5.2 (b) and (c)]. Some previous work has also reported the formation of Ga-O bonds occurring at the ZnO/GaN interface [141, 142]. It might be attributed to the potential diffusion of Ga into the ZnO layer as the substrate temperature of MOCVD-ZnO growth (around 500 °C) is enough for the GaN diffusion into ZnO [175]. Compared to the bare GaN substrate, a shift by  $\sim 0.35$  eV towards lower binding energy is seen in the spectra of the ZnO/GaN stacks.

### N 1s Spectra

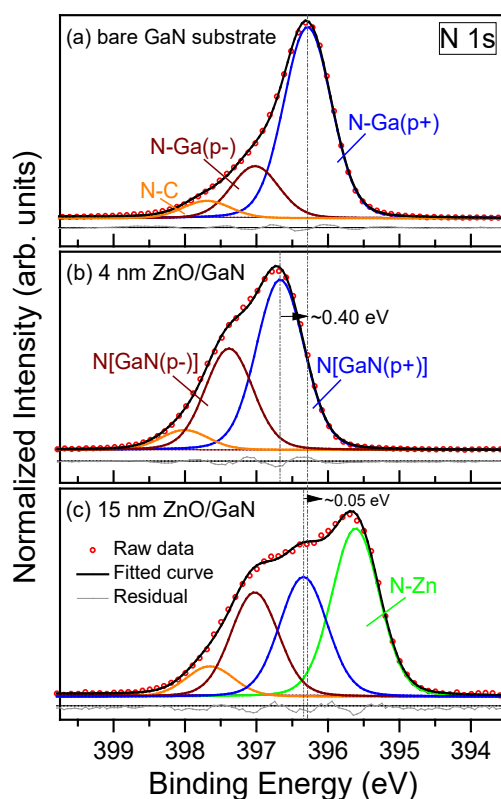


Figure 7.5.3: N 1s core-level spectra for (a) bare GaN substrate, (b) 4 nm and (c) 15 nm ZnO/GaN stacks on sapphire substrates. All spectra are collected at the excitation energy of 6

keV. The spectra have been fitted by Voigt (mixed Lorentzian-Gaussian) profiles with a linear background subtraction.

In Fig. 7.5.3 (a), three components are required to fit the N 1s spectrum of bare GaN substrate; one at  $(396.29 \pm 0.05)$  eV due to N-Ga (p+) bonds [165, 166], and the other one at  $(397.02 \pm 0.05)$  eV assigned to N-Ga (p-) bonds [167, 168], together with a high binding energy component generally originating from chemisorbed nitrogen, N-C bonds at  $(397.69 \pm 0.05)$  eV [167, 168]. The spectra of the ZnO/GaN stacks exhibit similar fitted components to that of bare GaN substrate [Fig. 7.5.3 (b) and (c)]. However, a prominent peak at the low binding energy of  $(395.61 \pm 0.05)$  eV is present in the spectrum of 15 nm ZnO/GaN stack, assignable to N-Zn bonds [176, 177]. The presence of N-Zn bonds is most likely attributed to a significant N diffusion into ZnO from the GaN layer. Little or no N-Zn bonds are observed in the spectrum of 4 nm ZnO/GaN stack, probably due to its very low signal-to-noise ratio. In addition, a shift by  $\sim 0.40$  eV towards higher binding energy is observed in the spectrum of 4 nm ZnO/GaN stack, in comparison with bare GaN substrate. While a very small shift of  $\sim 0.05$  eV towards higher binding energy is seen in the spectrum of 15 nm ZnO/GaN stack.

### Zn $2p_{3/2}$ Spectra

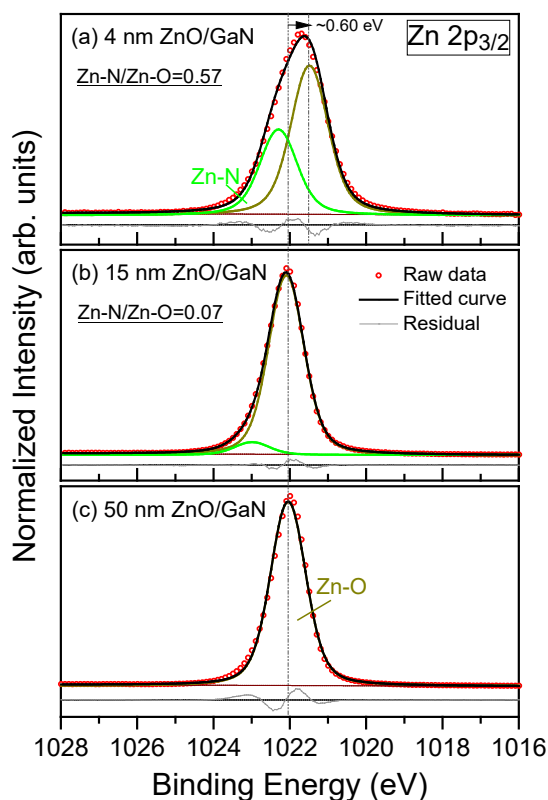


Figure 7.5.4: Zn 2p<sub>3/2</sub> core-level spectra for (a) 4 nm, (b) 15 nm and (c) 50 nm ZnO/GaN stacks on sapphire substrates. All spectra are collected at the excitation energy of 6 keV. The spectra have been fitted by Voigt (mixed Lorentzian-Gaussian) profiles with a linear background subtraction.

As for the Zn 2p<sub>3/2</sub> spectrum shown in Fig. 7.5.4 (c), the core line of 50 nm ZnO/GaN stack almost exhibits a single symmetric peak at (1022.05±0.05) eV, attributable to Zn-O bonds [178]. In terms of 4 nm ZnO/GaN stack, the spectrum shows two peaks centered at (1021.45±0.05) and (1022.30±0.05) eV [Fig. 7.5.4 (a)]. These binding energy peaks suggest the Zn-O and Zn-N bonds [178], respectively. The spectrum of 15 nm ZnO/GaN stack also shows the Zn-O and Zn-N components situated at (1022.10±0.05) and (1022.99±0.05) eV [Fig. 7.5.4 (b)], respectively. The existence of Zn-N bonds at 4 and 15 nm ZnO/GaN stacks is attributed to a large N diffusion during ZnO deposition, consistent with the observations in N 1s spectra. In addition, the signal intensity ratio (Zn-N/Zn-O) greatly decreases from 0.57 to 0.07 upon the ZnO thickness increasing from 4 to 15 nm on GaN film.

#### *O 1s Spectra*

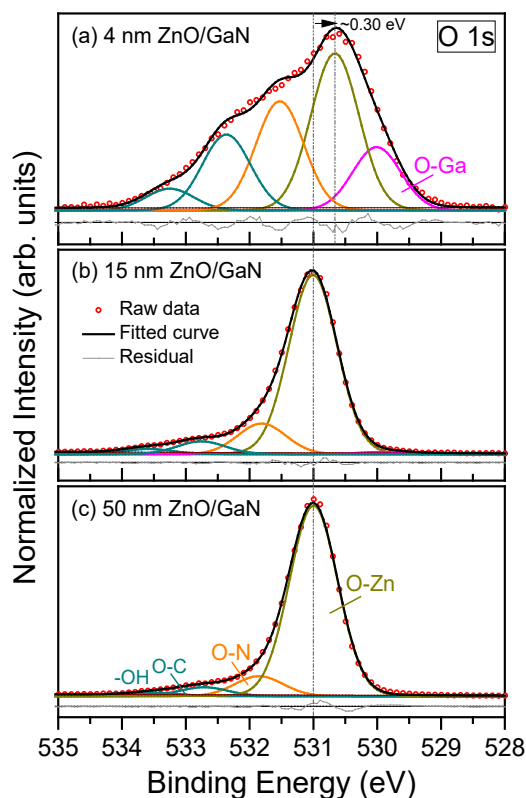


Figure 7.5.5: O 1s core-level spectra for (a) 4 nm, (b) 15 nm and (c) 50 nm ZnO/GaN stacks on sapphire substrates. All spectra are collected at the excitation energy of 6 keV. The spectra



have been fitted by Voigt (mixed Lorentzian-Gaussian) profiles with a linear background subtraction.

Fig. 7.5.5 shows O 1s core-level spectra for 4, 15 and 50 nm ZnO/GaN stacks on sapphire substrates measured with the excitation energy of 6 keV. For 50 nm ZnO/GaN stack [Fig. 7.5.5 (c)], the spectrum exhibits a prominent peak at  $(531.00 \pm 0.05)$  eV and a weak peak at  $(531.85 \pm 0.05)$  eV, together with two high binding energy peaks at  $(531.98 \pm 0.05)$  and  $(533.00 \pm 0.05)$  eV. These binding energy peaks are attributed to O-Zn bonds [177, 178], O-N bonds, -CO and -OH groups [178], respectively. In terms of 4 nm ZnO/GaN stack [Fig. 7.5.5 (a)], a well-resolved peak is observed at a low binding energy of  $(530.00 \pm 0.05)$  eV, which is assigned to O-Ga bonds [163], as well but rather weak for 15 nm ZnO/GaN stack [Fig. 7.5.5 (b)]. A shift by  $\sim 0.30$  eV towards lower binding energy is observed in the spectrum of 4 nm ZnO/GaN stack compared to that of 15 nm ZnO/GaN stack, mostly attributed to the presence of prominent O-Ga bonds.

### *Ga 3d & Zn 3d Spectra*

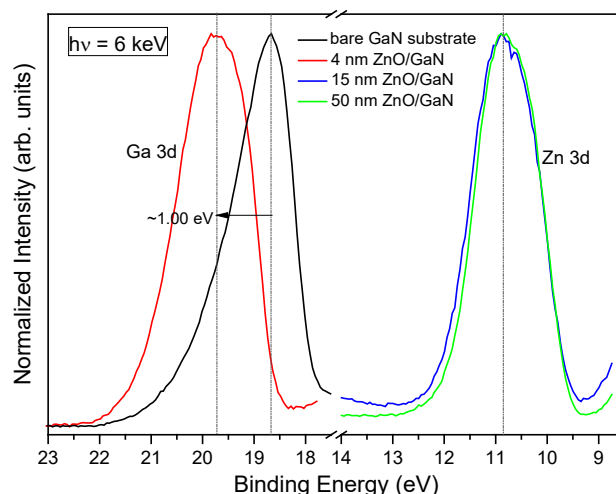


Figure 7.5.6: HAXPES spectra of Ga 3d and Zn 3d core levels for 4, 15 and 50 nm ZnO/GaN stacks on sapphire substrates together with bare GaN substrate. All spectra are collected at the excitation energy of 6 keV.

To further clarify the interfacial chemical changes between ZnO and GaN layers, the HAXPES analysis for the Ga 3d and Zn 3d core levels at the ZnO/GaN stacks are also carried out. As shown in Fig. 7.5.6, the Ga 3d peak for bare GaN substrate exhibits a slightly asymmetric main line, attributed to the different carrier concentrations between p+GaN (10 nm) and p-GaN (1  $\mu$ m) layers on the p-type GaN (0001) substrate. While a high binding energy feature located at  $(19.97 \pm 0.05)$  eV appears in the spectrum of 4 nm ZnO/GaN stack, corresponding to Ga-O bonds

[179], consistent with observations in the Ga 2p spectra [Fig. 7.5.2 (a)]. A shift of  $\sim 1.00$  eV towards higher binding energy is observed in the spectrum of 4 nm ZnO/GaN stack compared to bare GaN substrate. This could be attributed to the potential diffusion of Ga atoms into the ZnO layer during deposition, as described previously. Taking a careful check into the Zn 3d peak, one can note that the spectrum of 50 nm ZnO/GaN stack shows a highly symmetric peak at  $(10.9 \pm 0.05)$  eV, typically attributed to Zn-O bonds [177, 178]. However, a visible broadening in lineshape is present on the high binding energy side of the main peak in the spectrum of 15 nm ZnO/GaN stack, most likely due to the presence of Zn-N bonds.

### 7.5.3 Valence-band Structure

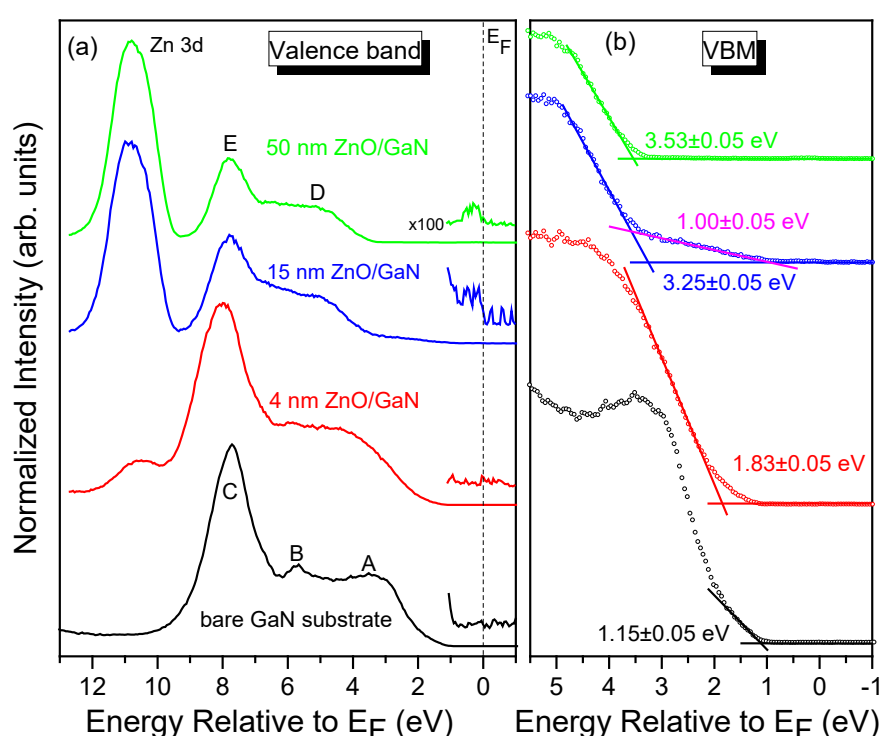


Figure 7.5.7: (a) HAXPES spectra of 4, 15 and 50 nm ZnO/GaN stacks on sapphire substrates in the region of the Zn 3d doublet and the valence band, together with bare GaN substrate. (b) Positions of valence-band maximum (VBM) relative to the Fermi level derived by a linear extrapolation of the band edge to the background.

The valence-band (VB) spectra for 4, 15 and 50 nm ZnO/GaN stacks on sapphire substrates together with the bare GaN substrate are shown in Fig. 7.5.7. All main features of VB spectra are indicated in the figure. As seen in Fig. 7.5.7 (a), the VB spectrum of bare GaN substrate exhibits three characteristic features: the low-energy feature (A) at around 5.0 eV and the high-

energy feature (C) at around 8.9 eV are related to Ga 4p-N 2p and Ga 4s-N 2p hybridization derived states, respectively, and the mid-energy feature (B) at around 6.7 eV may be related to the mixing of N 2p, Ga 4p, and Ga 4s derived states [180, 181]. This spectral structure is very similar to those observed for the N-polar surface of GaN [181]. The crystalline polarity of GaN has been previously confirmed by the HAXPES spectral shape in the VB region; the photoelectron intensity of feature “A” (about 5 eV relative to the Fermi level) is enhanced for the cation-polar (Ga) face compared to the anion-polar (N) face. Such a phenomenon has been reported for determining the polarity of a wurtzite crystal such as ZnO [182] and InN [183]. Similarly, the VB spectrum of 50 nm ZnO/GaN stack supports an O-polar ZnO. This also provides a great possibility for the N diffusion from GaN into ZnO, as well for the formation of Ga-O bonds. For 50 nm ZnO/GaN stack, the VB region consists of two main peaks: the well-defined peak at around 7.8 eV can be attributed to “mixed Zn 3d, 4s-O 2p derived states” (E); the weak peak at around 4.9 eV may be related to “Zn 3d-O 2p hybridization derived states” (D) [184]. Another prominent peak at the binding energy of 10.8 eV is seen, which is attributed to fully occupied Zn 3d derived states. The 15 nm ZnO/GaN stack shows a similar VB spectrum to 50 nm ZnO/GaN stack, having a strong Zn d-character (D, E). While the spectrum of 4 nm ZnO/GaN stack exhibits VB features of both: 50 nm ZnO/GaN stack and bare GaN substrate. It is worth noticing that a weak gap structure around the Fermi level is observed in the VB spectra of 15 and 50 nm ZnO/GaN stacks, as well but relatively weak for 4 nm ZnO/GaN stack. It is not surprising, as this feature is indicative of occupied gap states forming inside the band gap, generally seen for high degenerately doped semiconductors.

The position of valence-band maximum (VBM) relative to the Fermi level has been deduced by linearly extrapolating the VB edge to the background, as indicated in Fig. 7.5.7 (b). The VB spectrum of the bare GaN substrate gives a VBM of  $(1.15 \pm 0.05)$  eV. A VBM value of  $(3.53 \pm 0.05)$  eV is obtained for 50 nm ZnO/GaN stack. The optical-band gaps of GaN and ZnO have been reported to be 3.39 [52] and 3.37 eV [136] at room temperature, respectively. This means that the bare GaN substrate has a large p-type character, while a highly degenerate n-type character is suggested to 50 nm ZnO. In this case, the Fermi level in 50 nm ZnO is located slightly above the conduction-band edge, thereby giving rise to an occupied conduction-band state observed in Fig. 7.5.7 (a). Note that a marked emission around 2 eV is present in the spectrum of 15 nm ZnO/GaN stack. This feature gives a secondary VBM value of  $(1.00 \pm 0.05)$  eV, being very close to the reported optical-band gap of  $(1.23 \pm 0.02)$  eV for  $Zn_3N_2$  [177]. It further indicates that the N diffuses largely into ZnO and forms Zn-N bonds.

### 7.5.4 Interface Band Offsets

As mentioned in Sect. 7.3.4, the valence-band offset VBO ( $\Delta E_V$ ) and the conduction band offset CBO ( $\Delta E_C$ ) at the ZnO/GaN interface can be estimated according to Kraut's method [55],

$$\Delta E_V = \Delta E_{CL} + [E_{Ga\ 2p} - E_{VBM}]^{GaN} - [E_{Zn\ 2p} - E_{VBM}]^{ZnO}, \quad (7-10)$$

$$\Delta E_C = (E_g^{ZnO} - E_g^{GaN}) - \Delta E_V, \quad (7-11)$$

In this work, 50 nm ZnO/GaN stack can be treated as a bare ZnO substrate for the band offset calculations. For clarity, Table 7.4 summarizes the corresponding binding energy of the Ga 2p<sub>3/2</sub> and Zn 2p<sub>3/2</sub> peaks measured at the excitation energy of 6 keV, together with the VBM values for each sample.

TABLE 7.4: Energy positions (eV) of the Ga 2p<sub>3/2</sub> and Zn 2p<sub>3/2</sub> photoelectron peaks and VBM energies (eV) for each sample. The data is collected with the excitation energy of 6 keV. All energies are referenced to the Fermi level with the experimental errors of  $\pm 0.05$  eV.

States	bare GaN substrate	50 nm ZnO/GaN	15 nm ZnO/GaN	4 nm ZnO/GaN
Ga 2p <sub>3/2</sub>	1116.32	-	1115.89	1115.99
Zn 2p <sub>3/2</sub>	-	1022.04	1022.08	1021.44
VBM	1.15	3.53	3.25	1.83
$E_{CL} - E_{VBM}$	1115.17	1018.51	-	-
$\Delta E_{CL}$	-	-	-93.81	-94.55

By substituting the results given in Table 7.4 into Eqs. (7-10) and (7-11), an average value of the VBO ( $\Delta E_V$ ) and the corresponding CBO ( $\Delta E_C$ ) are determined to be (2.48 $\pm$ 0.10) and (-2.50 $\pm$ 0.10) eV for the ZnO/GaN heterostructure, respectively. A relatively large band offset ( $\Delta E_V$  in the range 1.0-2.2 eV) [185, 186] has also been previously reported for the (p-type) GaN/(n-type) ZnO heterointerface. This indicates there has a type-II band alignment at the ZnO/GaN heterointerface.

## 7.6 Interface Energy-level Alignment

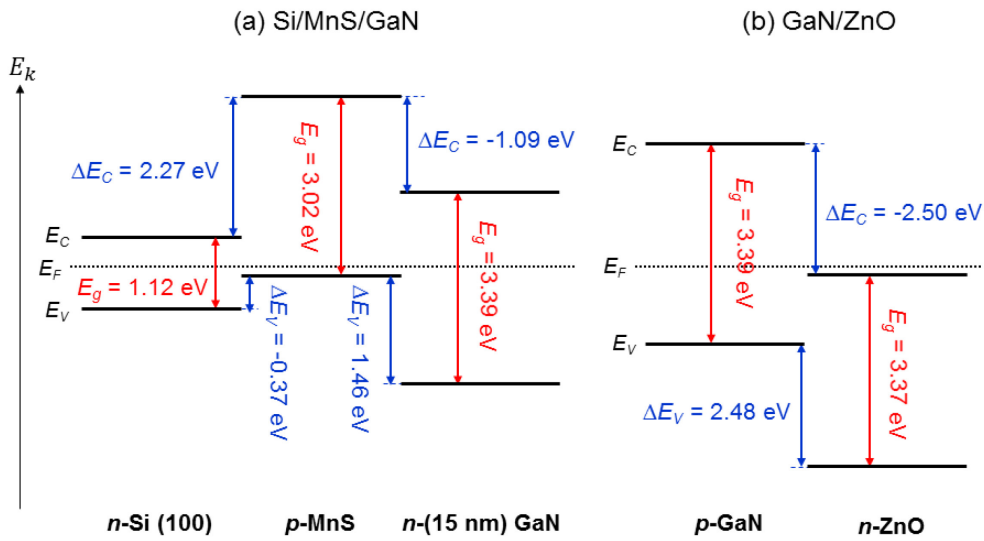


Figure. 7.6.1 Energy-level alignment at the respective ZnO/GaN/MnS/Si interfaces: (a) Si/MnS/GaN system [n-type Si (100) wafer/p-type (50 nm) MnS/n-type (15 nm) GaN] and (b) GaN/ZnO system [p-type bare GaN substrate/n-type (50 nm) ZnO] constructed from the average values of valence- ( $\Delta E_V$ ) and conduction-band offsets ( $\Delta E_C$ ) obtained from Kraut's method [55].  $E_C$ ,  $E_V$ , and  $E_F$  represent the conduction-band minimum (CBM), the valence-band maximum (VBM), and the Fermi level.

As mentioned previously, the knowledge of the energy-level alignment is of vital importance for the advancement of the heterostructure, allowing for the tuning of the electronic transport properties across the heterointerface. Fig. 7.6.1 summarizes our results on the energy-level alignment at the respective ZnO/GaN/MnS/Si heterointerfaces, including the respective band gaps and the average values for the conduction- and valence-band offsets. The values of valence- ( $\Delta E_V$ ) and conduction-band offsets ( $\Delta E_C$ ) obtained by Kraut's method [55] are employed in this work. In Fig. 7.6.1 (a), the MnS/Si heterointerface yields a quite low  $\Delta E_V$  of  $(-0.37 \pm 0.10)$  eV and a large  $\Delta E_C$  of  $(2.27 \pm 0.10)$  eV. In this situation, the holes accumulated at MnS layer can easily tunnel into n-type Si (100) wafer, but a high potential barrier would exist between MnS and Si (100) wafer. It has to be noted that the energy difference ( $\sim 0.75$  eV) between the VBM of p-type MnS and the CBM of the n-type Si is much less than the calculated  $\Delta E_C$  at the MnS/Si interface. Thus, it can produce some certain recombination through the interface. The GaN/MnS interface shows a  $\Delta E_V$  of  $(1.46 \pm 0.10)$  eV and the corresponding  $\Delta E_C$  of  $(-1.09 \pm 0.10)$  eV, respectively. In Fig. 7.6.1 (b), the ZnO/GaN interface shows a  $\Delta E_V$  of  $(2.48 \pm 0.10)$  eV and the corresponding  $\Delta E_C$  of  $(-2.50 \pm 0.10)$  eV, respectively. The calculated

$\Delta E_V$  has a value quite similar to the  $\Delta E_C$ , indicating that the electrons in n-type ZnO and holes in p-type GaN have almost equal barriers. It results in a very small possibility for the realization of the emission of ZnO.

## 7.7 Conclusion

Thickness series of ZnO/GaN/MnS layers were grown on Si (100) wafer, of which the interface information, i.e., the interfacial chemistry and energy-level alignment, was examined using photoelectron spectroscopy. At the MnS/Si interface, an interface-induced band bending (IIBB) appears in Si when MnS is grown on Si (100) wafer, which of values are found to be  $(0.15 \pm 0.07)$  and  $(0.23 \pm 0.07)$  eV for 4 and 15 nm MnS/Si stacks, respectively. In addition, the MnS/Si heterointerface shows a type-II (staggered) band lineup with a VBO of  $(-0.37 \pm 0.10)$  eV and the corresponding CBO of  $(2.27 \pm 0.10)$  eV. A significant diffusion of Mn into GaN takes place during GaN deposition at the GaN/MnS interface. This gives rise to the potential formation of Mn-N bonds mainly in 2+ charge states, i.e.,  $\text{Mn}_3\text{N}_2$ , at the GaN/MnS stacks. In addition, an interface-induced band bending (IIBB) by  $\sim 0.30$  eV is observed in MnS. The GaN/MnS interface shows a type-II (staggered) band lineup with a VBO of  $(1.46 \pm 0.10)$  eV and the corresponding CBO of  $(-1.09 \pm 0.10)$  eV. It was found that a significant N diffusion from GaN into ZnO takes place, i.e., Zn-N bonds, when ZnO is grown on the GaN layer. In addition, an interfacial oxide ( $\text{GaO}_x$ ) layer was formed during ZnO deposited on GaN films. The energy-level alignment at the ZnO/GaN heterointerface shows a type-II (staggered) band lineup with a VBO of  $(2.48 \pm 0.10)$  eV and the corresponding CBO of  $(-2.50 \pm 0.10)$  eV, respectively.

## 8. Conclusion and Outlook

Films of intrinsic and n-type doped (by Sn or H)  $\text{In}_2\text{O}_3$  variants before and after annealing were examined by X-ray diffraction. It was found that the undoped  $\text{In}_2\text{O}_3$  shows a polycrystalline structure independent on annealing, while a structural transformation from the amorphous-to-crystalline phase occurs in  $\text{In}_2\text{O}_3\text{:H}$  during annealing. Hall measurements of these films indicate that  $\text{In}_2\text{O}_3\text{:H}$  has a significantly improved electron mobility after annealing, which is caused by an annealing-induced solid phase crystallization. Hard X-ray photoelectron spectroscopy (HAXPES) was employed to investigate the core-level and valence electronic as well as the chemical structures of the  $\text{In}_2\text{O}_3$  variants. For O 1s and In  $3d_{5/2}$  core levels, a fitting model using three Voigt profiles (i.e., two main peaks with different widths “narrow” and “wide” specifically assigned to  $\text{In}_2\text{O}_3$ , and the other high binding energy peak related to hydroxide) was used and found that the indium hydroxide dehydroxylation occurs in  $\text{In}_2\text{O}_3\text{:H}$  during annealing. These results are well responsible for the amorphous-to-crystalline transition and a high mobility in annealed  $\text{In}_2\text{O}_3\text{:H}$ . As for the valence-band spectra, it was found that an evident shift of  $E_{VBM}$  ( $\sim 0.85$  eV) towards higher binding energy is present in  $\text{In}_2\text{O}_3$  upon doping, which mirrors the shifts ( $\sim 1.00$  eV) in the O 1s and In  $3d_{5/2}$  core-level spectra. It is attributed to the shift of  $E_F$  towards the conduction band caused by the Burstein-Moss (BM) shift via doping. When measured at 2 and 8 keV photon energies, the spectra show different shifts in  $E_{VBM}$ , indicating a small upward surface band bending in  $\text{In}_2\text{O}_3\text{:H}$  and ITO. The  $\text{In}_2\text{O}_3\text{:H}$  shows a shift of  $\sim 0.10$  eV in  $E_{VBM}$  towards higher binding energy after annealing, most likely due to the changes in crystal structure. A well-defined feature around the Fermi level is seen in doped  $\text{In}_2\text{O}_3$ , but very weak for undoped  $\text{In}_2\text{O}_3$ . It could either be attributed to occupied conduction-band states or occupied defect states or their both. A significant decrease in the intensity of occupied gap states is present in  $\text{In}_2\text{O}_3\text{:H}$  after annealing, possibly due to a decrease in carrier concentration. A surface depletion layer is present within the films, which could be deeper in undoped  $\text{In}_2\text{O}_3$  than the doped  $\text{In}_2\text{O}_3$  due to the different film thicknesses. Compared the HAXPES to XES & XAS measurements, a different coupling of O 2p-In 4d derived states is observed in annealed  $\text{In}_2\text{O}_3\text{:H}$ . Combining ellipsometry and photoelectron spectroscopy, the energy-level positions in relation to the gap disparity between the optical- and fundamental-band gaps upon doping is investigated before and after annealing. Doped  $\text{In}_2\text{O}_3$  variants have been found to have a quite deeper allowed transition level below the valence-band edge than undoped  $\text{In}_2\text{O}_3$ , which is suggested to be caused by the Burstein-Moss (BM) shift and the band-gap renormalization (BGR) effect via doping. This in particular applies to crystallized  $\text{In}_2\text{O}_3\text{:H}$ ,

most likely attributed to a change of the crystal structure upon annealing and/or a different O 2p-In 4d coupling near the VBM compared to amorphous In<sub>2</sub>O<sub>3</sub>:H.

SEM studies of the surface morphology of Ag/In<sub>2</sub>O<sub>3</sub>:H upon annealing indicates an annealing-induced modification of the Ag-topography (i.e., cluster formation). Ag/In<sub>2</sub>O<sub>3</sub>:H interface upon annealing is in-situ monitored by HAXPES, and it was found the overall Ag 3d intensity decreases with In 3d intensity increasing upon annealing. This suggests that the potential Ag diffusion into the bulk In<sub>2</sub>O<sub>3</sub>:H and/or a change of an annealing-induced Ag topography (i.e., cluster formation) occurs during annealing. A clear line broadening at high binding energy side of the Ag 3d spectra was observed upon annealing, which is due to Ag oxidation (i.e., Ag<sub>2</sub>O and AgO). With Ag deposition, it was found an initial downward band bending of (0.11±0.05) eV in In<sub>2</sub>O<sub>3</sub>:H, while the downward band bending reduces gradually upon annealing. This is attributed to a Schottky contact formed at the Ag/In<sub>2</sub>O<sub>3</sub>:H interface, but decreasing during annealing. In addition, a decrease in the density of states (DOS) around the Fermi edge is observed upon annealing, as well for the work function difference between bare In<sub>2</sub>O<sub>3</sub>:H and the Ag/In<sub>2</sub>O<sub>3</sub>:H samples. According to that, it can be inferred that the Schottky-barrier height at the Ag/In<sub>2</sub>O<sub>3</sub>:H interface also decreases during annealing, most likely attributed to the potential Ag diffusion into the bulk In<sub>2</sub>O<sub>3</sub>:H and/or an annealing-induced change of Ag topography (i.e., cluster formation) with a small Ag oxidation (i.e., Ag<sub>2</sub>O and AgO).

The MnS/Si interface shows an interface-induced band bending (IIBB) in Si, i.e., (0.15±0.07) and (0.23±0.07) eV for 4 and 15 nm MnS/Si stacks, respectively. A significant diffusion of Mn into the GaN layer takes place during GaN deposition, along with an interface-induced band bending (IIBB) by ~0.30 eV in MnS. A significant N diffusion from GaN into ZnO takes place, i.e., Zn-N bonds, when ZnO is grown on the GaN layer. In addition, an interfacial oxide (GaO<sub>x</sub>) layer was observed during ZnO deposited on GaN films. According to Kraut's method, a type-II (staggered) band lineup with a VBO of (-0.37±0.10) eV and the corresponding CBO of (2.27±0.10) eV is present at the MnS/Si interface. The quite low VBO ( $\Delta E_V$ ) would allow the holes accumulated at MnS layer easily to tunnel into n-type Si (100) wafer. However, the large CBO ( $\Delta E_C$ ) means a high potential barrier existing between MnS and Si (100) wafer. Even this, some certain recombination through the interface could occur due to a small energy difference (~0.75 eV) between the VBM of p-type MnS and the CBM of the n-type Si. The GaN/MnS interface shows a type-II (staggered) band lineup with a VBO of (1.46±0.10) eV and the corresponding CBO of (-1.09±0.10) eV. In addition, the ZnO/GaN heterointerface shows a type-II (staggered) band lineup with a VBO of (2.48±0.10) eV and the corresponding CBO of



( $-2.50 \pm 0.10$ ) eV. The quite similar values of the calculated  $\Delta E_V$  and  $\Delta E_C$  indicate that the almost equal barriers for the electrons in n-type ZnO and holes in p-type GaN to tunnel, thereby resulting in a very small possibility for the realization of the emission of ZnO. Knowing the band alignment of the respective ZnO/GaN/MnS/Si heterointerfaces facilitates the design of the GaN-based heterostructure devices. These findings will help to further optimize the GaN-based LED structures.



## Appendix A: Descriptions of ellipsometric analysis on $\text{In}_2\text{O}_3$ variants.

For undoped  $\text{In}_2\text{O}_3$  samples, a two-layer approach with additional surface roughness had to be implemented. In this case, two Tauc-Lorentz oscillators were sufficient to achieve excellent fits, which keeps the number of free parameters at bay. Only the upper layer was used for further evaluation. In this regard, the fitted spectra of undoped  $\text{In}_2\text{O}_3$  on the glass before annealing and  $\text{In}_2\text{O}_3\text{:H}$  on the  $c\text{-Si}$  wafer after annealing are shown in Fig. A.1 as examples.

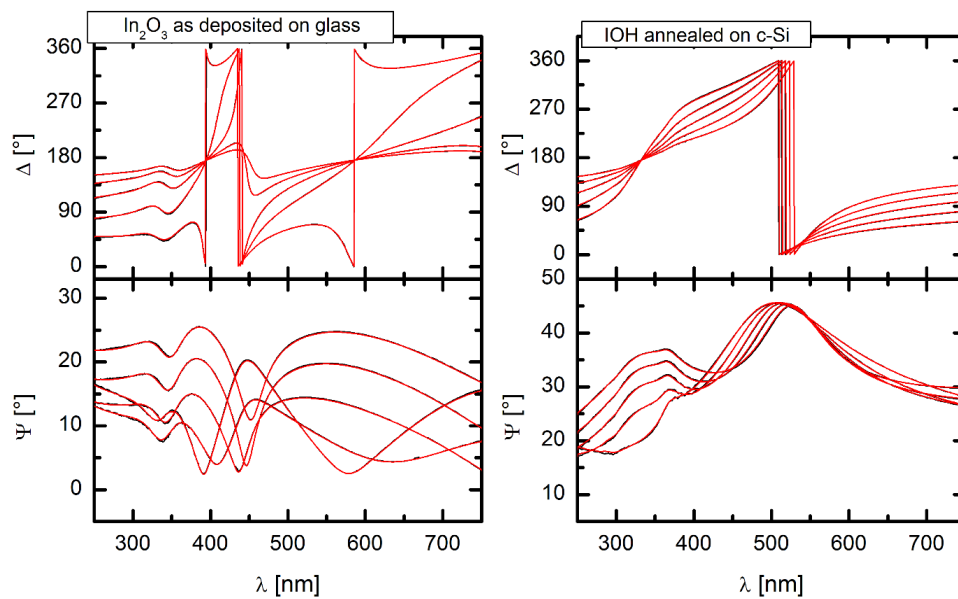


Figure A.1: Examples of fitted spectra for undoped  $\text{In}_2\text{O}_3$  on the glass before annealing (*left*) and  $\text{In}_2\text{O}_3\text{:H}$  on the  $c\text{-Si}$  wafer after annealing (*right*). In both cases, measured data is shown in black superimposed by the fit in red.

From the obtained fits the dielectric function of the film could be compiled. Using different models fits, it seems clear that a correct description of the measured data requires some form of sub-bandgap absorption describing absorption tails, an absorption onset with different slopes for different samples and an additional term for a correct description of the high energy part of the spectrum. This is shown in Fig. A.2.

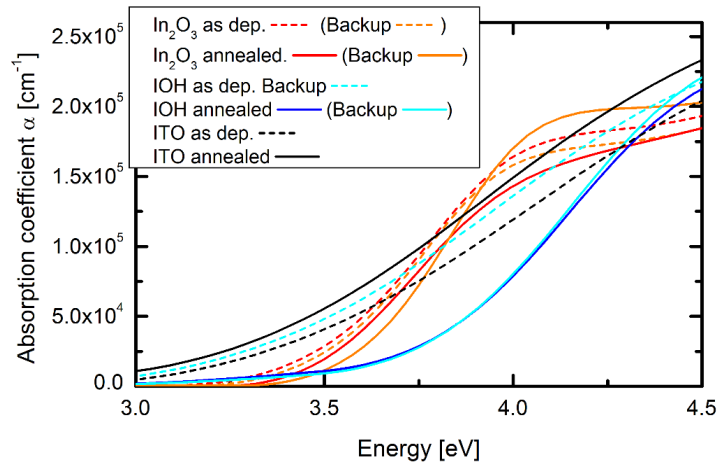


Figure A.2: Absorption coefficient determined by ellipsometry for all analyzed samples, including backup samples. Only the annealed backup sample of  $\text{In}_2\text{O}_3$  shows considerable deviations between original and backup sample.

Following the simple evaluation schemes proposed in [65], we determined the optical bandgap  $E_g$  (denoted  $W+\Delta E_g^{BM}$  in reference [65]) by locating the maximum of  $d\alpha/dE$ , where  $\alpha$  denotes the absorption coefficient and  $E$  is the photon energy, by fitting a Gaussian to the derivative, as shown in Fig. A.3. For comparison, we also extrapolated  $\alpha^2$  over  $E$  towards zero in order to facilitate comparison to other publications.

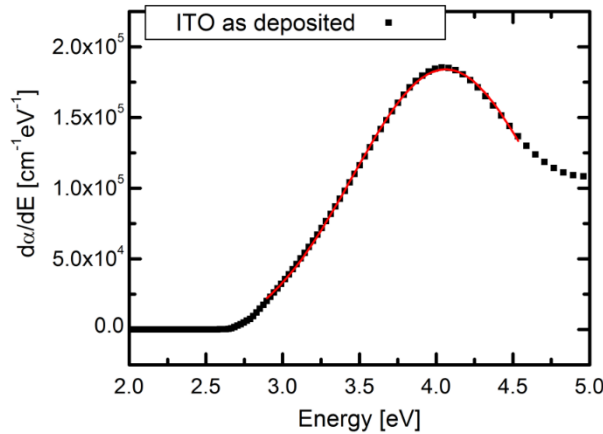


Figure A.3: Example for the bandgap determination using the derivative of the absorption coefficient  $\alpha$ .

The main source for uncertainties in the determined dielectric function is probably a possible growth-related vertical inhomogeneity. The effect on the finally determined bandgap is hard to estimate, but the general trend will be preserved.

## Bibliography

- [1] Hagiwara Y, Nakada T, Kunioka A. Improved Jsc in CIGS thin film solar cells using a transparent conducting ZnO:B window layer. *Solar Energy Materials and Solar Cells*. 2001; 67(1-4):267-71.
- [2] Pern F, Glick S, Li X, DeHart C, Gennett T, Contreras M, et al., editors. Stability of TCO window layers for thin-film CIGS solar cells upon damp heat exposures: part III. Reliability of Photovoltaic Cells, Modules, Components, and Systems II; 2009: International Society for Optics and Photonics.
- [3] Champness C, Xu Z. Effect of CdO interlayer on electrical characteristics in SeBi diodes. *Applied surface science*. 1998;123:485-9.
- [4] Burstein E. Anomalous optical absorption limit in InSb. *Physical Review*. 1954; 93(3):632.
- [5] Moss T. The interpretation of the properties of indium antimonide. *Proceedings of the Physical Society Section B*. 1954; 67(10):775.
- [6] Koida T, Kondo M, Tsutsumi K, Sakaguchi A, Suzuki M, Fujiwara H. Hydrogen-doped In<sub>2</sub>O<sub>3</sub> transparent conducting oxide films prepared by solid-phase crystallization method. *Journal of Applied Physics*. 2010; 107(3):033514.
- [7] Nakamura S, Mukai T, Senoh M. High-power GaN pn junction blue-light-emitting diodes. *Japanese Journal of Applied Physics*. 1991; 30(12A):L1998.
- [8] Sohn S, Han YS. Transparent conductive oxide (TCO) films for organic light emissive devices (OLEDs): InTech; 2011.
- [9] Chen H, Qiu C, Wong M, Kwok HS. DC sputtered indium-tin-oxide transparent cathode for organic light-emitting diode. *IEEE Electron Device Letters*. 2003; 24(5):315-7.
- [10] Jung YU, Park K-W, Hur S-T, Choi S-W, Kang SJ. High-transmittance liquid-crystal displays using graphene conducting layers. *Liquid Crystals*. 2014; 41(1):101-5.
- [11] Chopra K, Major S, Pandya D. Transparent conductors-a status review. *Thin solid films*. 1983; 102(1):1-46.
- [12] Dawar A, Joshi J. Semiconducting transparent thin films: their properties and applications. *Journal of Materials Science*. 1984; 19(1):1-23.
- [13] Stadler A. Transparent conducting oxides-an up-to-date overview. *Materials*. 2012; 5(4):661-83.

- [14] Kanai Y. Electrical properties of indium-tin-oxide single crystals. *Japanese Journal of Applied Physics*. 1984; 23(1A):L12.
- [15] Koida T, Fujiwara H, Kondo M. Hydrogen-doped  $\text{In}_2\text{O}_3$  as high-mobility transparent conductive oxide. *Japanese Journal of Applied Physics*. 2007; 46(7L):L685.
- [16] Hamberg I, Granqvist CG. Evaporated Sn-doped  $\text{In}_2\text{O}_3$  films: Basic optical properties and applications to energy-efficient windows. *Journal of Applied Physics*. 1986; 60(11):R123-R60.
- [17] Manificier J, Szepessy L. Efficient sprayed  $\text{In}_2\text{O}_3$ :Sn n-type silicon heterojunction solar cell. *Applied Physics Letters*. 1977; 31(7):459-62.
- [18] Granqvist CG, Hultåker A. Transparent and conducting ITO films: new developments and applications. *Thin solid films*. 2002; 411(1):1-5.
- [19] Zhang K, Lazarov V, Galindo P, Oropeza F, Payne D, Lai H-C, et al. Domain matching epitaxial growth of  $\text{In}_2\text{O}_3$  thin films on  $\alpha\text{-Al}_2\text{O}_3$  (0001). *Crystal Growth & Design*. 2012; 12(2):1000-7.
- [20] Tang L-M, Wang L-L, Wang D, Liu J-Z, Chen K-Q. Donor-donor binding in  $\text{In}_2\text{O}_3$ : Engineering shallow donor levels. *Journal of Applied Physics*. 2010; 107(8):083704.
- [21] Peng H, Li J, Li S-S, Xia J-B. First-principles study of the electronic structures and magnetic properties of 3d transition metal-doped anatase  $\text{TiO}_2$ . *Journal of Physics: Condensed Matter*. 2008; 20(12):125207.
- [22] Sabino FP, Besse R, Oliveira LN, Wei S-H, Da Silva JL. Origin of and tuning the optical and fundamental band gaps in transparent conducting oxides: The case of  $\text{M}_2\text{O}_3$  (M = Al, Ga, In). *Physical Review B*. 2015; 92(20):205308.
- [23] Sabino FP, de Oliveira LN, Da Silva JL. Role of atomic radius and d-states hybridization in the stability of the crystal structure of  $\text{M}_2\text{O}_3$  (M = Al, Ga, In) oxides. *Physical Review B*. 2014; 90(15):155206.
- [24] Weiher R, Ley R. Optical properties of indium oxide. *Journal of Applied Physics*. 1966; 37(1):299-302.
- [25] Ágoston P, Albe K, Nieminen RM, Puska MJ. Intrinsic n-type behavior in transparent conducting oxides: a comparative hybrid-functional study of  $\text{In}_2\text{O}_3$ ,  $\text{SnO}_2$ , and  $\text{ZnO}$ . *Physical review letters*. 2009; 103(24):245501.

- [26] Wager J, Mason T, Berry J, Poeppelmeier K, Ginley D, Perkins J, et al. Surface Origin of High Conductivities in Undoped In<sub>2</sub>O<sub>3</sub> Thin Films. 2012.
- [27] Agoston P. Point defect and surface properties of In<sub>2</sub>O<sub>3</sub> and SnO<sub>2</sub>: A comparative study by first-principles methods: Technische Universität; 2011.
- [28] Tomita T, Yamashita K, Hayafuji Y, Adachi H. The origin of n-type conductivity in undoped In<sub>2</sub>O<sub>3</sub>. Applied Physics Letters. 2005; 87(5):051911.
- [29] Pavesi L, Giannozzi P. Atomic and molecular hydrogen in gallium arsenide: A theoretical study. Physical Review B. 1992; 46(8):4621.
- [30] McCluskey M, Jokela S. Sources of n-type conductivity in ZnO. Physica B: Condensed Matter. 2007; 401:355-7.
- [31] Singh AK, Janotti A, Scheffler M, Van de Walle CG. Sources of electrical conductivity in SnO<sub>2</sub>. Physical Review Letters. 2008; 101(5):055502.
- [32] Limpijumnong S, Reunchan P, Janotti A, Van de Walle CG. Hydrogen doping in indium oxide: An ab initio study. Physical Review B. 2009; 80(19):193202.
- [33] King P, Lichti R, Celebi Y, Gil J, Vilão R, Alberto H, et al. Shallow donor state of hydrogen in In<sub>2</sub>O<sub>3</sub> and SnO<sub>2</sub>: Implications for conductivity in transparent conducting oxides. Physical Review B. 2009; 80(8):081201.
- [34] Köstlin H, Jost R, Lems W. Optical and electrical properties of doped In<sub>2</sub>O<sub>3</sub> films. physica status solidi (a). 1975; 29(1):87-93.
- [35] LM T, KQ C. Donor-donor binding in In<sub>2</sub>O<sub>3</sub>: Engineering shallow donor levels. 2010.
- [36] Rupprecht G. Untersuchungen der elektrischen und lichtelektrischen Leitfähigkeit dünner Indiumoxydschichten. Zeitschrift für Physik. 1954; 139(5):504-17.
- [37] Christou V, Etechells M, Renault O, Dobson P, Salata O, Beamson G, et al. High resolution x-ray photoemission study of plasma oxidation of indium-tin-oxide thin film surfaces. Journal of Applied Physics. 2000; 88(9):5180-7.
- [38] Jaffe J, Pandey R, Kunz A. Electronic structure of the rocksalt-structure semiconductors ZnO and CdO. Physical Review B. 1991; 43(17):14030.
- [39] Erhart P, Klein A, Egdell RG, Albe K. Band structure of indium oxide: Indirect versus direct band gap. Physical review B. 2007; 75(15):153205.

- [40] Walsh A, Da Silva JL, Wei S-H, Körber C, Klein A, Piper L, et al. Nature of the band gap of In<sub>2</sub>O<sub>3</sub> revealed by first-principles calculations and X-ray spectroscopy. *Physical Review Letters*. 2008; 100(16):167402.
- [41] Schmid P. Optical absorption in heavily doped silicon. *Physical Review B*. 1981; 23(10):5531.
- [42] Lu J, Fujita S, Kawaharamura T, Nishinaka H, Kamada Y, Ohshima T, et al. Carrier concentration dependence of band gap shift in n-type ZnO: Al films. *Journal of Applied Physics*. 2007; 101(8):083705.
- [43] Minami T. Transparent conducting oxide semiconductors for transparent electrodes. *Semiconductor science and technology*. 2005; 20(4):S35.
- [44] Fortunato E, Barquinha P, Martins R. Oxide semiconductor thin-film transistors: a review of recent advances. *Advanced materials*. 2012; 24(22):2945-86.
- [45] Nayak PK, Hedhili MN, Cha D, Alshareef HN. High performance In<sub>2</sub>O<sub>3</sub> thin film transistors using chemically derived aluminum oxide dielectric. *Applied Physics Letters*. 2013; 103(3):033518.
- [46] Braun F. Ueber die Stromleitung durch Schwefelmetalle. *Annalen der Physik*. 1875; 229(12):556-63.
- [47] Schottky W. Small-shot effect and flicker effect. *Physical Review*. 1926; 28(1):74.
- [48] Schroder DK. *Semiconductor material and device characterization*: John Wiley & Sons; 2006.
- [49] Schubert EF. *Light-emitting diodes*: E. Fred Schubert; 2018.
- [50] Shangsheng W. Progress in the Study of High Brightness Blue GaN-based LEDs. *Chinese Journal of Quantum Electronics*. 2003; 20(1):10-7.
- [51] Xiao-bai L. GaN-based electronic and photoelectric devices J. *Functional Materials and Devices*. 2000; 3:021.
- [52] Ejder E. Refractive index of GaN. *physica status solidi (a)*. 1971; 6(2):445-8.
- [53] [http://en.wikipedia.org/wiki/Light-emitting\\_diode](http://en.wikipedia.org/wiki/Light-emitting_diode).
- [54] Shockley W. *Electrons and holes in semiconductors: with applications to transistor electronics*: van Nostrand New York; 1950.



- [55] Waldrop J, Grant R, Kraut E. Measurement of GaAs/InP and InAs/InP heterojunction band offsets by X-ray photoemission spectroscopy. *Applied physics letters*. 1989; 54(19):1878-80.
- [56] Sze SM, Ng KK. *Physics of semiconductor devices*: John wiley & sons; 2006.
- [57] Amano H, Sawaki N, Akasaki I, Toyoda Y. Metalorganic vapor phase epitaxial growth of a high quality GaN film using an AlN buffer layer. *Applied Physics Letters*. 1986; 48(5):353-5.
- [58] Nahhas A, Kim HK, Blachere J. Epitaxial growth of ZnO films on Si substrates using an epitaxial GaN buffer. *Applied Physics Letters*. 2001; 78(11):1511-3.
- [59] Manasevit HM. Process for producing nitride films. Google Patents; 1975.
- [60] Lokhande C, Ennaoui A, Patil P, Giersig M, Muller M, Diesner K, et al. Process and characterization of chemical bath deposited manganese sulphide (MnS) thin films. *Thin Solid Films*. 1998; 330(2):70-5.
- [61] Bashar SA. Study of indium tin oxide (ITO) for novel optoelectronic devices. UMIST, Manchester. 1998:106-9.
- [62] Hughes W, Rowland Jr W, Johnson M, Fujita S, Cook Jr J, Schetzina J, et al. Molecular beam epitaxy growth and properties of GaN films on GaN/SiC substrates. *Journal of Vacuum Science & Technology B: Microelectronics and Nanometer Structures Processing, Measurement, and Phenomena*. 1995; 13(4):1571-7.
- [63] Lips K, Starr D, Bär M, Schulze T, Fenske F, Christiansen S, et al., editors. *EMIL: The energy materials in situ laboratory Berlin*. 2014 IEEE 40th Photovoltaic Specialist Conference (PVSC); 2014: IEEE.
- [64] Hüfner S. *Photoelectron spectroscopy: principles and applications*: Springer Science & Business Media; 2013.
- [65] Hamberg I, Granqvist CG, Berggren KF, Sernelius BE, Engstrom L. Band-Gap Widening in Heavily Sn-Doped In<sub>2</sub>O<sub>3</sub>. *Physical Review B*. 1984; 30(6):3240-9.
- [66] Schaefers F, Mertin M, Gorgoi M. KMC-1: A high resolution and high flux soft X-ray beamline at BESSY. *Review of Scientific Instruments*. 2007; 78(12):123102.
- [67] Ikenaga E, Kobata M, Matsuda H, Sugiyama T, Daimon H, Kobayashi K. Development of high lateral and wide angle-resolved hard X-ray photoemission spectroscopy at BL47XU in SPring-8. *Journal of Electron Spectroscopy and Related Phenomena*. 2013; 190:180-7.

- [68] Jia J, Callcott TA, Yurkas J, Ellis AW, Himpsel FJ, Samant MG, et al. First experimental results from IBM/TENN/TULANE/LLNL/LBL undulator beamline at the advanced light source. *Review of scientific instruments*. 1995; 66(2):1394-7.
- [69] Jellison Jr G. Data analysis for spectroscopic ellipsometry. *Thin Solid Films*. 1993; 234(1-2):416-22.
- [70] Ley RLWaRP. *Apply Phys Letter* 1980; 37(163).
- [71] Ma CAPaTP. *Journal Apply Phys* 1996; 37(299).
- [72] Matino F, Persano L, Arima V, Pisignano D, Blyth R, Cingolani R, et al. Electronic structure of indium-tin-oxide films fabricated by reactive electron-beam deposition. *Physical Review B*. 2005; 72(8):085437.
- [73] Scherg-Kurmes H, Körner S, Ring S, Klaus M, Korte L, Ruske F, et al. High mobility  $\text{In}_2\text{O}_3\text{:H}$  as contact layer for a-Si:H/c-Si heterojunction and  $\mu\text{-Si:H}$  thin film solar cells. *Thin Solid Films*. 2015; 594:316-22.
- [74] Tanuma S, Powell CJ, Penn DR. Calculations of electron inelastic mean free paths (IMFPs). IV. Evaluation of calculated IMFPs and of the predictive IMFP formula TPP-2 for electron energies between 50 and 2000 eV. *Surface and interface analysis*. 1993; 20(1):77-89.
- [75] Henke BL, Gullikson EM, Davis JC. X-ray interactions: photoabsorption, scattering, transmission and reflection  $E = 50\text{-}30,000$  eV,  $Z = 1\text{-}92$ . 1993.
- [76] Petrik P, Fodor B, Agócs E, Kozma P, Nádor J, Kumar N, et al., editors. *Methods for optical modeling and cross-checking in ellipsometry and scatterometry. Modeling Aspects in Optical Metrology V*; 2015: International Society for Optics and Photonics.
- [77] Koida T, Shibata H, Kondo M, Tsutsumi K, Sakaguchi A, Suzuki M, et al. Correlation between oxygen stoichiometry, structure, and opto-electrical properties in amorphous  $\text{In}_2\text{O}_3\text{:H}$  films. *Journal of Applied Physics*. 2012; 111(6):063721.
- [78] Song PK, Akao H, Kamei M, Shigesato Y, Yasui I. Preparation and crystallization of tin-doped and undoped amorphous indium oxide films deposited by sputtering. *Japanese journal of applied physics*. 1999; 38(9R):5224.
- [79] Morikawa H, Sumi H, Kohyama M. Crystal growth of ITO films prepared by DC magnetron sputtering on C film. *Thin Solid Films*. 1996; 281:202-5.

- [80] Ma R-R, Jiang F-X, Qin X-F, Xu X-H. Effects of oxygen vacancy and local spin on the ferromagnetic properties of Ni-doped  $\text{In}_2\text{O}_3$  powders. *Materials Chemistry and Physics*. 2012; 132(2-3):796-9.
- [81] Macco B, Knoops HC, Kessels WM. Electron scattering and doping mechanisms in solid-phase-crystallized  $\text{In}_2\text{O}_3\text{:H}$  prepared by atomic layer deposition. *ACS applied materials & interfaces*. 2015; 7(30):16723-9.
- [82] Wardenga HF, Frischbier MV, Morales-Masis M, Klein A. In situ hall effect monitoring of vacuum annealing of  $\text{In}_2\text{O}_3\text{:H}$  thin films. *Materials*. 2015; 8(2):561-74.
- [83] Bellingham J, Phillips W, Adkins C. Electrical and optical properties of amorphous indium oxide. *Journal of Physics: Condensed Matter*. 1990; 2(28):6207.
- [84] Yeh J, Lindau I. Atomic subshell photoionization cross sections and asymmetry parameters:  $1 \leq Z \leq 103$ . *Atomic data and nuclear data tables*. 1985; 32(1):1-155.
- [85] Scofield J. Lawrence Livermore National Laboratory. 1973; Report No. UCRL-51326.
- [86] Donley C, Dunphy D, Paine D, Carter C, Nebesny K, Lee P, et al. Characterization of Indium-Tin oxide interfaces using X-ray photoelectron spectroscopy and redox processes of a chemisorbed probe molecule: effect of surface pretreatment conditions. *Langmuir*. 2002; 18(2):450-7.
- [87] Nelson A, Aharoni H. X-ray photoelectron spectroscopy investigation of ion beam sputtered indium tin oxide films as a function of oxygen pressure during deposition. *Journal of Vacuum Science & Technology A: Vacuum, Surfaces, and Films*. 1987; 5(2):231-3.
- [88] Kim J, Ho P, Thomas D, Friend R, Cacialli F, Bao G-W, et al. X-ray photoelectron spectroscopy of surface-treated indium-tin oxide thin films. *Chemical Physics Letters*. 1999; 315(5-6):307-12.
- [89] Banerjee K, Ghosh S, Plis E, Krishna S. Study of short-and long-term effectiveness of ammonium sulfide as surface passivation for InAs/GaSb superlattices using X-ray photoelectron spectroscopy. *Journal of electronic materials*. 2010; 39(10):2210-4.
- [90] Fan JC, Goodenough JB. X-ray photoemission spectroscopy studies of Sn-doped indium-oxide films. *Journal of Applied Physics*. 1977; 48(8):3524-31.
- [91] Major S, Kumar S, Bhatnagar M, Chopra K. Effect of hydrogen plasma treatment on transparent conducting oxides. *Applied Physics Letters*. 1986; 49(7):394-6.

- [92] Kameswara Rao L, Vinni V. Novel mechanism for high speed growth of transparent and conducting tin oxide thin films by spray pyrolysis. *Applied physics letters*. 1993; 63(5):608-10.
- [93] De Carvalho CN, Do Rego AB, Amaral A, Brogueira P, Lavareda G. Effect of substrate temperature on the surface structure, composition and morphology of indium-tin oxide films. *Surface and coatings technology*. 2000; 124(1):70-5.
- [94] Zhang F, Li X, Zhao Q, Zhang Q, Tadé M, Liu S. Fabrication of  $\alpha$ -Fe<sub>2</sub>O<sub>3</sub>/In<sub>2</sub>O<sub>3</sub> composite hollow microspheres: A novel hybrid photocatalyst for toluene degradation under visible light. *Journal of colloid and interface science*. 2015; 457:18-26.
- [95] Sanjinés R, Rosenfeld D, Gozzo F, Alméras P, Perez L, Lévy F, et al. ESCA investigation of SnO<sub>x</sub> films used as gas sensors. *Surface and interface analysis*. 1994; 22(1-12):372-5.
- [96] Wang R, Beling C, Djurišić A, Li S, Fung S. Properties of ITO thin films deposited on amorphous and crystalline substrates with e-beam evaporation. *Semiconductor science and technology*. 2004; 19(6):695.
- [97] Kotani A, Toyozawa Y. Photoelectron spectra of core electrons in metals with an incomplete shell. *Journal of the Physical Society of Japan*. 1974; 37(4):912-9.
- [98] Chazalviel J-N, Campagna M, Wertheim G, Shanks H. Final-state effects in the X-ray photoelectron spectra of cubic sodium-tungsten bronzes. *Physical Review B*. 1977; 16(2):697.
- [99] Körber C, Krishnakumar V, Klein A, Panaccione G, Torelli P, Walsh A, et al. Electronic structure of In<sub>2</sub>O<sub>3</sub> and Sn-doped In<sub>2</sub>O<sub>3</sub> by hard X-ray photoemission spectroscopy. *Physical Review B*. 2010; 81(16):165207.
- [100] Egdell R, Rebane J, Walker T, Law D. Competition between initial-and final-state effects in valence-and core-level X-ray photoemission of Sb-doped SnO<sub>2</sub>. *Physical Review B*. 1999; 59(3):1792.
- [101] Langreth D. *Proceedings of Nobel Symposium 24 in Medicine and Natural Science*. Academic Press New York and London; 1973.
- [102] Warschkow O, Ellis DE, González GB, Mason TO. Defect Structures of Tin-Doped Indium Oxide. *Journal of the American Ceramic Society*. 2003; 86(10):1700-6.

- [103] Mott NF. Conduction in non-crystalline materials: III. Localized states in a pseudogap and near extremities of conduction and valence bands. *Philosophical Magazine*. 1969; 19(160):835-52.
- [104] Mott N. *Electronic processes in non-crystalline materials*. London, Oxford University Press; 1971.
- [105] Robertson J. Disorder and instability processes in amorphous conducting oxides. *physica status solidi (b)*. 2008; 245(6):1026-32.
- [106] Sallis S, Butler K, Quackenbush N, Williams D, Junda M, Fischer D, et al. Origin of deep subgap states in amorphous indium gallium zinc oxide: Chemically disordered coordination of oxygen. *Applied Physics Letters*. 2014; 104(23):232108.
- [107] Nahm HH, Kim YS, Kim DH. Instability of amorphous oxide semiconductors via carrier-mediated structural transition between disorder and peroxide state. *physica status solidi (b)*. 2012; 249(6):1277-81.
- [108] I. Hamberg CG, K. Berggren,. *Phys Rev B: Condensed Matter* 2009; 80(11).
- [109] Fujiwara H, Kondo M. Effects of carrier concentration on the dielectric function of ZnO:Ga and In<sub>2</sub>O<sub>3</sub>:Sn studied by spectroscopic ellipsometry: analysis of free-carrier and band-edge absorption. *Physical Review B*. 2005; 71(7):075109.
- [110] Rosén J, Warschkow O. Electronic structure of amorphous indium oxide transparent conductors. *Physical Review B*. 2009; 80(11):115215.
- [111] Feneberg M, Nixdorf J, Lidig C, Goldhahn R, Galazka Z, Bierwagen O, et al. Many-electron effects on the dielectric function of cubic In<sub>2</sub>O<sub>3</sub>: Effective electron mass, band nonparabolicity, band gap renormalization, and Burstein-Moss shift. *Physical Review B*. 2016; 93(4):045203.
- [112] Jain S, McGregor J, Roulston D. Band-gap narrowing in novel III-V semiconductors. *Journal of applied physics*. 1990; 68(7):3747-9.
- [113] Sans J, Sánchez-Royo J, Segura A, Tobias G, Canadell E. Chemical effects on the optical band-gap of heavily doped ZnO:M III (M = Al, Ga, In): an investigation by means of photoelectron spectroscopy, optical measurements under pressure, and band structure calculations. *Physical Review B*. 2009; 79(19):195105.
- [114] Jia J, Takasaki A, Oka N, Shigesato Y. Experimental observation on the Fermi level shift in polycrystalline Al-doped ZnO films. *Journal of Applied Physics*. 2012; 112(1):013718.

- [115] Hilfiker J. In situ spectroscopic ellipsometry (SE) for characterization of thin film growth. In *In Situ Characterization of Thin Film Growth*: Elsevier; 2011. p. 99-151.
- [116] Tauc J, Grigorovici R, Vancu A. Optical properties and electronic structure of amorphous germanium. *physica status solidi (b)*. 1966; 15(2):627-37.
- [117] von Wenckstern H, Splith D, Schmidt F, Grundmann M, Bierwagen O, Speck J. *APL Mater.* 2, 046104 (2014). CrossRef. Web of Science® Times Cited.7.
- [118] Nazarzadehmoafi M, Machulik S, Neske F, Scherer V, Janowitz C, Galazka Z, et al. Schottky contact by Ag on In<sub>2</sub>O<sub>3</sub> (111) single crystals. *Applied Physics Letters*. 2014; 105(16):162104.
- [119] Barraud L, Holman Z, Badel N, Reiss P, Descoedres A, Battaglia C, et al. Hydrogen-doped indium oxide/indium tin oxide bilayers for high-efficiency silicon heterojunction solar cells. *Solar Energy Materials and Solar Cells*. 2013; 115:151-6.
- [120] Ferraria AM, Carapeto AP, do Rego AMB. X-ray photoelectron spectroscopy: silver salts revisited. *Vacuum*. 2012; 86(12):1988-91.
- [121] Bao X, Muhler M, Schedel-Niedrig T, Schlögl R. Interaction of oxygen with silver at high temperature and atmospheric pressure: a spectroscopic and structural analysis of a strongly bound surface species. *Physical Review B*. 1996; 54(3):2249.
- [122] Kaushik VK. XPS core level spectra and Auger parameters for some silver compounds. *Journal of Electron Spectroscopy and Related Phenomena*. 1991; 56(3):273-7.
- [123] Kaspar TC, Droubay T, Chambers SA, Bagus PS. Spectroscopic evidence for Ag (III) in highly oxidized silver films by X-ray photoelectron spectroscopy. *The Journal of Physical Chemistry C*. 2010; 114(49):21562-71.
- [124] Hoflund GB, Hazos ZF, Salaita GN. Surface characterization study of Ag, AgO, and Ag<sub>2</sub>O using X-ray photoelectron spectroscopy and electron energy-loss spectroscopy. *Physical Review B*. 2000; 62(16):11126.
- [125] Chuang T, Brundle C, Rice D. Interpretation of the X-ray photoemission spectra of cobalt oxides and cobalt oxide surfaces. *Surface Science*. 1976; 59(2):413-29.
- [126] Bagus PS, Pacchioni G, Sousa C, Minerva T, Parmigiani F. Chemical shifts of the core-level binding energies for the alkaline-earth oxides. *Chemical physics letters*. 1992; 196(6):641-6.
- [127] McMillan J. Higher Oxidation States of Silver. *Chemical Reviews*. 1962; 62(1):65-80.

- [128] Kittel C, McEuen P, McEuen P. Introduction to solid state physics: Wiley New York; 1996.
- [129] Davies D. Waves, atoms and solids: Addison-Wesley Longman Ltd; 1978.
- [130] Scofield JH. Theoretical photoionization cross sections from 1 to 1500 keV. California Univ.; 1973.
- [131] Muhsien MA, Hamdan HH. Preparation and characterization of p-Ag<sub>2</sub>O/n-Si heterojunction devices produced by rapid thermal oxidation. Energy Procedia. 2012; 18:300-11.
- [132] Bhaskaran M, Iniewski K, Sriram S. Energy harvesting with functional materials and microsystems: CRC Press; 2013.
- [133] Lang O, Pettenkofer C, Sánchez-Royo JF, Segura A, Klein A, Jaegermann W. Thin film growth and band lineup of In<sub>2</sub>O<sub>3</sub> on the layered semiconductor InSe. Journal of applied physics. 1999; 86(10):5687-91.
- [134] Fender B, Jacobson A, Wedgwood F. Covalency Parameters in MnO,  $\alpha$ -MnS, and NiO. Journal of Chemical Physics. 1968; 48(3):990-4.
- [135] Ito T, Ito K, Oka M. Magnetic susceptibility, thermal expansion and electrical resistivity of MnSe. Japanese Journal of Applied Physics. 1978; 17(2):371.
- [136] Klingshirn C. The luminescence of ZnO under high one-and two-quantum excitation. physica status solidi (b). 1975; 71(2):547-56.
- [137] Özgür Ü, Alivov YI, Liu C, Teke A, Reshchikov M, Doğan S, et al. A comprehensive review of ZnO materials and devices. Journal of applied physics. 2005; 98(4):11.
- [138] Bhargava R. Properties of wide bandgap II-VI semiconductors: IET; 1997.
- [139] Choi Y-S, Kang J-W, Hwang D-K, Park S-J. Recent advances in ZnO-based light-emitting diodes. IEEE Transactions on electron devices. 2010; 57(1):26-41.
- [140] Wang ZL. Zinc oxide nanostructures: growth, properties and applications. Journal of physics: condensed matter. 2004; 16(25):R829.
- [141] Hong S, Ko H, Chen Y, Hanada T, Yao T. ZnO/GaN heterointerfaces and ZnO films grown by plasma-assisted molecular beam epitaxy on (0001) GaN/Al<sub>2</sub>O<sub>3</sub>. Journal of Vacuum Science & Technology B: Microelectronics and Nanometer Structures Processing, Measurement, and Phenomena. 2000; 18(4):2313-21.

- [142] You J, Zhang X, Zhang S, Wang J, Yin Z, Tan H, et al. Improved electroluminescence from n-ZnO/AlN/p-GaN heterojunction light-emitting diodes. *Applied Physics Letters*. 2010; 96(20):201102.
- [143] Takahashi K. <https://www.comet-nht.com/company-e.html>.
- [144] Choi YJ, Won S-J, Jung H-S, Park S, Cho D-Y, Hwang CS, et al. Effects of Oxygen Source on Film Properties of Atomic-Layer-Deposited La-Silicate Film Using La [N(SiMe<sub>3</sub>)<sub>2</sub>]<sub>3</sub>. *ECS Solid State Letters*. 2012; 1(1):N4-N6.
- [145] Wojdyr M. Fityk: peak fitting software. *J Appl Cryst*. 2010; 43:1126-8.
- [146] Nelson A, Reynolds JG, Roos JW. Core-level satellites and outer core-level multiplet splitting in Mn model compounds. *Journal of Vacuum Science & Technology A: Vacuum, Surfaces, and Films*. 2000; 18(4):1072-6.
- [147] Kim W-B, Matsumoto T, Kobayashi H. Ultrathin SiO<sub>2</sub> layer with a low leakage current density formed with ~100% nitric acid vapor. *Nanotechnology*. 2010; 21(11):115202.
- [148] Çopuroğlu M, Sezen H, Opila RL, Suzer S. Band-bending at buried SiO<sub>2</sub>/Si interface as probed by XPS. *ACS applied materials & interfaces*. 2013; 5(12):5875-81.
- [149] Weinberger B, Peterson G, Eschrich T, Krasinski H. Surface chemistry of HF passivated silicon: X-ray photoelectron and ion scattering spectroscopy results. *Journal of applied physics*. 1986; 60(9):3232-4.
- [150] Lai Y-H, Yeh C-T, Lin Y-H, Hung W-H. Adsorption and thermal decomposition of H<sub>2</sub>S on Si (100). *Surface science*. 2002; 519(1-2):150-6.
- [151] Yoo Y-Z, Song J-H, Konishi Y, Kawasaki M, Koinuma H, Chikyow T. Sulfide and Oxide Heterostructures For the SrTiO<sub>3</sub> Thin Film Growth on Si and Their Structural and Interfacial Stabilities. *Japanese journal of applied physics*. 2006; 45(3R):1788.
- [152] Fantauzzi M, Rigoldi A, Elsener B, Atzei D, Rossi A. A contribution to the surface characterization of alkali metal sulfates. *Journal of Electron Spectroscopy and Related Phenomena*. 2014; 193:6-15.
- [153] Kumbhar VS, Lee YR, Ra CS, Tuma D, Min B-K, Shim J-J. Modified chemical synthesis of MnS nanoclusters on nickel foam for high performance all-solid-state asymmetric supercapacitors. *RSC Advances*. 2017; 7(27):16348-59.
- [154] Finster J, Schulze D. Studies of the Si/SiO<sub>2</sub> interface by angular dependent X-ray photoelectron spectroscopy. *physica status solidi (a)*. 1981; 68(2):505-17.



- [155] Saitoh T, Bocquet A, Mizokawa T, Namatame H, Fujimori A, Abbate M, et al. Electronic structure of  $\text{La}_{1-x}\text{Sr}_x\text{MnO}_3$  studied by photoemission and X-ray-absorption spectroscopy. *Physical Review B*. 1995; 51(20):13942.
- [156] Zampieri G, Abbate M, Prado F, Caneiro A. Mn-2p XPS spectra of differently hole-doped Mn perovskites. *Solid state communications*. 2002; 123(1-2):81-5.
- [157] Hishida T, Ohbayashi K, Saitoh T. Hidden relationship between the electrical conductivity and the Mn 2p core-level photoemission spectra in  $\text{La}_{1-x}\text{Sr}_x\text{MnO}_3$ . *Journal of Applied Physics*. 2013; 113(4):043710.
- [158] Horiba K, Taguchi M, Chainani A, Takata Y, Ikenaga E, Miwa D, et al. Nature of the Well Screened State in Hard X-Ray Mn 2p Core-Level Photoemission Measurements of  $\text{La}_{1-x}\text{Sr}_x\text{MnO}_3$  Films. *Physical review letters*. 2004; 93(23):236401.
- [159] Hishida T, Ohbayashi K, Kobata M, Ikenaga E, Sugiyama T, Kobayashi K, et al. Empirical relationship between X-ray photoemission spectra and electrical conductivity in a colossal magnetoresistive manganite  $\text{La}_{1-x}\text{Sr}_x\text{MnO}_3$ . *Journal of Applied Physics*. 2013; 113(23):233702.
- [160] Horiba K, Maniwa A, Chikamatsu A, Yoshimatsu K, Kumigashira H, Wadati H, et al. Pressure-induced change in the electronic structure of epitaxially strained  $\text{La}_{1-x}\text{Sr}_x\text{MnO}_3$  thin films. *Physical Review B*. 2009; 80(13):132406.
- [161] Van der Heide H, van Bruggen C. Characterization of the valence band of  $\alpha$ -MnS by comparison of UPS and XPS spectra. *Materials Research Bulletin*. 1982; 17(12):1517-21.
- [162] Gryko J, McMillan PF, Marzke RF, Ramachandran GK, Patton D, Deb SK, et al. Low-density framework form of crystalline silicon with a wide optical band gap. *Physical Review B*. 2000; 62(12):R7707.
- [163] Wolter S, Luther B, Waltemyer D, Öneby C, Mohny S, Molnar R. X-ray photoelectron spectroscopy and X-ray diffraction study of the thermal oxide on gallium nitride. *Applied Physics Letters*. 1997; 70(16):2156-8.
- [164] Carin R, Deville J, Werckmann J. An XPS study of GaN thin films on GaAs. *Surface and Interface Analysis*. 1990; 16(1-12):65-9.
- [165] Yang Y-G, Ma H-L, Xue C-S, Zhuang H-Z, Hao X-T, Ma J, et al. Preparation and structural properties for GaN films grown on Si (111) by annealing. *Applied Surface Science*. 2002; 193(1-4):254-60.

- [166] Hashizume T, Ootomo S, Inagaki T, Hasegawa H. Surface passivation of GaN and GaN/AlGaIn heterostructures by dielectric films and its application to insulated-gate heterostructure transistors. *Journal of Vacuum Science & Technology B: Microelectronics and Nanometer Structures Processing, Measurement, and Phenomena*. 2003; 21(4):1828-38.
- [167] Saha NC, Tompkins HG. Titanium nitride oxidation chemistry: An X-ray photoelectron spectroscopy study. *Journal of Applied Physics*. 1992; 72(7):3072-9.
- [168] Tabet N, Faiz M, Al-Oteibi A. XPS study of nitrogen-implanted ZnO thin films obtained by DC-Magnetron reactive plasma. *Journal of Electron Spectroscopy and Related Phenomena*. 2008; 163(1-3):15-8.
- [169] Ottaviano L, Passacantando M, Verna A, D'Amico F, Gunnella R. Mn  $L_{2,3}$  X-ray absorption spectra of a diluted Mn-Ge alloy. *Applied physics letters*. 2007; 90(24):242105.
- [170] Kang J-S, Kim G, Wi S, Lee S, Choi S, Cho S, et al. Spatial chemical inhomogeneity and local electronic structure of Mn-doped Ge ferromagnetic semiconductors. *Physical review letters*. 2005; 94(14):147202.
- [171] Hwang J, Ishida Y, Kobayashi M, Hirata H, Takubo K, Mizokawa T, et al. High-energy spectroscopic study of the III-V nitride-based diluted magnetic semiconductor  $Ga_{1-x}Mn_xN$ . *Physical Review B*. 2005; 72(8):085216.
- [172] Bogusławski P, Bernholc J. Fermi-level effects on the electronic structure and magnetic couplings in (Ga, Mn)N. *Physical Review B*. 2005; 72(11):115208.
- [173] Yang X, Chen Z, Wu J, Pan Y, Zhang Y, Yang Z, et al. Magnetic and magneto-transport properties of  $Ga_{1-x}Mn_xN$  grown by MOCVD. *Journal of crystal growth*. 2007; 305(1):144-8.
- [174] Goldberg S, Fadley C, Kono S. Photoionization cross-sections for atomic orbitals with random and fixed spatial orientation. *Journal of Electron Spectroscopy and Related Phenomena*. 1981; 21(4):285-363.
- [175] Baji Z, Lábadi Z, Molnár G, Pécz B, Vad K, Horváth ZE, et al. Highly conductive epitaxial ZnO layers deposited by atomic layer deposition. *Thin Solid Films*. 2014; 562:485-9.
- [176] Haider MB. XPS Depth Profile Analysis of  $Zn_3N_2$  Thin Films Grown at Different  $N_2/Ar$  Gas Flow Rates by RF Magnetron Sputtering. *Nanoscale research letters*. 2017; 12(1):5.

- [177] Futsuhara M, Yoshioka K, Takai O. Structural, electrical and optical properties of zinc nitride thin films prepared by reactive rf magnetron sputtering. *Thin Solid Films*. 1998; 322(1-2):274-81.
- [178] Gangil S, Nakamura A, Yamamoto K, Ohashi T, Temmyo J. Fabrication and EL emission of ZnO-based heterojunction light-emitting devices. *Journal of Korean Physical Society*. 2008; 53:212-7.
- [179] Mishra M, Krishna T, Rastogi P, Aggarwal N, Chauhan AKS, Goswami L, et al., New approach to clean GaN surfaces. *Materials Focus*. 2014; 3(3):218-23.
- [180] Magnuson M, Mattesini M, Höglund C, Birch J, Hultman L., Electronic structure of GaN and Ga investigated by soft X-ray spectroscopy and first-principles methods. *Physical Review B*. 2010; 81(8):085125.
- [181] Ohsawa T, Ueda S, Suzuki M, Tateyama Y, Williams JR, Ohashi N. Investigating crystalline-polarity-dependent electronic structures of GaN by hard X-ray photoemission and ab-initio calculations. *Applied Physics Letters*. 2015; 107(17):171604.
- [182] Williams J, Yoshikawa H, Ueda S, Yamashita Y, Kobayashi K, Adachi Y, et al. Polarity-dependent photoemission spectra of wurtzite-type zinc oxide. *Applied Physics Letters*. 2012; 100(5):051902.
- [183] Veal T, King P, Jefferson P, Piper L, McConville C, Lu H, et al. In adlayers on c-plane InN surfaces: A polarity-dependent study by X-ray photoemission spectroscopy. *Physical Review B*. 2007; 76(7):075313.
- [184] King P, Veal TD, Schleife A, Zúñiga-Pérez J, Martel B, Jefferson P, et al. Valence-band electronic structure of CdO, ZnO, and MgO from X-ray photoemission spectroscopy and quasi-particle-corrected density-functional theory calculations. *Physical Review B*. 2009; 79(20):205205.
- [185] Park WI, Yi GC. Electroluminescence in n-ZnO nanorod arrays vertically grown on p-GaN. *Advanced Materials*. 2004; 16(1):87-90.
- [186] Nakayama T, Murayama M. Electronic structures of hexagonal ZnO/GaN interfaces. *Journal of crystal growth*. 2000; 214:299-303.



## Acknowledgements

Firstly, I would like to express my deep-felt respect and sincere gratitude to my advisor *Prof. Dr. Marcus Bär* for the continuous support during my Ph.D. study, for his patience and motivation on helping me during the whole research and writing this thesis. To be honest, he opens the door of science for me. I really thank him to offer this great opportunity for my Ph.D. career, otherwise I would be a little girl in my small world. Many thanks!

Besides my advisor, I would like to thank *Dr. Regan Wilks* for his immense insightful comments, positive encouragement and kind understanding. He motivated me to insist on my research and write my thesis.

My sincere thanks also go to all the members of my department for their patience and support through my Ph.D. career. What a lovely place to work with you guys!

Also, I have to thank all those (*Dr. F. Ruske, Dr. D. Gerlach, Dr. X. X. Liao, Dr. H. Scherg-Kurmes, Dr. M. Meixner, and D. Erfurt*) who have helped me in carrying out the research and given me invaluable guidance.

I would also like to thank the members of my Ph.D. committee, *Prof. Dr. Marcus Bär, Dr. Florian Ruske, Prof. Dr. Ingo Flege, Prof. Dr. Götz Seibold, and Prof. Dr. Inga Fischer*, for their time and efforts in helping me develop my thesis. Thanks!

A very special gratitude goes out to *China Scholarship Council (CSC)* and *Helmholtz Association* for supporting and funding for my research.

Last but not the last, I would like to thank my family: *my parents, my brother, and sister* for supporting me spiritually and believing in me unconditionally throughout my life.



## Conferences

1. BESSY II Tender X-Ray Workshop
2. 5th HZB Joint BESSY and BER II USER MEETING 2013, PVcomB HZB
3. 6th HZB Joint BESSY and BER II USER MEETING 2014 with a joint poster “Metal oxide compounds in thin-film solar cell structures illuminated by tender X-rays”
4. 8th HZB Joint BESSY and BER II USER MEETING 2016
5. 2016 E-MRS Fall Meeting in Warsaw University of Technology, from September 19th to 22nd, 2016, poster presentations: Annealing-induced (optoelectronic) structure changes of  $\text{In}_2\text{O}_3$  variants
6. Visiting National Institute for Materials Science (NIMS) in Japan to study the preparation of GaN-based LED materials by the molecular beam epitaxy (MBE) method